NASA CR-54397
GE 65SD4251

STUDY OF NUCLEAR BRAYTON CYCLE POWER SYSTEM

by

S.I. Freedman

prepared for

NATIONAL AERONAUTICS AND SPACE ADMINISTRATION

CONTRACT NASw-980

GENERAL ELECTRIC

MISSILE AND SPACE DIVISION
Valley Forge Space Technology Center
P.O. Box 8555 • Philadelphia 1, Penna.

NOTICE

This report was prepared as an account of Government sponsored work. Neither the United States, nor the National Aeronautics and Space Administration (NASA), nor any person acting on behalf of NASA:

A.) Makes any warranty or representation, expressed or implied, with respect to the accuracy, completeness, or usefulness of the information contained in this report, or that the use of any information, apparatus, method, or process disclosed in this report may not infringe privately woned rights; or

B.) Assumes any liabilities with respect to the use of, or for damages resulting from the use of any information, apparatus, method or process disclosed in this report.

As used above, "person acting on behalf of NASA" includes any employee or contractor of NASA, or employee of such contractor, to the extent that such employee or contractor of NASA, or employee of such contractor prepares, disseminates, or provides access to, any information pursuant to his employment or contract with NASA, or his employment with such contractor.

Requests for copies of this report should be referred to

National Aeronautics and Space Administration
Office of Scientific and Technical Information
Attention: AFSS-A
Washington, D.C. 20546

NASA CR-54397
GE 65SD4251

TOPICAL REPORT

STUDY OF NUCLEAR BRAYTON CYCLE POWER SYSTEM

by

S.I. Freedman

Prepared for

NATIONAL AERONAUTICS AND SPACE ADMINISTRATION

CONTRACT NASw-980

August 5, 1965

Technical Management
NASA Lewis Research Center
Cleveland, Ohio
Space Electric Power Office
Lloyd Shure

GENERAL ELECTRIC
MISSILE AND SPACE DIVISION
Valley Forge Space Technology Center
P.O. Box 8555 • Philadelphia 1, Penna.

ABSTRACT

29967

A parametric analysis and system optimization was made of reactor heated Brayton cycle space powerplants in the 50 to 200 KWe range. Models of gas and liquid-metal cooled reactors, shields, turbomachinery, heat exchangers, piping, and gas and liquid-metal filled radiators were synthesized. Application to manned and unmanned missions enabled evaluations to be made of reactors and shield configurations and system integration influences over a wide range of requirements. Turbomachinery performance was based on the efficiencies of the NASA/Lewis two-shaft solar Brayton system. Dependence of optimized system specific weight on shield requirements, turbine inlet temperature and power rating were determined.

TABLE OF CONTENTS

SECTION 1
INTRODUCTION

This report describes the results of Phase I, NASA Contract NASw-980, entitled "Study of Nuclear Brayton Cycle Power System". The objective of this study is to investigate the capabilities of a nuclear Brayton cycle for space applications in the 50-200 KWe range. Two classes of mission were considered as a basis for design and analysis.

1. A manned orbiting spacecraft (Figure 1-1) where the power is used primarily for on-board electrical requirements, (non-propulsion)

2. An unmanned interplanetary probe where the power is used for both instrumentation and terminal electric propulsion.

Emphasis has been placed upon the nuclear reactor heat source, the radiator, and powerplant arrangements as they are influenced by spacecraft integration problems. Phase I of the program consisted of a parametric evaluation of various system configurations, including single-, two-, and three-loop arrangements with different combinations of liquid and gas cooled reactors and radiators. This work involved parametric description of each powerplant subsystem, the incorporation of these models into an overall cycle performance evaluation program, and the optimization of the various powerplants. During Phase II, specific systems are to be selected for each of the two mission classes, and detailed powerplant-vehicle integration studies performed.

A summary of guidelines selected for this program are outlined below:

NUCLEAR BRAYTON CYCLE STUDY GUIDELINES

1. Reactor

   Four reactor concepts are considered:

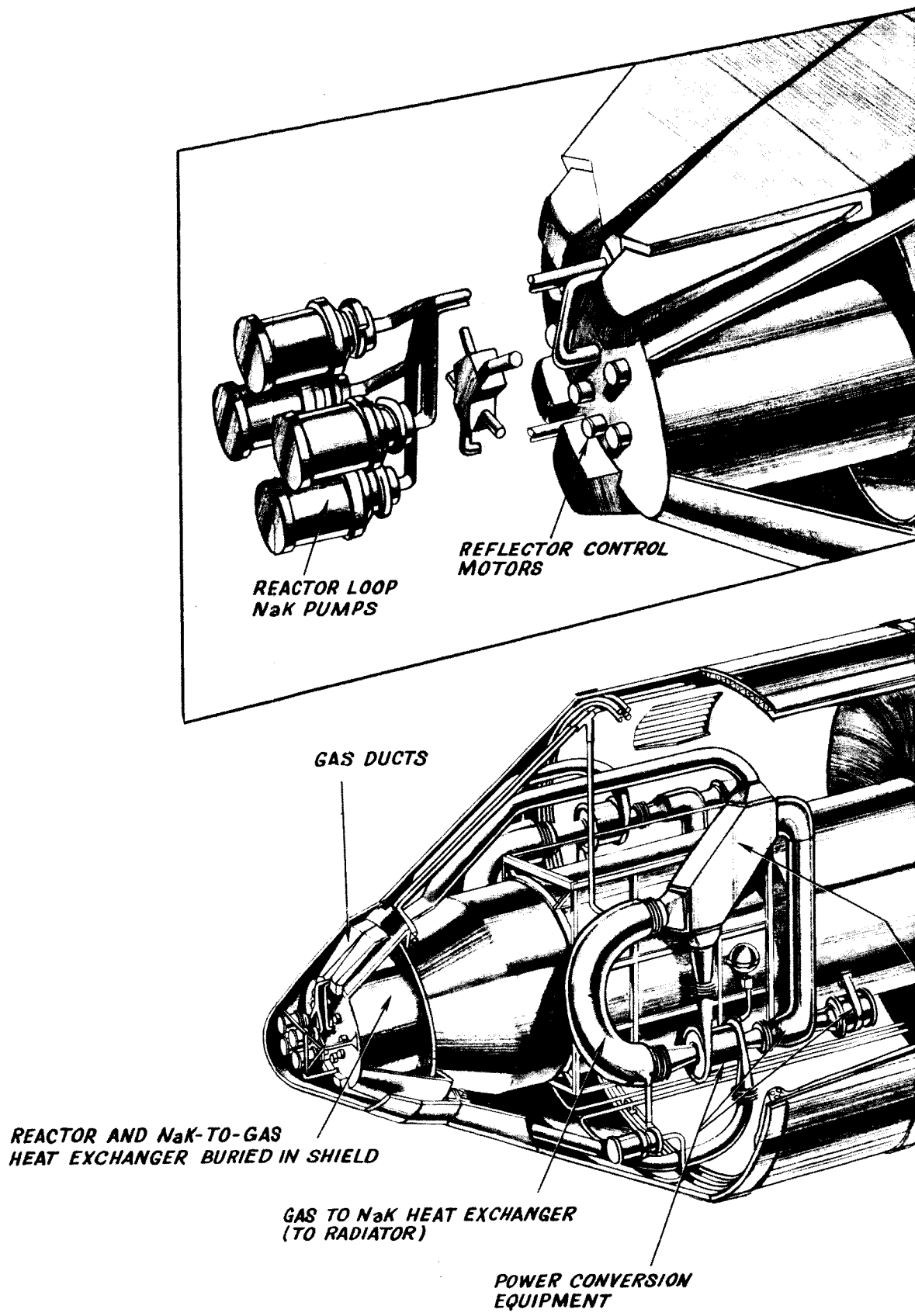
REACTOR LOOP
NaK PUMPS
REFLECTOR CONTROL
MOTORS
GAS DUCTS
REACTOR AND NaK-TO-GAS
HEAT EXCHANGER BURIED IN SHIELD
GAS TO NaK HEAT EXCHANGER
(TO RADIATOR)
POWER CONVERSION
EQUIPMENT

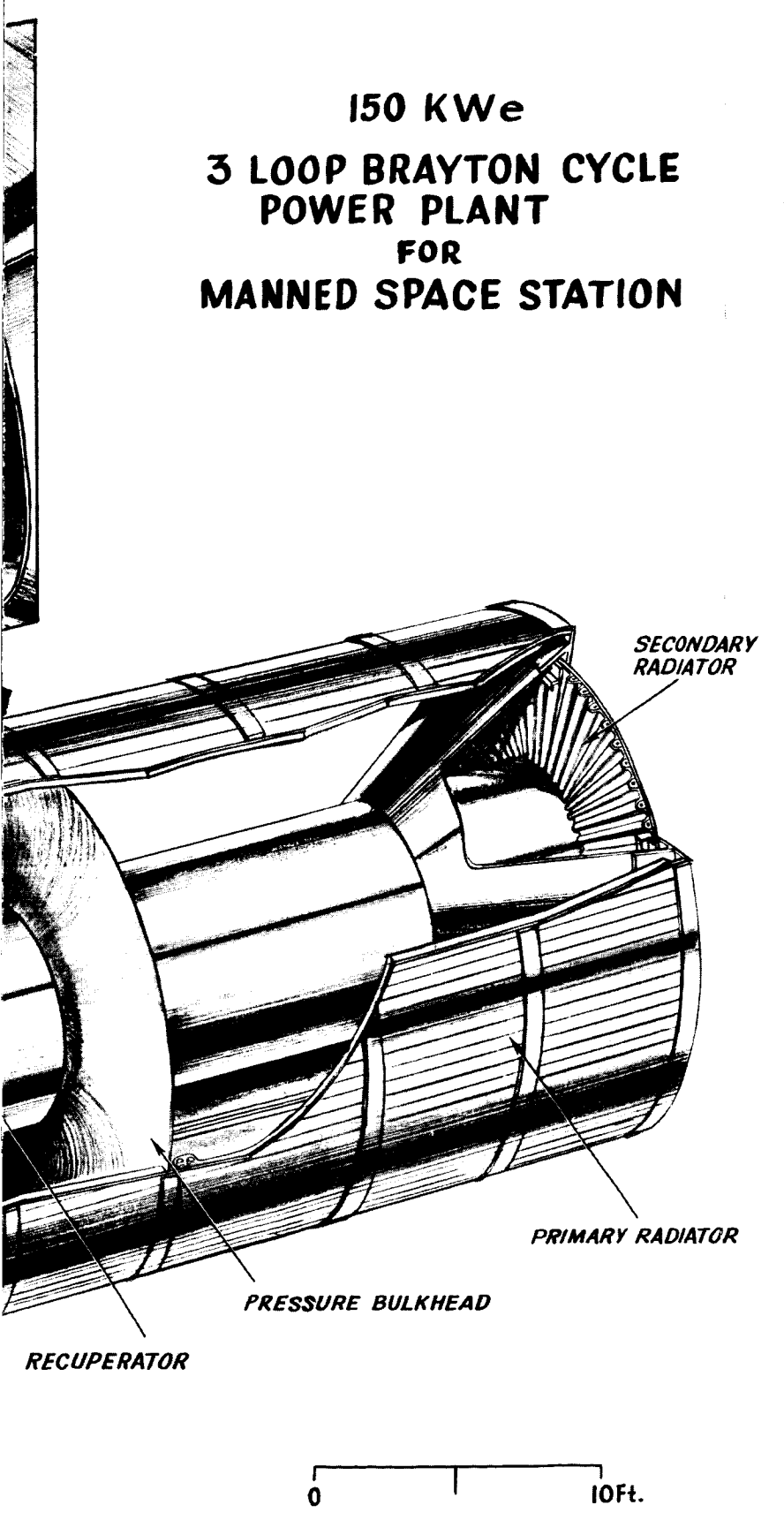

Figure 1-1. 150 KWe Three Loop Brayton Cycle Power Plant for Manned Space Station

a. A gas-cooled, UO_2 fueled, Hastelloy-X clad, pin-type core with $1550^{o}F$ maximum clad.

b. A NaK-cooled, UC fueled Cb-1Zr clad, pin-type core with a maximum clad temperature of $1900^{o}F$

c. A gas-cooled, UC fueled Cb-1Zr clad, pin-type core with $1900^{o}F$ maximum clad

d. A gas-cooled, UO_2-W cermet fueled, refractory clad, matrix reactor with $2600^{o}F$ maximum clad.

2. Powerplant Arrangements

a. An all-gas single loop

b. A gas-cooled reactor and power conversion loop, and a NaK filled radiator

c. A NaK-cooled reactor, gas power conversion loop, and a NaK filled radiator

3. Radiator

a. Material - conventional aluminum, stainless steel, and/or stainless steel clad copper

b. Meteoroid criteria - Whipple 1963A

c. Emissivity - 0.90

d. Solar Absorptivity - 0.40.

4. Working Fluids

a. Argon

b. Neon

5. Turbine inlet temperature range, 1350^{o}-$2200^{o}F$

6. Sink Temperature, $450^{o}R$

7. Power range, 50-200 KWe

8. Turbo-machinery - (See Table 7-1)

a. High Pressure - NASA two shaft solar Brayton machine

b. Low pressure - machine specifications furnished by NASA-Lewis

9. Alternator Efficiency - 88%

SECTION 2
SUMMARY

The results of the parametric analyses and system optimizations, presented in detail in Section 7, are summarized in Figures 2-1 and 2-2. These results were obtained using a Brayton cycle optimization program developed by General Electric to simultaneously analyze interactions between the various subsystems. Appropriate subsystem models were derived for reactors, shields, turbomachinery, heat exchangers, piping, and radiators.

Studies of a typical manned application for the nuclear Brayton cycle were based upon a three-arm, spoke-type, rotating space station. This configuration was chosen because it presents some of the more difficult integration problems. Other space station concepts would yield somewhat different values for optimum system specifications. However, the comparisons and trends shown here are representative of manned stations in general. Radiator envelope limits were established on the assumption that the Saturn IB would be used to launch the initial powerplant as well as any replacements, even though the space station itself is launched on a Saturn V.

The specific weights of powerplants optimized for the space station application are shown in Figure 2-1. A 140-KWe three-loop, powerplant with a 1900^{o}F maximum clad temperature can be accommodated on the present Saturn IB (2200 ft^{2} area limit) at a specific weight of 110 or 170 pounds/KWe (depending on shield amortization). Large power ratings can be accomplished by increasing the Saturn IB envelope, increasing the reactor coolant temperature, employing radiators with more efficient (heavier)fins, increasing the performance levels (and weight) of the heat exchangers and piping, or resorting to deployable radiators. The shield consists of a permanent section attached to the station spoke, plus a section that is attached to, and with the powerplant. The upper curve of Figure 2-1 gives the system specific weight when the entire shielding is written off against a single powerplant. The middle curve (effective weight) applies when the permanent shield weight is averaged over 5 powerplants. The bottom curve represents the specific weight of replacement plants, ignoring permanent shield weight.

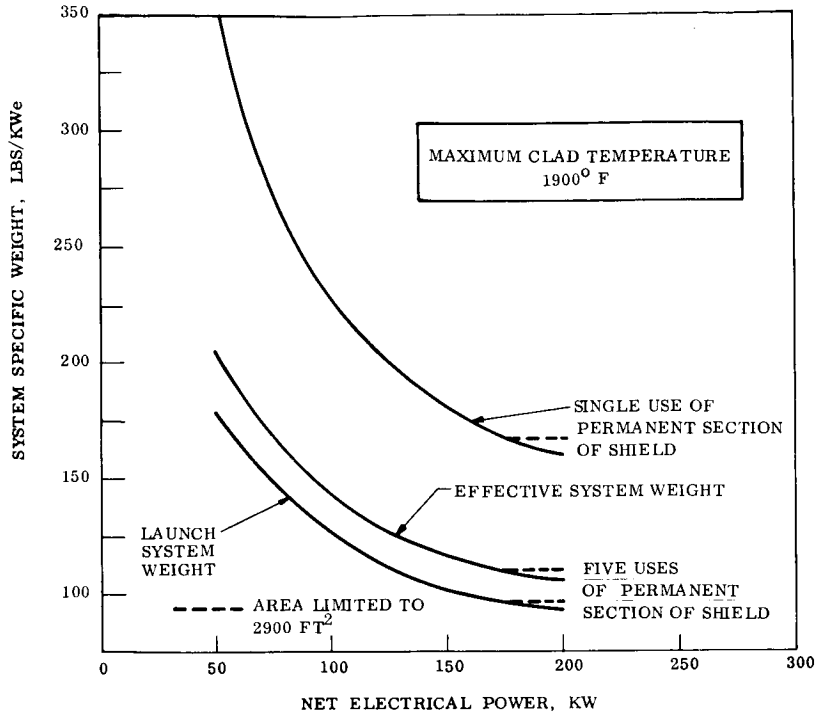

Figure 2-1. Summary of Performance of Brayton Cycle Powerplants for Use with Manned Space Station – Three Loop Systems, Dual Redundancy

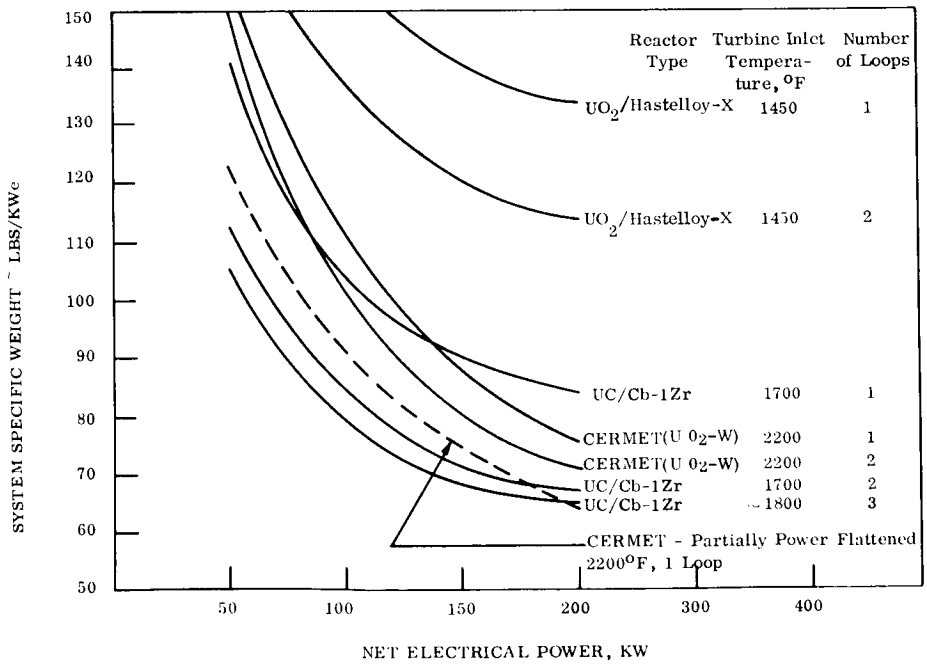

Figure 2-2. Specific Weight of Optimized Powerplants

Powerplants larger than the 140-KWe system could be fitted to the Saturn IB by accepting a weight penalty for a non-optimum radiator. Effects of area limits upon specific weight are discussed in more detail in Section 7. Another possibility for increasing power ratings with fixed radiator configurations is afforded by the potential increase in Saturn IB (SIVB) shroud length allowance. A growth to 2900 ft^2 is projected. This would permit an 185-KWe output with the 1900^{o}F reactor, while still retaining optimum specific weights (95 to 130 lb/KWe from Figure 2-1).

In all cases, the large radiator of the Brayton cycle system can be designed to withstand launch loads with little or no weight penalties for structural additions, other than the tubes, fittings, fins and attachments needed to complete the radiator assembly. It has been found that radiators designed for optimum thermal performance generally have sufficient stiffness and overall strength to meet shock, vibration, and aerodynamic load criteria.

Only the three loop systems (liquid cooled reactor and radiator) were analyzed for the manned applications. This section was based upon crew dose limitations and their effect upon loop activation requirements. A leakage of only 10^{-5} of total fission product inventory, for example, would exceed safe dose levels if permitted to escape into the power conversion loop and radiator. An additional consideration in the choice of an independent liquid metal primary loop is the fact that minimum core diameter, and hence minimum shield weight,will be realized with this arrangement. Shield weight is, of course, the most important single weight factor in the manned space station powerplant application.

The specific weight of optimized one-, two- and three-loop powerplants applied to the typical unmanned spacecraft selected for this study (scientific probe launched by Saturn V) are shown in Figure 2-2. Here, both liquid and gas cooled reactors are considered, since the larger core diameter of a gas cooled reactor has less influence upon system weight with a shadow shield than is the case with a 4π shield on a manned space station. Because of the mission profile for deep space probes, powerplant startup may be deferred for periods of a year or more while the vehicle coasts towards its target under the influence of initial Saturn V Boost. For this reason, an all gas system has the attractive feature of eliminating liquid metal freezing problems during the long coast period.

Use of cermet matrix fuel reactors or refractory clad pin type reactors results in roughly comparable system weights in the 150-200 KWe range of interest. Figure 2-2 shows that these specific weights are typically 75 to 88 pound/KWe, and in both cases power levels of 200-KWe can be achieved with less than the 2900 ft^2 available for radiator area on the three stage Saturn V. In the case of a lower temperature pin type reactor with super-alloy clad, the system is limited to 100-KWe at 2900 ft^2 and the optimum specific weight of this sized powerplant 160 pound/KWe.

Gas-filled radiators were found to be approximately 20 percent smaller and lighter when internal fins (vanes) are built into the radiator tubes. A parametric model of such a gas-filled radiator was synthesized. The effect of radiator structural weight has been included in this model, and the influence of this parameter upon overall system optimization was determined. Effects of turbomachinery pressure level were also investigated. Results indicate that any gains in turbine and compressor efficiency, obtained through the use of lower pressure levels, will be more than offset by the added reactor diameter and weight, and the increased pressure drop in the heat transfer equipment. Reduction in system operating pressure is only attractive in liquid-metal cooled reactor systems, where the turbomachinery loop can be divorced from the reactor.

Based upon the parametric studies covered in this report, work is continuing in Phase II to define operational requirements and design details for the selected powerplant concepts.

SECTION 3
REACTOR PARAMETRIC ANALYSIS

Three types of fast spectrum reactor heat sources have been studied for the Brayton cycle power system:

a. A reactor containing cylindrical UO_2 fuel pins and Hastelloy-X cladding, with inert gas coolant

b. A UC fuelded reactor with Cb-1Zr cladding, with either Nak (indirect cycle) or inert gas coolants

c. A UO_2-W cermet fueled reactor with refractory cladding with inert gas coolant

The maximum turbine inlet temperatures assumed for each of these conceptual designs were:

a. $1450^{o}F$ (UO_2 fuel, Hastelloy-X clad)

b. $1700^{o}F$ (UC fuel, Cb-1Zr clad) with gas coolant, $1800^{o}F$ with NaK coolant

c. $2200^{o}F$ (UO_2-W Cermet fuel, refractory clad)

Reactor nuclear, thermal, and hydraulic design model, and the parametric performance summary are classified and are contained in Volume II of this report. The results summarize the reactor core diameter-reactor overall pressure drop tradeoff relationships used in the system optimization. The weight of the various reactors are shown as functions of the core diameter. A mechanical model of the reactors is presented in order that the overall envelope, which requires shielding, can be related to the core diameter.

SECTION 4
SHIELDING AND RADIATION ANALYSIS

In any nuclear reactor system, the required shield configuration and weight are extremely sensitive to the specific application. For this reason, a purely parametric presentation of the shield is difficult to obtain. Nevertheless, it is important that some model for shielding be developed, so that this influence can be factored into the Brayton Cycle System optimization. In this section, the basic shield weight relationship and the effects of coolant loop activation are determined for two particular mission and vehicle configurations; an unmanned scientific probe and a manned orbiting space station.

4.1 SHIELD WEIGHTS

4.1.1 UNMANNED SYSTEM

An unmanned space vehicle, such as that shown in the powerplant design section, was selected as the basis for shield weight analysis. Reactor fluxes of 3.32×10^{16} neutrons per second MWth, and 1.29×10^{17} Mev per second MWth, gamma, were assumed.* Attenuation was computed on the basis of single scattering.

Tungsten and lithium hydride (LiH) were selected for gamma and neutron shielding. The required thickness of the materials are determined by:

$$t_{LiH} = \frac{t_{LiH_o}}{1 - x} - \frac{t_{W_o} \lambda_{LiH_n}}{(1 - x) \lambda_{W_n}}$$

$$t_W = \frac{t_{W_o}}{1 - x} - \frac{t_{LiH_o} \lambda_{W_\gamma}}{(1 - x) \lambda_{LiH_\gamma}} \qquad (1)$$

*Cochran, D.L., and Friedman, S.T., Preliminary Shield Design for Nuclear Electric Space Powerplants, AIEE paper 62-1236.

where:

$( )_o$ refers to the thickness of LiH required for neutron flux attenuation before allowance for neutron absorbtion by W, and to the thickness of W required for gamma flux attenuation before allowance for gamma absorbtion by LiH.

$$x = \frac{\lambda_{W_\gamma} \lambda_{LiH_n}}{\lambda_{W_n} \lambda_{LiH_\gamma}}$$

λ = attenuation length

The factor 1-x accounts for the correction for attenuation by the secondary material. An average shield density is obtained from a model consisting of a homogeneous mixture of tungsten and steel-encapsulated lithium hydride, and is given by:

$$\rho = \frac{t_W \rho_W + t_{LiH} \rho_{LiH}}{t} \qquad (2)$$

$\rho_W = 1185$ lbs/ft^3

$\rho_{LiH} = 57.1$ lbs/ft^3. (including the weight of the stainless steel encapsulation)

Previous shielding studies performed in conjunction with the design of powerplants for unmanned electric* propulsion missions have shown tha the scatter shield should provide a total flux attenuation approximately 1/20 that of the direct shield (3 relaxation lengths less). For the lower range of power levels in this study, no gamma scatter shield is needed, and only LiH is required for that portion of the shield obscuring the radiator from the reactor. Unmanned shield geometry is shown in Figure 4-1. The primary shield protects the payload and is sufficient if only a shallow angle conical radiator is used. The

*Study of Electrical Propulsion for Unmanned Scientific Missions, Volume II, Comparisons of Nuclear Power Systems, 1965, NASA CR-54348.

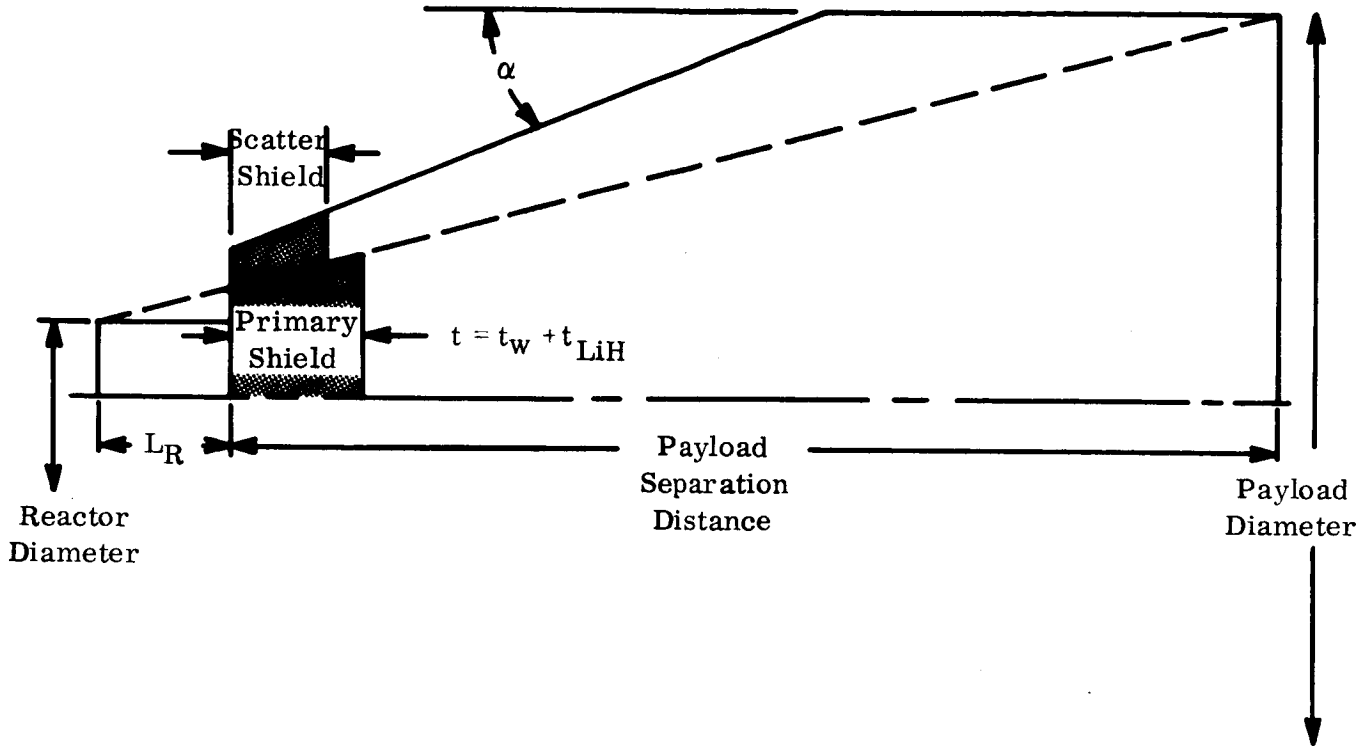

Figure 4-1. Shield Geometry for Unmanned Spacecraft

scatter shield is required for blunt nosed designs which may be used to maximize available radiator area. The scatter shield sufficiently reduces the dose contribution from forward scattering by the radiator structure. Permissible payload dose was assumed to be 10^{11} nvt and 10^{6} rad (gamma), measured at the base of the radiator. Using the resultant shield model as a subroutine in the system evaluation, consistent values for shielded reactor weights can be obtained as a function of reactor length, power, diameter, or radiator cone angle.

Figures 4-2 and 4-3 show shield weights for reactors with length to diameter (L/D) ratios of 1.0 and 1.2 as functions of reactor diameter for 300 and 1200 KW thermal. Both blunt nose (30 degree half angle) and purely conical radiators are given. The shallow conical half angle varies between 14 and 18 degrees, depending upon the reactor diameter and L/D. Payload diameter of 260 inches, and payload separation distance of 40 feet, are held constant. These values are representative of either Saturn V (escape) or Saturn IB (orbit) launched spacecraft. Shield weights are found to be quite sensitive to both reactor diameter and

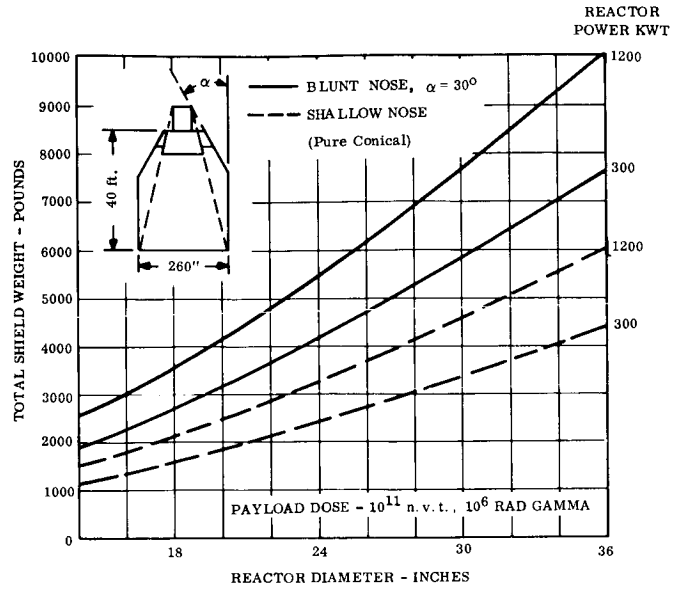

Figure 4-2. Unmanned Vehicle Shield Weights, Reactor L/D = 1.0

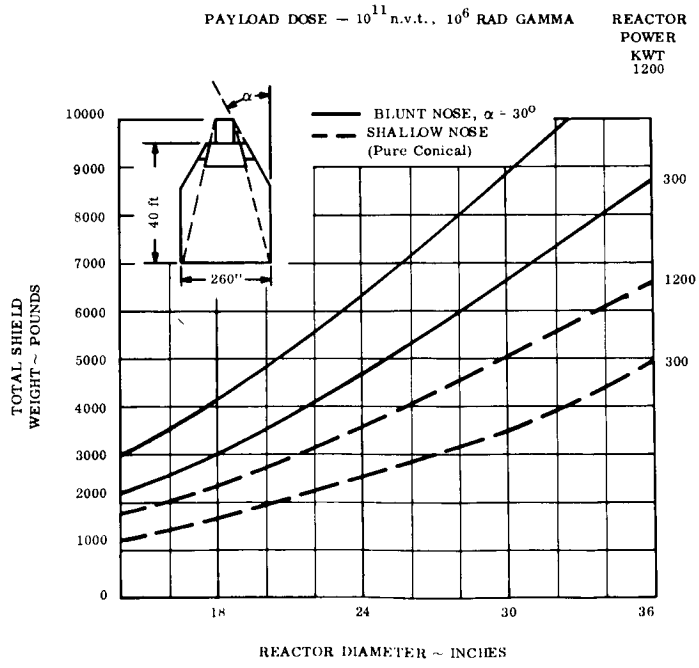

Figure 4-3. Unmanned Vehicle Shield Weights, Reactor L/D = 1.2

radiator cone angle. Power level and reactor L/D have lesser effects for the unmanned case, but are still important. Figures 4-4 and 4-5 show the weight of the shields for unmanned applications as a function of the reactor thermal power. Figure 4-4 shows lines of constant reactor diameter for a cone half angle of 15° and for reactor envelope L/D ratios of 1.0, 1.5, and 2.0. Figure 4-5 shows lines of constant cone half-angle for a reactor L/D ratio of 1.5.

4.1.2 MANNED SYSTEM

A three-arm, rotating space station was selected for the manned application.* The requirement that the radiation fluxes at the base of the radiator be low enough for use in conjunction with a manned space station, and the requirement for rendezvous shielding results in substantially heavier shields than for the unmanned application and places even greater importance on obtaining minimum reactor diameter. Dose distribution and station geometry were held constant, as shown in Figure 4-6 and shield weights calculated for different reactor and power system options.

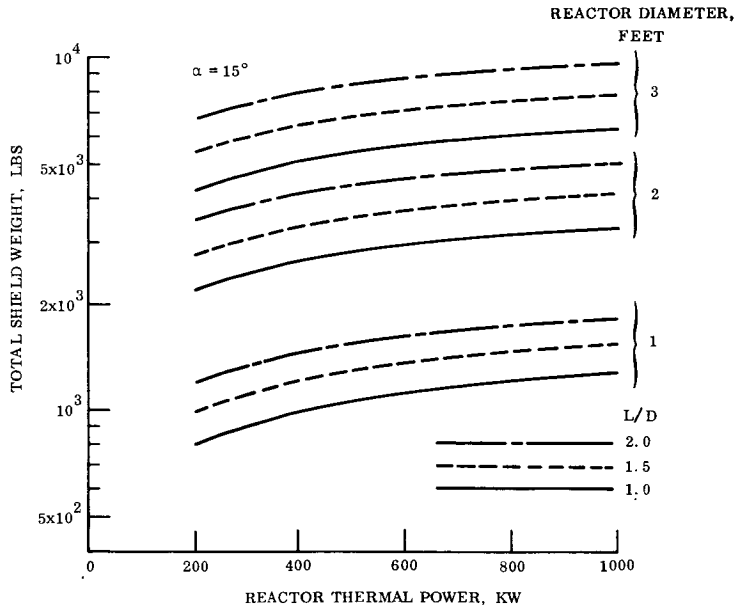

Figure 4-4. Total Shield Weight versus Reactor Thermal Power Reactor Envelope L/D Ratios of 1.0, 1.5 and 2.0

*Study on Application of Nuclear Electric Power to Manned Orbiting Space Stations. Final Summary Report. Sept. 1964, NASA CR-54161.

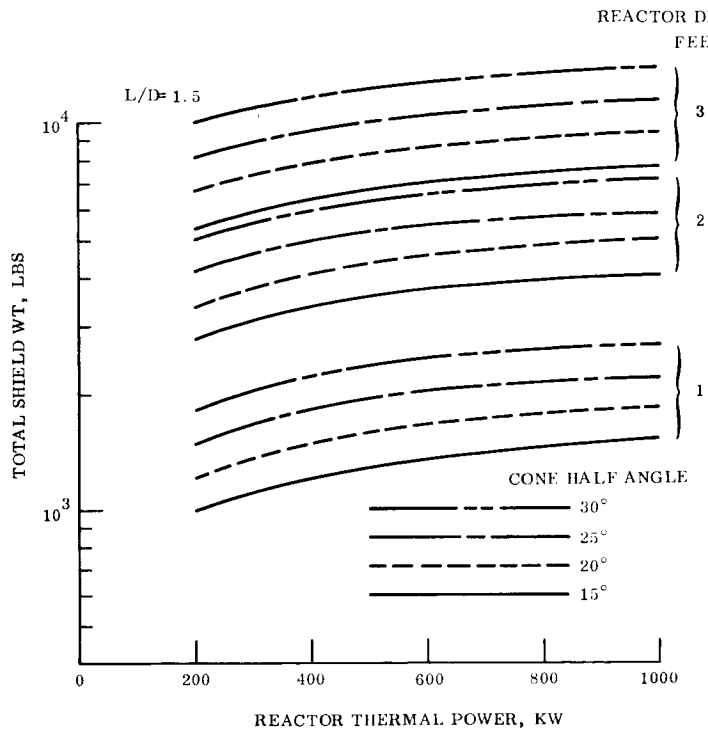

Figure 4-5. Total Shield Weight versus Reactor Thermal Power Reactor Envelope L/D Ratio of 1.5

Figure 4-7 shows the generalized shield geometry, which provides for replacement of a powerplant without discarding the main shield. Also included in this design is space for a liquid metal-to-gas heat exchanger within the shield. This may be required in a manned system to avoid loop contamination. The liquid metal-to-gas heat exchanger is also attractive as a means of obtaining the smallest possible shield weight.

Shield weight versus reactor diameter for representative reactor configurations is shown in Figure 4-8. Power level has a fairly strong effect on configuration, due to the fact that much of the volume is represented by the rendezvous shield section which has a substantial percentage thickness change with power (high dose rates - low attentuation). The direct shield portion is much thicker, and hence, less affected (on a percentage basis) by changing power.

Since only part of the shield is replaced with each powerplant, an amortization factor should be included in any system logistics analysis using the shield weights of Figure 4-8. Figure

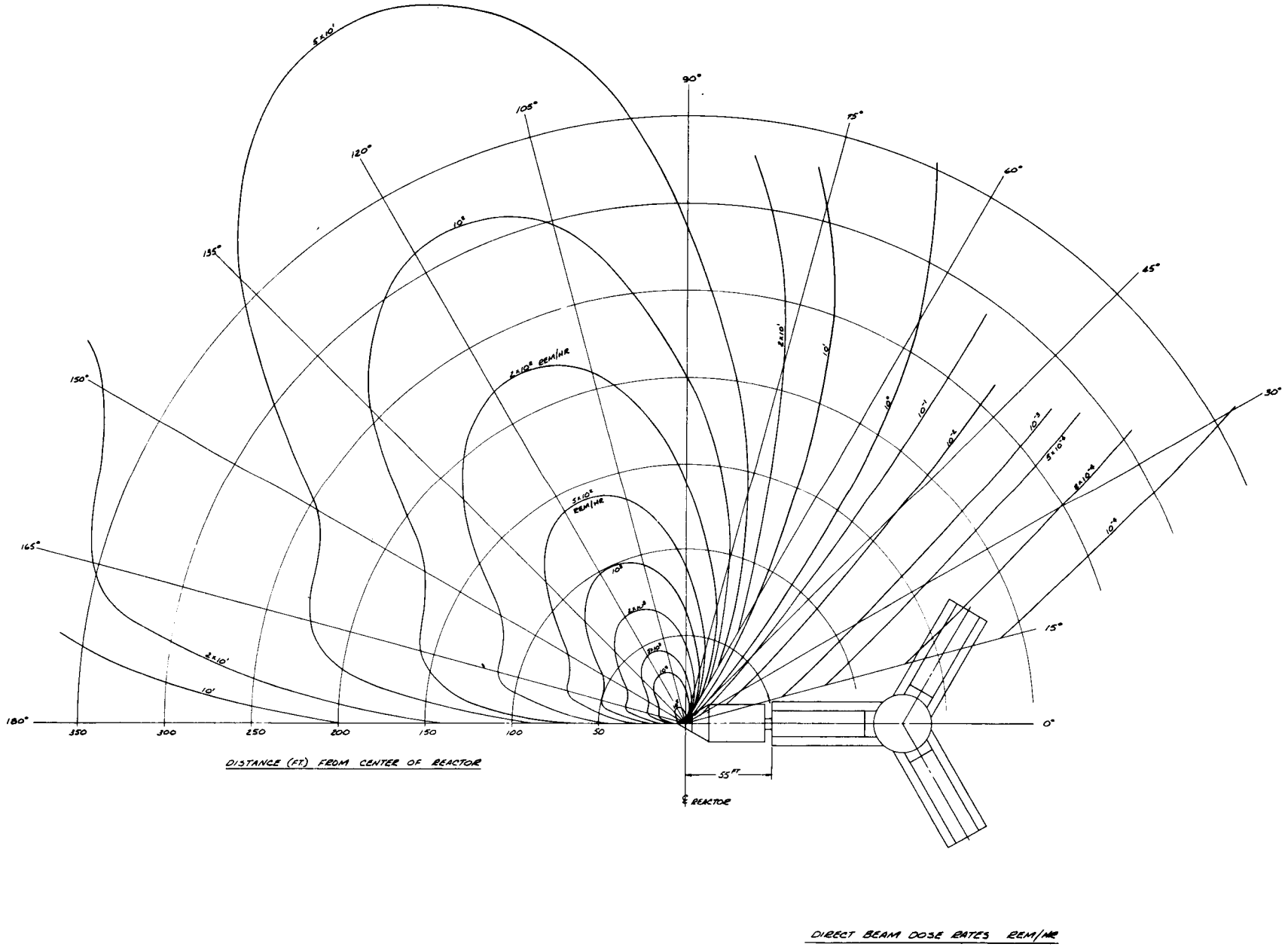

Figure 4-6. Direct Beam Dose Rates REM/HR

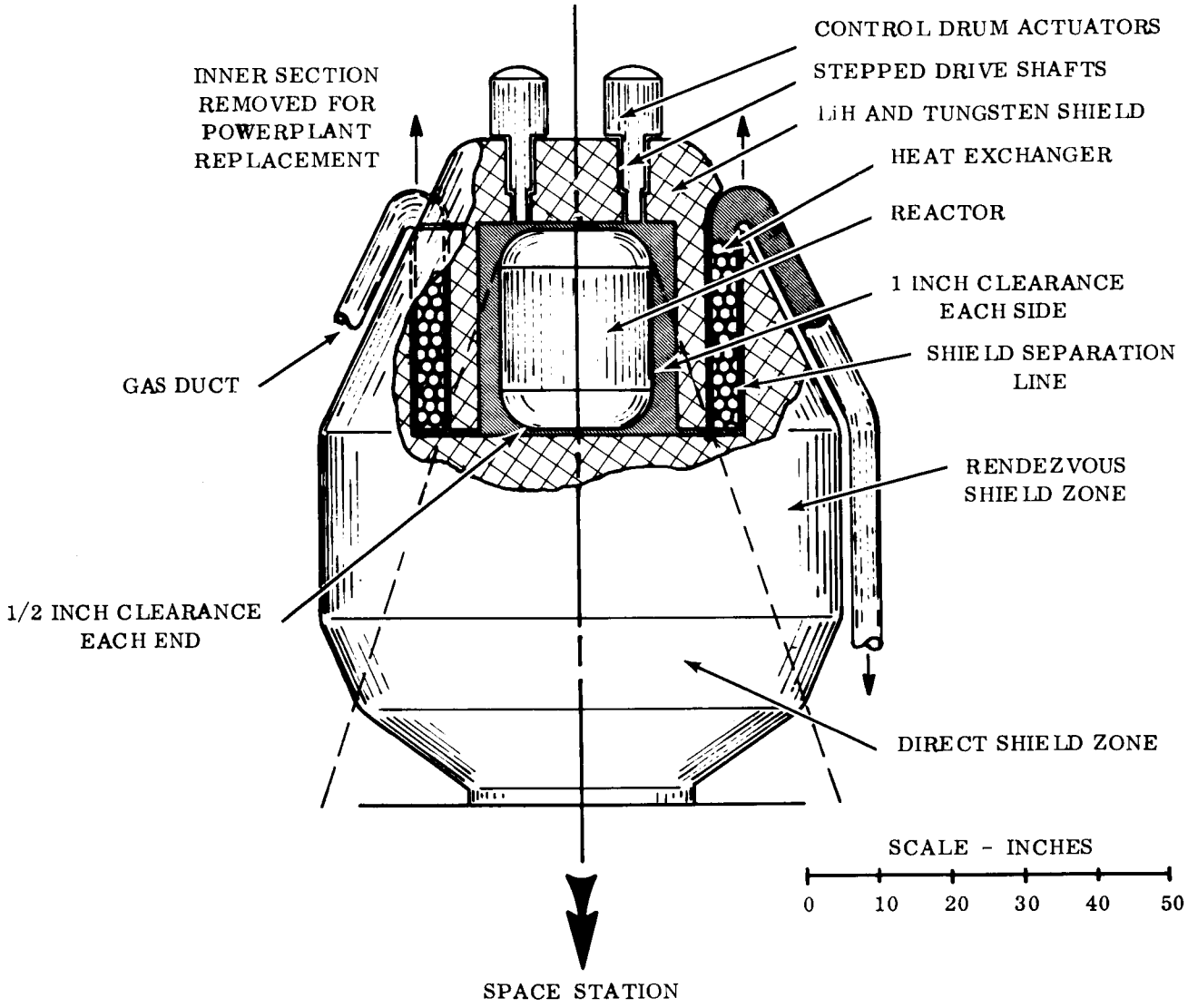

Figure 4-7. Typical Shield Configuration for Spoke Mounted Powerplant on Three Arm Station

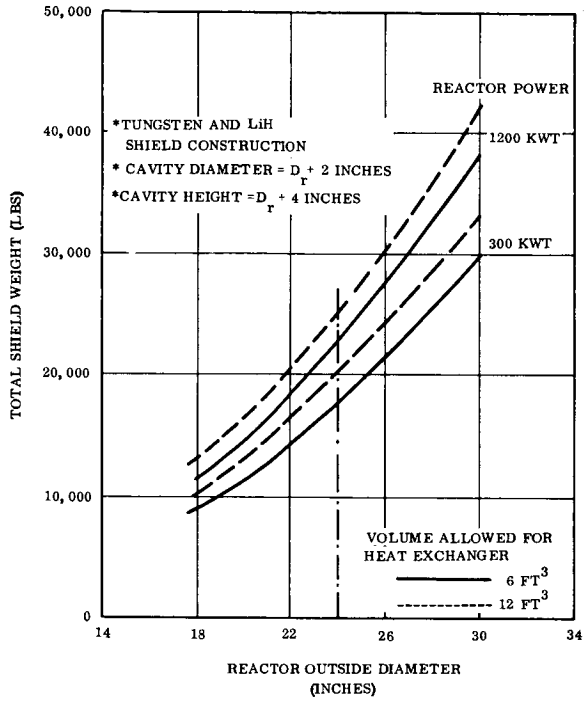

Figure 4-8. Shield Weight - Spoke Mounted Powerplant on Three Arm Space Station

4-9 indicates the effective shield weight multiplier plotted against total number of powerplants used in the complete mission. The replacement weight fraction was found to be almost constant at 15 percent of total weight, regardless of reactor diameter, power level, or heat exchanger volume.

A cross plot of weight versus heat exchanger volume is shown in Figure 4-10 for two typical reactor diameters. The slope of these curves is on the order of 500 to 1000 pounds of shield per cubic foot of heat exchanger. The influence of power level, as identified in Figure 4-11, is found to be 4 to 10 pounds of shield per thermal KW of reactor rating over the 300 to 1200 KWt range of interest.

Of all the effects discussed here, the most significant by far is that of reactor diameter. This represents from 2000 to 3000 pounds per inch of reactor diameter in the appropriate sizes, and exerts a strong influence on the choice of reactor type (liquid versus gas cooled) for a manned application of this type.

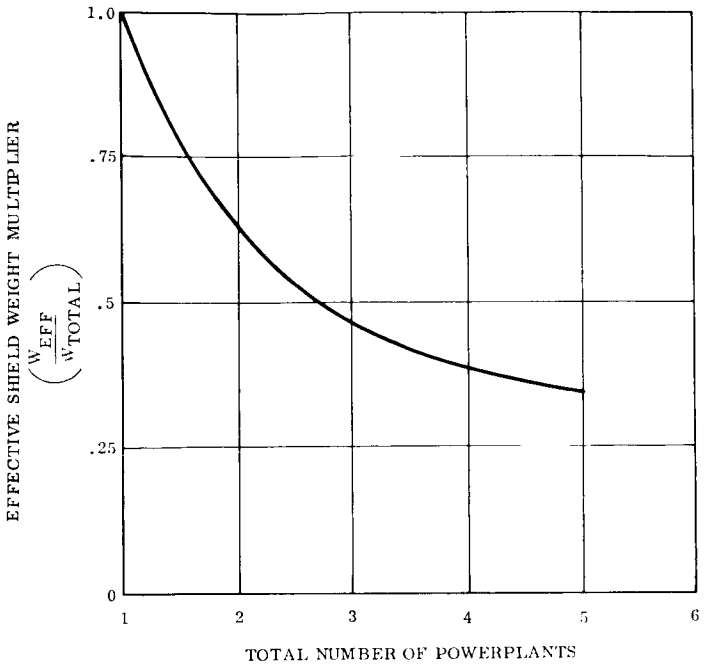

Figure 4-9. Shield Weight Amortization Factor for Manned Space Station

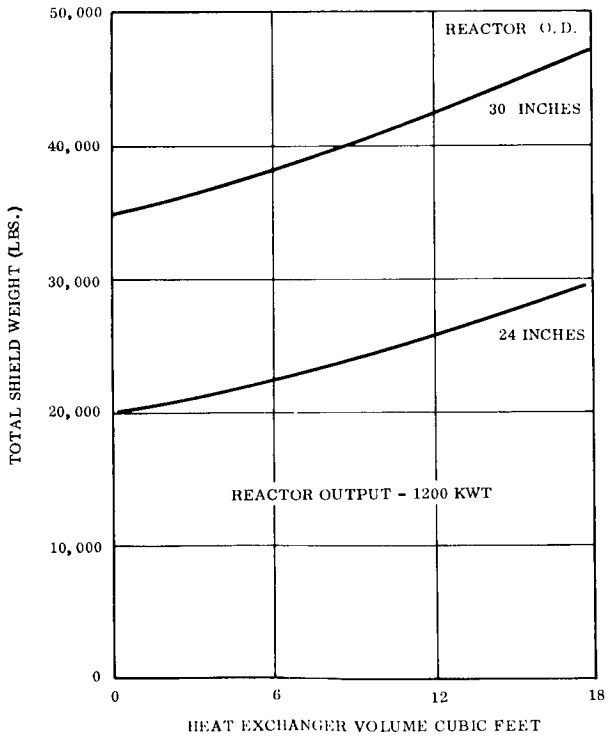

Figure 4-10. Shield Weight vs Heat Exchanger Volume

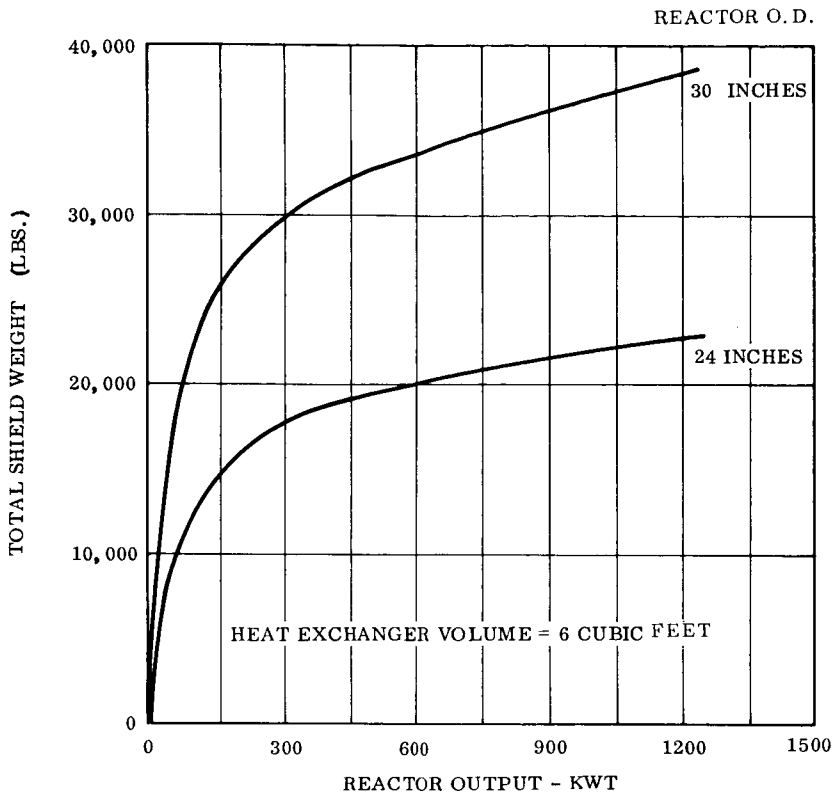

Figure 4-11. Shield Weight vs Power Level

4.2 COOLANT ACTIVATION ANALYSIS - SINGLE LOOP

For single loop Brayton Cycle System, it is necessary to consider the payload radiation dose caused by coolant activation. Calculations were performed on a typical configuration to identify the magnitude of this problem. A three-arm, rotating space station with the powerplant mounted on one spoke was selected for the analysis. Neutron induced activities were determined for both neon and argon as the coolant, and gaseous fission-product activities were calculated as functions of release rates. Direct beam isodoses in the space station due to the gamma rays emitted during the transit and decay of radioactive nuclei in the conical and cylindrical radiators were also calculated. Additional computations determined the dose rate at a single axial position due to scattering of A^{41} decay gamma rays from the radiators. Since the reactor, for this application, is buried in the shield, reflector cooling is required. This is accomplished by passing the incoming gas over the reflectors. Such a cooling technique exposes the gas to a large flux of thermal neutrons.

4.2.1 POWER SYSTEM DESCRIPTION

The power system assumed for this investigation is shown schematically in the cycle diagram of Figure 4-12. The energy source is a fast-spectrum, cermet reactor, with a moderating reflector, operating at a thermal power of one megawatt. The powerplant arrangement with a conical/cylindrical radiator containing the gas coolant is shown in Figure 4-13. Dimensions of an average radiator section are shown in Figure 4-14. Construction materials chosen were 304 stainless steel and copper in one case, and aluminum in the second case. The volume of the radiators and associated piping was ten cubic feet, the average pressure 40 psia, and the mean temperature 500°F. The volume of the turbo-machinery and regenerator was five cubic feet, and the mean temperatures of the turbine and compressor sections were 1400° and 300°F, respectively. The average reactor pressure was 100 psia, with coolant flow rates of 4.165 pounds per second and 8.26 pounds per second for neon and argon, respectively.

Table 4-1. Gas Conditions for Coolant Activation Analyses

Component	Average Press (Psia)	Average Temp (°F)	Average Density (Lb/Ft^3)		Transit Time (Sec)	
			Neon	Argon	Neon	Argon
Radial Reflector	100	755	0.155	0.307	0.127	0.127
End Reflector	100	755	0.155	0.307	0.304	0.0302
Core	100	1218	0.112	0.222	0.00312	0.00312
Radiator	46	500	0.0784	0.155	0.188	0.188
Turbine	73.1	1400	0.0739	0.146	0.0295	0.0295
Compressor	68.4	300	0.169	0.335	0.0675	0.0675
Regenerator	76.9	819	0.113	0.224	0.0452	0.0452
System			0.1059	0.210	0.491	0.491

It is further assumed that $N_i^b(0) = N_{i\gamma}^b \rho_i/\rho_{i-1}$, where ρ is the gas density, to correct for gas density change from region i-1 to i.

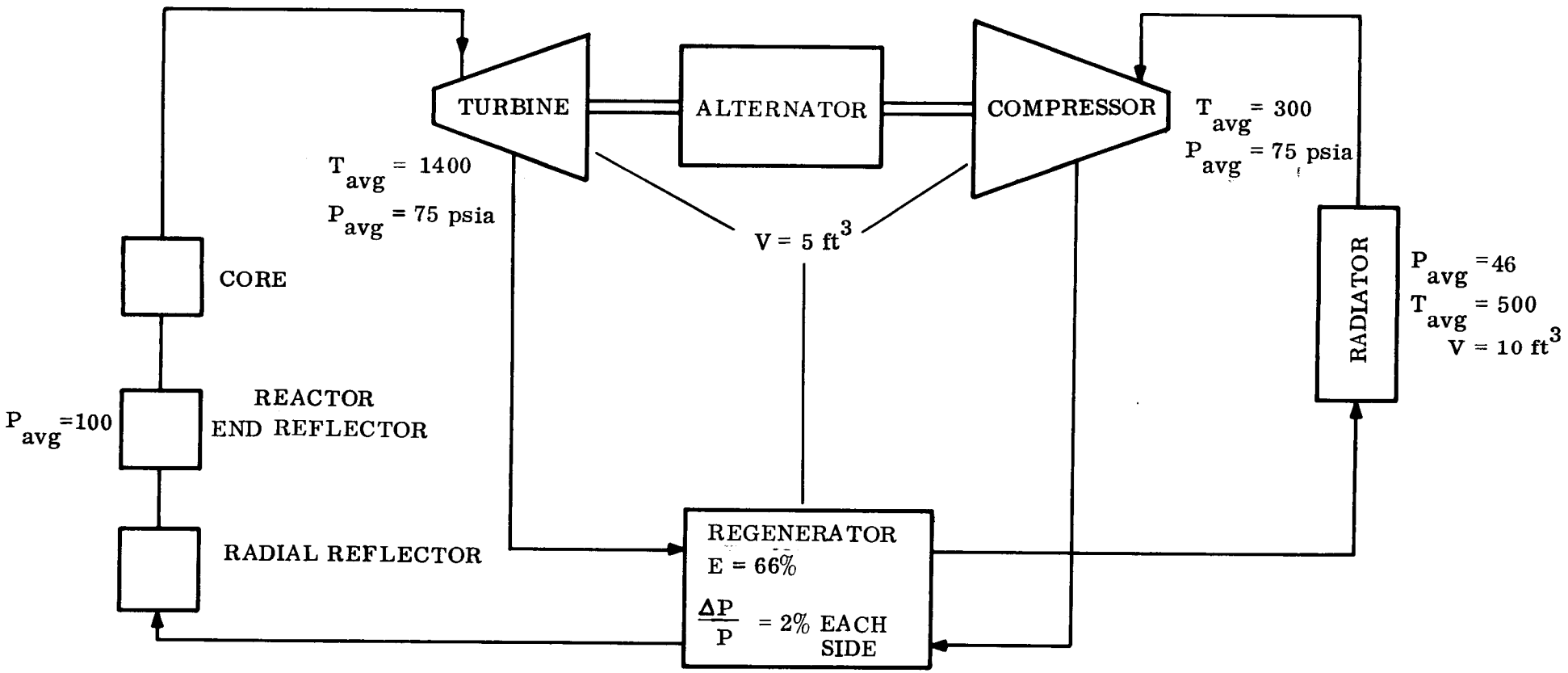

Figure 4-12. Cycle Diagram for Gas System Used in Activation Analysis

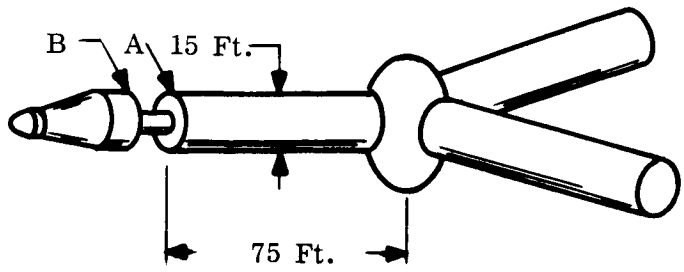

Figure 4-13. Powerplant-Space Station Configuration Used in Activation Analysis

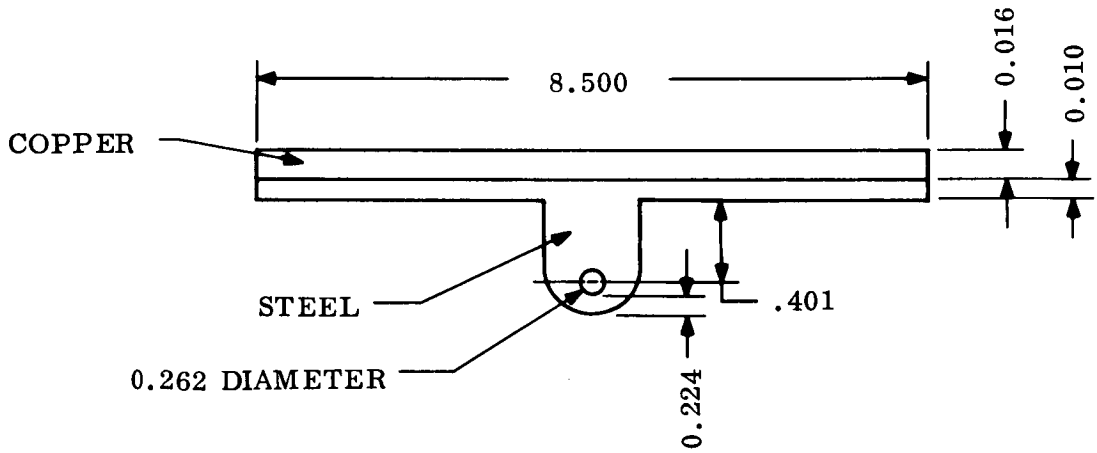

Figure 4-14. Typical Radiator Cross-Section for Loop Activation Analysis
All Aluminum Design Also Considered

N = Number density

Radial Reflector:

$$N_{RR}^{b} = \frac{N_{RR}^{a}\,\bar{\sigma}^{a}\,\bar{\phi}_{RR}}{\lambda^{b}} + \left(N_{RECC}^{b}\,\frac{\rho_{RR}}{\rho_{REGC}} - \frac{N_{RR}^{a}\,\bar{\sigma}^{a}\,\bar{\phi}_{RR}}{\lambda^{b}} \right) e^{-\lambda^{b} t_{RR}} \tag{3}$$

End Reflector:

$$N_{ER}^{b} = \frac{N_{ER}^{a}\,\bar{\sigma}^{a}\,\bar{\phi}_{ER}}{\lambda^{b}} + \left(N_{RR}^{b}\,\frac{\rho_{ER}}{\rho_{RR}} - \frac{N_{ER}^{a}\,\bar{\sigma}^{a}\,\bar{\phi}_{ER}}{\lambda^{b}} \right) e^{-\lambda^{b} t_{ER}} \tag{4}$$

Core:

$$N_{C}^{b} = \frac{N_{C}^{a}\,\bar{\sigma}^{a}\,\bar{\phi}_{c}}{\lambda^{b}} + \left(N_{ER}^{b}\,\frac{\rho_{C}}{\rho_{ER}} - \frac{N_{C}^{a}\,\bar{\sigma}^{a}\,\bar{\phi}_{c}}{\lambda^{b}} \right) e^{-\lambda^{b} t_{c}} \tag{5}$$

Turbine:

$$N_{T}^{b} = N_{a}^{b}\,\frac{\rho_{T}}{\rho_{c}}\; e^{-\lambda^{b} t_{T}} \tag{6}$$

Regenerator - Hot Side:

$$N_{REGH}^{b} = N_{T}^{b}\,\frac{\rho_{REGH}}{\rho_{T}}\; e^{-\lambda^{b} t_{REGH}} \tag{7}$$

Radiator:

$$N^b_{RAD} = N^b_{REGH} \frac{\rho_{RAD}}{\rho_{REGH}} e^{-\lambda^b t_{RAD}} \tag{8}$$

Compressor:

$$N^b_{COMP} = N^b_{RAD} \frac{\rho_{COMP}}{\rho_{RAD}} e^{-\lambda^b t_{COMP}} \tag{9}$$

Regenerator - Cold Side:

$$N^b_{REGC} = N^b_{COMP} \frac{\rho_{REGC}}{\rho_{COMP}} e^{-\lambda^b t_{REGC}} \tag{10}$$

An equilibrium, N_i^b will remain constant with time for each region. Hence, substitute Equations 3, 4, 5, 6, 8, 9, and 10 into Equation 7 to obtain the atom density of b at the exit of the hot side of the regenerator.

$$N^b_{REGH} = \left\{ \frac{N^a_C \bar{\sigma}^a \phi_C}{\lambda^b} + \left\{ \frac{\rho_C}{\rho_{ER}} \left\{ \frac{N^a_{ER} \bar{\sigma}^a \bar{\phi}_{ER}}{\lambda^b} + \left[\frac{\rho_{ER}}{\rho_{RR}} \left[\frac{N^a_{RR} \bar{\sigma} \bar{\phi}_{RR}}{\lambda^b} \right.\right.\right.\right.\right.$$

$$\left.\left.\left.\left.\left. + \left(\frac{\rho_{RR}}{\rho_{REGH}} N^b_{REGH} e^{-\lambda^b (t_{REGC} + t_{COMP} + t_{RAD})} - \frac{N^a_{RR} \bar{\sigma}^a \bar{\phi}_{RR}}{\lambda^b} \right) e^{-\lambda^b t_{RR}} \right] \right.\right.\right.\right.$$

$$\left.\left.\left. - \frac{N^a_{ER} \bar{\sigma}^a \bar{\phi}_{ER}}{\lambda^b} \right] e^{-\lambda^b t_{ER}} \right\} - \frac{N^a_C \bar{\sigma}^a \bar{\phi}_C}{\lambda^b} \right\} e^{-\lambda^b t_C} \left\{ \frac{\rho_{REGH}}{\rho_C} e^{-\lambda^b (t_{REGH} + t_T)} \right. \tag{11}$$

Equation 11 was solved for argon and neon using region-averaged neutron fluxes in two energy groups and the group-averaged activation cross sections tabulated in Table 4-2. Activation by neutrons above 0.025 Mev was neglected.

Table 4-2. Activation Cross Section

Energy Group	$\sigma_{act} A^{40}$, barns	$\sigma_{act} Ne^{22}$, barns
0.08897 ev → 0.025 Mev	0.00429	0.00061
Thermal (775°F)	0.28262	0.0186

Other nuclear data used in the analysis were as follows:

A^{40} 99.6% abundance A = 39.96238^4

$Ne^{40} = 5.340 \times 10^{-5}$ atoms/cm^3

$N_{ER}^{40} = 7.384 \times 10^{-5}$ atoms/cm^3

$N_{RR}^{40} = 7.384 \times 10^{-5}$ atoms/cm^3

A^{41} $\lambda^{41} = 1.052 \times 10^{-4}$ sec^{-1}

E_{γ}^{41} = 1.29 Mev - 99% of disintegrations

Ne^{22} 8.82% abundance A = 21.99138^4

$Ne^{22} = 4.335 \times 10^{-6}$ atoms/cm^3

$N_{ER}^{22} = 5.999 \times 10^{-6}$ atoms/cm^3

$N_{RR}^{22} = 5.999 \times 10^{-6}$ atoms/cm^3

Ne^{23} $\lambda^{23} = 1.824 \times 10^{-2}$ sec^{-1}

E_{γ}^{23} = 0.44 Mev - 33% of disintegrations

The resulting radionuclide densities at the exit of the hot side of the regenerator were:

$$N^{41} = 1.904 \times 10^{10} \text{ atoms/cm}^3$$

$$N^{23} = 6.265 \times 10^{5} \text{ atoms/cm}^3$$

The specific activities at the entrance to the radiator were from

$$\frac{d\, N^{b}_{REGH}}{dt} \frac{\rho_{RAD}}{\rho_{REGH}} = -\lambda^{b} N^{b}_{REGH} \frac{\rho_{RAD}}{\rho_{REGH}}, \; b \frac{\text{disintegrations}}{\text{cm}^3 - \text{sec}} \qquad (12)$$

$$\lambda^{41} N^{41} \frac{\rho_{RAD}}{\rho_{REGH}} = 1.390 \times 10^{6} \text{ disintegrations/cm}^3 \text{-sec}$$

$$\lambda^{23} N^{23} \frac{\rho_{RAD}}{\rho_{REGH}} = 7.930 \times 10^{3} \text{ disintegrations/cm}^3 \text{-sec}$$

4.2.2 DIRECT BEAM RADIATION ANALYSIS

Point Kernel Program 14-1 was used to compute direct beam dose rates at nine selected positions to the rear of the radiator. Because of program limitations, separate approximate solutions were required for the conical and cylindrical radiator sections.

The cylindrical section was approximated by seven tubes and end caps at a radius of 330.2 centimeters (cm). Each tube had an OD of 1.803 cm and an ID of 0.665 cm, and the end caps were 0.569 cm thick. The program considered exponential attenuation and buildup through the tube and integrated over a line source along the axis of each tube. Ten source nodal points were used to describe each line source. The seven tubes were assumed typical of a total of 96 longitudinal tubes on the inner surface of the cylindrical radiator shell. The results for each tube were multiplied by the appropriate symmetry factor to account for

adjacent tubes. The tube material was 304 stainless steel in one case, and aluminum in the other. Appropriate energy dependent gamma ray linear absorption coefficients and buildup coefficients were used for these materials. Energy dependent factors were used to convert from energy flux to absorbed dose rate in rads (tissue) per hour. The fin, or shell, material did not enter into these direct beam calculations, and all material located inside the radiators was neglected.

The conical radiator section was approximated by a 304 stainless steel conical shell of 0.569 cm normal thickness. The program in this case integrated over 12 equally spaced ring sources located on the outer surface of the conical shell. This conical shell approximation will effect a higher than actual average attenuation thickness. However, the point kernel analysis will underestimate the buildup in slant penetration calculations. Nevertheless, the error should be small, since the material attenuation will be very small compared to the geometrical attenuation.

The previously quoted specific activities at the radiator entrance gave line source densities of 6.157×10^5 and 3.965×10^2 Mev/cm-sec, respectively, for A^{41} and Ne^{23} decay in the tubes of the cylindrical radiator. The specific activities were converted to equivalent cylindrical surface source strengths of 2.235×10^4 and 1.275×10^2 disintegrations/cm^2 -sec for A^{41} and Ne^{23}, respectively, and assumed to apply to the conical radiator surface. Thus, ring source strengths in Mev/radian-sec appropriate to each ring were derived for input to the program.

Figures 4-15, 4-16, 4-17, and 4-18 illustrate direct beam isodoses in the space station for Ne^{23} decay with 304 stainless steel cylindrical radiator, Ne^{23} decay with an aluminum cylindrical radiator, A^{41} decay with a 304 stainless steel cylindrical radiator, and A^{41} decay with an aluminum cylindrical radiator, respectively.

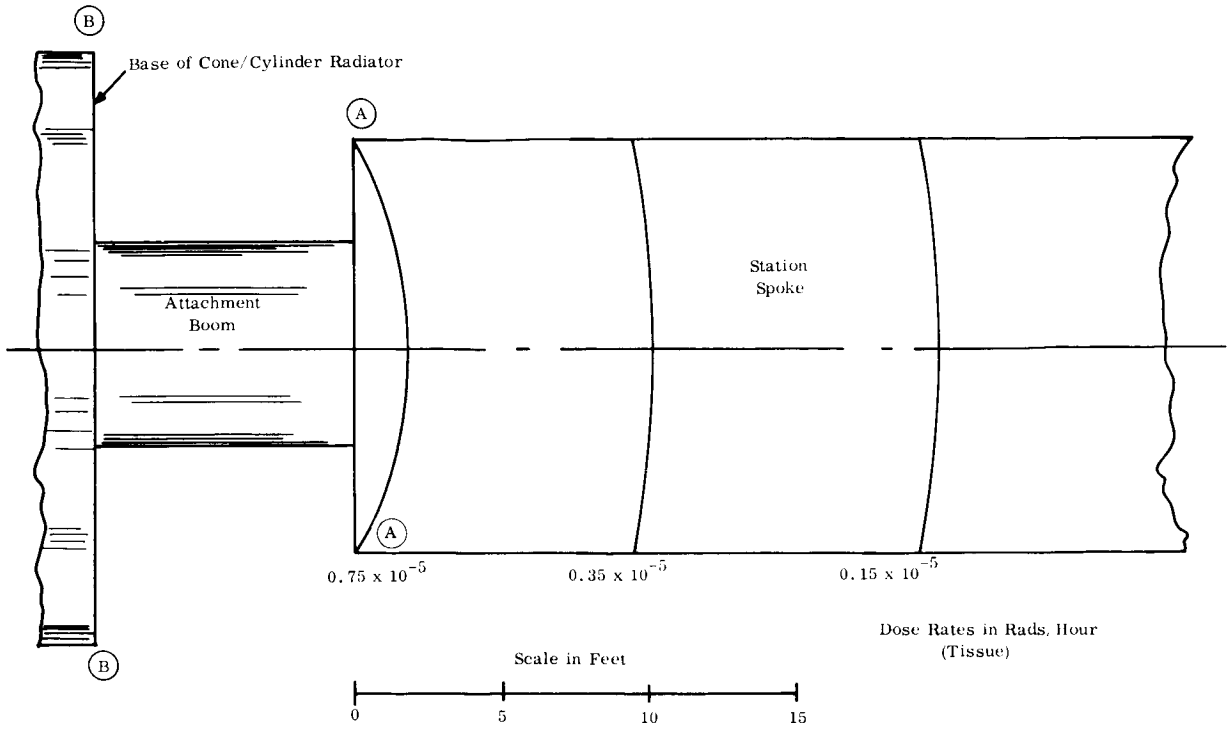

Figure 4-15. Ne^{23} Decay Gamma Ray Isodoses for Stainless Steel Radiator

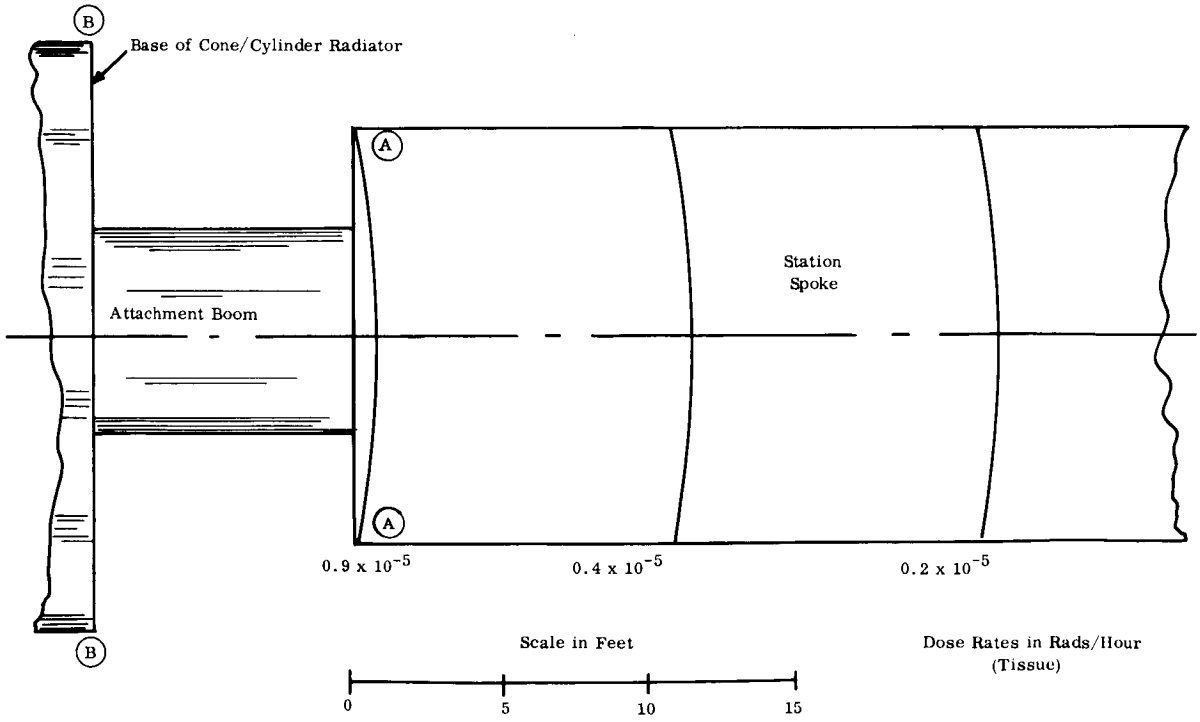

Figure 4-16. Ne^{23} Decay Gamma Ray Isodoses for Aluminum Radiator

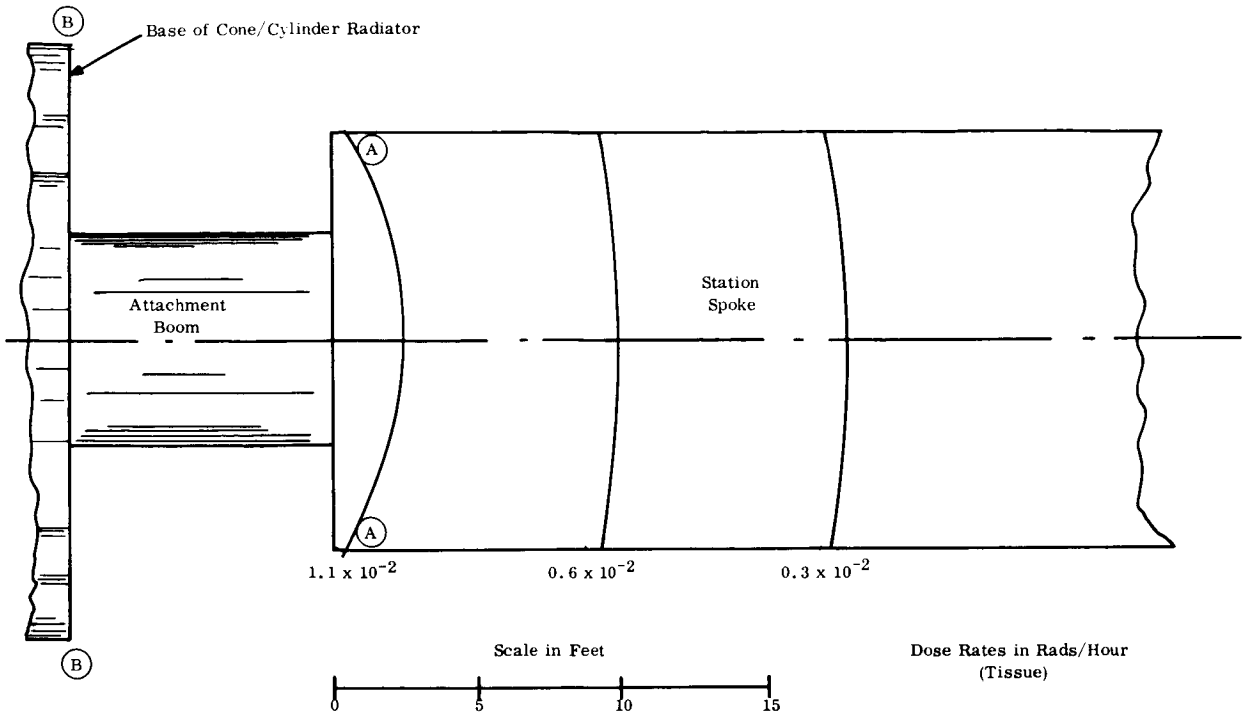

Figure 4-17. A^{41} Decay Gamma Ray Isodoses for Stainless Steel Radiator

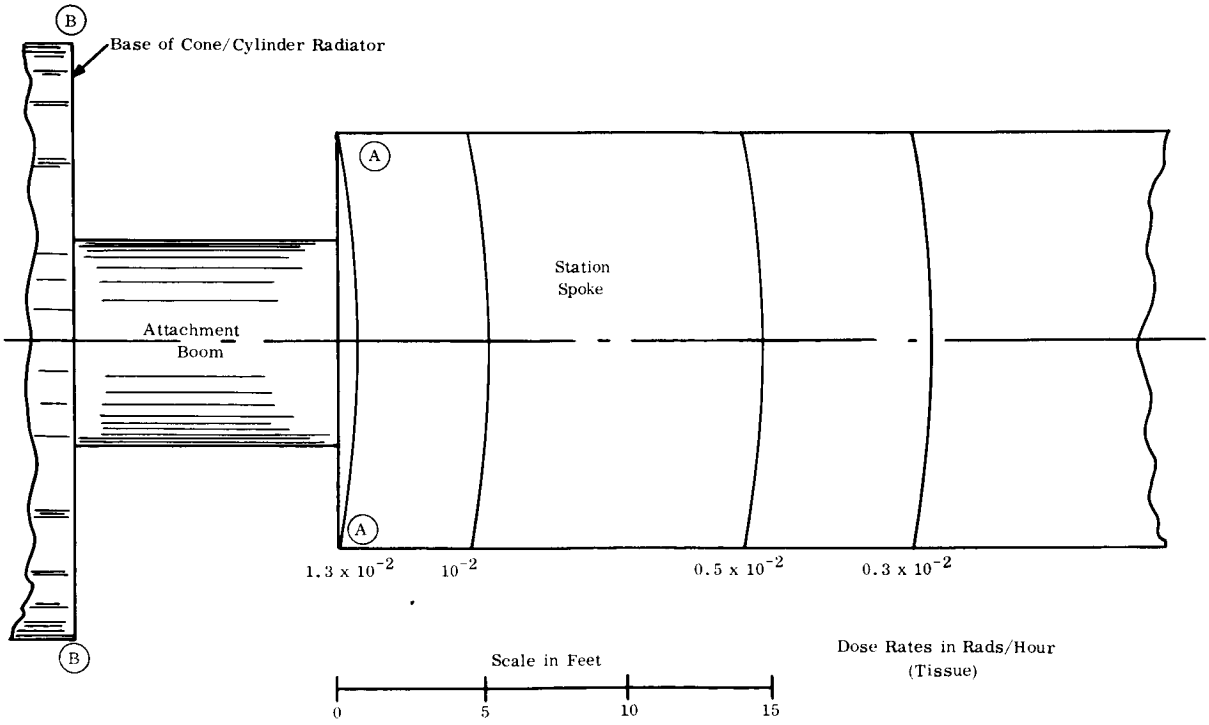

Figure 4-18. A^{41} Decay Gamma Ray Isodoses for Aluminum Radiator

4.2.3 SINGLE - SCATTERING ANALYSIS

The importance of A^{41} decay gamma ray scattering from the radiator fin surface was calculated for a single axial position to the rear of the radiator. Since the shells are thin, a single-scattering analysis was considered adequate. Only the 304 stainless steel and copper shells were considered and the materials in those were assumed mixed homogeneously.

The following equations for single-scattering of gamma rays from conical surface sources by thin conical shells to an axial receiver were derived and solved using program PANACEA. As in the direct-beam analysis, all materials located in the cavity inside the radiators were neglected. Coordinates and dimensions in these equations are defined in Figure 4-19.

$$D_3 = 2.391 \times 10^{-2} \sum_{i=1}^{I=20} \sum_{j=1}^{J=20} \sum_{k=1}^{K=20} \frac{S_1(E_1)\, R_1\, \Delta Z_{1i} \sec \beta_1\, R_2\, t_2\, \Delta \phi_{2i}\, \Delta Z_{2k} \sec \beta_2}{\rho_1^2\, \rho_2^2}$$

$$\delta_2\, (Z/A)_2 \frac{d\sigma'}{d\Omega} \frac{E_1\, K(E_z)}{1 + \frac{E_1}{0.51}(1-\cos\theta)}, \frac{\text{Rad (tissue)}}{\text{hr}} \qquad (13)$$

$$\rho_1^2 = (R_2 \cos\phi_2 - R_1 \cos\phi_1)^2 + (R_2 \sin\phi_2 - R_1 \sin\phi_1)^2 + (Z_2 - Z_1)^2 \qquad (14)$$

$$\rho_2^2 = R_2^2 + (Z_3 - Z_2)^2 \qquad (15)$$

$$\theta = \arccos \left[\left(\frac{R_2 \cos\phi_2 - R_1 \cos\phi_1}{\rho_1} \right) \left(\frac{-R_2 \cos\phi_2}{\rho_2} \right) \right.$$

$$\left. + \left(\frac{R_2 \sin\phi_2 - R_1 \sin\phi_1}{\rho_1} \right) \left(\frac{-R_2 \sin\phi_2}{\rho_2} \right) + \left(\frac{Z_2 - Z_1}{\rho_1} \right) \left(\frac{Z_3 - Z_2}{\rho_2} \right) \right] \qquad (16)$$

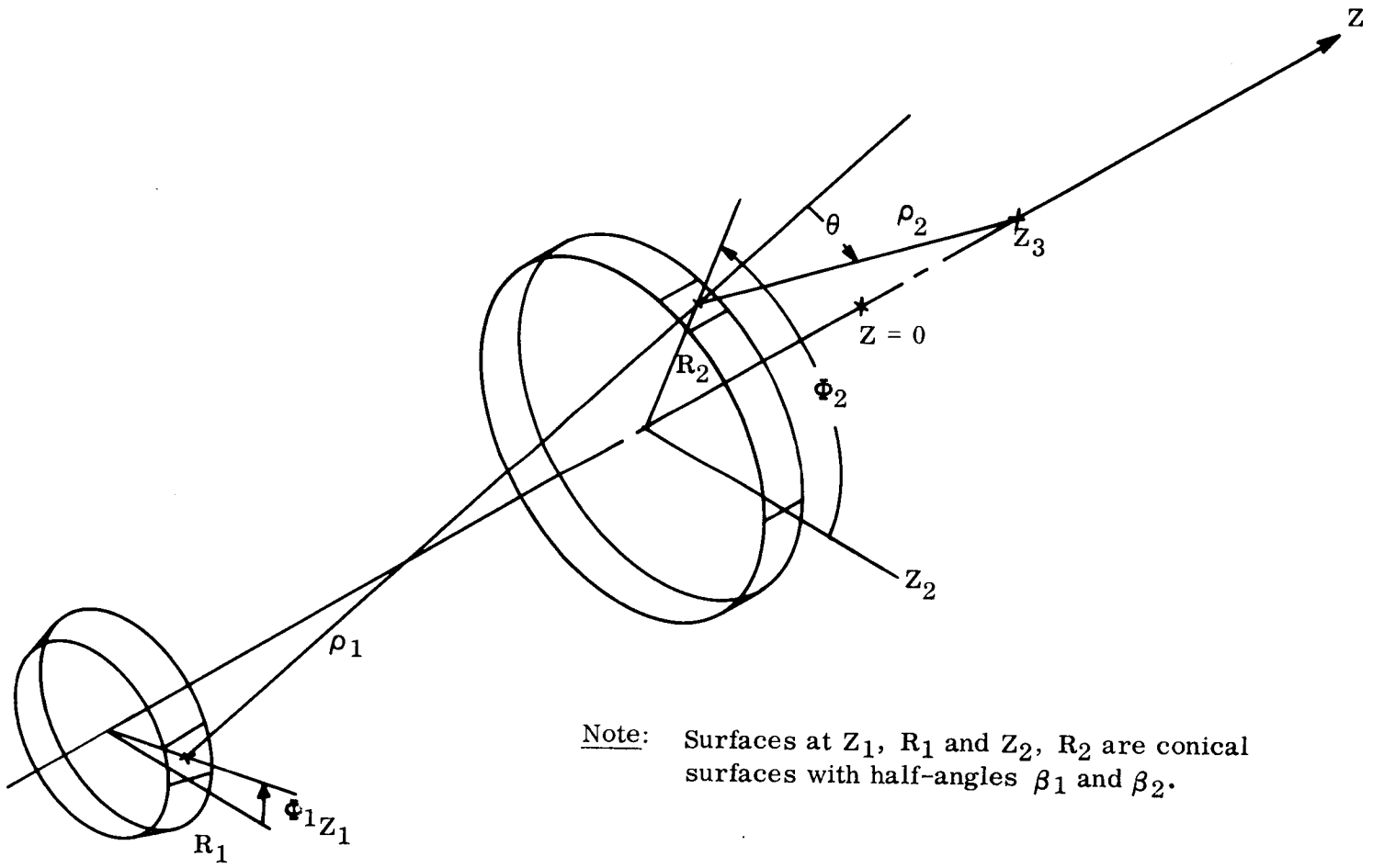

Note: Surfaces at Z_1, R_1 and Z_2, R_2 are conical surfaces with half-angles β_1 and β_2.

Figure 4-19. Schematic for Single Scattering Analysis

$$\frac{E_2}{E_1} = \frac{1}{1 + \frac{E_1}{0.51}(1 - \cos\theta)} \tag{17}$$

$$\frac{d\sigma'}{d\Omega} = \frac{E_2}{E_1} - \left(\frac{E_2}{E_1}\right)^2 \sin^2\theta + \left(\frac{E_2}{E_1}\right)^3 \tag{18}$$

where:

$$S_1(E_1) = \frac{\text{source photons of } E_1 \text{ Mev}}{\text{cm}^2 - \text{sec}}$$

$K(E_2)$ = factor to convert from Mev/cm^2 - sec to Rad (tissue)/hr at E_2 Mev

R_1, Z_{1i} = coordinates of source area $2\pi R_1 \Delta Z_{1i} \sec \beta_1$

$R_2, Z_{2k} \phi_{2j}$ = coordinates of scattering area $R_2 \Delta \phi_{2j} \Delta Z_{2k} \sec \beta_2$

t_2 = thickness of shell at R_2, Z_2, cm

δ_2 = density of shell at R_2, Z_2, gm/cm^3

$(Z/A)_2$ = atomic number/atomic weight of scattering material at R_2, Z_2

Equation 13 was solved using 20 equal values each of ΔZ_{1i}, ΔZ_{2k}, and $\Delta \phi_{2j}$. Because of symmetry it was necessary to sum over ϕ_{2j} only from 0 to π. A uniform source of 2.235×10^4 photons of 1.29 Mev per cm^2-sec from A^{41} decay was used. Attenuation through the radiator tubes was thus neglected. However, this is not a serious error, and the result is conservative. These calculations gave a scattered dose rate of 2.976×10^{-4} rad (tissue)

per hour at an axial position 287 centimeters from the rear of the cylindrical radiator. This is negligible compared to a direct beam A^{41} decay gamma dose rate of 1.28×10^{-2} at the same point with the same radiators.

4.2.4 RELEASED FISSION PRODUCT ANALYSIS

Equilibrium dose rates in the space station due to decay in the radiator of gaseous fission products released by the fuel elements were determined by using calculated fission product specific activities to renormalize the dose rates due to Ne^{23} decay. Differences in attenuation through the radiator walls were safely ignored because of the negligible importance of material attenuation in this configuration.

If fission-product gases continuously escape from the fuel element to the coolant at the rate $\alpha_x Y_x K$ atoms per second, the build-up of radioactive atoms in the coolant is given by

$$\frac{d N_x}{d t} = \alpha_x Y_x K - \lambda_x N_x, \text{ atoms/sec} \tag{19}$$

and

$$\frac{d N_y}{d t} = \alpha_y Y_y K + \lambda_x N_x - \lambda_y N_y \text{ atoms/sec}, \tag{20}$$

where

N_x = number of active atoms of isotope X in the coolant

N_y = number of active atoms of daughter isotope Y in the coolant

Y_x = fission yield of isotope X, atoms/fission

Y_y = fission yield of isotope Y, atoms/fission

K = fission rate, fissions/sec

λ_x = decay constant of parent isotope X, sec^{-1}

λ_y = decay constant of daughter isotope Y, sec^{-1}

α_x = fraction of the number of atoms is isotope X that is released to the coolant

α_y = fraction of the number of atoms of isotope Y that is released to the coolant

It is assumed that there is no filtration or leakage from the coolant system.

Solution of Equations 19 and 20 for the condition that $N_x = N_y = 0$ at $t = 0$ gives:

$$N_x = \frac{\alpha_x Y_x K}{\lambda_x} \left(1 - e^{-\lambda_x t}\right), \frac{\text{atoms}}{\text{sec}} \tag{21}$$

and

$$N_y = \frac{\alpha_y Y_y K}{\lambda_y} \left(1 - e^{-\lambda_y t}\right) + \frac{\alpha_x Y_x K}{\lambda_y} \left(1 - e^{-\lambda_x t}\right), \frac{\text{atoms}}{\text{sec}} \tag{22}$$

Multiplying these equations by the appropriate decay constants gives the following equations for disintegration rate:

$$\lambda_x N_x = \alpha_x Y_x K \left(1 - e^{-\lambda_x t}\right), \frac{\text{dis}}{\text{sec}} \tag{23}$$

and

$$\lambda_y N_y = \alpha_y Y_y K \left(1 - e^{-\lambda_y t}\right) + \alpha_x Y_x K \left(1 - e^{-\lambda_x t}\right), \frac{dis}{sec}, \quad (24)$$

At equilibrium Equations 23 and 24 reduce to:

$$\lambda_x N_x = \alpha_x Y_x K, \frac{dis}{sec} \quad (25)$$

and

$$\lambda_y N_y = (\alpha_y Y_y + \alpha_x Y_x) K, \frac{dis}{sec} \quad (26)$$

The total fission-product activity in the system was divided by the product of the number of pounds of coolant in the system and the fraction of the mass of coolant in the radiator to obtain the activity per pound of coolant in the radiator. This was then multiplied by the density of the coolant in the radiator to determine the specific activity in the radiator. Thus, Equations 25 and 26 become

$$\lambda_x N_x = 3.531 \times 10^{-6} \alpha_x Y_x K, \frac{dis}{cm^3 - sec} \quad (27)$$

and

$$\lambda_y N_y = 3.531 \times 10^{-6} (\alpha_y Y_y + \alpha_x Y_x) K, \frac{dis}{cm^3 - sec} \quad (28)$$

Equation 27 was used to compute specific disintegration rates for release fractions of 10^{-7} for Kr^{87} and Kr^{88}; and 2×10^{-7} for Kr^{85m}, Xe^{133}, Xe^{135}, and Xe^{138}. Equation 28 was used to compute specific disintegration rates for Rb^{88}, Rb^{89}, and Cs^{138} assuming α_y equal zero. Fission yields reported by Katcoff* were used.

*Katoff, S., "Fission-Product Yields from Neutron-Induced Fission", Nucleonics, Nov. 1960.

The ratio of fission product decay gamma ray dose rate to the dose rate due to Ne^{23} decay was determined from:

$$\frac{D_{FP}}{D_{Ni}{}^{23}} = \frac{\sum_x \sum_y \sum_o \left[\lambda_x N_x E_{\gamma xi} f_{\gamma xi} K(E_{\gamma i}) + \lambda_y N_y E_{\gamma yi} f_{\gamma yi} K(E_{\gamma i})\right]}{\lambda^{23} N^{23} f_{\gamma i} E_{\gamma i} K(E_{\gamma i})} \tag{29}$$

where

$E_{\gamma i}$ = gamma energy by transition i

$f_{\gamma i}$ = fraction of disintegrations by transition i

$K(E_{\gamma i})$ = conversion factor, $\frac{\text{rad (tissue)}}{\text{Mev/cm}^2\text{-sec}}$

Using 2.137×10^{-3} rad (tissue)/hr-cm as the numerator of the above equation gave D_{FP}/D_{Ne} 23 equal 0.668. Kr^{88} and Cs^{138} contributed nearly one-half the total dose rate due to fission-product decay gamma rays.

Thus, a fission product dose rate of about 6×10^{-5} rads/hr would occur at the worst point in the space station if fuel element leakage fraction is no worse than 10^{-7}. This represents only 1/1000 of 1 percent of the total inventory of one fuel element in a typical reactor (~100 elements). If leakage is increased to 4×10^{-5} of total inventory, dose rate reaches 2.8 mr/hr at the closest point in the station (25 rem per year), which represents the probable maximum allowance. A leakage therefore, of only 0.04 percent of the fission products in one fuel element, would be intolerable. Note, however, than an unmanned payload could take at least 10^5r per year, and this represents all of the inventory from 16 out of 100 elements.

The total gamma dose due to neon activation and fission fragment release is shown in Figure 4-20 as a function of the Xe^{133} release fraction. At leakages below 10^{-8} the neon activation is the principle contributor. At higher leakages the fission fragments are the chief sources of radiation.

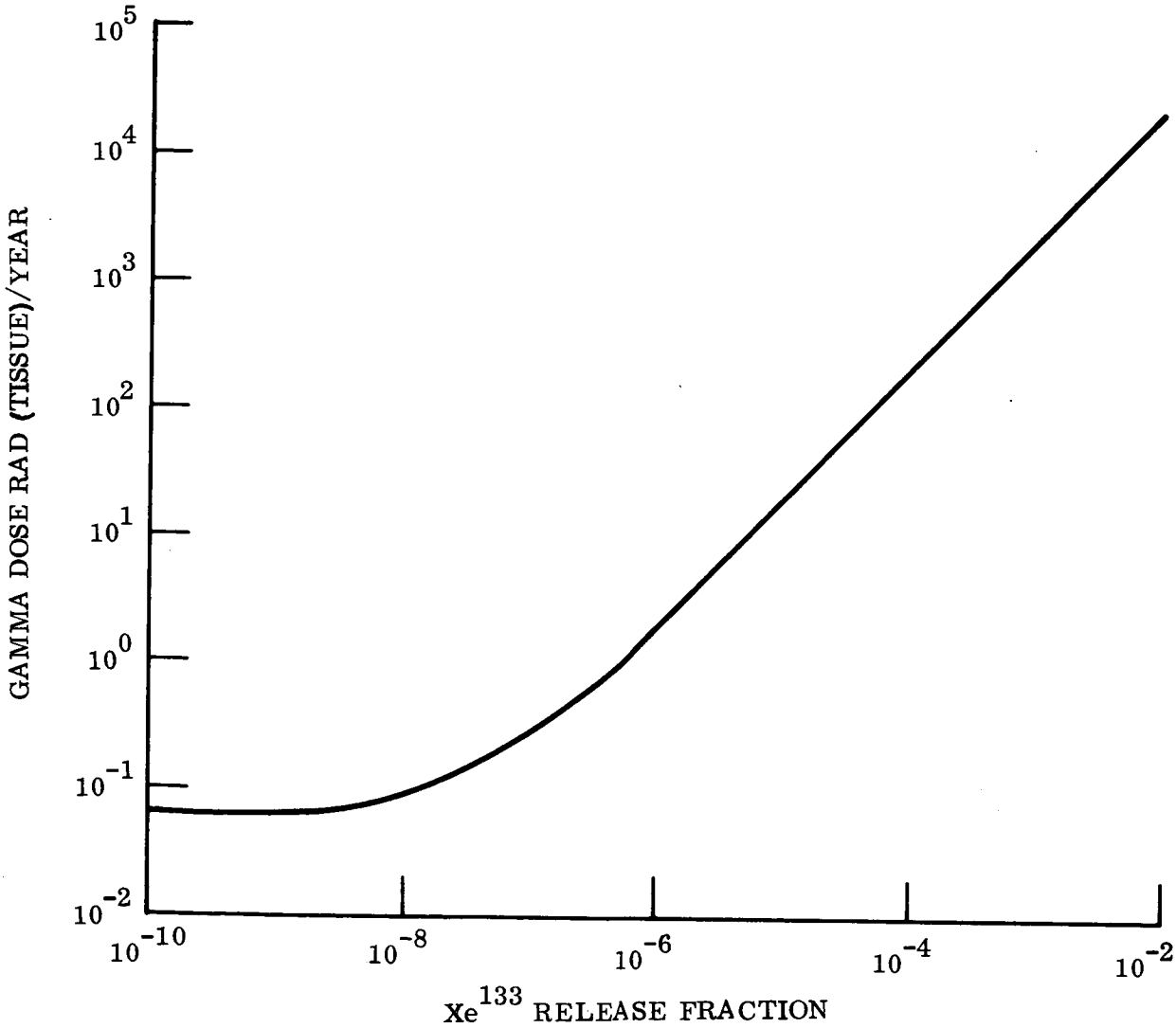

Figure 4-20. Gamma Dose Due to Neon Activation and Fission Fragment Release

4.2.5 CONCLUSIONS ON LOOP ACTIVATION

Although these calculations represent only one typical power system and payload configuration, the results are sufficiently definitive to permit drawing the following conclusions:

- Direct beam dose with Ne^{23} is tolerable in either a manned or unmanned application

- Direct beam A^{41} dose exceeds the specification of 25 Rem/yr. in manned application when the reactor coolant is used to cool the reflector, but appears to be acceptable for unmanned vehicles.

- When the reactor coolant is exposed only to a fast neutron spectrum the direct beam A^{41} dose appears to be acceptable for manned application.

- Fission-product dose rate, due to fuel element leakage, is excessive in a manned application for all but the strictest clad integrity criteria ($\sim 10^{-5}$ leakage). For unmanned vehicles, however, extremely high leakage can be accepted.

On the basis of these findings, emphasis in the study is being directed towards a single loop-all gas system for the unmanned applications, and an indirect system with liquid metal primary loop for the manned space station.

SECTION 5
RADIATOR SUBSYSTEM

5.1 DESIGN GROUND RULES AND METHODS

For use in the Brayton cycle powerplant optimization, radiators were analyzed parametrically for both gaseous and liquid working fluids. The various general criteria, ground rules, and methods used for these analyses are discussed in detail in this section. Included are the meteoroid environment and how it is handled in the analysis, the thermal environment, the probability and design life assumptions, the ground rules affecting materials selection, the radiator analysis models for both the matrix and feed lines, and a brief description of the analysis computer programs used.

5.1.1 METEOROID CRITERIA

As required by the contract work statement, the meteoroid armor thickness determination used in this study is based on the 1963A Whipple criterion. With the various data on meteoroid velocity, density, flux, and other pertinent factors, the armor thickness may be expressed as

$$t = \frac{S}{2.54}\,\sigma\left(\frac{6}{\pi}\right)^{1/3}\rho_p^{-1/3}\left(\frac{62.4\rho_p}{\rho_t}\right)^{\phi}\left(\frac{\bar{v}}{c}\right)^{\theta}\left(\frac{\alpha A\tau}{-\ell n P_o}\right)^{1/3\beta}\left(\frac{2}{3\eta\,\theta\,\beta+2}\right)^{1/3\beta}$$

where

t = required armor thickness, in.

S = 1.75 (thin plate spalling factor

σ = 2.0 (material proportionality constant)

ρ_p = 0.44 gm/cm^3 (meteoroid particle density)

ρ_t = target material density, lbs/ft^3

$\bar{v}$ = 98,400 ft/sec (average meteoroid velocity)

$c = 12\sqrt{\frac{E_t\, g}{\rho_t}}$ (sonic velocity in target material)

where E_t is Young's modulus at operating temperature and g is the gravitational constant (32.2 ft/sec^2)

$\phi = 1/2$
$\theta = 2/3$ } penetration constants

$\alpha = 5.3 \times 10^{-11}$
$\beta = 1.34$ } constants for flux distribution curve

A = external surface area of components (ft^2)

τ = mission time (days)

P_o = probability of no meteoroid penetration

η = 1.0 (damage factor for oblique impact)

Reduction of this equation yields the more convenient form

$$t = \frac{0.256S}{\rho_t^{1/6}\, E_t^{1/3}} \left(\frac{A\,\tau}{-\ell n\, P_o}\right) .249$$

in which the variables have the same definition as above

or

$$t_a = \frac{0.256S}{\gamma^{1/6} E^{1/3}} \left(\frac{AT}{-\ell n P_o} \right)^{0.249}$$

where

t_a = armor thickness, in.

γ = specific weight of vulnerable material, lb/in^3

E = modulus of elasticity of vulnerable material, psi

A = vulnerable area, ft^2

T = time for which protection is desired, hr

P_o = probability of no meteoroid penetration

S = thin plate and spalling factor, normally 1.75

Consistent with NASA-Lewis recommendations, the vulnerable area of the tubes is defined as the external surface area of the armor. In computing the armor requirements for this study, the vulnerable area was taken as the total external surface area of all the tubes, headers, and feeds.

To protect radiator headers, feed lines, and parts of the tubes themselves, a meteoroid bumper criterion is required. Figure 5-1 illustrates the criterion used (Reference 1). The protected wall thickness (t_w) is shown related to the bumper thickness (t_b) and the spacing between the bumper and the wall (s). All quantities are expressed dimensionlessly in terms of the equivalent armor thickness (t_a). The equation shown in the figure is a curve fit relating the criterion to test data (References 2 and 3). In applying this criterion to a design, the first step is the determination of the required armor thickness by means of the armor

$$\frac{t_w}{t_a} = \frac{2}{\pi} \tan^{-1} \left[\frac{2(1-t_b/t_a)}{\frac{t_b}{t_a}\left(2-\frac{t_b}{t_a}\right)\left[\frac{4}{3} + \frac{10.4\,(s/t_a)^2}{1+3.6\,(s/t_a)^2}\right]} \right] - \frac{2(s/t_a)^2}{1+3.6(s/t_a)^2} \left[e^{-3.5\, t_b/t_a} \right] \sin 2\pi \frac{t_b}{t_a}$$

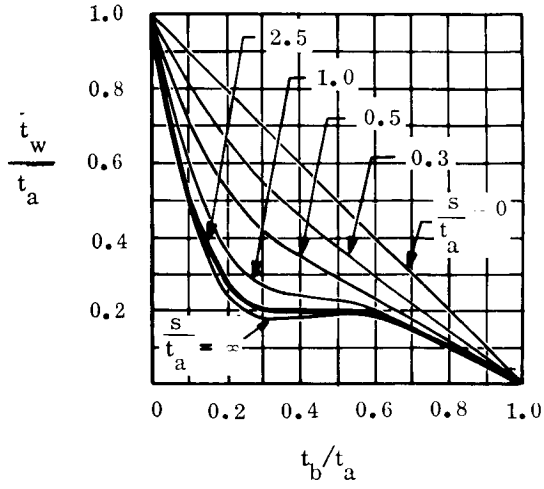

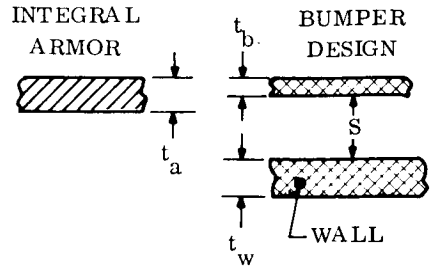

Figure 5-1. Meteoroid Bumper Criterion

criterion as though bumpers are not being used. Following this, the relative thicknesses of bumper and wall are determined using this reference armor thickness and Figure 5-1 as a basis. The vulnerable area is not considered to be altered by the use of a bumper, since damage to the bumper by a meteoroid which would not normally have impacted the wall is of secondary concern. In the normal context of a bumper as applied to the outer shell of a space station, for example, this vulnerable area philosophy would not be important; however, in the case of a radiator the general reference is to the situation of a small diameter pipe (e.g., a two-inch diameter feed line) enclosed within a large diameter shell (e.g., a 260-inch diameter radiator).

Although the use of an inert gas for the working fluid in a radiator eliminates the corrosion problem, there is still a good reason for incorporating a liner in the radiator tube design. This centers on the spallation phenomenon associated with hypervelocity impact. It has been shown (Reference 4) that the use of a liner can permit a reduction in the armor

thickness by reducing the spallation factor (S) in the armor thickness equation. Pending a more complete quantitative evaluation of this effect, no attempt has been made to numerically capitalize on it; however, it is apparently appropriate to compare Brayton and Rankine cycles on the basis of utilizing a liner in both since both gain the same advantage from the spallation protection afforded. Therefore, the radiators for this study were designed and analyzed based on the use of a 0.015-inch thick, stainless steel liner in the tubes.

The effect of the liner can be translated into either a weight reduction or into an increase in the survival probability. Figure 5-2 illustrates the matrix weight (excluding structure) sensitivity of a representative radiator to the spallation constant and the various other major factors affecting armor thickness. Each of the abscissa scales shown in this figure must be used independently to determine the effect on radiator matrix weight. The variation of the probability of survival with changes in the spallation factor is illustrated in Figure 5-3.

5.1.2 MISSION ORIENTED PARAMETERS

Several parameters significant in determining the weight and geometry of the radiator are directly related to the mission requirements. For purposes of developing an analytical model, the following values were assumed and held constant throughout the study:

a. Sink Temperature = $-10^{\circ}F$
b. Probability of no meteoroid puncture = 0.95
c. Meteoroid survival time = 10,000 hours.

These values were used for both the gas (neon) and liquid (NaK) radiators thereby permitting a comparison on the same basis. The selection of a $450^{\circ}R$ sink temperature represents the most severe of the conditions of interest. In the Spartan computer programs, the equivalent sink temperature is calculated from input parameters such as emittance, absorptance, view factors and incident heat flux. Neglecting earth radiation and earth albedo, the equivalent sink temperature is calculated by

$$\sigma T_s^4 = \frac{S\alpha F_\alpha}{\epsilon F_e}$$

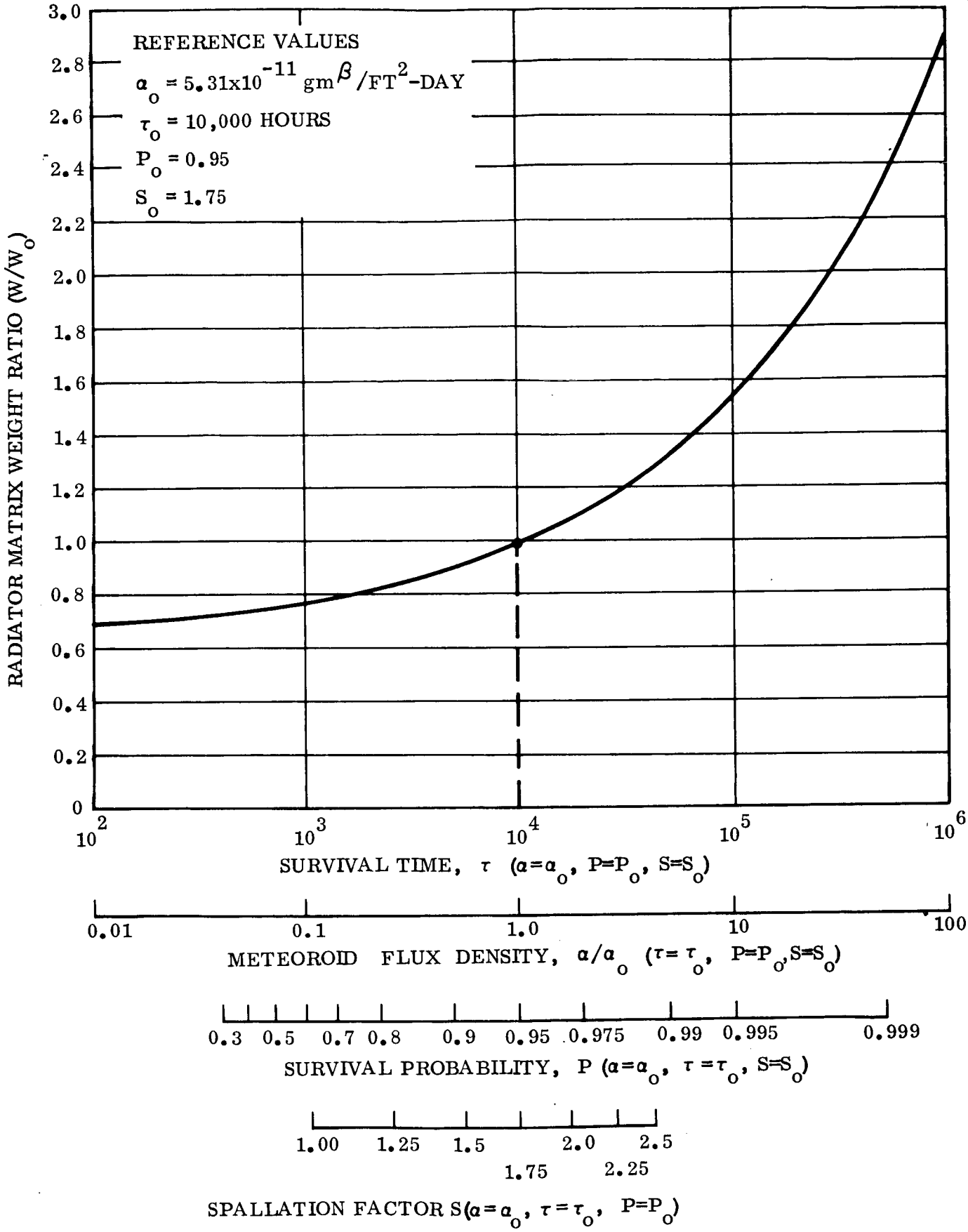

Figure 5-2. Effect of α, τ, P, and S on Radiator Weight

where

T_s = equivalent sink temperature (^oR)

σ = Stefan-Boltzman constant

S = incident solar flux (BTU/HR-FT^2)

α = absorptivity of radiator surface

ϵ = emissivity of radiator surface

F_α = view factor to incident flux

F_e = view factor to sink.

For a specified radiation configuration and orientation with respect to the solar flux, the equivalent sink temperature is completely defined by the selection of an α/ϵ ratio. For a cylindrical radiator in near-earth oribt, with its longitudinal axis normal to the incident solar flux, the values of F_α, F_e and S are 0.318, 1.0 and 450 Btu/hr-ft^2 respectively. With this arrangement, any values of emittance and absorptance satisfying $\alpha/\epsilon = 0.489$ will yield the desired 450^oR sink temperature.

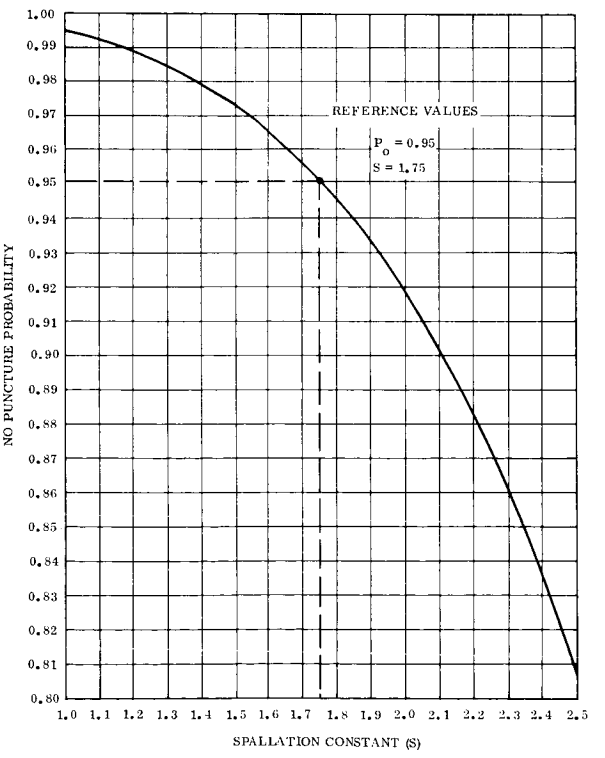

Figure 5-3. No Puncture Probability Variation with Spallation Constant for Constant Matrix Weight

For the unmanned conceptual designs, a survival probability of 0.9 was specified for a 10,000-hour life following a 10,000-hour pre-start-up waiting period. Thus the design values above imply a 0.907 reliability of surviving the 20,000-hour unmanned mission requirement.

An estimate of the implications of a higher waiting period reliability can be obtained from Figure 5-2. For example, 10,000 hours at 0.99 survival probability followed by 10,000 hours at 0.9 corresponds to a combined 10,000-hour survival probability of 0.991. Comparing this with the 0.95 value used in this study, Figure 5-2 shows an estimated radiator matrix weight increase of about 35 percent. It is also interesting to note from Figure 5-3 that a reduction in the spallation constant from 1.75 to 1.15 would give the same reliability for no change in weight. Thus, use of a radiator tube liner may be already providing this kind of reliability; only a comprehensive experimental evaluation of the effect of a liner on the spallation constant can fully define the true survival probability of the designs studied.

5.1.3 MATERIALS SELECTION

Parametric data and conceptual designs of the radiators for this study were based on the following materials choices:

a. All aluminum with stainless steel tube liners for the gas radiators

b. Aluminum with stainless steel tube liners combined with a copper-steel composite for the liquid metal radiators.

The radiator temperature range to be expected for the presently considered Brayton cycle systems has a maximum value of approximately $1000^{o}F$. Since beryllium was ruled out for this study by the work scope definition, this upper bound on the temperature range somewhat complicates the problem of materials selection. Straightforward use of a choice such as a steel-copper combination unreasonably penalizes this power cycle concept. By

its very nature, the gas cycle radiator has the major part of its radiating area operating at a comparatively low temperature level, strongly endorsing the use of aluminum or magnesium; it remains then to find a way to cope with the small amount of high temperature area at the radiator inlet end.

Where the working fluid is a gas, the characteristic temperature drop across the boundary layer automatically permits a substantially higher gas inlet temperature than can be tolerated by the containment material. Since initial calculations of the film temperature drop showed it to be on the order of 200°F at the hot end, and pressure drop considerations for the gas radiator indicated a likely maximum useful gas inlet temperature of 900°F, a maximum metal temperature of 700°F was indicated. Although this is considerably higher than normally recommended for aluminum or magnesium there is ample justification for considering either of these materials for the gas radiators.

SNAP 8 radiator studies have been based on using aluminum at temperatures approaching 700°F. The supporting argument relies on the fact that the material is far below this operating temperature during launch when the structural loading is at a maximum, and the loads are negligible during system operation. Because of the substantial amount of cross-sectional area afforded by the meteoroid armor, preliminary calculations of stresses resulting from such forces as lunar gravity, artificial gravity, or electric propelled missions show them to be compatible with the 700°F properties of aluminum and magnesium alloys. As margin to this argument, it should be noted that such alloys as Al-Mag and APM aluminum are described as being applicable to temperatures as high as 900°F. The possibility of such choices gives some leeway to the fact that internal finning of the radiator tubes will reduce the film temperature drop and correspondingly raise the 700°F maximum metal temperature. In any case, only the upper limits of the range of variables examined for the gas radiators begin to push this limit, and even then, only a very small portion of the area is affected.

Calculations show magnesium to yield a lighter weight radiator than aluminum under the same design ground rules; however, magnesium has a higher vapor pressure at

corresponding temperatures, and sublimation removes the meteoroid armor at an intolerable rate. The inhibitive effect of surface coatings on the sublimation rate is not adequately known, and there are always the uncertainties associated with coating damage. Although magnesium cannot be completely discounted, the sublimation problem was considered justification enough to limit this study to the selection of aluminum where the temperature allowed. Specifically, material properties were based on the 6061-0 aluminum alloy.

For the case of the liquid metal radiators wherein the maximum considered inlet temperature is 1000^{o}F and the film temperature drop is small, aluminum cannot reasonably be considered for the initial part of the radiator. To circumvent this problem, a fairly recent materials joining development can be applied. By means of coextrusion techniques, thick walled tubes have been manufactured wherein the final form of the tube consists of an all steel section making a transition to an all aluminum section (Reference 5) as illustrated in Figure 5-4. Where only one to two feet out of eight to ten feet of tube length must utilize a steel-copper composite, this type of joint is clearly attractive and can result in weight savings compared to an all steel-copper radiator. For the case in point, the presence of a stainless steel liner within the aluminum tube section represents a deviation from presently achieved technology. However, fabrication research carried out under General Electric Company sponsorship has demonstrated lined aluminum tubes, as long as four-foot, by coextrusion; hence achievement of a tube of the configuration illustrated in Figure 5-5 appears to be a reasonable fabrication development goal.

Another problem presented by this composite material joint concerns the fins. The hot end fins are a steel-copper, two-plate laminate which must be joined to the aluminum fins concurrent with the transition from a steel to an aluminum tube. Many ways of accomplishing this can be visualized, some of these are very unsophisticated and involve techniques which are virtually standard practice. For example, oversize round tubes formed by the coextrusion process could be machined to the shape illustrated in Figure 5-6. The stub fins permit the main heat rejection fins to be welded or brazed into place independently on the two sections of the tube with a braze, weld, or riveted joint connecting the fins at the

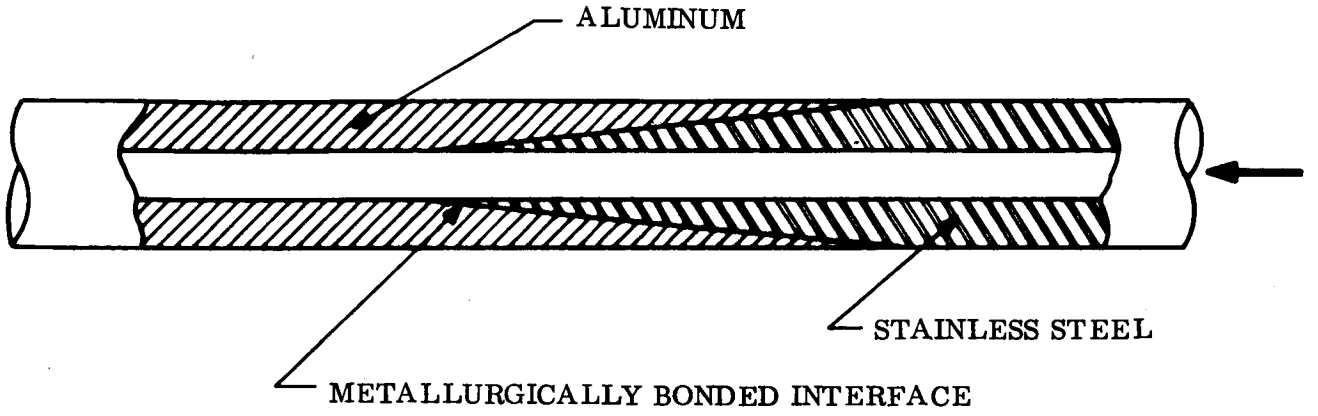

Figure 5-4. Longitudinal Tube Material Transition Joint

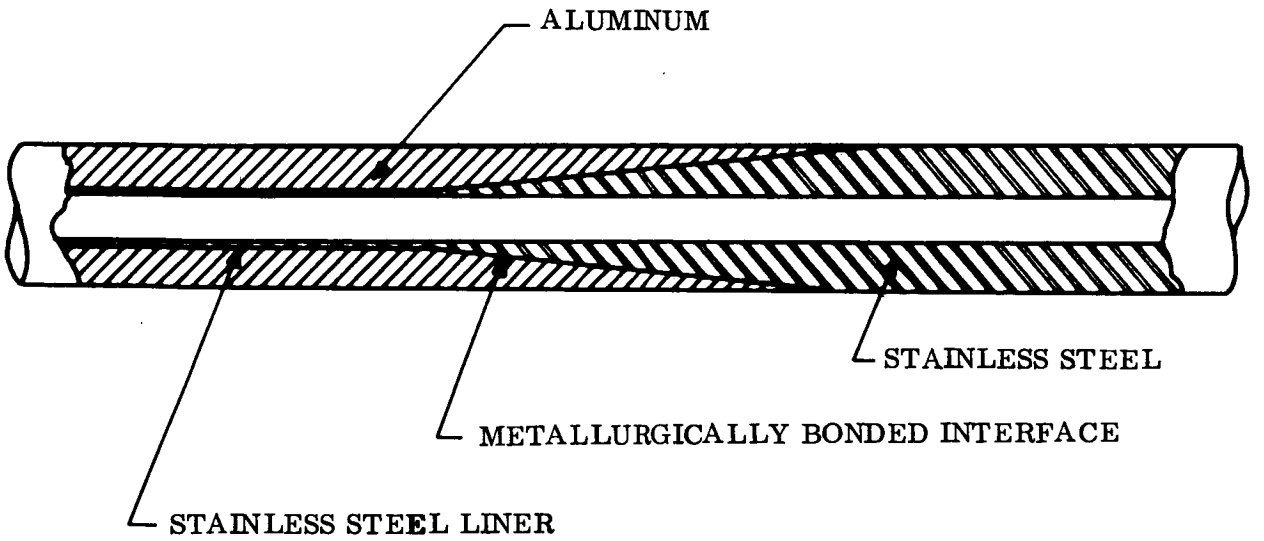

Figure 5-5. Tube Transition Joint with Continuing Liner

interface as shown in Figure 5-7. Electron beam welding would probably be the preferred joining approach. At the other extreme, exploitation of roll forming and/or roll bonding presents possibilities of fabricating the entire matrix in one piece. Alcoa's steel to aluminum Duranel is an example of the capabilities of roll bonding.

In the unlikely event that fabrication development should fail to achieve the results illustrated in Figure 5-7, there is always the possibility of physically separating the steel-copper portion of the radiator and bridging the gap with connecting pigtails as illustrated in Figure 5-8. This represents a somewhat crude and heavy concept for accomplishing the fabrication objective; however, it is obviously fully feasible.

5.1.4 RADIATOR ANALYSIS MODEL

The geometric configuration selected for analysis is a cylindrical radiator with a diameter of 21.66 feet (the S IV Stage Diameter) and a length determined by the thermal load. The cylinder is subdivided into bays ranging in length from six to twelve feet. Each bay, in turn, is composed of two 180-degree panels. The basic "building block" of the radiator systems is the fin-tube element; these are arranged with the tubes paralleling the cylinder axis and are of a length equal to that of the associated bay.

Figure 5-9 illustrates the typical cross-sectional geometry of the offset fin-tube element. The reduced armor thickness on the inward facing side of the tube is made possible by accounting for the bumper effect provided by the fins of the cylindrical radiator. A thin wall liner is used to provide compatibility with the transport fluid and as an aid in reducing possible failure due to spallation resulting from meteoroid impact. Composite fins are used for those radiators using an armor material of relatively low thermal conductivity, and internal vanes are considered to reduce the boundary layer temperature drop in the gas radiators.

Feed line systems used in generating the analytical radiator model are typified by the schematic illustration in Figure 5-10. The feed pipe diameters are sized to maintain a

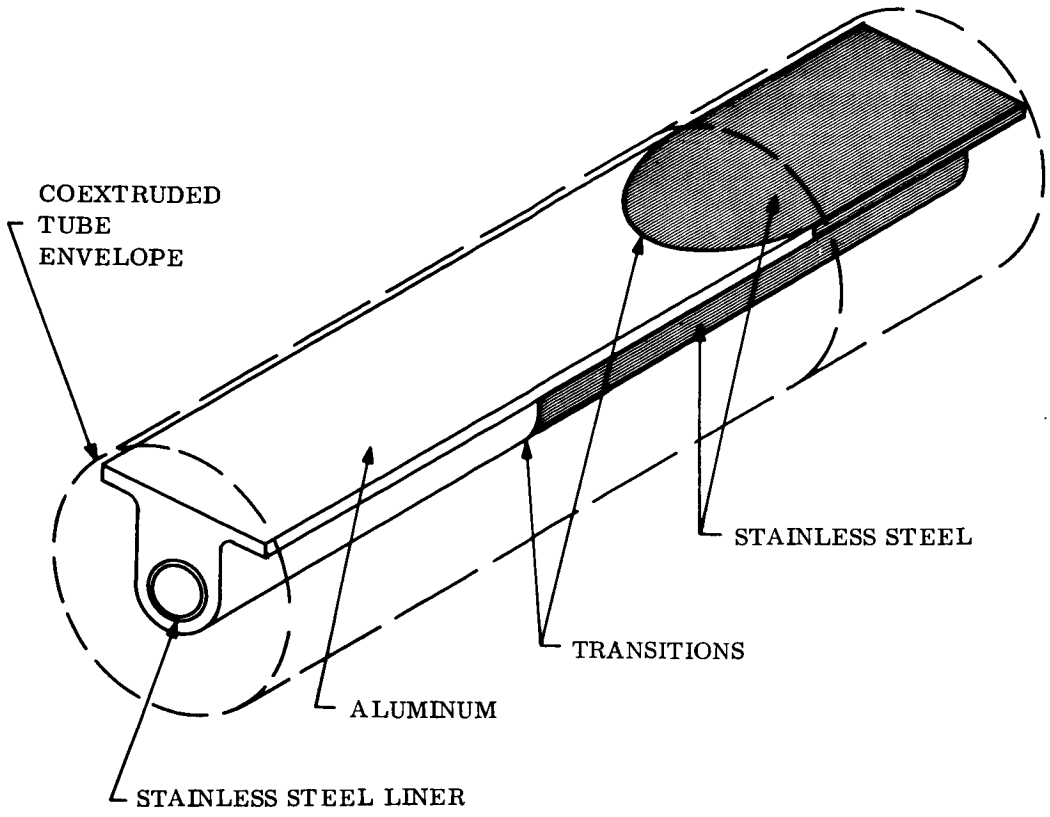

Figure 5-6. Finished Composite Tube Geometry

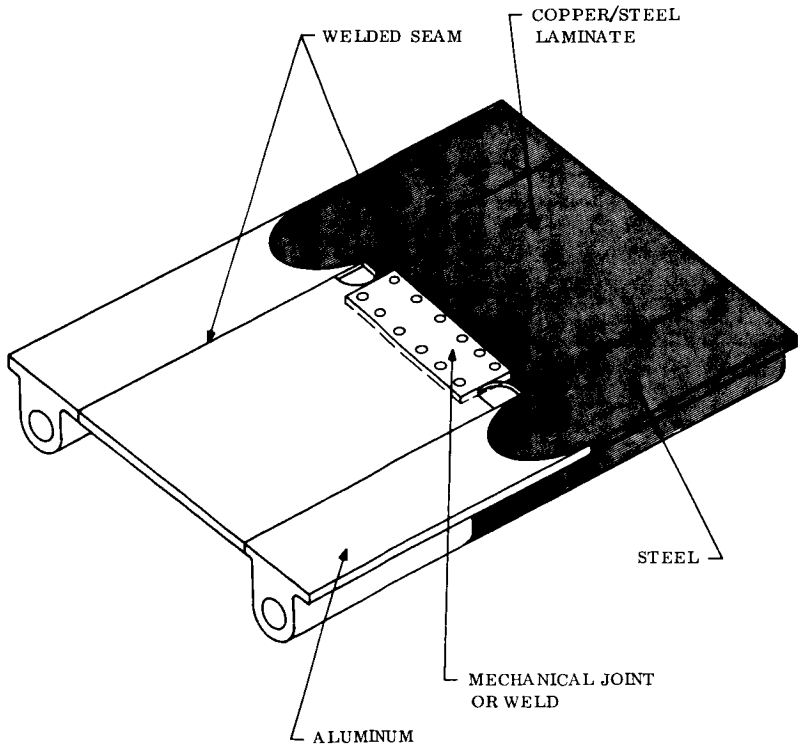

Figure 5-7. Transition Joint in Fins

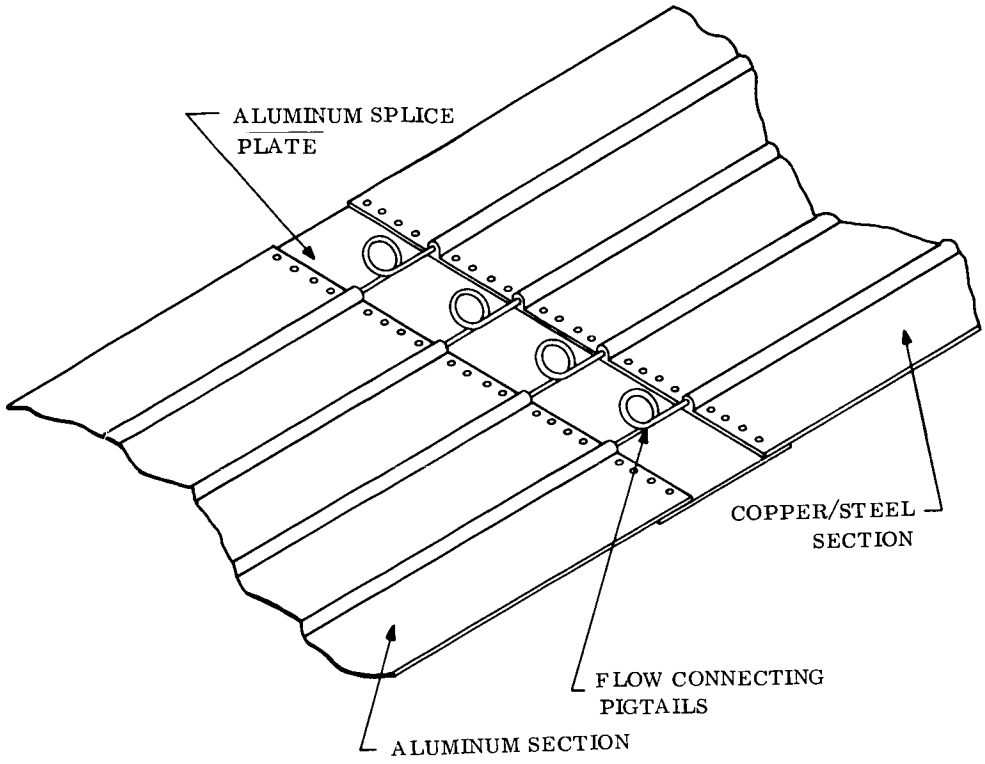

Figure 5-8. Pigtail Method for Joining Composite Radiator

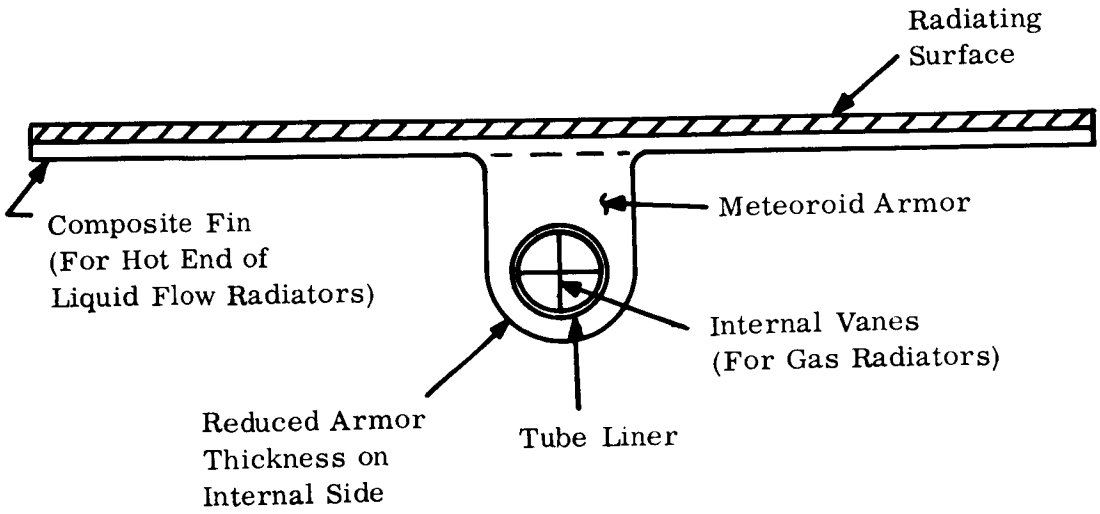

Figure 5-9. Typical Fin-Tube Cross-Section Geometry

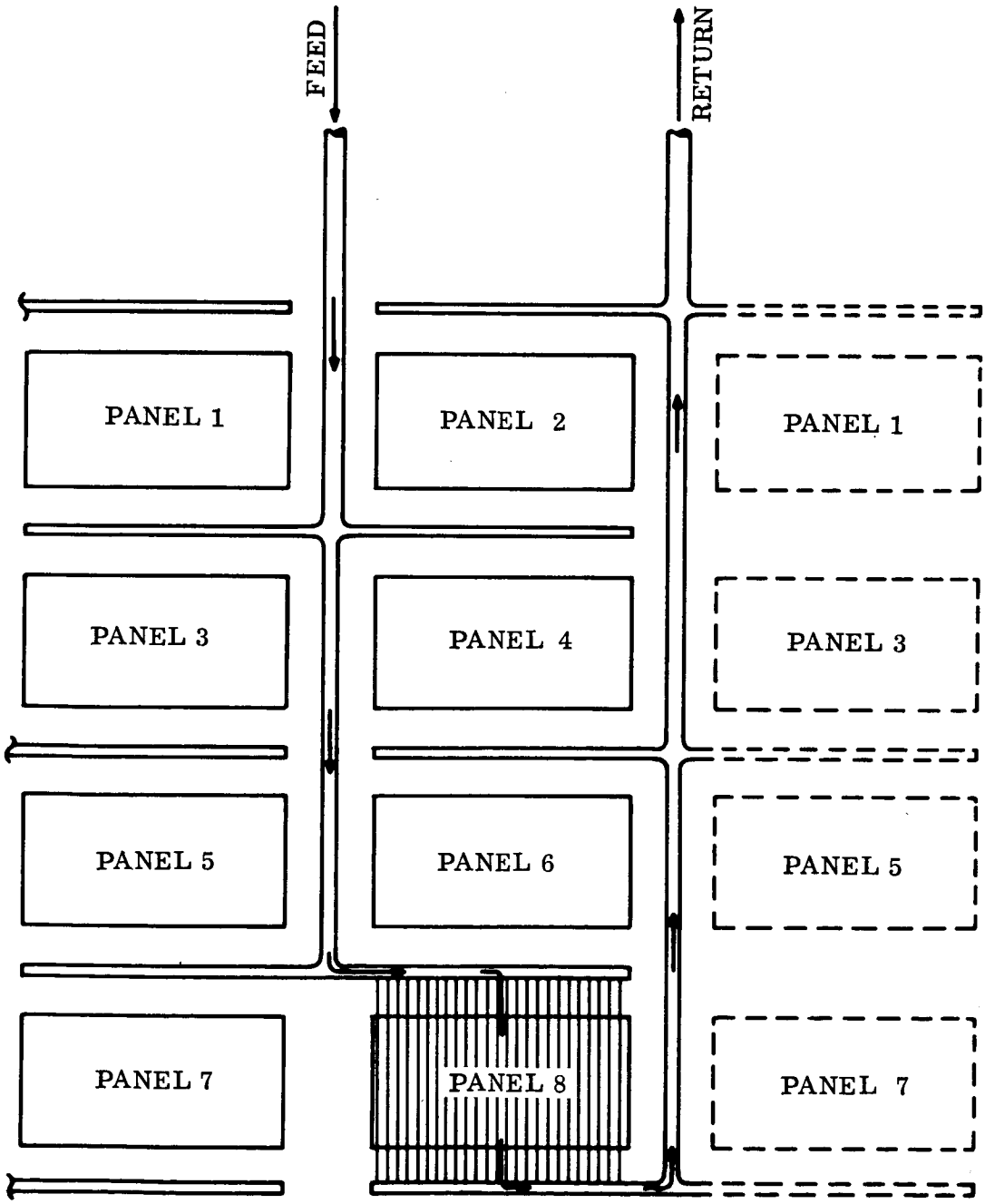

Figure 5-10. Typical Feed Line Configuration

constant fluid velocity throughout the feed system, but not necessarily equal to that in the radiator tubes in the system. Practical geometric considerations preclude the use of equal length feed lines to each panel; hence pressure drop calculations are computed for the most remote panel. In practice the flow balance would be achieved by either orificing the other headers or reducing the feed pipe diameters to yield equal panel pressure drops.

5.1.5 RADIATOR ANALYSIS COMPUTER PROGRAMS

Weight optimization of the various Brayton cycle radiator studies was accomplished with the aid of computer codes identified as the Spartan III and Spartan IV Radiator Analysis Programs. Input for these programs includes:

- THERMAL REQUIREMENTS
  1. heat rejection rate
  2. fluid inlet temperature
  3. fluid temperature drop in radiator

- GEOMETRIC FACTORS
  1. number of radiator panels
  2. number of tubes per panel
  3. tube spacing
  4. tube inside diameter
  5. fin thickness

- ENVIRONMENTAL FACTORS
  1. meteoroid protection requirements
  2. incident heat flux
  3. surface emittance
  4. surface absorptance
  5. view factors

GENERAL ELECTRIC COMPANY

MISSILE AND SPACE DIVISION

VALLEY FORGE SPACE TECHNOLOGY CENTER (MAIL: P. O. BOX 8555, PHILA., PA. 19101) . . TEL. 969-2000

Subject: Contract NASw-980

Gentlemen:

The Missile and Space Division of the General Electric Company encloses herewith for your retention Volume I Technical Report entitled Parametric Results prepared under subject Contract. This Report is furnished to you in accordance with instructions from NASA, Lewis Research Center.

A. A. Gayuski
Contract Administrator

:js

- PHYSICAL PROPERTY DATA
  1. Young's Moduli
  2. material densities
  3. thermal conductivities
  4. fluid viscosity
  5. fluid specific heat

- CONFIGURATION FACTORS
  1. Fin-tube design (offset or central tube)
  2. Header shape (parabolic or constant dia.)
  3. length and diameter of feed lines
  4. pressure loss coefficients

With this input data, the mechanics of the program are such as to satisfy simultaneously, the thermal requirements and the meteoroid protection considerations. The relationships for meteoroid armor requirements include allowances for bumper effects and are consistent with the criteria described in Section 5.1.1. Thermal balance for the radiator is effected by varying the length of the fin-tube elements. Outputs from the programs are as follows:

- TEMPERATURE DISTRIBUTION
  1. fin root temperature at tube inlet
  2. fin root temperature at tube outlet
  3. effective average fin root temperature
  4. fin efficiency
  5. effective sink temperature

- VULNERABLE AREAS & ARMOR REQUIREMENTS
  1. total thickness of armor required
  2. reduction in armor thickness due to fin bumper
  3. vulnerable areas of components (tubes, headers, etc.)

- RADIATOR GEOMETRY
  1. fin length
  2. tube length
  3. header diameter
  4. radiator area

- FLOW CHARACTERISTICS
  1. mass flow rate
  2. fluid velocity in tubes and headers
  3. Reynold number in tubes and headers
  4. pressure drop in feed lines
  5. pressure drop in headers
  6. pressure drop in tubes
  7. pressure drop at tube inlet
  8. pressure drop at tube outlet
  9. total pumping power

- WEIGHT SUMMARY
  1. Fluid weight
  2. feed line weight
  3. header weight
  4. tube weight
  5. fin weight

For purposes of optimization, a parameter called "radiator effective weight" is introduced. This parameter is defined as

$$\text{EFF WT} = \text{RADIATOR WT.} + \frac{(\text{HYDRAULIC POWER})\ (\text{SYSTEM SPECIFIC WT.})}{\text{PUMP EFFICIENCY}}$$

The second term on the right side of this equation essentially adds to the radiator weight that portion of the powerplant weight which is necessary to generate the electrical power required to satisfy the radiator pumping requirements. To determine an optimum radiator design, those parameters not fixed by the boundary conditions are varied until a combination yielding a minimum value of "effective weight" is achieved. Incorporated in the optimization logic is the facility to impose an arbitrary upper limit on radiator area, total pressure drop or hydraulic power. With this feature it is possible to obtain, for example, an optimum design satisfying certain thermal and reliability requirements while not exceeding the area available for the radiator.

Figure 5-11 illustrates schematically the optimization logic used in the Spartan programs. The design represented by point A corresponds to the reference design selected in a rather arbitrary manner. About this base point, the values of radiator effective weight and radiator area are computed for the positive and negative increments of the parameters to be optimized (indicated as parameters P1 and P2). The line connecting the points P1 + ΔP1

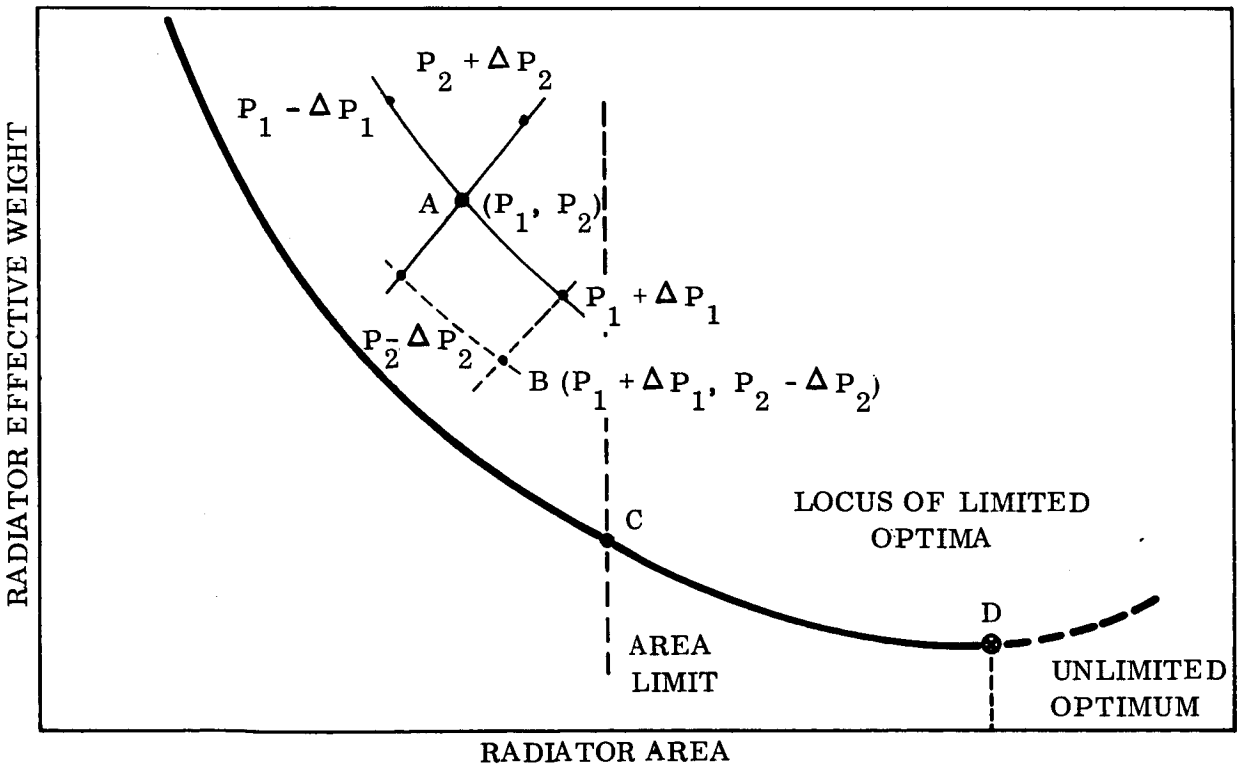

Figure 5-11. Radiator Effective Weight Related to Area

and P1 - ΔP1 shows the variation of effective weight and area for variations of the parameter P1 with all other parameters held constant. A similar curve is shown for parameter P2. The procedure employed then compares and selects the values of these parameters yielding the lowest effective weight; in this case P1 + ΔP1 and P2 - ΔP2. Using these values of P1 and P2, a new base point is computed and the procedure repeated until the optimum design is found. As illustrated, this new base point is indicated by point B. Experience has shown that, in most instances, the design resulting from changing the initial values of P1 and P2 to those of P1 + Δ P1 and P2 - Δ P2 can be predicted by a method approximating the parallelogram law of addition for vectors when plotted as in Figure 4-11. For the sake of clarity, the variation of only two parameters is shown here; in practice the optimization logic can accommodate up to twenty.

The vertical dashed line of Figure 4-11 represents an area limit imposed on the design. With this restriction, the minimum achievable effective weight is that corresponding to point C. The curve generated by point C as the area limit is varied, is termed the locus of area limited optima. The point D on this curve represents an unlimited optimum design and corresponds to the design attained if no area limit is imposed.

The Spartan III radiator program was written primarily for radiators using liquids with their inherently "small" temperature drops and incompressible fluid flow. Consideration of the effects of large fluid temperature changes from the radiator inlet to outlet lead to consideration of variable material physical properties and segmental fin-tube heat balance calculations. These considerations along with the desirability of improving the analysis of conical radiators prompted the writing of the Spartan IV Radiator Analysis Program. The approach used is similar to that of the early program and the optimization technique is virtually identical. However, the advantage of Spartan IV for gas radiators lies in its ability to include the following factors in the numerical computations:

a. Compressible flow relationships

b. Physical properties varying with temperature.

c. Incremental fin tube heat balance and pressure drop calculations (each tube "segment" having a relatively small temperature change from end to end).

d. Conical radiators (tapered tube spacing and different inlet and outlet header lengths).

e. Three flow regimes.

f. Internal fins (vanes) in the tubes to cut down temperature drop across the gas film.

g. Different diameter inlet and outlet headers, and feed and return lines.

h. Bimetallic fins; using one layer primarily for heat conduction and the other primarily for meteoroid protection.

i. Independent feed and return lines which can be of different materials and based on different minimum diameters.

The penalty for these features has been an increase in computer time per radiator. Primarily for this reason, Spartan III has been used in this study to obtain preliminary results which are being verified and refined, where necessary, by Spartan IV.

5.2 LIQUID METAL RADIATORS

The primary goal of the radiator study was to develop an analytical expression for the radiator weight suitable for incorporation into an over-all cycle optimization analysis. In addition, graphical data was developed showing the relationship between weight and the major cycle interfacing parameters.

5.2.1 ANALYTICAL APPROACH

Principal quantities relating the liquid metal radiator to the remainder of the cycle are:

a. The thermal load
b. The fluid inlet temperature
c. The fluid outlet temperature

Since the pumping requirement of the liquid radiator does not directly influence the cycle conditions, the expression for radiator weight was developed independent of radiator pressure drop. However, to maintain realistic pressure drops and pumping requirements, the radiators were optimized with respect to the anticipated system specific weight and estimated pump efficiencies. In this case, the specific system weight was taken as 100 lbs/KWe and pump efficiency as 33 percent.

For the turbine inlet temperatures and applications being considered, preliminary cycle studies suggested the following ranges for the cycle interfacing parameters:

a. Thermal load from 250 KW to 1000 KW
b. Fluid inlet temperature from 700^{o}F to 1000^{o}F
c. Fluid outlet temperature from 150^{o}F to 400^{o}F.

Since the inlet temperature is always 700^{o}F or above, most of the results for the liquid metal radiators reflect the use of a materials transition along the axis of the radiator panels.

To determine the point of transition from steel-copper construction to aluminum construction it is necessary to first calculate the temperature distribution along the radiator tube. A rigorous solution is needlessly complex for input purposes. Such a solution is incorporated in the sophistication of the Spartan IV radiator computer code; however, some assessment of the temperature distribution is required in order to determine the material inputs for the computer analysis. It turns out that the iteration necessary to optimize the transition location

is overly sophisticated when measured against practical considerations. The simplified approach used to obtain this temperature distribution consists of balancing the radiation losses against the change in sensible heat convection inputs for the finless model illustrated in Figure 5-12. The two equations are,

$$-dq = w\ C_p\ dT$$

and

$$dq = \sigma \epsilon\ \ell\ dy\ (T^4 - T_s^4),$$

where w is the flow rate, C_p is the fluid specific heat, T is the local temperature, ℓ is the overall panel width, and T_s is the effective sink temperature. Assuming that $T >> T_s$, the resulting temperature distribution is given by

$$\frac{T}{T_{in}} = \left[\left(\frac{T_{in}^3}{T_{out}^3} - 1 \right) \frac{y}{L} + 1 \right]^{-1/3} \qquad (1)$$

Figure 5-13 is a graphical presentation of this equation and illustrates the rapid temperature fall-off at the hot end of the panel. Proper consideration of the effects of conduction through the armor, fin efficiency variation, and heat sink would slightly change the curves shown. Consideration of the heat sink temperature would affect the low temperature region of the radiator significantly. However, since the transition region (Copper/SS to Aluminum) takes place at a relatively high temperature, ~700°F, this analysis is adequate to locate the point at which transition should occur. For example, neglecting a 420°R sink at an 1160°R surface temperature overestimates the heat rejection by about three percent. Since the transition section from steel to aluminum will probably be in the order of three to four inches in length and the thermal behavior in this region will be affected by the exact shape of the conical overlap of materials, these effects are judged to be relatively trivial.

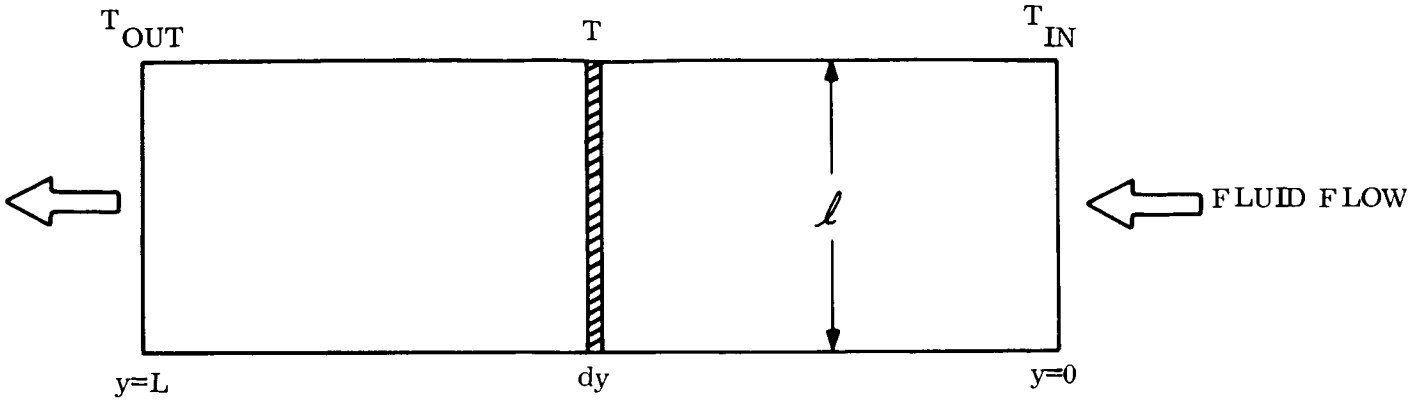

Figure 5-12. Longitudinal Temperature Distribution Analysis Model For Materials Interface Location

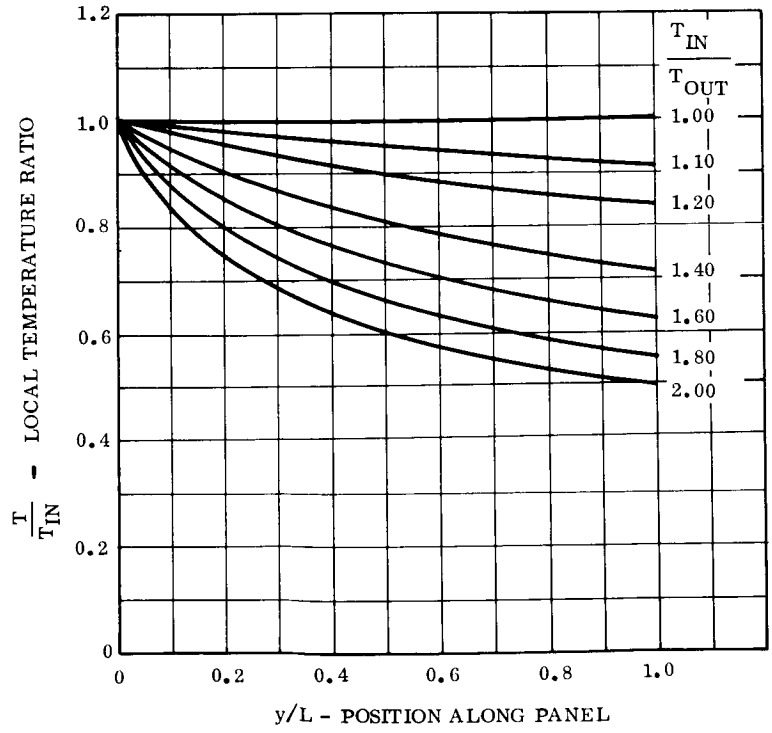

Figure 5-13. Simplified Radiator Longitudinal Temperature Distribution Neglecting Sink Temperature

The steel-copper portion of the radiator is actually composed of steel armor with a composite copper-steel fin. Equal thicknesses of copper and steel are used thereby taking advantage of the high thermal conductivity of copper to maintain high fin efficiency and utilizing the mechanical properties of stainless steel to provide an economical meteoroid bumper effect. The effective thermal and mechanical properties of a composite copper-steel fin, pertinent to the radiator design, are given by

$$\rho_e = a\rho_s + b\rho_c,$$

$$k_e = ak_s + bk_c,$$

and

$$E_e = \left(a E_s^{1/3} + b E_c^{1/3}\right)^3 \left(a\rho_s^{1/6} + b\rho_c^{1/6}\right)^3 \left(a\rho_s + b\rho_c\right)^{-1/2}$$

where

ρ = density
k = thermal conductivity
E = Young's Modulus
a = fractional thickness of steel
b = fractional thickness of copper

and e, s, and c subscripts refer to effective, steel, and copper properties respectively.

Figure 5-14 graphically illustrates these equations for a fin with equal thicknesses of copper and stainless steel.

To facilitate the generation of data from which the analytical radiator model was to be derived, it was judged more expedient to analyze a radiator of equivalent material rather than analyze the aluminum and steel portions individually with their associated boundary conditions.

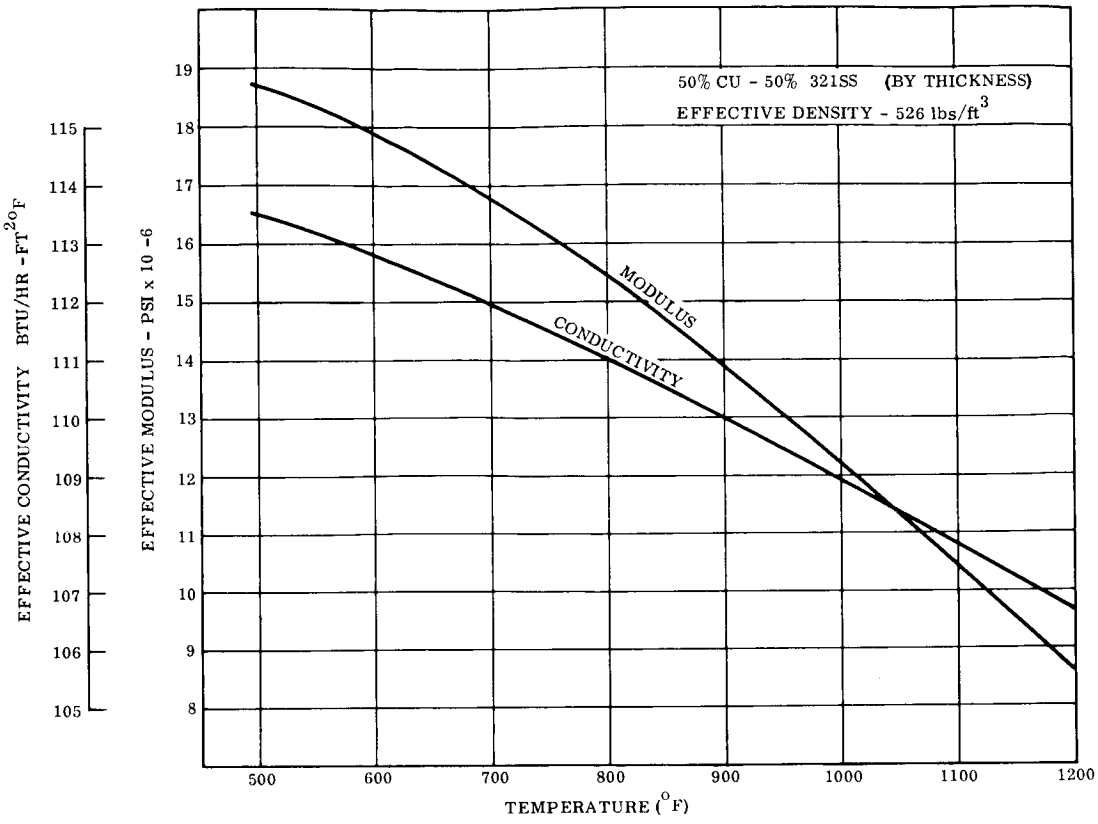

Figure 5-14. Properties of Copper-Steel Composite Fins

To use this approach, it is necessary to determine the equivalent material properties as a function of inlet and outlet temperatures. The properties in question are:

a. Fin Density
b. Fin Elastic Modulus
c. Fin Thermal Conductivity
d. Armor Density
e. Armor Elastic Modulus
f. Armor Thermal Conductivity

The first of these, fin density, is readily found by

$$\rho_{fe} = (1 - \phi)\ \rho_{alum} + \phi\ \rho_{cu\text{-}ss}$$

where

ρ_{alum} = density of aluminum

ρ_{cu-ss} = density of composite copper-steel fin

ϕ = length fraction of tube at temperature above $700^{o}F$

The value of ϕ is obtained from Figure 5-13 for the inlet and outlet temperatures being considered. Similarly, the effective density of the armor material is given by

$$\rho_{ae} = (1 - \phi)\ \rho_{alum} + \phi\ \rho_{steel}$$

Equivalent modulus of elasticity for the fin is taken as an area weighted average and can be found from

$$E_{fe} = (1 - \phi)\ E_{alum} + \phi\ E_{cu-ss}$$

where

E_{alum} = elastic modulus of aluminum at $T = 1/2\ (700^{o}F - T_{out}\ ^{o}F)$

E_{cu-ss} = elastic modulus of cu-ss at $T = 1/2\ (T_{in}\ ^{o}F + 700^{o}F)$

The equivalent modulus for the armor material, by comparable reasoning, is

$$E_{fa} = (1 - \phi)\ E_{alum} + \phi\ E_{ss}$$

where E_{ss} = elastic modulus of stainless steel at $T\ ^{o}F = 1/2\ (T_{in}\ ^{o}F + 700^{o}F)$

The thermal conductivity of 6061 aluminum is essentially constant, about 105 Btu/hr-ft^2-^{o}F, over the temperature range considered. From Figure 5-14, the thermal conductivity of the composite copper-steel fin is seen to vary only slightly over the 1000^{o}F to 700^{o}F temperature range and is very nearly equal to that of aluminum. Hence, with little sacrifice in accuracy, the equivalent fin thermal conductivity can be considered constant at 105 Btu/hr-ft^2 -^{o}F.

For the armor, an exact determination of the equivalent conductivity is more complex; however, since it is not a first order effect, sophistication is not warranted. As shown in Figure 5-15, the effective value of the armor thermal conductivity for any value of ϕ between unity and zero must be bounded by the values for aluminum and stainless steel. If the specific heat rejection rate from the tube were constant with respect to length, a linear relationship, denoted by the line A, would be appropriate. However, since the mechanism of heat transfer involved is radiation, it is known that the heat rejection rate is relatively large at the hot end of the tube and drops off quite rapidly along the length. It is apparent then that the low conductivity steel armor at the hot end of the tube will have a greater influence on reducing the effective conductivity than is indicated by line A in the figure. The physics of the situation suggests the use of the heat rejection fractions as the weighting factors giving the equation,

$$K_e = K_{alum}\left(\frac{Q_{alum}}{Q}\right) + K_{steel}\left(\frac{Q_{steel}}{Q}\right)$$

Evaluating this equation for the inlet and outlet temperature combinations used in the liquid metal radiator analysis yields the points shown in Figure 5-15 under the line A. As expected, increasing the inlet temperature for the same outlet temperature reduces the effective conductivity. Part of this stems from the increase in the length of steel-copper; however, most of the reduction reflects the increased armor temperature drop resulting from the higher hot end heat flux density.

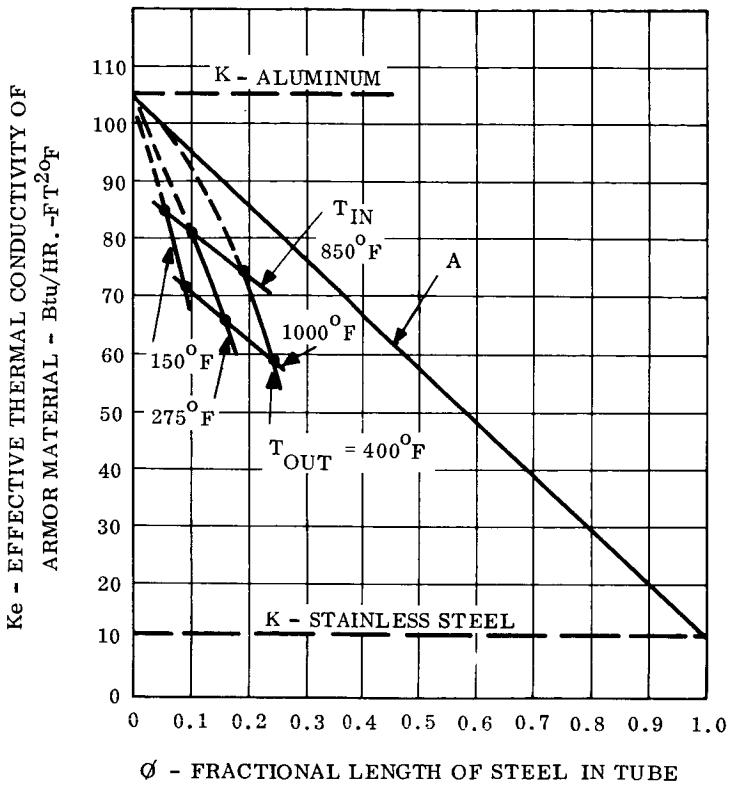

Figure 5-15. Equivalent Armor Thermal Conductivity as a Function of the Fractional Length of Steel in the Tube

5.2.2 PARAMETRIC DATA

Using the data inputs described in Section 5.2.1 and the Spartan III Radiator Analysis program described in Section 5.1.5, the curves of Figure 5-16 were generated to relate the total weight of the radiator system to the operating temperatures and the thermal load. Each point on the curves represents an optimum design for a particular combination of the interfacing parameters. Independent parameters optimized by the analysis are:

a. Tube Spacing
b. Fin Thickness
c. Tube Inside Diameter
d. Feed Line Diameter

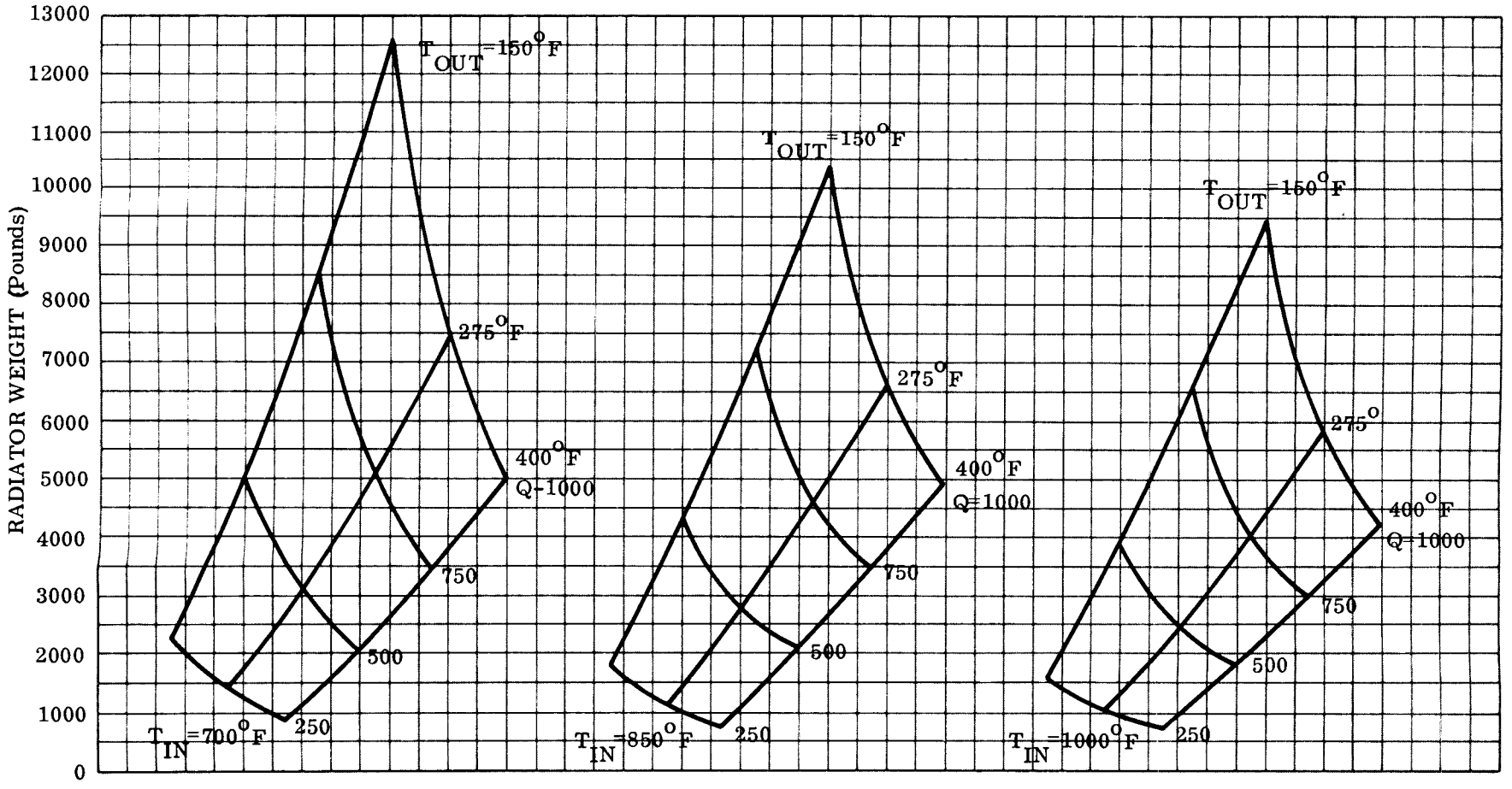

Figure 5-16. Liquid Metal (NaK) Radiator Weight Related to T_{in}, T_{out}, and Heat Rejection for T_{sink} =-10°F and Emissivity = 0.9

The data is presented in the form of a carpet plot thereby facilitating interpolation of the independent variables, and providing a clearly visible picture of the behavior of radiator weight with respect to these variables. With one exception, these curves behave as expected; weight increases with increasing thermal load and decreasing outlet temperature, and in general, increases with decreasing inlet temperature. However, for an outlet temperature of $400^{\circ}F$, the weights corresponding to inlet temperatures of 700° and $850^{\circ}F$ are essentially identical over the heat load range considered. This apparent inconsistency results from the heavier steel-copper construction at the high temperature end of the tube. The higher the value of the radiator exit temperature, the greater is the required fraction of steel-copper construction for a given inlet temperature. Thus for $T_{out} = 400^{\circ}F$, increasing T_{in} above $700^{\circ}F$ introduces the steel-copper weight penalty at a rate greater than the normal savings associated with elevated inlet temperature. These effects compensate for each other at the $850^{\circ}F$ inlet temperature value. Above this temperature the reduced area afforded by the higher effective radiating temperature begins to dominate yielding a net weight reduction. Carrying this reasoning further, it is to be expected that data for outlet temperatures higher than $400^{\circ}F$ would result in the break-even point moving to higher values of inlet temperature.

5.2.3 PARAMETRIC MODEL

The data presented in Figure 5-16 clearly illustrates the variation of radiator weight with the selected independent parameters. However, it does not lend itself conveniently to the derivation of a mathematical model. Figure 5-17 shows the same data in an alternate form with radiator area included as an additional variable and the radiator weight expressed as radiator specific weight, lbs/ft^2. In addition, the independent variables T_{in} and T_{out} have been combined to give a single independent parameter T_{eff}. This parameter is readily computed by the equation:

$$\frac{-4}{U} = \frac{4\,(U_i - U_o)}{\ell n \left[\left(\frac{e^{2\tan^{-1} U_o}}{e^{2\tan^{-1} U_i}} \right) \left(\frac{U_o + 1}{U_i + 1} \right) \left(\frac{U_i - 1}{U_o - 1} \right) \right]} + 1 \qquad (2)$$

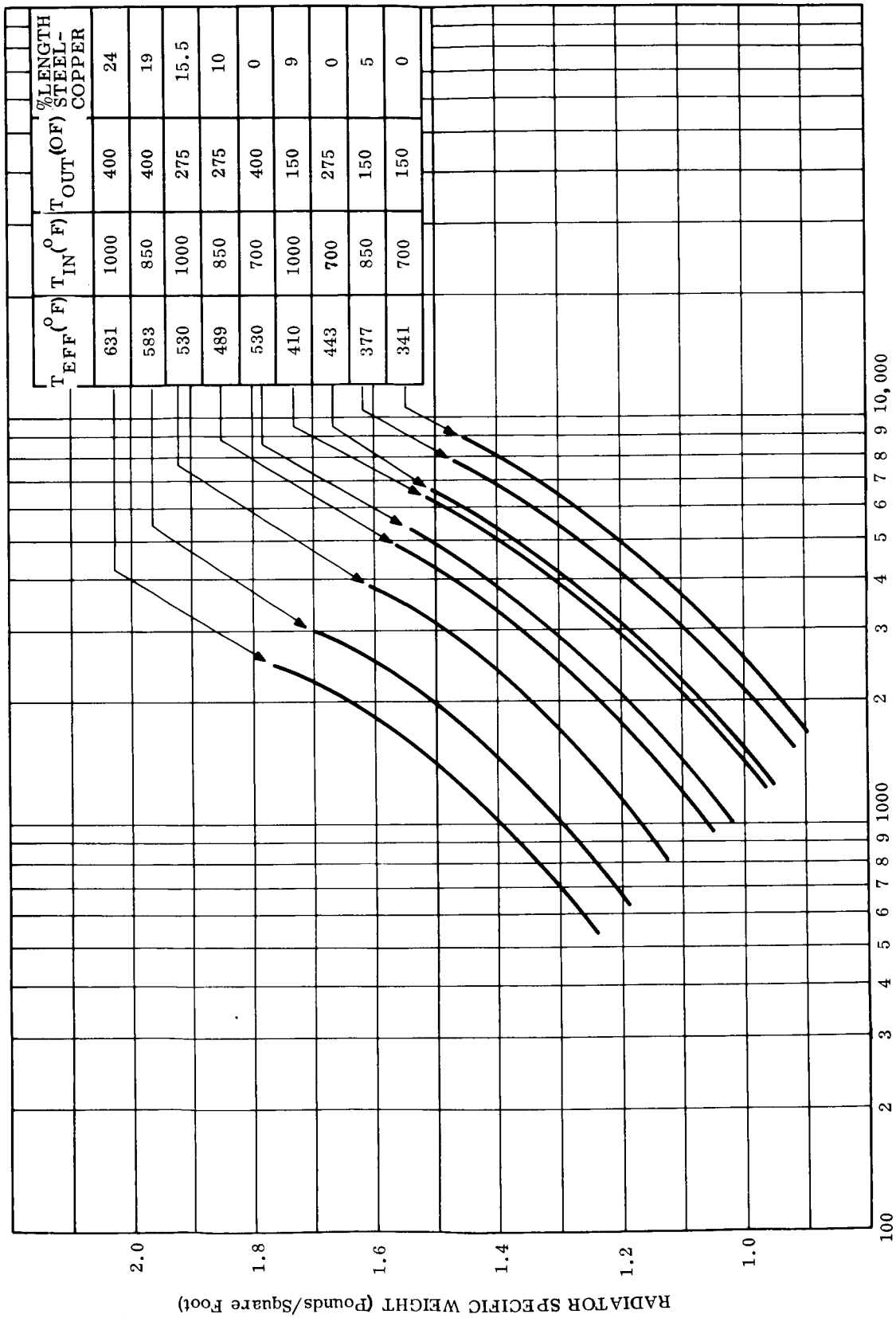

Figure 5-17. Liquid Metal Radiator Specific Weights Related to Area and T_{eff}

where:

$$\overline{U} = T_{eff}/T_{sink}$$

$$U_i = T_{tube\ in}/T_{sink}$$

$$U_o = T_{tube\ out}/T_{sink}$$

The values of $T_{tube\ in}$ and $T_{tube\ out}$ used above are the temperatures of the radiator tube surface at its extremities and differ from the inlet and outlet fluid temperatures by the film liner, and armor temperature drops. The effective radiating area is for a black surface with a fin efficiency of unity. The actual area is obtained by dividing the effective area by the product of the fin efficiency and the emissivity. Since $T_{tube\ in}$ and $T_{tube\ out}$ are not among the selected interfacing parameters, it is desirable to express them in terms of the corresponding fluid temperatures, T_{in} and T_{out}. Thus a more convenient way to define the variables of equation 2 is

$$\overline{U} = (T_{eff} + \theta)/T_{sink}$$

$$U_i = T_{in}/T_{sink}$$

$$U_o = T_{out}/T_{sink}$$

where θ is a correction factor applied directly to T_{eff}. From the parametric data it is found that the correction factor θ can be adequately described by

$$\theta = 0.03\, T_{in} - 23.8 \qquad (1160 \leq T_{in}\ (^{o}R) \leq 1460)$$

$$\theta = 11.0 \qquad (T_{in}\ (^{o}R) < 1160)$$

where T_{in} = fluid inlet temperature (^{o}R)

This linear approximation provides a satisfactory correlation over the range $700 \leq T_{in}$ (^{o}F) ≤ 1000. For values of fluid inlet temperatures less than $700^{o}F$, the use of $\theta = 11.0$ is slightly conservative.

It should be noted that the curves of Figure 5-17 do not increase monotonically with respect to T_{eff} as might be expected; furthermore, there are two distinct curves for the $T_{eff} = 530^{o}F$ value. This apparent inconsistency is due to two factors: first, for a given value of T_{eff} there are an infinite number of combinations of T_{in} and T_{out} which satisfy Equation 2, and second, the material composition of the various radiators is dependent upon their operating temperatures as described in Section 5.2.1.

Figure 5-18 depicts curves analogous to those of Figure 5-17; however, in this case they represent the weights of radiators constructed entirely of aluminum. Comparison of corresponding curves on Figures 5-17 and 5-18 show a weight penalty of approximately 0.01 lbs/ft^2 for each percentage point of tube length having the copper-steel construction. This factor, although it varies slightly over the area range considered, provides a convenient correlation between the data of Figure 5-17 and Figure 5-18.

Replotting Figure 5-18 on log scales yields curves which can be expressed in the form

$$RSW = e^{\left[K \ell n (AREA) + B\right]}$$

as shown by Figure 5-19. Solving for the appropriate values of K and B the equation describing the entire system of data is found to be

$$RSW = e^{\left(0.2516 \ell n \left\{AREA\right\} + 0.00138 T_{eff} - 3.071\right)} \quad (3)$$

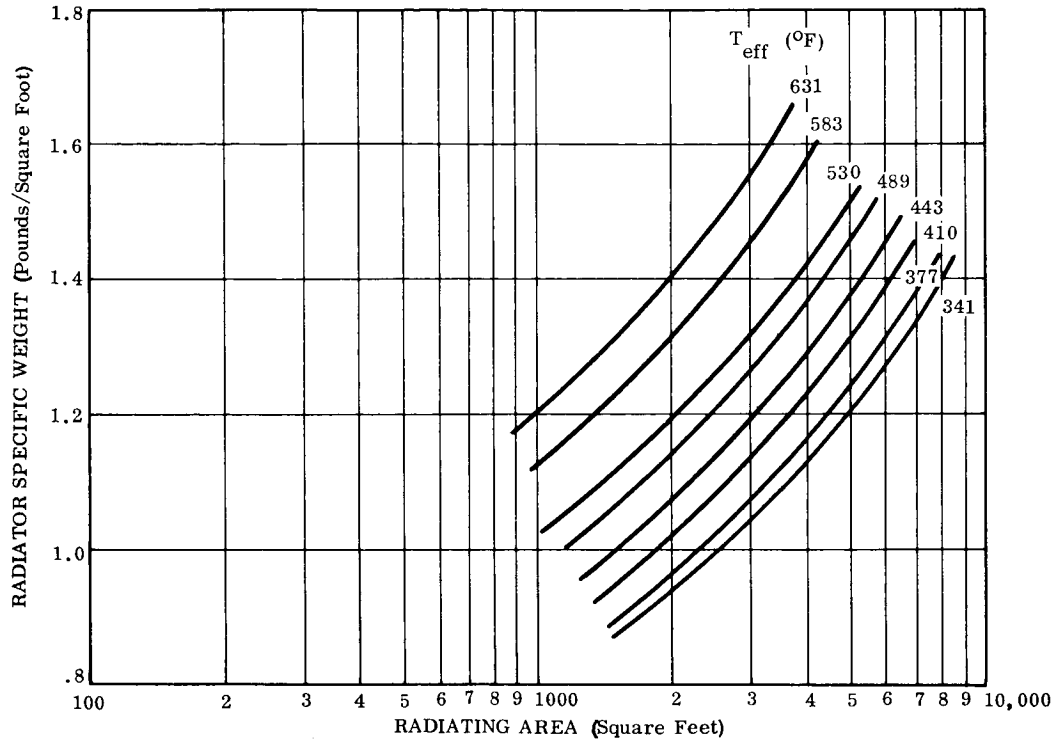

Figure 5-18. Radiator Specific Weights for All Aluminum Radiators

where

RSW = radiator specific weight - lbs/ft^2

AREA = radiator area - ft^2

T_{eff} = effective radiating temp - ^oR

Evaluation of this equation will yield the specific weight of an aluminum radiator and requires further modification to give weights corresponding to the combination radiators described by Figure 5-17.

The fractional length of steel-copper tube required can be found by evaluation equation 1 for the appropriate values of fluid inlet and outlet temperatures and setting T equal to 1160^oR (the transition temperature).

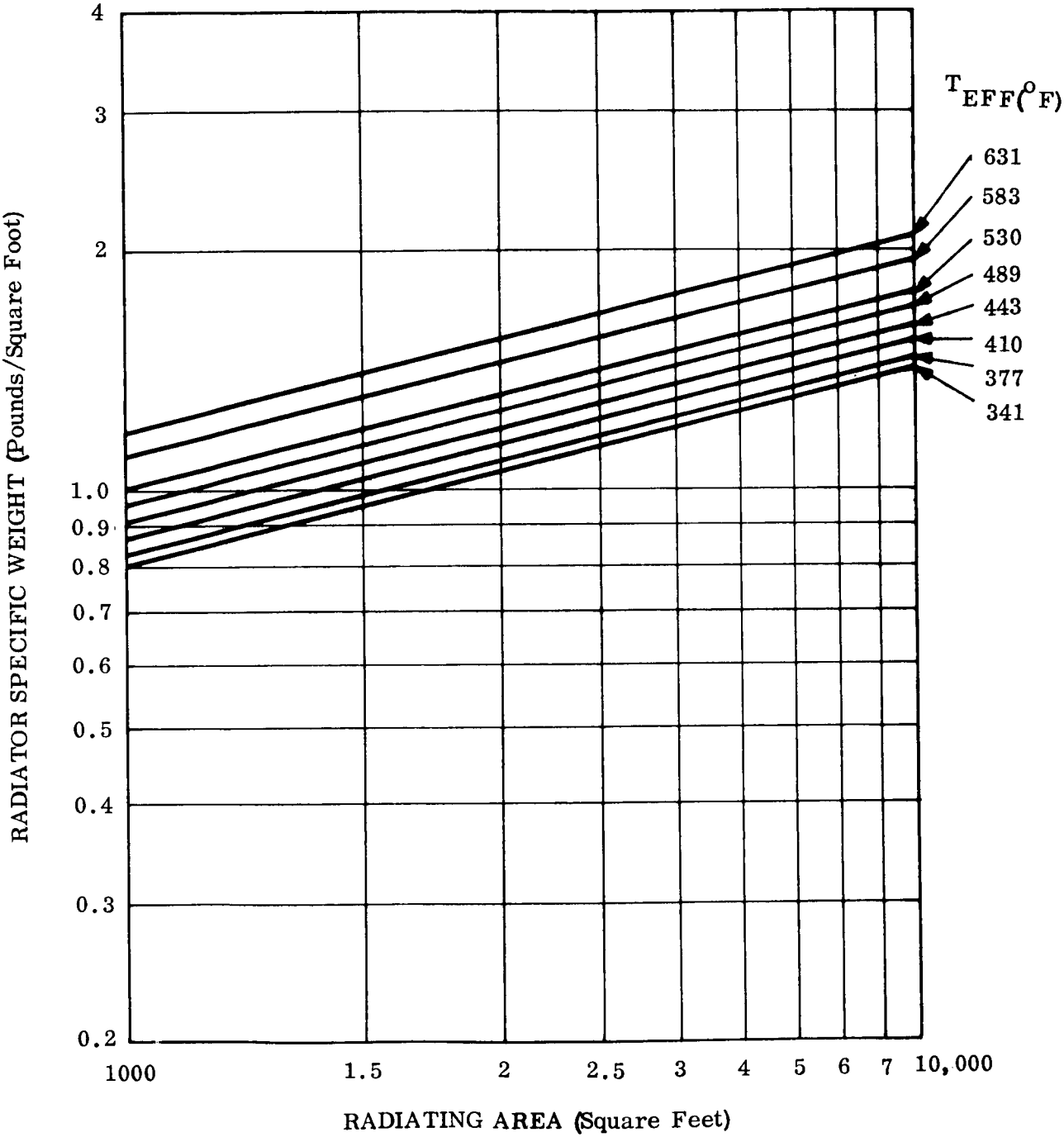

Figure 5-19. Log Log Plot of Aluminum Radiator Data

Thus

$$\phi' = \frac{\left[\frac{T_{in}\,(^{o}R)}{1160}\right]^{3} - 1}{\left[\frac{T_{in}\,(^{o}R)}{T_{out}\,(^{o}R)}\right]^{3} - 1}$$

where ϕ' is the fractional distance along the tube measured from the inlet to the point at which the fluid temperature is $1160^{o}R$.

Applying the steel-copper weight correction factor described above gives

$$\phi\ (\text{lbs/ft}^2) = \frac{0.01\ \text{lbs/ft}^2}{\%\ \text{length of copper-steel}} \times 100\ \phi'$$

and ϕ is seen to be numerically equal to ϕ'. Adding this factor to equation 3 yields the desired expression for radiator specific weight of the composite radiator. These equations and the Stefan-Boltzmann radiation law complete the required mathematical model. For the liquid metal radiators it may be summarized by,

$$\text{AREA} = \frac{3.15 \times 10^{12}\ Q}{(T_{eff}^{4} - T_{s}^{4})\ \eta_{fin}\ \epsilon}$$

$$\text{RSW} = \phi + e^{\left[0.2516\ \ell n(\text{AREA}) + 0.00138 T_{eff} - 3.071\right]}$$

where

AREA = radiator area (ft^2)

RSW = radiator specific weight (lbs/ft^2)

Q = thermal load (KW)

T_{eff} = effective radiating temperature (^{o}R)

$$\phi = \frac{\left[\frac{T_{in}\,(^{o}R)}{1160}\right]^{3} - 1}{\left[\frac{T_{in}\,(^{o}R)}{T_{out}\,(^{o}R)}\right]^{3} - 1} \quad \text{for } T_{in} \geq 1160^{o}R$$

and $\phi = 0.0$ for $T_{in} < 1160^{o}R$

5.3 GAS RADIATORS (NEON WORKING FLUID)

Both the parametric data and the mathematical model for the gas radiators were developed along lines similar to those discussed for the liquid radiator. In the case of gas radiators, however, an additional complexity is introduced in the form of a fourth independent interfacing variable, namely, radiator pressure drop.

5.3.1 ANALYTICAL APPROACH

For the all gas system the radiator pressure drop has a direct and significant influence on the cycle performance and must be included in the radiator model. The desired relationship can be stated mathematically as

$$\text{RAD. WT.} = f(Q,\ T_{in},\ T_{out},\ \Delta P/P)$$

where

RAD. WT. = radiator weight

Q = thermal load

T_{in} = gas inlet temperature

T_{out} = gas outlet temperature

$\Delta P/P$ = ratio of radiator pressure drop to radiator inlet pressure

The range of independent variables over which the gas radiator model was developed is as follows:

a. Thermal Load, Q = 250 KW to 1000 KW
b. Gas Inlet Temperature, T_{in} = $600^{o}F$ to $900^{o}F$
c. Gas Outlet Temperature, T_{out} = $200^{o}F$ to $500^{o}F$
d. Pressure Loss Fraction, $\Delta P/P$ = 0.01 to 0.04

Certain combinations of these variables (for example, T_{in} = $600^{o}F$ and T_{out} = $500^{o}F$) are not conditions normally encountered in Brayton cycle systems and were not included. Another parameter which exhibits influence on the radiator design is pressure level. Although an argument could be made to add this variable to the existing list of independent parameters, it was judged that a satisfactory model could be developed by assuming a linear variation of pressure level with thermal load. The relationship selected for this study is,

$$P = 0.12Q$$

where P is the inlet pressure in psia and Q is the radiator thermal load in kilowatts.

In view of the large boundary layer temperature drops, inherent to gas-filled radiators, it appeared likely that the use of internal fins (vanes) within the tubes might result in a large enough increase in radiator temperature, and reduction in radiator area, to justify the added weight necessary to maintain the same pressure drop. Use was made of the Spartan IV computer program to compare optimized gas-filled radiators with and without vanes. Table 5-1 shows the results of analysis performed for internally finned radiators of different material combinations. The radiation using magnesium-thorium for fin, armor

and vane material, and no liner, is seen to experience a 20 percent reduction in both area and weight when internal vanes are used. As indicated earlier, the designs used for this study advocate the use of a tube liner, and, for practical reasons, the vanes and liner are of the same material. Nickel is a suitable candidate and its selection gives a moderately good thermal conductivity to the vanes. As is evident from Table 5-1, the advantage of vanes is somewhat reduced when nickel is used, however, a saving of 15 percent on weight and area is still realized. A correlation for use with the Spartan III computer program was based on the data generated with Spartan IV and is used to develop the gas radiator model presented herein.

TABLE 5-1. EFFECT OF INTERNAL VANES

Fin & Armor Material	Magnesium	Aluminum	Aluminum
Vane Material	Magnesium	Nickel	Nickel
Tube Liner Material	None	Nickel	Nickel
Thermal Load (KW)	500	1000	500
Gas Inlet Temp (^{o}F)	815	900	750
Gas Outlet Temp (^{o}F)	315	400	300
Gas Inlet Pressure (PSIA)	40	120	60
Reduction in Area (%)*	20	15	16
Reduction in Weight (%)*	21	16	14

*Comparison of optimized finned and unfinned radiators for identical materials, pressure level and drop, thermal load and temperatures.

5.3.2 PARAMETRIC DATA

As with the liquid metal radiators, carpet plots are again used to present the gas radiator parametric data. These are shown in Figures 5-20 through 5-23. Over the range considered it is seen that radiator outlet temperature produces the most significant changes in radiator weight. The variation due to fractional pressure drop remains approximately constant at

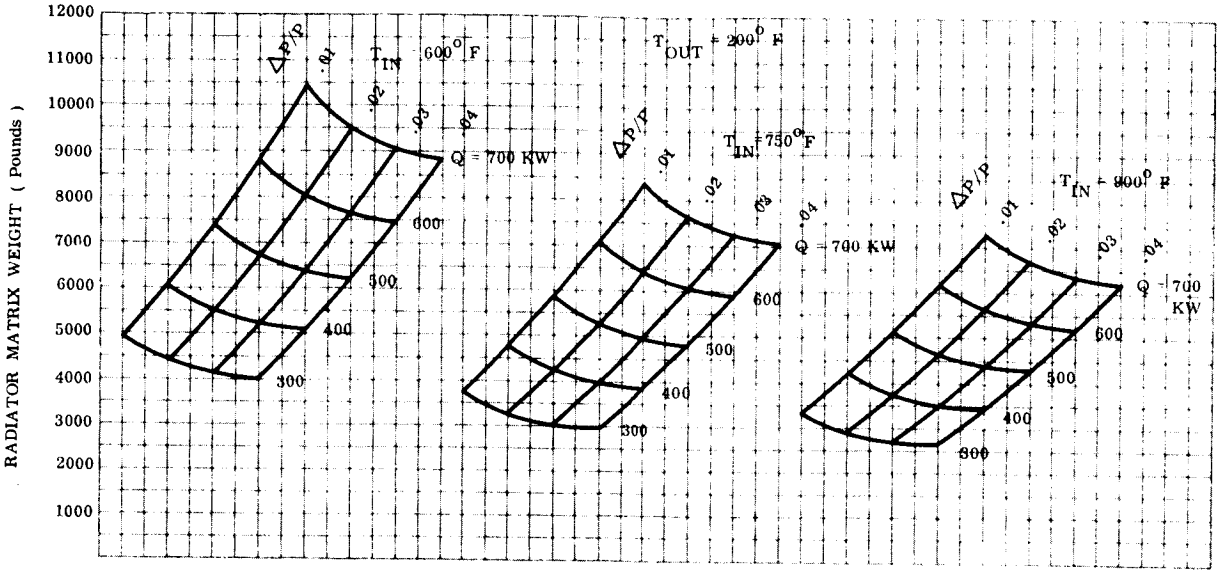

Figure 5-20. Optimized Gas (Neon) Radiator Weight Related to T_{in}, $\Delta P/P$, and Heat Rejected for $T_{out} = 200^{o}F$, $T_{sink} = -10^{o}F$, Emissivity = 0.9

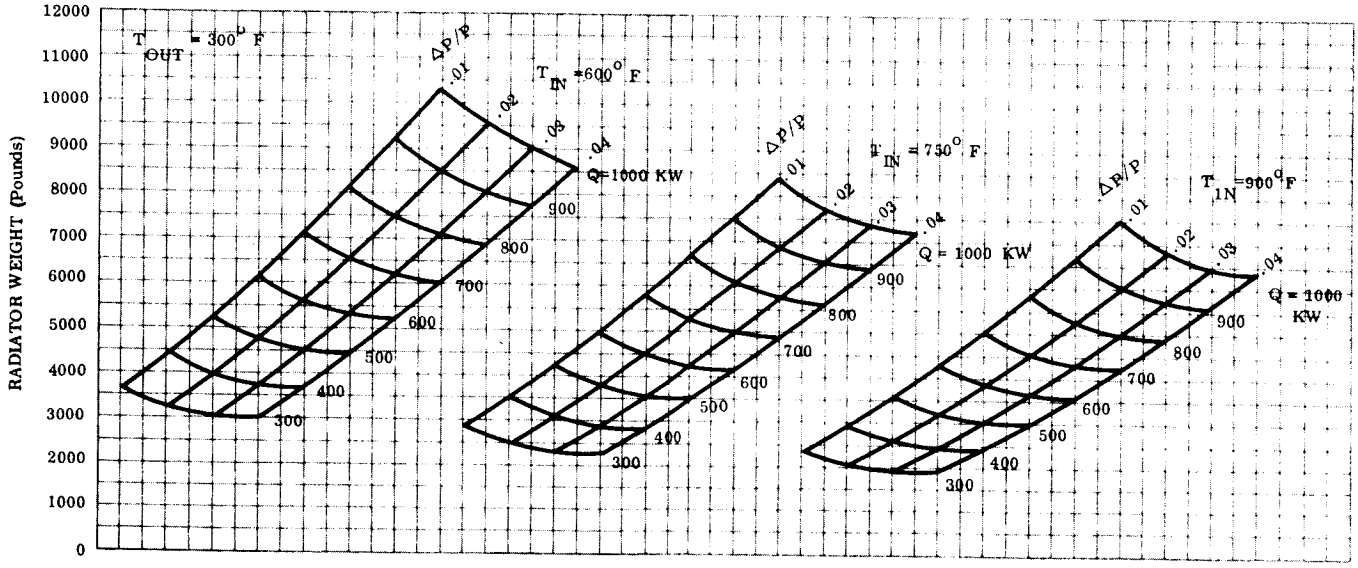

Figure 5-21. Optimized Gas (Neon) Radiator Weight Related to T_{in}, $\Delta P/P$, and Heat Rejected for $T_{out} = 300^{o}F$, $T_{sink} = -10^{o}F$, Emissivity = 0.9

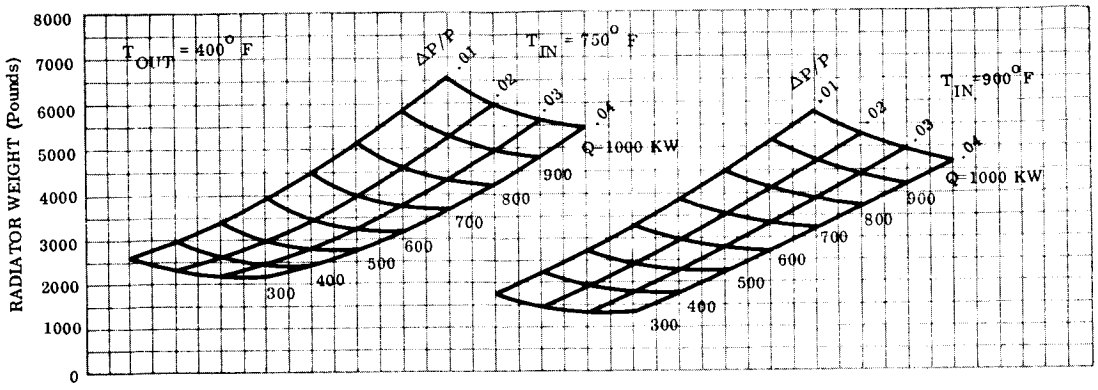

Figure 5-22. Optimized Gas (Neon) Radiator Weight Related to T_{in}, $\Delta P/P$, and Heat Rejected for T_{out} = 400°F, T_{sink} = -10°F, Emissivity = 0.9

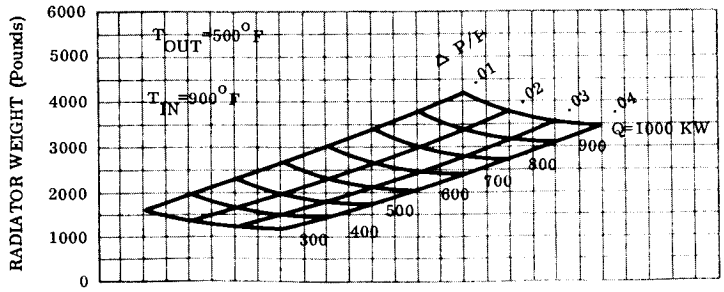

Figure 5-23. Optimized Gas (Neon) Radiator Weight Related to T_{in}, $\Delta P/P$, and Heat Rejected for T_{out} = 500°F, T_{sink} = -10°F, Emissivity = 0.9

15 percent throughout, and the over-all weight range approaches an order of magnitude. At a 200°F outlet temperature data is not presented for thermal loads above 700 kilowatts because the resultant weights and areas far exceed the range of current interest.

5.3.3 MATHEMATICAL MODEL

To facilitate the development of the analytical model, it is again found convenient to replot the parametric data on logarithmic coordinates of radiator specific weight and $\Delta P/P$ as is shown by Figure 5-24. Although a certain amount of scatter is evident, the various combinations of thermal load and inlet temperature behave in a manner permitting adequate approximation by the superimposed dashed line. The equation describing this line is of the form

$$\ln RSW = K \ln (\Delta P/P) + B$$

Simultaneous solution for the appropriate values of K and B and a rearrangement gives the desired equation:

$$RSW = e^{(-0.1352 \ln (\Delta P/P) + 0.00058 T_{out} - 0.392)} \quad (4)$$

where

RSW = radiator specific weight (lbs/ft^2)

$\Delta P/P$ = fractional pressure drop

T_{out} = gas outlet temperature (^{o}R)

While this equation satisfactorily describes the data presented it does not, in itself, constitute a complete analytical model. It remains to determine a correlation for thermal load, inlet temperature, and total radiator area.

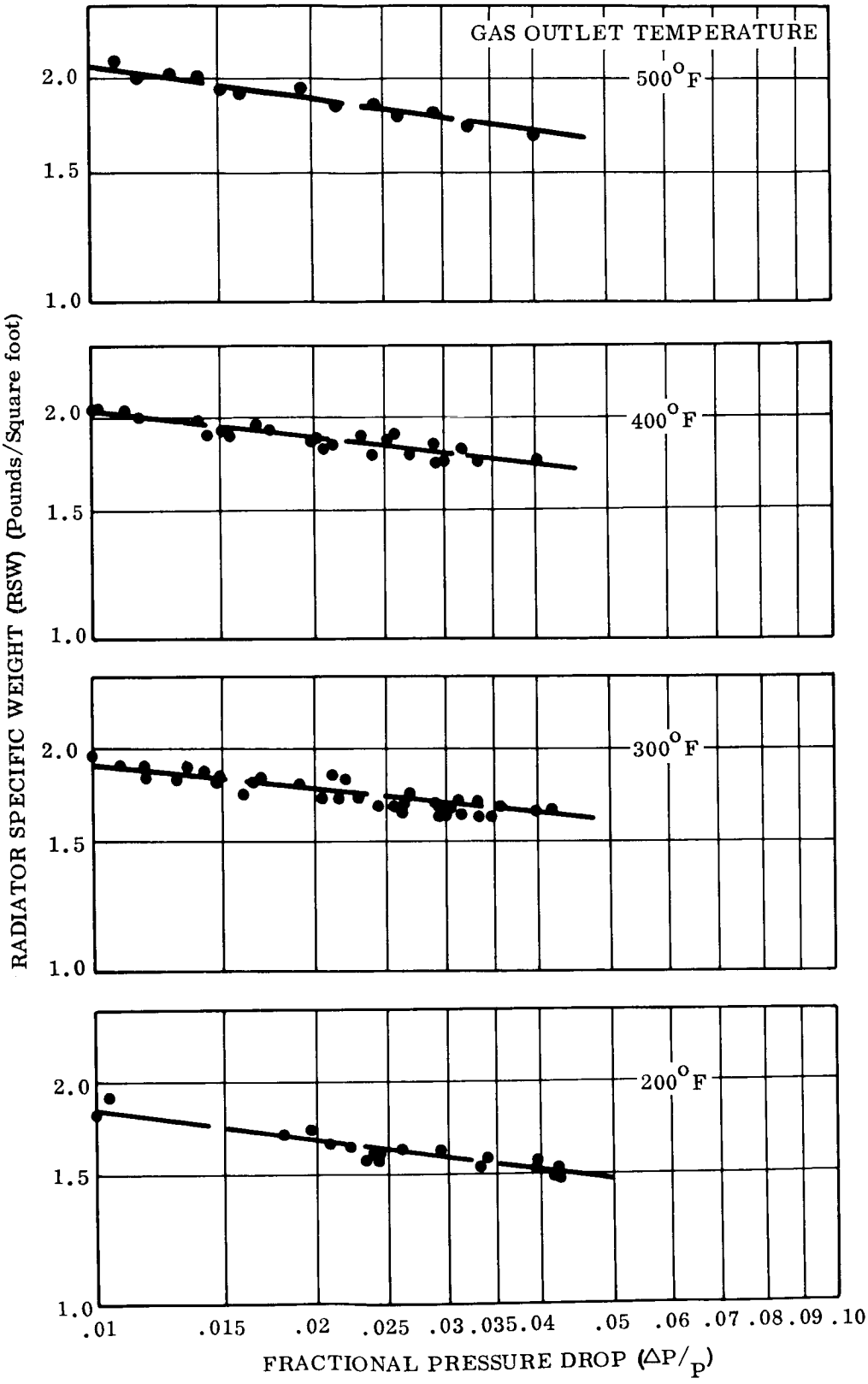

Figure 5-24. Radiator Specific Weight of Optimized Neon Gas Radiators

Figure 5-25 depicts the variation of effective radiating temperature, T_{eff}, with the parameter $\Delta P/P$ for selected combinations of gas inlet and outlet temperatures. Here too, a degree of scatter is noticeable, but within the warranted accuracy, each family of points can be represented by a linear relation. By means of a curve fit an equation relating effective temperature to fractional pressure drop, fluid inlet, and fluid outlet temperature can be constructed as follows:

$$T_{eff} = 250\ (\Delta P/P) + 1.4\ T_{out} + 0.666\ T_{in} - 5.33 \times 10^{-4}\ (T_{in} \cdot T_{out}) - 486. \qquad (5)$$

where

T_{eff} = effective radiating temperature (^{o}R)

T_{in} = gas inlet temperature (^{o}R)

T_{out} = gas outlet temperature (^{o}R)

$\Delta P/P$ = fractional pressure drop

With this relationship the equation for radiation heat transfer can be solved to determine the required radiator area

$$AREA = \frac{2.72 \times 10^{12}\ Q}{(T_{eff}^{4} - T_{s}^{4})} \qquad (6)$$

where

AREA = radiator area (ft^2)

Q = thermal load (KW)

T_{eff} = effective radiating temperature (^{o}R)

T_s = sink temperature (^{o}R)

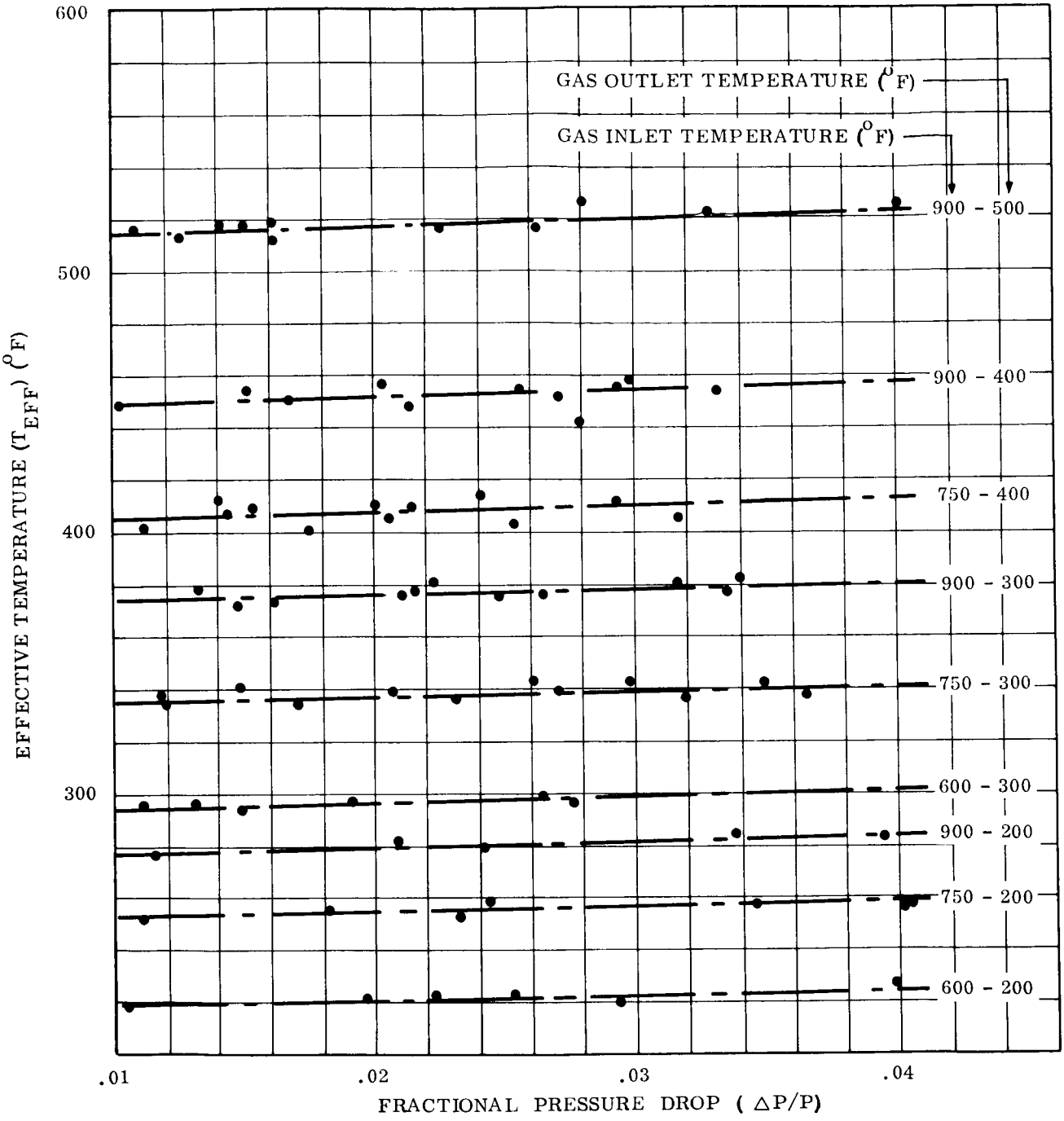

Figure 5-25. Effective Radiating Temperature of Optimized Gas (Neon) Radiators

Equations 5 and 6 provide the desired relationship for area, thermal load, and gas inlet temperature. Used in conjunction with equation 4 they complete the analytical gas radiator model.

5.3.4 EFFECT OF SINK TEMPERATURE

5.3.4.1 Liquid Metal Filled Radiators

The technique used for determining the effective radiating temperature in the NAK radiator model is dependent upon the value of sink temperature and comparison with exact evaluated using the Spartan computer program shows that no additional factor is required to account for sink temperature variations over the range between $-459.6^{\circ}F$ and $+100^{\circ}F$.

5.3.4.2 Gas Filled Radiators

In the generation of the basic gas radiator model for a sink temperature of $-10^{\circ}F$ it was found that, for an area unlimited optimum design, the fin efficiency remains essentially constant at 73% over the range of interest. A change of sink temperature however, shifts the fin efficiency of the optimum radiator and a compensating factor must be incorporated. A linear variation of fin efficiency with sink temperature provides a satisfactory means of describing the effects of sink temperature. Figure 5-26 illustrates the variations of weight and area with pressure loss ratio and sink temperature for a typical neon filled radiator. The discrete points represent the values determined by the Spartan computer program and the solid lines show the values resulting from the gas radiator model used in the cycle optimization studies. The effect of sink temperature on fin efficiency is given by:

$$\eta \text{rad} = 0.77 - 7.33 \times 10^{-5} T_{\text{sink}}$$

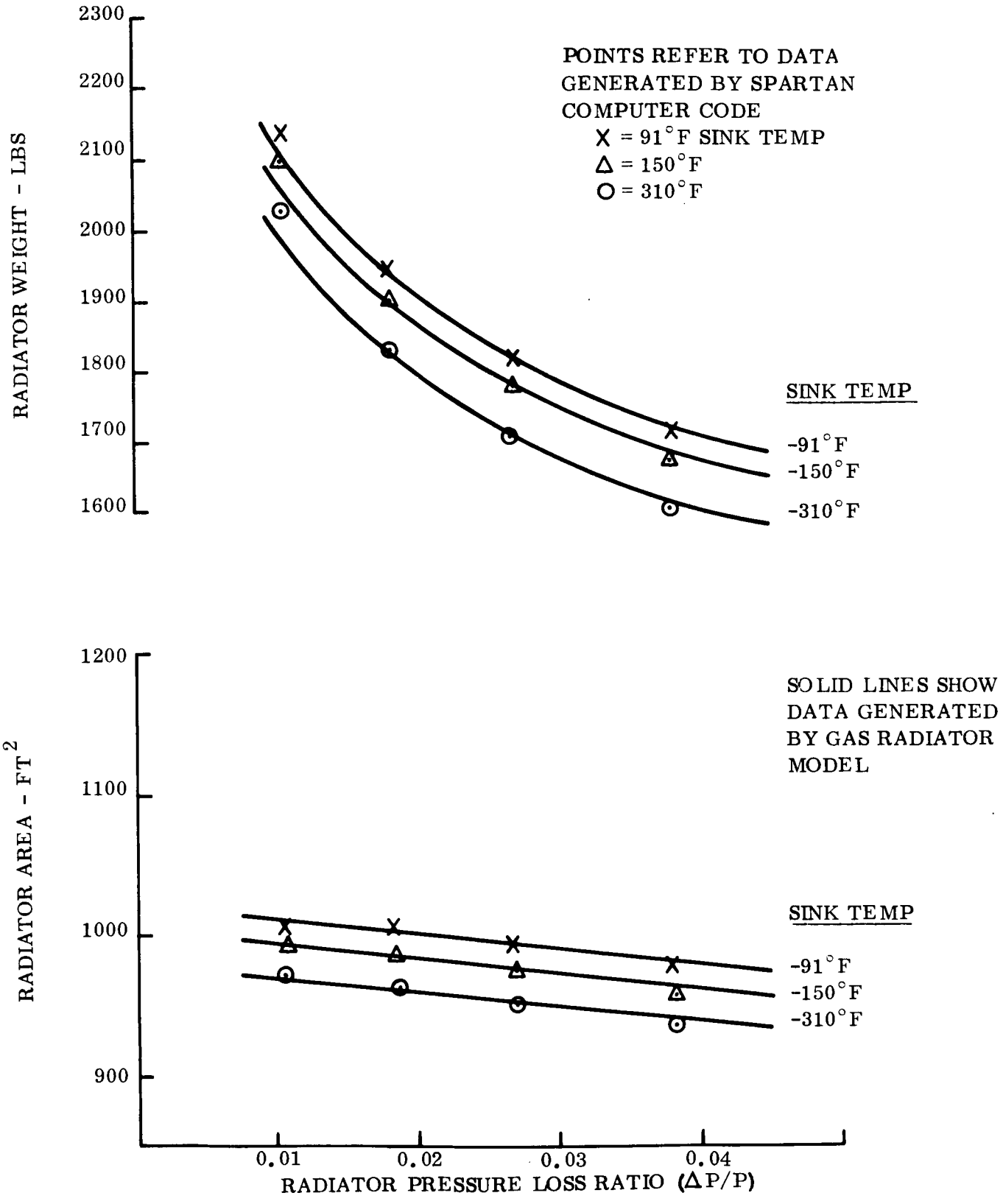

Figure 5-26. Effect of Sink Temperature on the Weight and Area of Neon Filled Radiators

5.4 STRUCTURAL REQUIREMENTS

All of the above material has been concerned with the radiator strictly in its capacity as a functioning component of the thermodynamic cycle. The parametric data and mathematical models in no way reflect the weight required to convert the radiator into a practical usable component. Structural additions are required not only to sustain the launch loads, but also to effect the physical joining of the various elements of the radiator circuit to each other. The weights of these additional items are much more difficult to express parametrically because of the nature of the assumptions associated with their definition. However, this in no way justifies ignoring them; they are a significant part of the Brayton cycle optimization tradeoff analysis, and their exclusion would significantly compromise the value of the study results.

Prior studies (Reference 1) of space radiators have indicated that earth-launched designs should also act as the spacecraft structure. The thermal optimization requires the use of tubes in the length range of 8 to 12 feet which introduces a set of ring members which serve to physically tie the ends of the radiator panels together, support the header piping, and (in some cases) provide meteoroid bumper protection to the headers. Between these rings, the fin/tube matrix acts as a semi-monocoque structure. As a result of the meteoroid armor the radiator tubes are quite stiff in bending and very strong in pure compression along their axes. The fins partially stabilize the tubes against buckling and the header support rings provide end constraints which add to the effective panel stiffness.

The over-all radiator matrix is fairly heavy and strong attachments would be required to support it from an independent structure. In order to insure that such an independent structure would carry the launch loads, it would have to be considerably stiffer in all loading directions than the radiator matrix it is carrying. In view of the inherent stiffness of the latter an inordinately heavy structure would be required. An alternative would be to segment the radiator axially and provide flexibility in the attachments to prevent the trans-

mission of structural loads along the matrix. Such an approach is inconsistent with the task of supporting the heavy matrix and controlling dynamic responses during passage through the launch load environment.

As a measure of the effectiveness of the radiator for use as a structure the data display of Figure 5-27 is used. Here the tube spacing is related to fin thickness for various values of fin efficiency which of course correspond to values of radiator heat rejection area. For a given set of design assumptions there is an optimum radiator design which is represented by point A on the graph. Any change in position on the graph from this point must be accompanied by an increase in the weight of the radiator. Therefore, this point represents the bottom of a weight contour map. Starting from such an optimum design, increasing the fin efficiency has the effect of reducing the required radiator area and increasing the weight. Due to limitations in the booster payload envelope it is frequently necessary to design such area limited radiators. Within the bounds of an area limit there is again a minimum weight radiator. Point B on the map illustrates a typical minimum weight area limited radiator otherwise known as an area limited optimum. The dashed line passing through points A and B represents a locus of area limited optimum radiators. Again, moving in any direction from the area limited optimum along a constant fin efficiency line must result in an increase in radiator weight. Lines of constant weight may be constructed on the map as illustrated. Thus, for a given weight there are many choices of tube spacing and fin thickness; however, the radiator heat rejection area and corresponding fin efficiency must be adjusted to maintain the constant weight.

At this point then, the figure shows how tube spacing and fin thickness are related to weight and area from a strictly thermal performance viewpoint. We know also that from a structural viewpoint the tube and fin assembly represents a semi-monocoque type of structure; this also has an optimum relationship between the tube spacing and fin thickness. Computation of the structural requirements is subject to many assumptions involving the

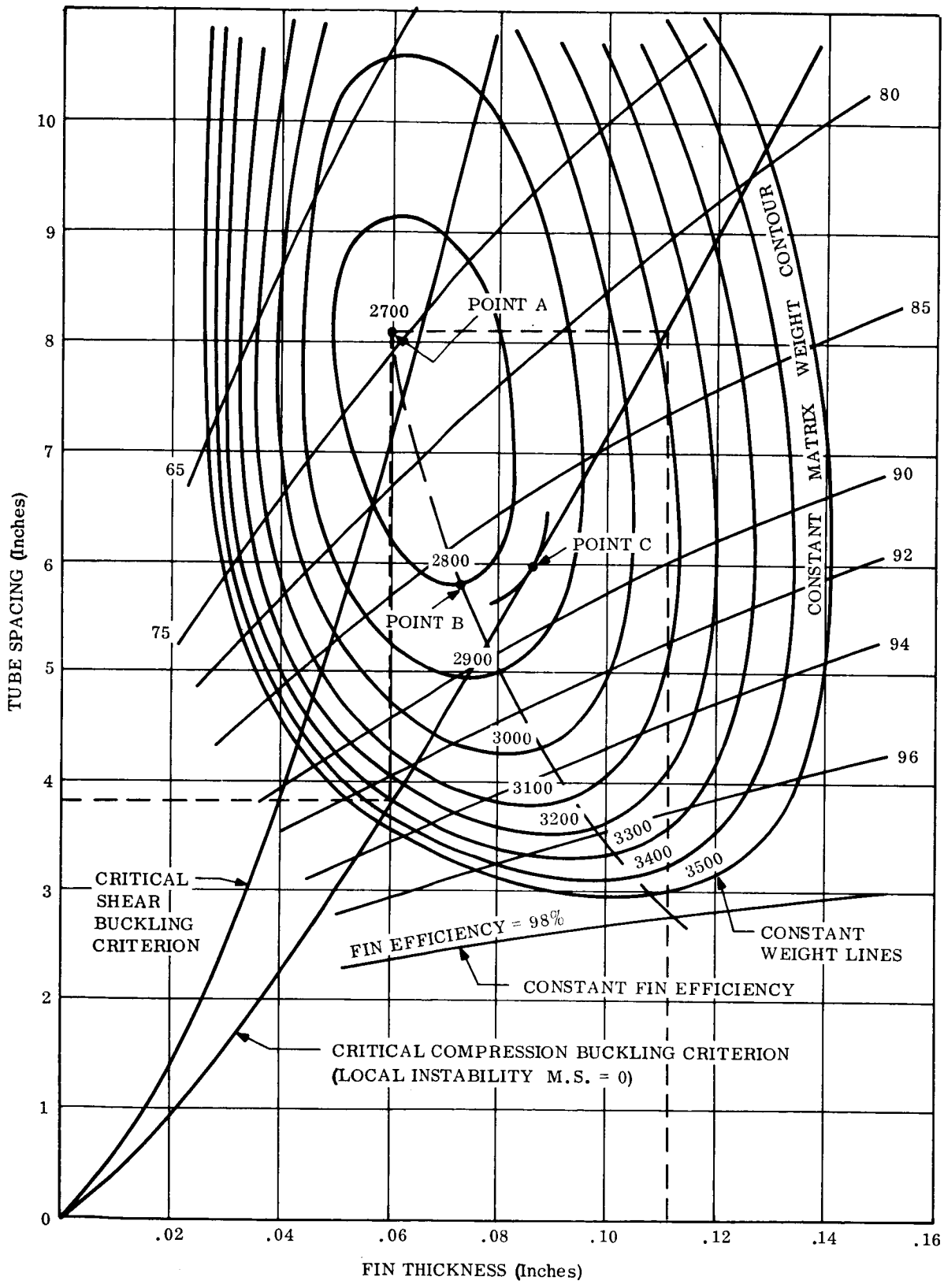

Figure 5-27. Radiator Thermal/Structural Design Interactions (600 KW Heat Rejection Aluminum Rankine Cycle Radiator Example)

loads, the mission, the total shape and size of the radiator, etc. However, a reasonable assessment can be made based on the practical knowledge of how these systems generally go together in a systems study. The case in point represents a radiator using the total payload capability of a three stage Saturn V booster. Thus the loads are reasonably determined for preliminary analysis purposes. Two lines are identified on the graph indicating the structural requirements. One of them is the fin shear buckling associated with the bending action of aerodynamic loads. The other line is local instability resulting from compression loads tending to buckle the fins. Obviously the latter is the determining factor for the case in point. As such it represents a zero margin design. The absolute minimum weight radiator denoted by point A is obviously not meeting the structural requirements. If the fin thickness were maintained constant the tube spacing would have to be cut in half to obtain the critical compression buckling limit line. Conversely, if the tube spacing were maintained constant, the fin thickness would be required to almost double. In practice neither of these routes to the structural stability line would represent the optimum way of climbing out of the thermal design "valley." The optimum design from both a structural and thermal viewpoint would be that design for which the constant weight contour is tangent to the structural limit line. Point C then represents this optimum design and it is seen that both tube spacing and fin thickness are adjusted to achieve it. The weight increase for this example is seen to be approximately 150 pounds out of a total of 2700 pounds. Thus to modify the optimum thermally designed panels to include the structural capability (launch loads and fairing aerodynamic loads) requires a weight increase of only five and one-half percent. In many cases, the assumed loading places the structural design criteria line to the left of the unlimited optimum point indicating the complete structural adequacy of the thermal panels. The gas radiator case illustrated in Figure 5-28 illustrates this point. In this case the loading assumption was based on using the Saturn 1B launch vehicle.

Whereas the above examples numerically illustrate the basic compatibility of the radiator panel thermal and structural performance requirements despite a wide variation in loading assumptions, they do not indicate the actual magnitude of the additional structural needs. With the local stability established by the panel geometry, structural rings are required to

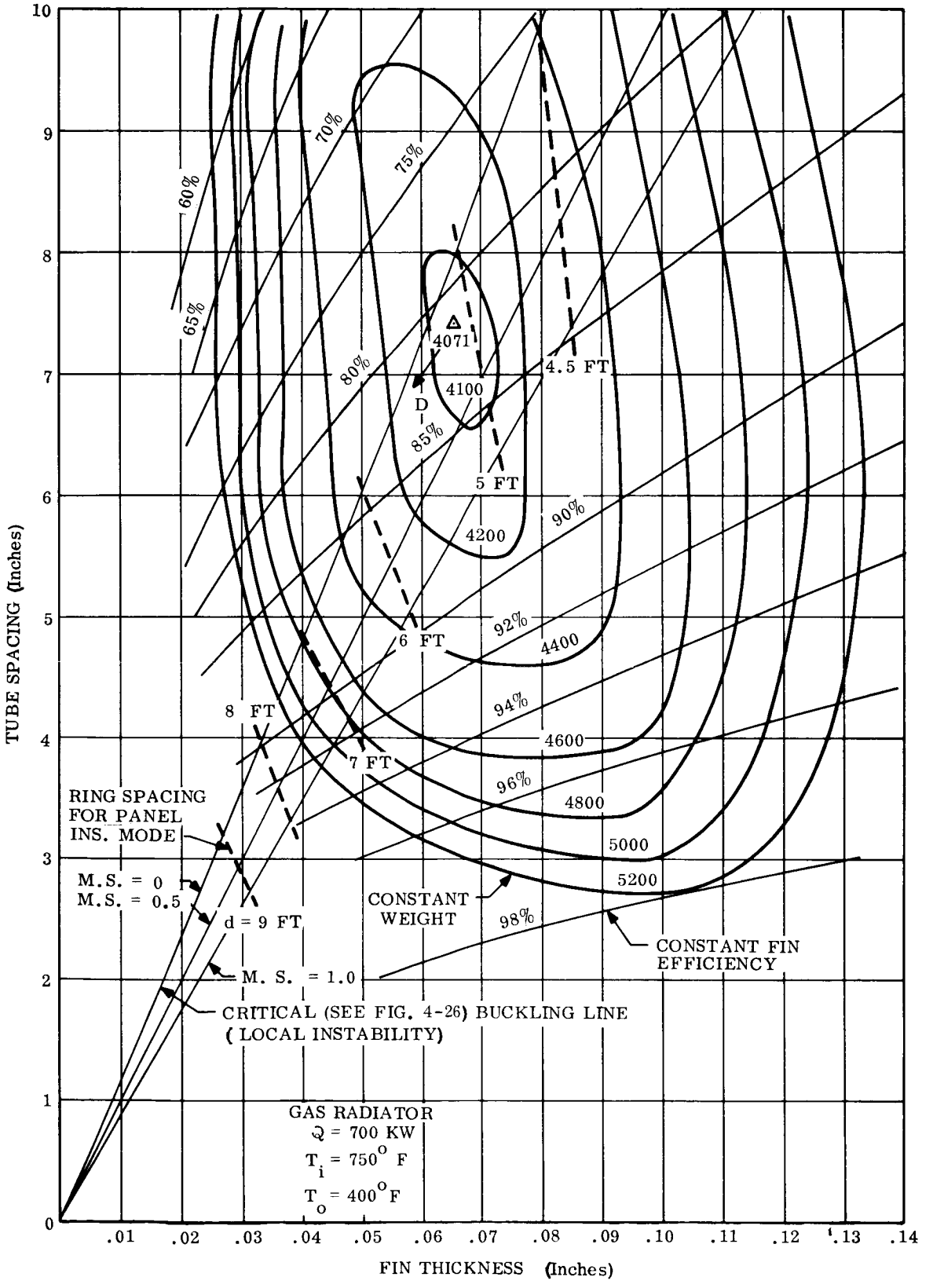

Figure 5-28. Radiator Thermal/Structural Design Interactions (700 KW Heat Rejection Aluminum Brayton Cycle Radiator Example)

stabilize the entire assembly. Additional structural limit lines are included in Figure 5-27 for margin of safety values of 0.5 and 1.0 in addition to zero. Lines of constant ring spacing are also shown to illustrate this structural aspect. Ring spacing to prevent panel instability is determined from

$$d = \sqrt{\frac{c\pi^2 E I_s}{\left[(M.S.)\ \sigma_s + 1\right] A_s}}$$

where

c = 2 (partial fixed end condition)

E = 8,000,000 psi

I_s = Moment of inertia of panel

A_s = Cross-sectional area of panel

σ_s = Compressive stress in panel

M.S. = Margin of Safety

As expected, for a given margin of safety, the required ring spacing is seen to increase as the matrix becomes heavier. Near the radiator optimum it is in the order of five feet. Clearly, then, the optimum design would see a shift in the direction D to economize on the ring weights. In practice the ring spacing is partly determined by the tube length selected since there is an advantage in using the joint structure as the stabilizing ring with suitable modifications. Thus with a ten foot length, this analysis indicates the need for auxiliary rings between the main bay joint rings.

A large part of the additional structural weight is associated with the simple matter of joining the panels to each other, providing a base mounting ring, thermal control hardware, and other such items. The state-of-the-art has not yet placed the systems evaluation of these aspects on a par with the thermal aspects; however, the above examples show the

kinds of approaches supporting the structural assumptions used in this study. For the purposes of the cycle optimization analysis the radiator structural requirements were approximated by examining previous design point studies in relation to the specific nature of the Brayton radiator. The net result was a simple logarithmic relationship to radiator area. Figure 5-29 illustrates the resultant weight adder to be applied to the basic matrix weights given by the results of Sections 5.2 and 5.3. Since this adder is a weight element approaching the size of the radiator matrix itself, and has a substantially higher uncertainty factor, the actual cycle optimizations were run with and without it to assess its effect on the over-all optimization conclusions.

Factors considered in the development of the curve presented in Figure 5-29 can be subdivided into two basic categories: 1) load carrying and 2) parasitic. Table 5-2 lists these items specifically and Figure 5-30 illustrates their locations in a typical bay joining concept.

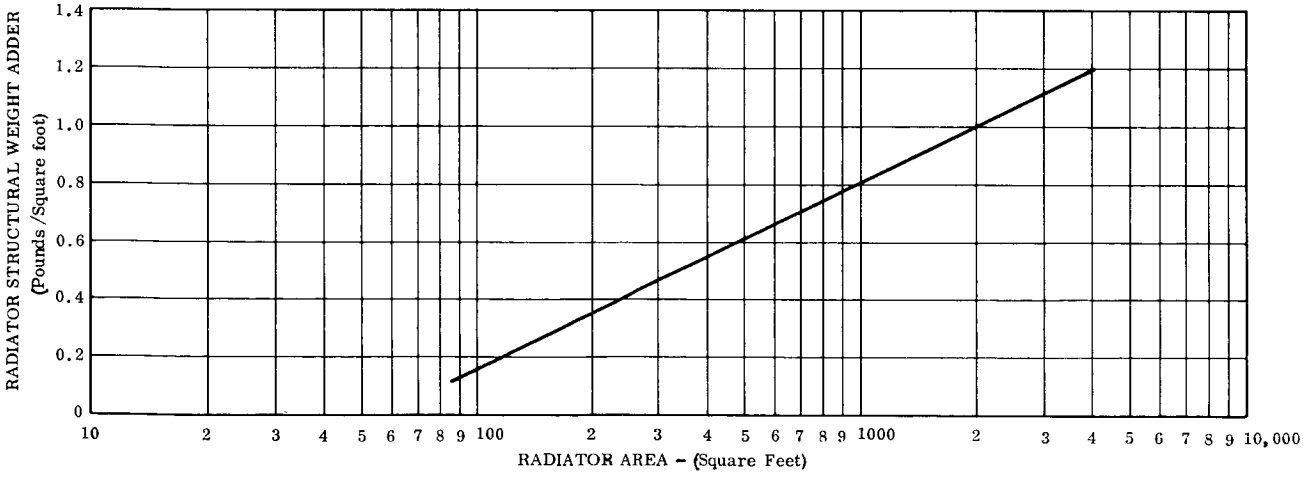

Figure 5-29. Weight Increment to Account for Practical Design Considerations and Mechanical Integrity Requirements

TABLE 5-2. STRUCTURAL WEIGHT ADDERS

Load Carrying	Parasitic
Splice Plates	Feed & Header Bumpers
Additional Fin Thickness	Piping Supports
Stabilizing Rings	Fillets
Panel End Stiffening	Coatings
Welds & Fasteners	Thermal Control
	Manufacturing Tolerances

REFERENCES

(1) "Research on Spacecraft and Powerplant Integration Problems," GE No. 64SD892, NASA Contract NAS No. CR 54159, July, 1964.

(2) Wallace, R.R. et al, "Effects of Hypervelocity Particles on Shielded Structures," ARS Journal, Vol. 23, No. 8, August 1962, pp 1231-1237.

(3) Nysmith, C.R. and Summers, J.L., "Preliminary Investigation of Impact on Multiple-Sheet Structures and an Evaluation of the Meteoroid Hazard to Space Vehicles," NASA TN D-1039, September 1961.

(4) Gehring, J.W. and Lieblein, S., "Preliminary Results on Effects of Hypervelocity Impacts on Space Radiator Tubes," ARS Paper 2544-62, November 1962.

(5) "Bonding Dissimilar Tubes," MACHINE DESIGN, February 18, 1965, p. 6.

(6) Hagen, K.G., "Integration of Large Radiators with Nuclear Electric Spacecraft Systems," SAE 845D, 1964.

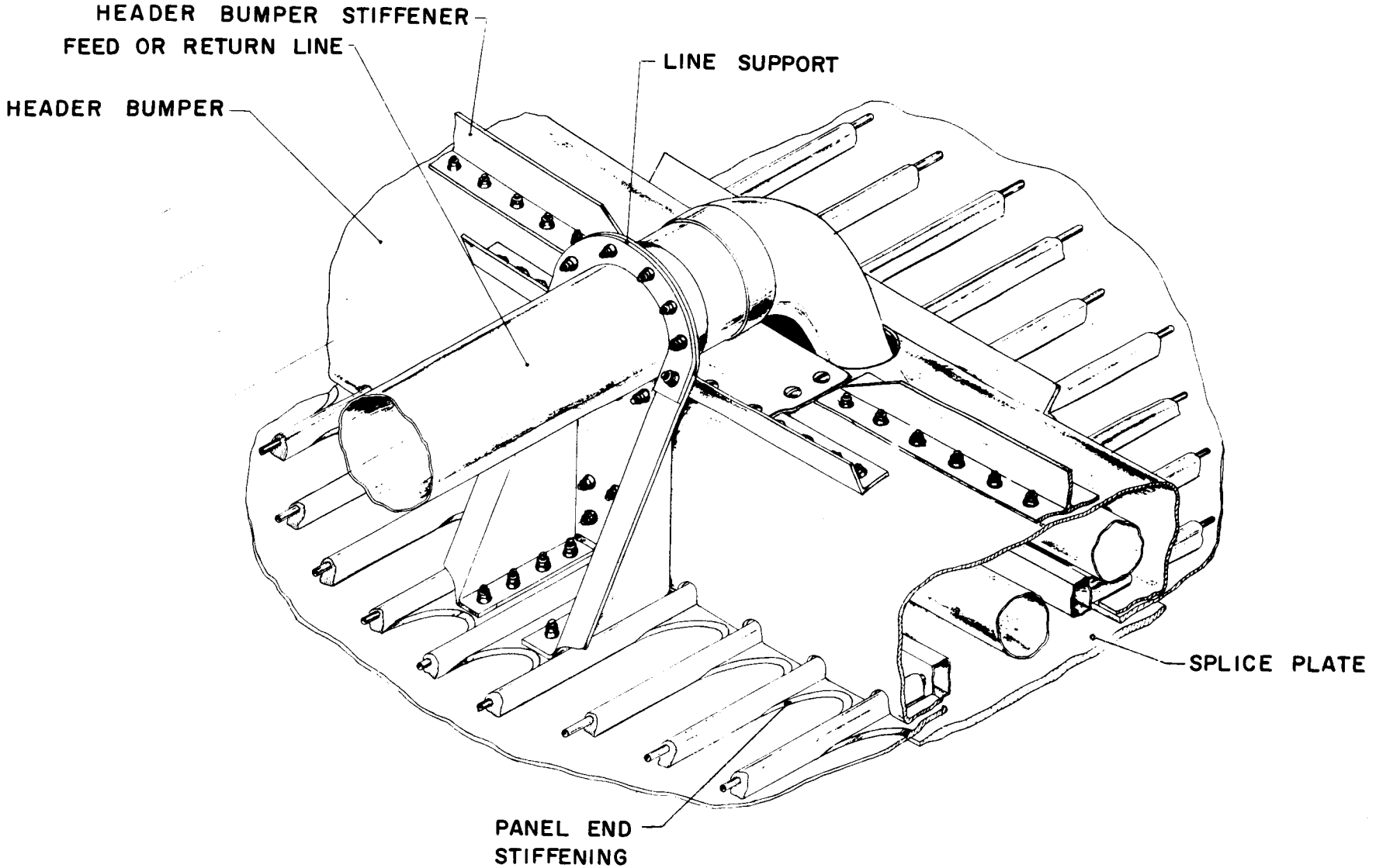

Figure 5-30. Bay Joining Concept

SECTION 6
HEAT EXCHANGER AND PIPING

6.1 HEAT EXCHANGERS

Heat exchangers are used in the Brayton cycle powerplant in up to three locations. A liquid metal-to-gas heat exchanger must be used with liquid cooled reactors; all powerplants have a gas-to-gas recuperator; and in some cases, a gas to -NaK heat exchanger is required for systems with liquid filled radiators. The heat exchanger models are based on a series of analytical counterflow designs. The models have an extended surface matrix and entrance and exit headers. Because of the shapes of the locations into which they must fit, thermodynamic considerations, and the topology of the fluid paths, three different shapes of heat exchangers were required.

The recuperator model is illustrated in Figure 6-1. The recuperator is made by stacking alternate layers of flat and corrugated plates. Alternate corrugated plates may differ in thickness, height, and wavelength to accommodate the different pressure and temperature level gases. The ends of the plates have turning vanes and the outer vane serves as the seal. The headers are connected to transition pieces and in turn to the interturbomachine pipes. The weight of the recuperator consists of the central matrix weight and an allowance of an additional length, equal to the width of the recuperator, to account for the headers. The fluid flow and heat transfer model is based on counterflow in parallel passages. The prediction of heat exchanger performance includes an evaluation of the heat transfer coefficient and friction factor, with separate correlations used in the laminar, transition, and turbulent regimes. Temperature dependent variable gas and metal properties are used in all calculations. Since gas exit temperatures, and hence the effectiveness, are not known a priori, an iterative routine is used to bring the estimates of the temperatures within a specified tolerance. The program output includes the effectiveness, matrix volume, weight, and pressure drop. The values of the matrix weight, volume, and pressure drop are modified to account for the entrance and exit headers. The casing weight is included in the

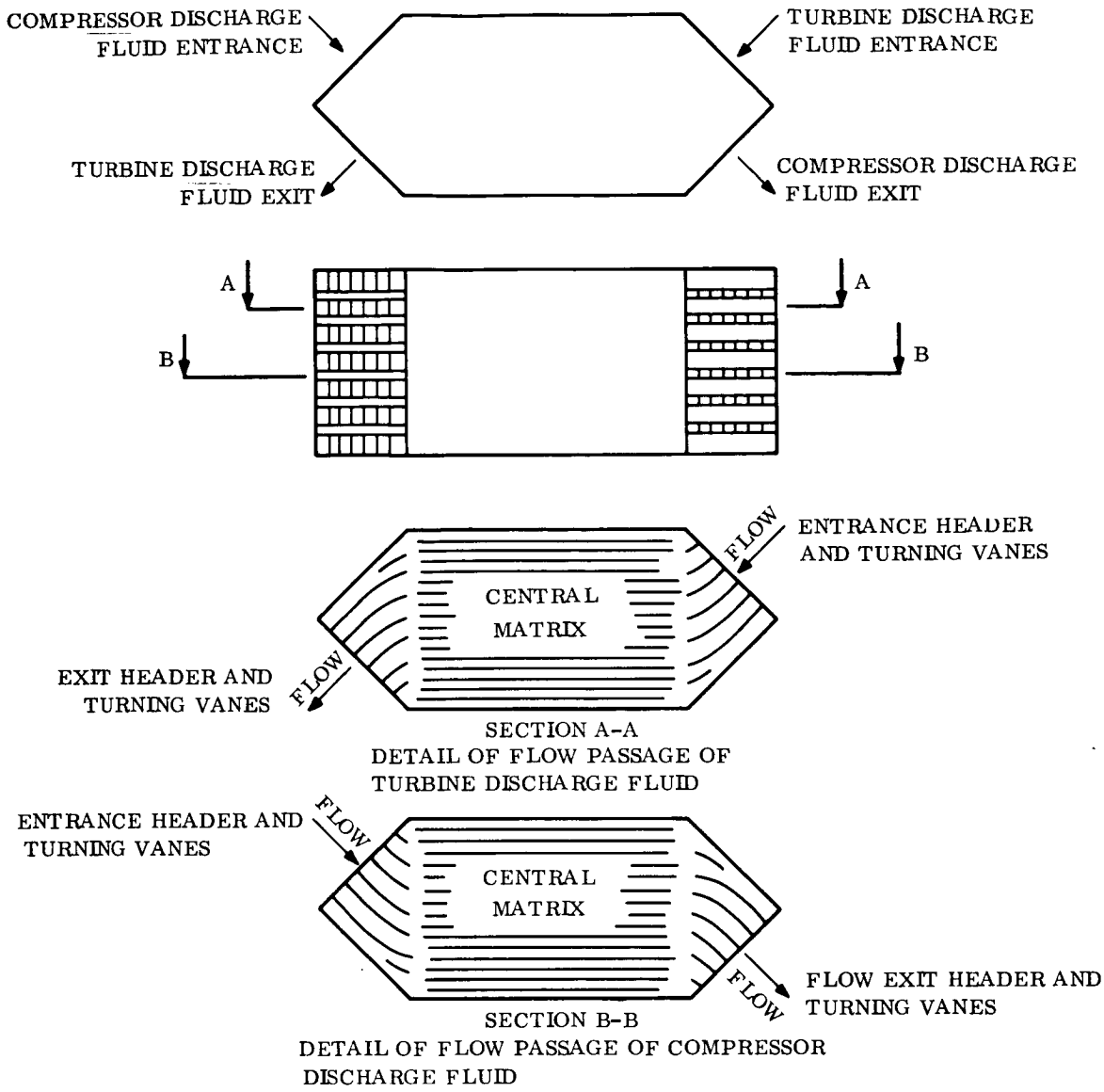

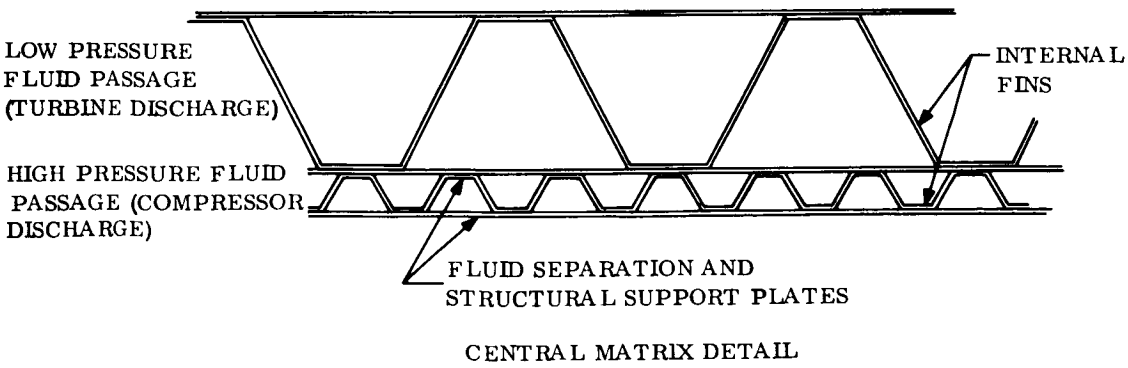

Figure 6-1. Recuperator Model

power conversion loop piping weight. The reactor coolant heat exchanger model is shown in Figure 6-2. The liquid-metal cooled reactor was studied for use on a powerplant for a manned space station, which contained two, independent, parallel power conversion loops. The reactor coolant heat exchanger was, therefore, one with two gas passages, each in counterflow with the same liquid metal stream. The two power conversion loops are intended for non-simultaneous use. Therefore, gas will be flowing in only one of the two heat exchangers. The liquid metal will be isothermal in the matrix of the heat exchanger of the non-operating loop, and experiences its complete temperature drop in the heat exchanger of the operating loop. Parallel operation of both sets of power generation equipment is possible with this arrangement, provided that each system operates at a fractional pressure and mass flow level proportional to its share of the total power. The weight, volume, and pressure drop includes allowance for the headers.

The model of the gas-to-NaK heat exchanger used to couple the power conversion system to the liquid-metal filled radiator is shown in Figure 6-3. The heat exchanger is of shell-and-tube design. Since no special headers are needed to mate with the adjacent piping, the weight, volume, and pressure drop were computed for the central matrix only. The model assumed an equal temperature change in both fluids while passing through the heat exchanger.

Since the fluid circulating in the radiator loop must leave the radiator at a temperature below the compressor inlet temperature determined by

$$\Delta T = \frac{(1 - E)}{E} \int_{T_{out}}^{T_{in}} dT$$

$$E = \text{Effectiveness} = \Delta T \text{ gas} / (T_{\text{hot in}} - T_{\text{cold in}})$$

where $\int_{T_{out}}^{T_{in}} dT$ is the change in fluid temperature in the radiator, an increase in

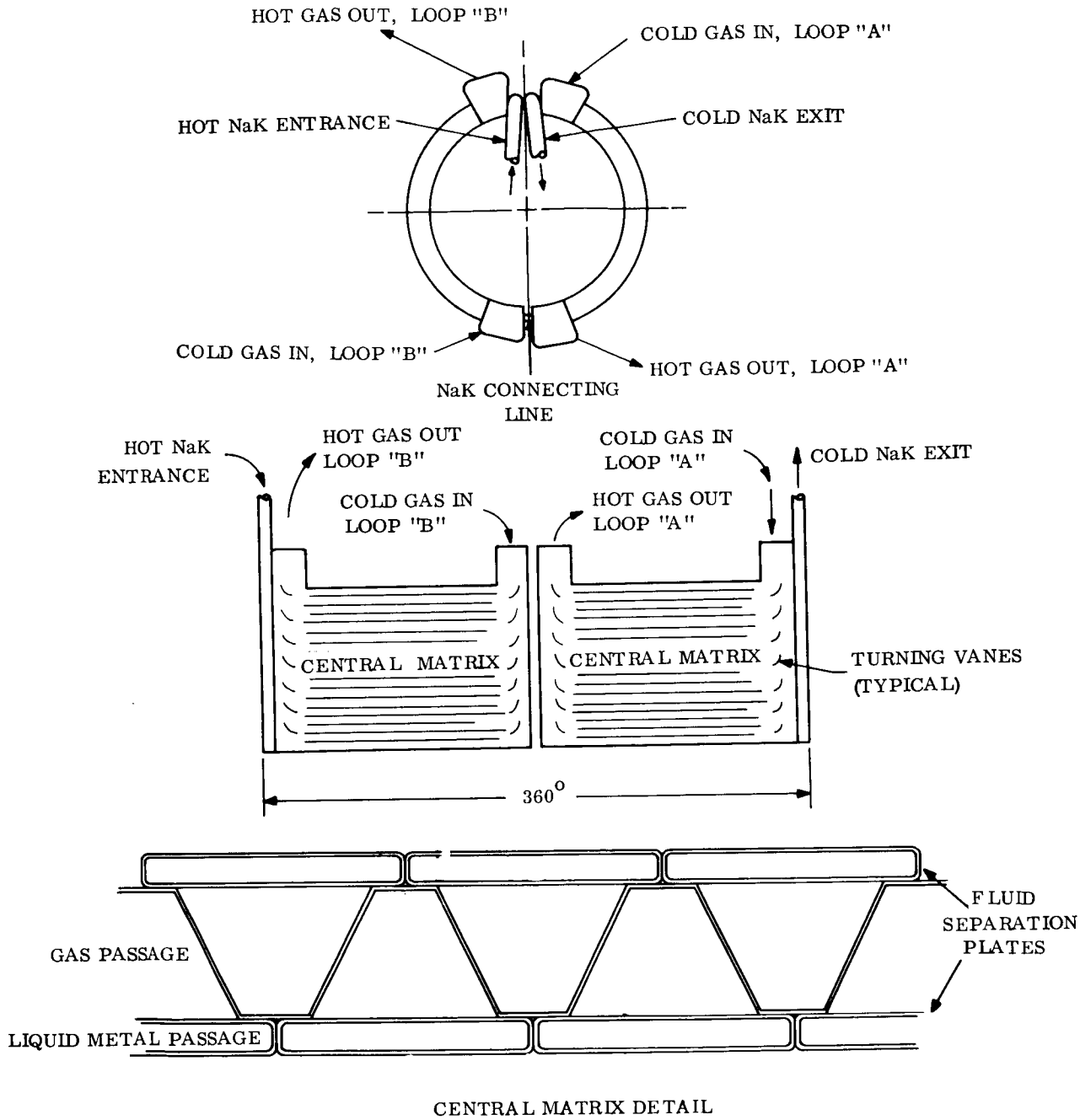

Figure 6-2. Reactor Coolant Heat Exchanger Model

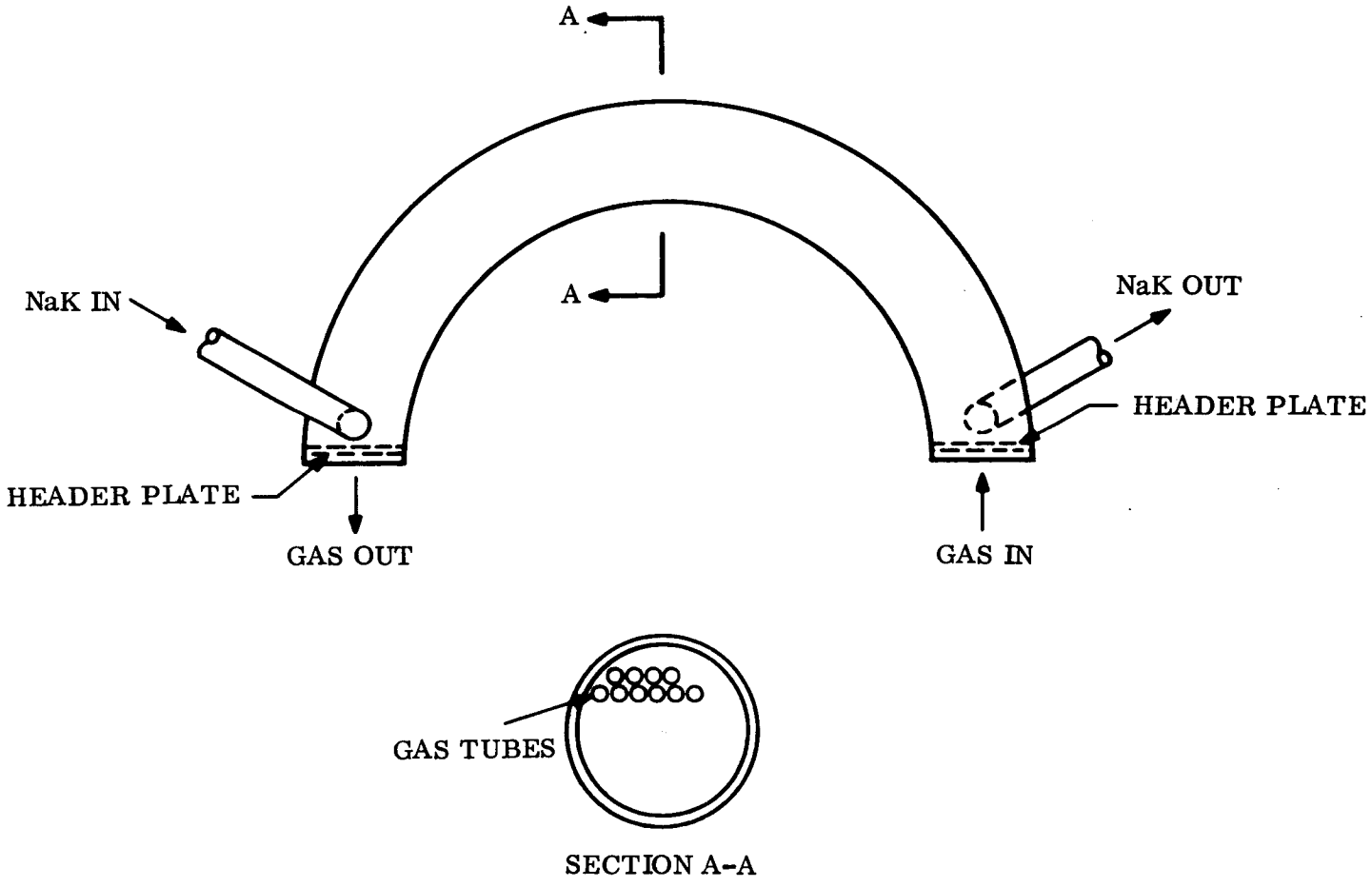

Figure 6-3. Gas to NaK Heat Exchanger (Liquid Metal Radiator Loop)

radiator fluid mass flow rate would only lower the radiator inlet temperature, and hence the average radiator temperature. A lowering of the radiator fluid mass flow rate would lower the heat transfer rate and require a lower radiator outlet temperature in order to achieve the same compressor inlet temperature, as compared with an equal specific heat rate design.

Specific designs were evaluated for effectiveness between 0.70 and 0.95, and for pressure drops on each gas side of 0.01, 0.02, and 0.03. The weight of the central matrix of these designs correlated well with a simple model established for average properties. This model predicts that the area of the heat transfer matrix is related to the effectiveness and pressure drop according to the following relationships:

- Recuperator

$$A = \frac{\dot{m}\, 8\, Pr}{p\, f} \left(\frac{E}{1-E}\right)^{3/2} \sqrt{\frac{2RT}{g\Delta P/P}}$$

- Reactor Heat Exchanger (assuming isothermal liquid metal)

$$A = \frac{\dot{m}\, 8\, Pr}{p\, f} \left(\ell n \frac{1}{1-E}\right)^{3/2} \sqrt{\frac{RT}{g\Delta P/P}}$$

- Radiator Heat Exchanger (assuming equal temperature changes)

$$A = \frac{\dot{m}\, 8\, Pr}{p\, f} \left(\frac{E}{1-E}\right)^{3/2} \sqrt{\frac{RT}{g\Delta P/P}}$$

The designs which were evaluated had plate thicknesses of 10 mils, and internal fin thicknesses of 5 mils. Curves of normalized matrix weights for various matrix pressure drops are shown in Figures 6-4, 6-5, and 6-6. The proportionality constant differed for the various heat exchangers, since their internal geometries were not the same.

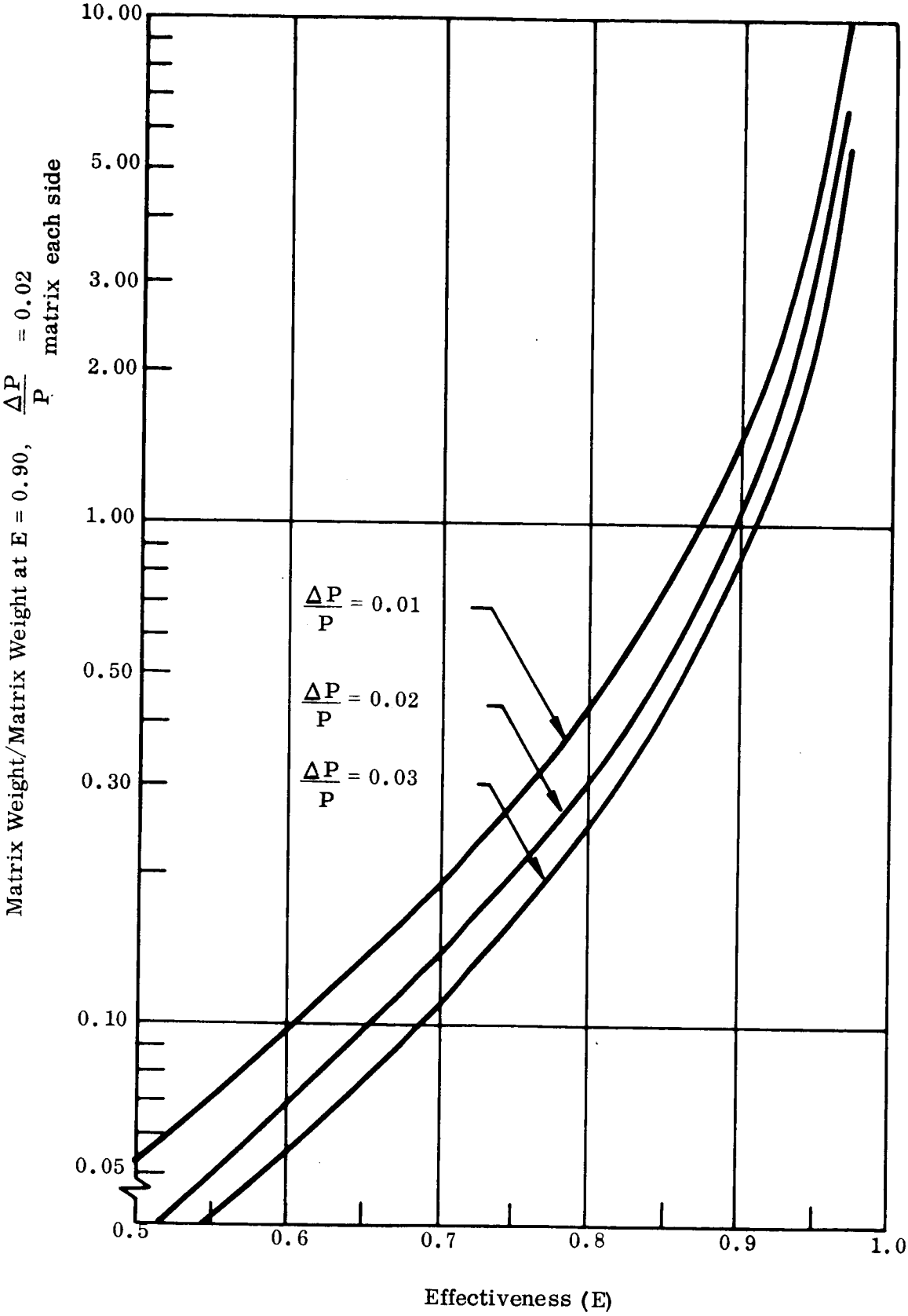

Figure 6-4. Normalized Matrix Weight of Counterflow Heat Exchanger With Equal Temperature Changes as a Function of Pressure Drop and Effectiveness

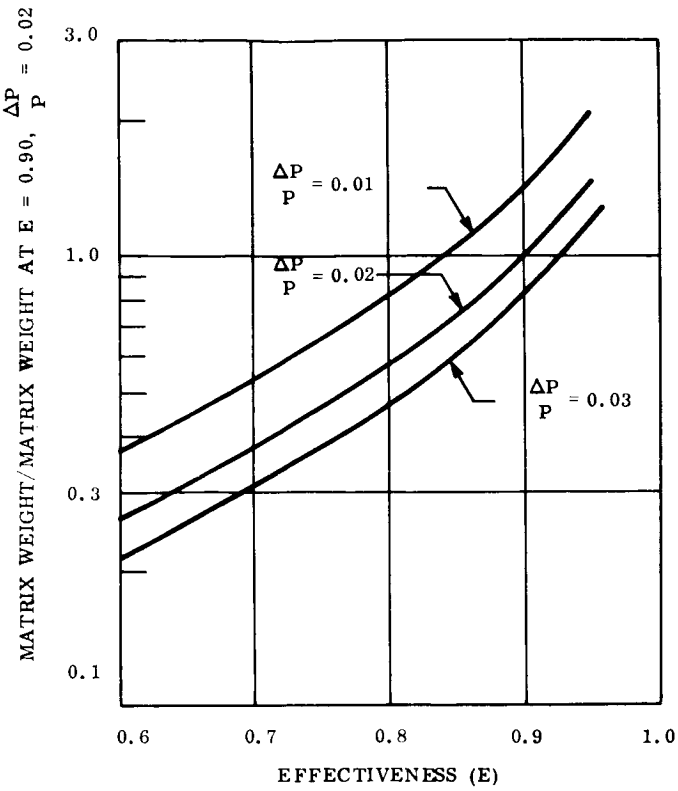

Figure 6-5. Normalized Matrix Weight of Heat Exchanger With One Fluid Isothermal as a Function of Pressure Drop and Effectiveness

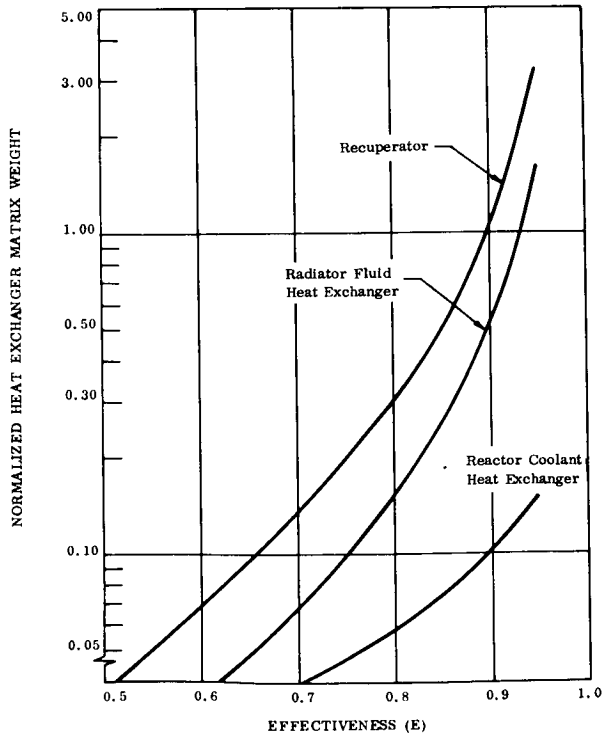

Figure 6-6. Comparison of Normalized Weight of the Three Heat Exchanger Designs

The model used in the system studies to trade-off recuperator weight against effectiveness and pressure drop consisted of a matrix whose weight was scaled from the reference solar Brayton design using the above criteria, and two header sections whose combined pressure drop and weight were equal to an equivalent length of heat exchanger. The normalized value of the matrix weight was 160 pounds at an effectiveness of 0.90, and a pressure drop of 0.02 for each side (total $\Delta P/P = 0.04$). These results are essentially in agreement with previous parametric studies of recuperator performance.*

6.2 PIPING SYSTEM WEIGHTS

Preliminary layouts have shown that a considerable length of piping is included in the Brayton cycle power conversion loop. Much of this weight is accounted for by the lines which connect the turbomachinery and recuperator package with the reactor heat source. The length of these lines will be essentially the same for both gas-cooled reactor and liquid-metal cooled reactor heat sources. The length of the lines interconnecting the turbines, recuperator, and compressor are the same for gas and liquid-metal cooled reactor systems. When a liquid-metal filled radiator is used, the gas-to-liquid-metal heat exchanger replaces a single six-foot length horseshoe pipe, but otherwise the power conversion ducting is untouched. The turbomachinery layout is shown in the powerplant design section. The feeds, headers and other gas radiator piping weights are included in the radiator weight computations. Table 6-1 shows the lengths of piping associated with the various loop arrangement options, for both optimistic and conservative estimates. These lengths were obtained from preliminary layouts of the powerplants.

*Anderson, A. F., Felszeghy, S. F., "Parametric Design Study Recuperator Development Program Solar Brayton Cycle System", NAS 3-2793, Report L-9372, AiResearch Manufacturing Division, Los Angeles, March 10, 1964.

Table 6-1. Piping Length

Loop Arrangement Option	Length		Number of "EL"s	
	Optimistic	Conservative	Optimistic	Conservative
Liquid Metal Filled Radiator	40	60	8	12
Gas Radiator	60	80	12	16

The allowable pipe thickness was based on the pressure level-power level relationship established for the NASA solar Brayton cycle turbomachinery. This relationship is

$$P\ (psi)_{\text{heat source}} = 1.45\ KW\ (shaft)$$

$$P\ (psi)_{\text{heat rejection}} = 0.63\ KW\ (shaft)$$

or, assuming an 88 percent generator efficiency

$$P\ (psi)_{\text{heat source}} = 1.555\ KWe$$

$$P\ (psi)_{\text{heat rejection}} = 0.715\ KWe$$

The allowable pipe wall stresses were limited to 5000 psi in the high temperature reactor return line, and 10,000 psi in the modest temperature reactor feed line, based on 10,000 hour stress rupture data for the material. The high temperature reactor return line was assumed to be made from a refractory alloy (tantalum, or tantalum-rhenium), and the reactor feed line from a nickel or cobalt based superalloy (Waspalloy, S-816 or L602).

The weight of the piping then is

$$\text{Weight} = \frac{\pi D^2 L \rho_c KWe}{2\sigma_c} \left[0.69 \left(\frac{\rho_h \sigma_c}{\rho_c \sigma_h} + 1 \right) + 0.12 \right]$$

where

ρ_c = Density of cooler pipe material = 495 lbs/ft^3

ρ_h = Density of hotter pipe material = 555 lbs/ft^3

σ_c = Allowable stress in cooler pipe material = 10,000 psi

σ_h = Allowable stress in hotter pipe material = 5,000 psi

The low pressure pipe diameter is 30 percent greater than the hot high pressure line in order to have the same Mach number in both passages. Ninety percent of the ducting length was assumed to carry the high pressure gas, being split in half between the moderate temperature reactor feed line and the high temperature return line.

The pressure drop predictions are based on an estimated friction factor of 0.04 and a loss of 0.2 heads per 90 degree turn.

$$\Delta p = \left(f \frac{L}{D} + NK \right) \frac{\rho V^2}{2 g}$$

The fractional pressure drop is

$$\frac{\Delta P}{P} = K_{total} \frac{\gamma M^2}{2}$$

The average temperature in the high pressure lines is given by

$$\frac{L_{total}}{T_{av}} = \frac{L_h}{T_h} + \frac{L_m}{T_m}$$

where

$$L_h = L_m = L/2$$

Assuming hot and moderate temperatures of 1900° and 1300°F respectively, the average temperature is 2015°R. The average sonic speed is 2875 ft/sec., for neon.

The total number of heads lost were estimated, based on a one-foot diameter pipe, to be 3.2 for the optimistic estimate in the liquid-metal radiator systems, 4.8 for the optimistic estimate with a gas-filled radiator and conservative estimate with a liquid-metal radiator, and 6.4 for the conservative estimate with a gas-filled radiator.

The velocity in the ducts is given by

$$V = \frac{4\dot{m}\,RT}{\rho \pi D^2}$$

The mass flow rate was taken as 120 pounds/hour per kilowatt (e). The pressure in the high pressure line was previously given as 1.555 psi/KWe. The velocity then is

$$V = \frac{31.8}{D^2} \text{ ft/sec}$$

The fractional pressure drop becomes

$$\frac{\Delta P}{P} = 1.008 \times 10^{-4} \frac{K_{total}}{D^4}$$

The piping weight is

$$\text{Weight} = 0.131\ D^2 L\ \text{KWe}$$

or

$$\text{Weight} = 13.1 \times 10^{-4} \sqrt{\frac{K_{total}}{\Delta P / P}} \bullet L \bullet \text{KWe.}$$

The above calculations have been made for the pressure-power proportionality which exists for the NASA solar Brayton cycle turbomachinery. A similar model was established for the higher efficiency, lower pressure level, turbomachinery used in this study. This higher efficiency, higher volume flow rate, lower pressure level machine has a pressure-power proportionality which is lower than that of the solar machine by a factor of 0.325. The wall thickness required for a given diameter, and hence the pipe weight, will decrease by this factor. However, the velocity increases in an inverse proportionality resulting in an increase in the pressure drop. Since the weight is inversely proportional to the square root of the pressure drop, there will be no net change in the weight-pressure drop relationship for the low pressure turbomachinery system, even though pipe diameters and wall thicknesses change.

The weight-pressure drop relationships are shown in Figures 6-7 and 6-8. Figure 6-7 shows a comparison of the pressure drops, or weights for different lengths of piping and total fluid turning angle. The diameter accompanying each curve is shown on a second scale at the top of the illustration. Figure 6-8 shows a comparison of the piping weights and pressure drops at various power levels for the intermediate estimate of flow losses. The pipe diameter for each system is also shown at the top of the illustration.

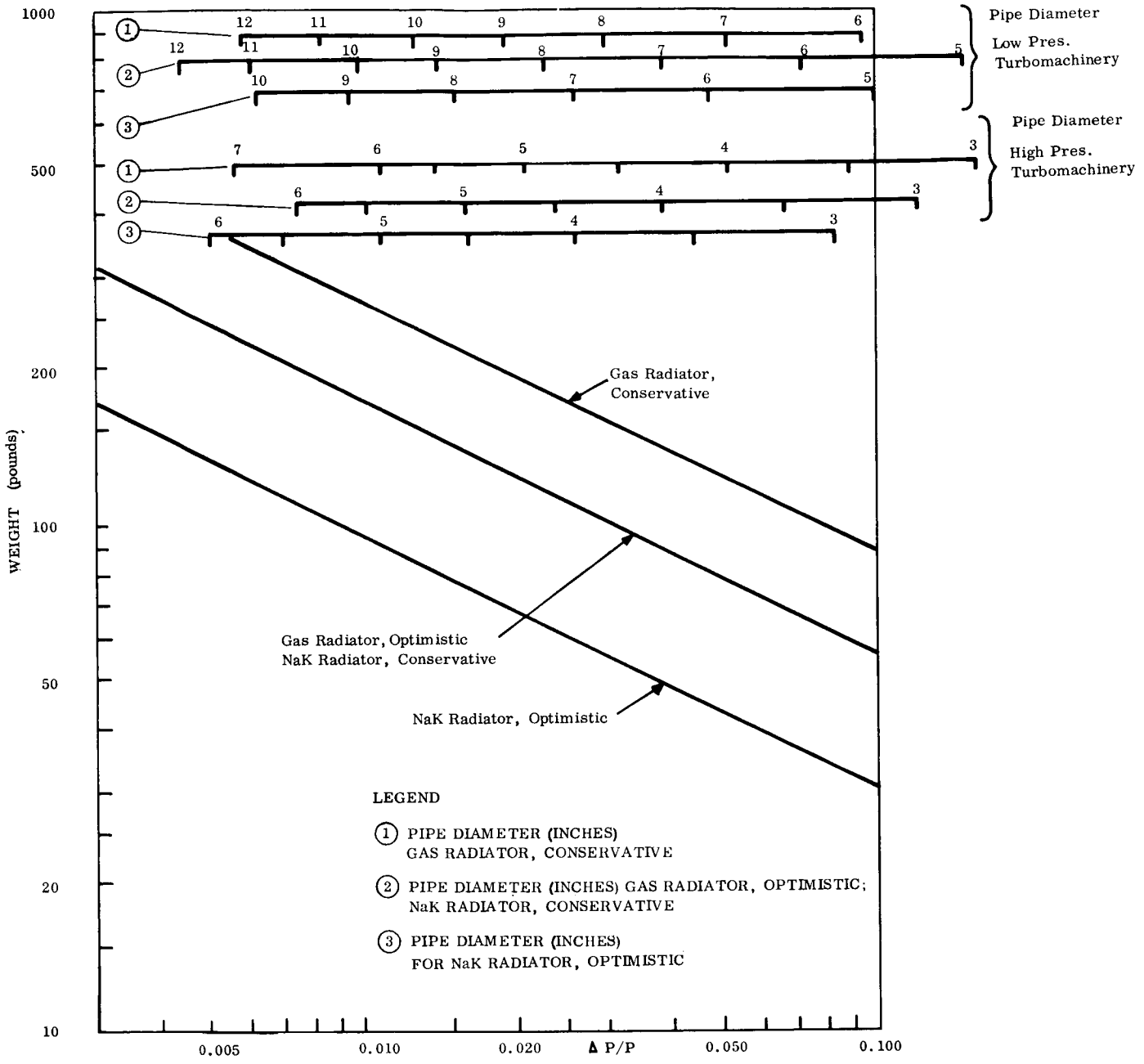

Figure 6-7. Weight of Piping for 100 KWe Systems

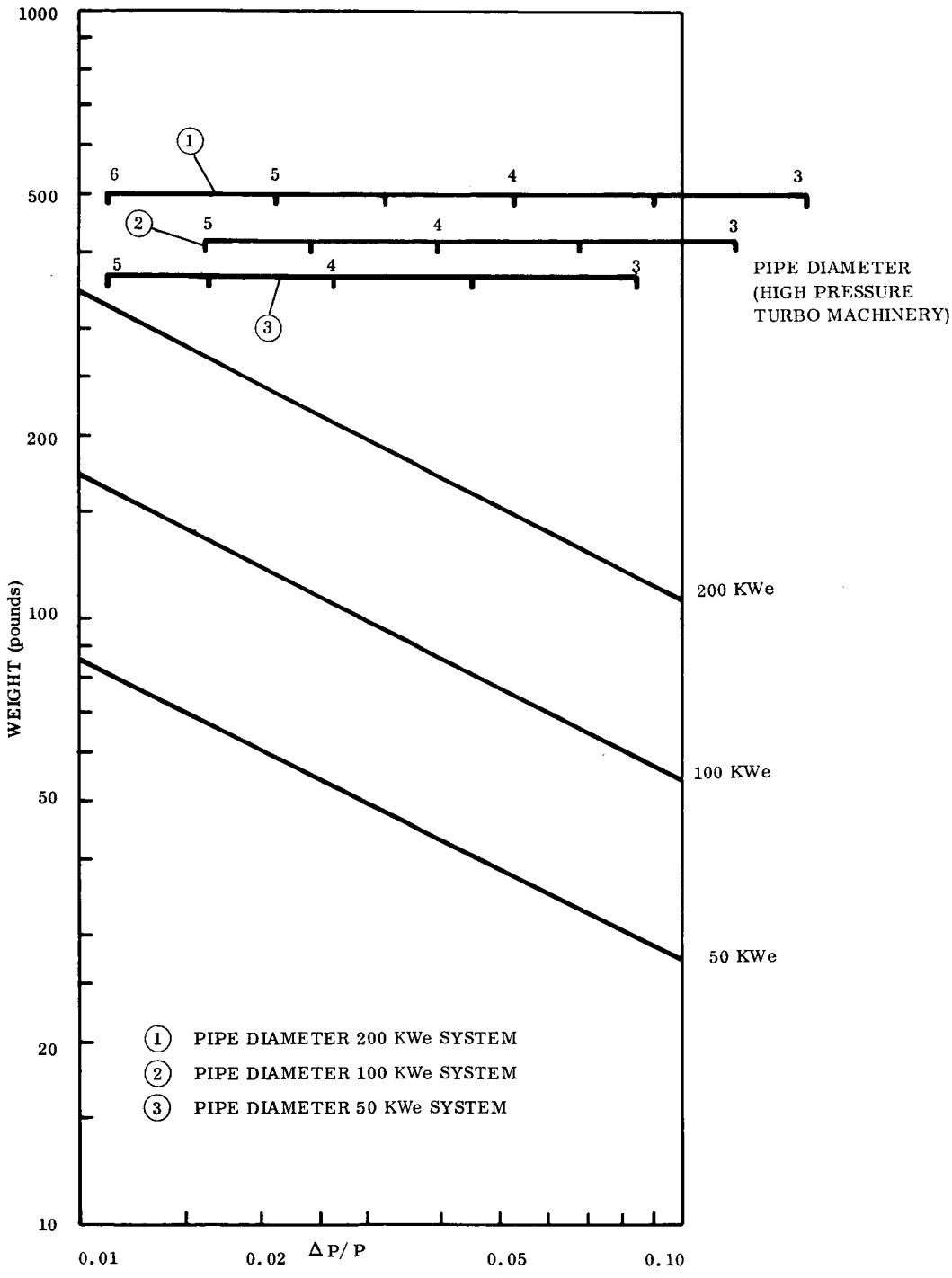

Figure 6-8. Weight of Piping for Optimistic Gas Radiator System and Conservative NaK Radiator System for Various System Power Levels

SECTION 7
SYSTEM OPTIMIZATION

Brayton cycle powerplants exhibit complex relationships among the many cycle variables; consequently, simple tradeoff studies are insufficient to establish adequately meaningful optimizations of system weight for comparative evaluation with respect to other cycles. Sections 3, 4, 5, and 6 of this report have discussed the primary components of the cycle and have developed analytical models relating their performance to suitable interfacing parameters. In this section these components are integrated into an optimization analysis of the entire system.

7.1 CYCLE DESCRIPTION

The thermodynamic diagram of the Brayton cycle is shown in Figure 7-1 while Figure 8-4 shows a plan view of the power conversion equipment illustrating the physical path of the gas through the cycle. Entering the compressor at its lowest temperature and pressure (state 1 on Figure 7-1) the gas is compressed to its highest pressure (process 1-2) and enters the recuperator. Here (process 2-3), the gas receives heat from the turbine discharge flow, and undergoes a pressure loss. The cycle heat addition (process 3-4) may occur either in the reactor or, in the case of an indirect cycle, in a separate heat exchanger. Following energy extraction by the turbine (process 4-5), the working fluid enters the second side of the recuperator (process 5-6), and finally rejects heat (process 6-1) either directly in the radiator or in a separate heat exchanger (process 6'-1') cooled by an additional radiator loop.

The ideal cycle heat addition (constant pressure) is shown as a dotted line in Figure 7-1, as is the ideal cycle heat rejection. It can be seen that the effect of the pressure losses is to reduce the available turbine power and to increase the required compressor work. Expressed mathematically, these are:

$$\left(\frac{\text{d Power}}{\text{d Pressure Ratio}}\right)_{\text{turbine}} = \dot{m}\, C_p\, \eta_t\, T_{\text{inlet}}\, \frac{(\gamma-1)}{\gamma}\, (\text{Pressure Ratio})^{\frac{1-2\gamma}{\gamma}}$$

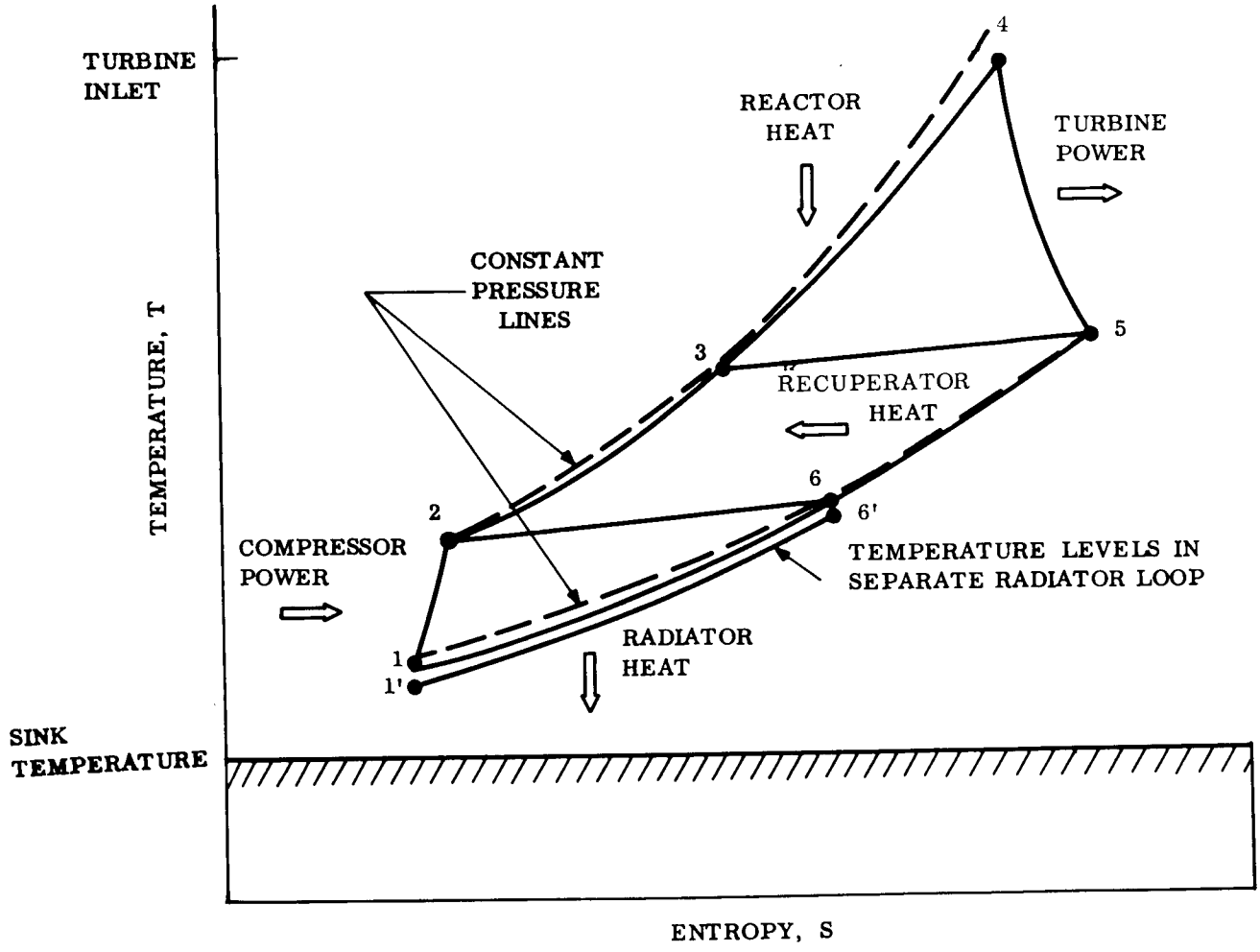

Figure 7-1. Thermodynamic Diagram Of Brayton Cycle

and

$$\left(\frac{\text{d Power}}{\text{d Pressure Ratio}}\right)_{\text{compressor}} = \frac{\dot{m} C_p T_{\text{inlet}}}{\eta_c} \quad \frac{(\gamma-1)}{\gamma} \quad (\text{Pressure Ratio})^{-\frac{1}{\gamma}},$$

or

$$\text{d Power}_{\text{turbine}} = \dot{m}(\eta_t C_p T_{\text{inlet}} - \text{Power}) \frac{(\gamma-1)}{\gamma} \frac{\text{d (Pressure Ratio)}}{\text{(Pressure Ratio)}}$$

and

$$\text{d Power}_{\text{compressor}} = \dot{m} \left(\text{Power} - \frac{C_p T_{\text{inlet}}}{\eta_c}\right) \frac{(\gamma-1)}{\gamma} \frac{\text{d (Pressure Ratio)}}{\text{(Pressure Ratio)}} .$$

The recuperator effectiveness and fractional pressure drops are related to each other and to the effective surface area; thus, recuperator weight can be traded off against pressure drop or effectiveness. The pressure drop-effectiveness relationship for a recuperator flow passage is,

$$\frac{\Delta P}{P} = \frac{E}{1-E} \quad 2\gamma M^2 P_r^{2/3},$$

where Pr is the Prandtl number. Since the Mach number is directly related to flow cross-sectional area, it is seen that the fractional pressure drop can be reduced by using bulkier recuperators and heat exchangers. Thus, in cases of radiator area limited systems the recuperator can be made heavy and very large in volume with a resulting high effectiveness and low pressure drops in order to achieve a high ratio of actual cycle efficiency to ideal cycle efficiency (zero pressure drop and complete recuperation).

In the case of the reactor, or an indirect heat exchanger, pressure drop can be lowered by either increasing flow area (with the corresponding increase in heat exchanger or reactor and shield weight) or by lowering the gas discharge temperature. Both of these effects

must be traded against the effect of gains in cycle efficiency due to a reduction of the pressure drop. A similar tradeoff occurs in the radiator loop between radiator temperature level and its effect on area, weight, and pressure drop.

7.2 PARAMETRIC OPTIMIZATION ANALYSIS

In order to obtain parametric evaluation of the extensive number of powerplant combinations, a multivariable system optimization computer program was written. The application, loop arrangements, reactor, and radiator combinations studied were:

MANNED SYSTEM POWERPLANT - Dual redundant power conversion loops, with a liquid metal cooled reactor.

Three loop system - NaK radiator

a. Unlimited Radiator Area
b. Limited Radiator Area

UNMANNED SYSTEM POWERPLANT - Unlimited radiator area, with a gas cooled reactor

One loop system - gas radiator

a. Cermet fuel, matrix type elements
b. Refractory clad fuel, pin type elements
c. Superalloy clad fuel, pin type elements

Two loop system - NaK radiator

a. Cermet fuel, matrix type elements
b. Refractory clad fuel, pin type elements
c. Superalloy clad fuel, pin type elements

The basic program consists of an optimization routine and a system weight evaluation subroutine. All of the options regarding powerplant component specification and loop arrangements are contained in the evaluation subroutine and this part of the program is used to compute the entire powerplant weight for each set of independent variables determined by the optimization routine. The optimization procedure consists of an iterative technique for varying each independent variable repetitively until the system weight passes through a minimum and the iterative variation is within a specified tolerance. When the increment in total system weight accompanying a variation in an independent variable is negative the system continues the variation, doubling the increment when the change in system weight is smaller than the final tolerance. When the increment is positive (i.e., when the variation results in a net increase in system weight), the computer reverses the sign of the increment in the variable, halves the increment value, resets the magnitude of the variable to its previous level, and re-establishes the previous case before proceeding with the iteration. Since the initial variation may not be in the proper direction, two reversals in the sign of the increment in the system weight are required to establish that a minimum has indeed been reached.

The program takes each independent variable in turn and optimizes the system weight with respect to it. In order to eliminate the effects of the order in which the variables are operated on, the option exists for making multiple passes through the list of variables. It has been found that the second pass with the optimization technique results in an improvement in the system weight of about one to two percent when the starting conditions are reasonably near the optimum. A third pass usually results in a fractional improvement of less than one tenth of one percent.

An optimization sequence for a 150 KWe three-loop, liquid-metal cooled reactor powerplant with a wrap-around shield for the manned application is illustrated in Figure 7-2. The pattern of weight reductions accompanying changes in cycle independent variables is shown in the figure for the following sequence of variable optimization:

a. Reactor core diameter
b. Reactor heat exchanger pressure drop

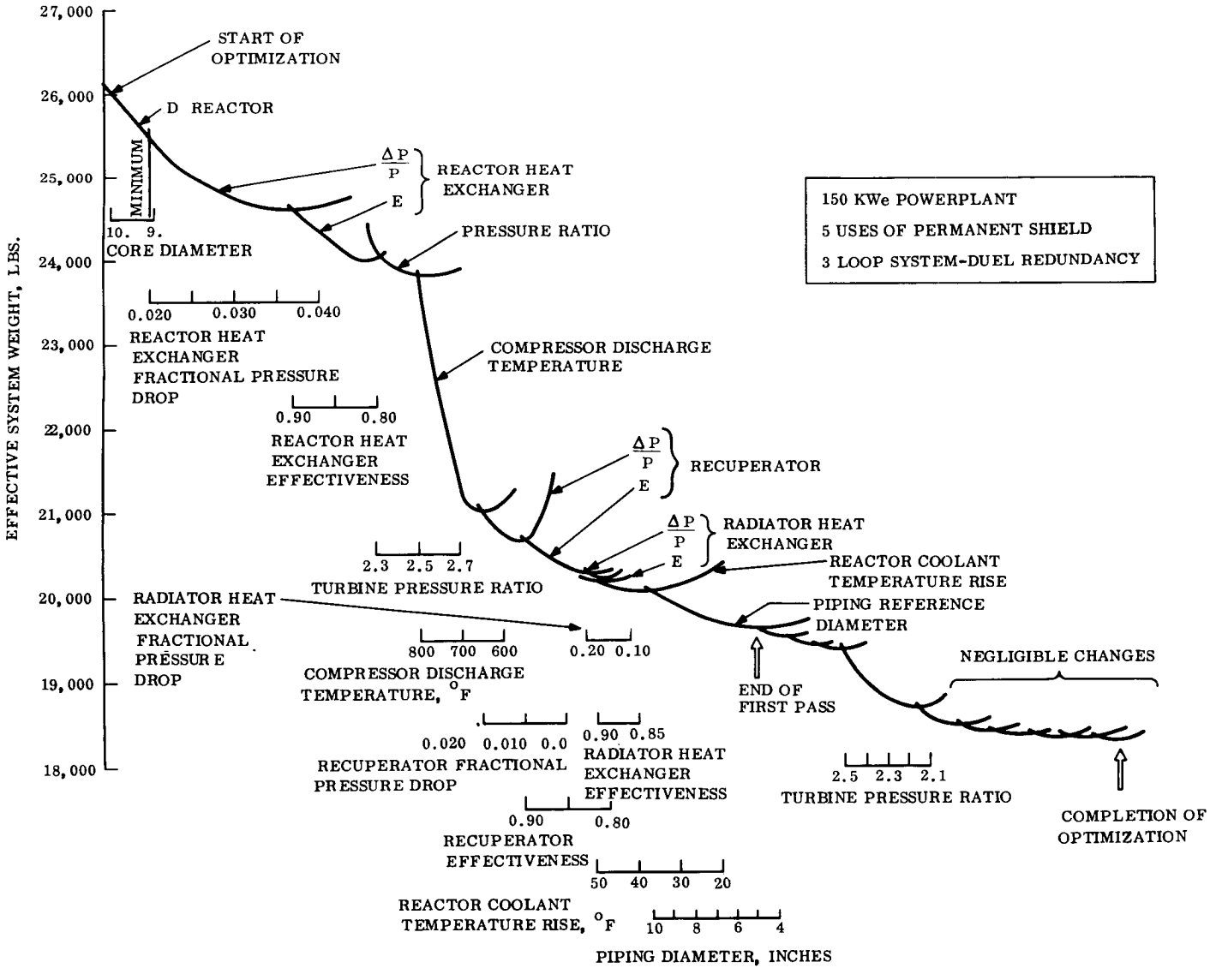

Figure 7-2. Optimization Sequence

c. Reactor heat exchanger effectiveness

d. Turbine pressure ratio

e. Compressor discharge temperature

f. Recuperator pressure drop

g. Recuperator effectiveness

h. Radiator heat exchanger pressure drop (gas side)

i. Radiator heat exchanger effectiveness

j. Temperature rise of the reactor coolant fluid

k. Piping diameter

Since the reactor and shield are the heaviest components, the optimization sequence first attacks the cycle variables affecting these elements. In Figure 6-2 the reactor diameter is seen to have first increased, and, when this proved to be the wrong direction, it reversed direction and decreased it until the minimum reactor diameter was reached. This minimum diameter can also be set into the program as an input where nuclear physical considerations and practicality set a limit to the reactor size. The next variables optimized are the pressure drop and the effectiveness of the heat exchanger used to transfer heat from the reactor loop to the gaseous working fluid (used in the manned system). Since the volume occupied by this heat exchanger must be included in the shield cavity, and therefore exerts a strong influence on shield weight, optimization of these variables involves a substantial portion of the total system weight.

The cycle thermodynamic variables (pressure ratio and compressor discharge temperature) are handled next. Since the initial estimate of the optimum compressor discharge temperature for this example was a poor choice, Figure 7-2 reflects the large weight savings resulting from the systematic optimization process. Furthermore, since the cycle temperatures which existed prior to the pressure ratio optimization are considerably off optimum, the pressure ratio is driven to a value which improves the immediate situation but requires reoptimization during the second pass. Indeed, the pressure ratio is the only variable which is significantly changed during the second pass.

The program next optimizes the recuperator and radiator heat exchanger pressure drop and effectiveness values. Because these components are comparatively light in weight and have no influence on other components (other than through the cycle thermodynamics), the system weight is found to be fairly insensitive to their optimization where realistic initial values are selected. The final variables optimized are the temperature rise of the reactor coolant fluid and the piping diameter. A decrease in the temperature rise of the reactor coolant fluid results in a higher reactor outlet temperature and, hence, a higher turbine inlet temperature. This gain is balanced against the additional reactor pumping power required for the increased fluid circulation rate. As the fluid velocity in the core increases, decreases occur in both the maximum clad-to-discharge temperature difference and the coolant fluid temperature rise; both effects are considered in the analysis. The last item, piping diameter, refers to the reactor heat exchanger feed line. This is one of the long runs of piping in the system. The diameter of the reactor heat exchanger return line is related to the feed line diameter by the requirement that the fluid in both lines travel at the same Mach number.

The program used to optimize the powerplants for the unmanned vehicle is similarly constructed. In this case the variables pertaining to the reactor coolant loop, fluid temperature rise, and heat exchanger effectiveness and frictional pressure drop are omitted. Fractional pressure drop in the reactor is directly related to its diameter, as explained in Volume 2 of this report.* The graphical data developed was approximated by logarithmic functions in the appropriate size range for use in the weight evaluation subroutine computations. Each combination of reactor type and outlet temperature was treated individually. Since the pressure drop to diameter relationship of many of the reactors for high pressure level turbo-machinery systems merged into a single curve, the obvious analytical modeling economy was made. The reactors for the low pressure turbo-machinery were only attainable at the high power levels. Compared to those for the high pressure turbo-machinery, the pressure drops at the same reactor diameters (conversely, the diameter at the same pressure drop) were found to be considerably larger. The achievable reactor configurations were again approximated by a logarithmic relationship. Since these systems proved heavier than the high pressure systems (despite the lower turbo-machinery efficiency of the latter) no further work below the 200 KWe level was attempted.

* Brayton Cycle Reactor Design (C-RD), CR-54398.

The gas and NaK radiator model synthesis was described in Section 5 and the resulting empirical equations were used to obtain the radiator specific weight for both cases. For the systems having the NaK radiators a gas-to-NaK heat exchanger was used. The radiator temperature level and heat rejection loop fractional pressure drop tradeoffs were made for this heat exchanger coupled to the NaK radiator. The pressure drop in the NaK radiator reacts with the system through the pump work power penalty factor and this item was included as part of the radiator effective weight. In the case of the gas radiator systems the heat rejection loop temperature level and fractional pressure drop optimization was handled directly by the powerplant analysis program.

7.3 PARAMETRIC RESULTS

7.3.1 POWERPLANTS FOR MANNED APPLICATION

The powerplant concept studied for use on a manned space station is a three loop, liquid-metal filled radiator, and a gas power conversion loop. Performance of the three loop system is summarized in Figures 7-3 and 7-4. Figure 7-3 shows specific weight related to electric power for powerplants in the range of 50 to 200 kilowatts, wherein the station shield is amortized against one unit. The major weight item is the shield, Since it has an almost constant magnitude, the curve of specific weight is hyperbolic. At larger power levels more shielding is required, hence the increase in weight. Radiator specific weight is almost constant; the bow in the curve reflects the increasing armor requirement at higher power levels. Since the system optimizes at the minimum reactor diameter, its weight is constant. The turbo-machinery, heat exchangers, and recuperator are combined into a single power conversion equipment weight item. Its specific weight is seen to decrease as the power level increases; however, the actual weight of this equipment increases slightly with power level.

Area limited systems are also shown in Figure 7-3. Since the radiator area of these constrained systems is fixed, the radiator specific weight decreases with increasing power, reflecting an almost constant radiator weight. In order to achieve the higher power rating the cycle must reoptimize at a higher efficiency. The increase in cycle efficiency is

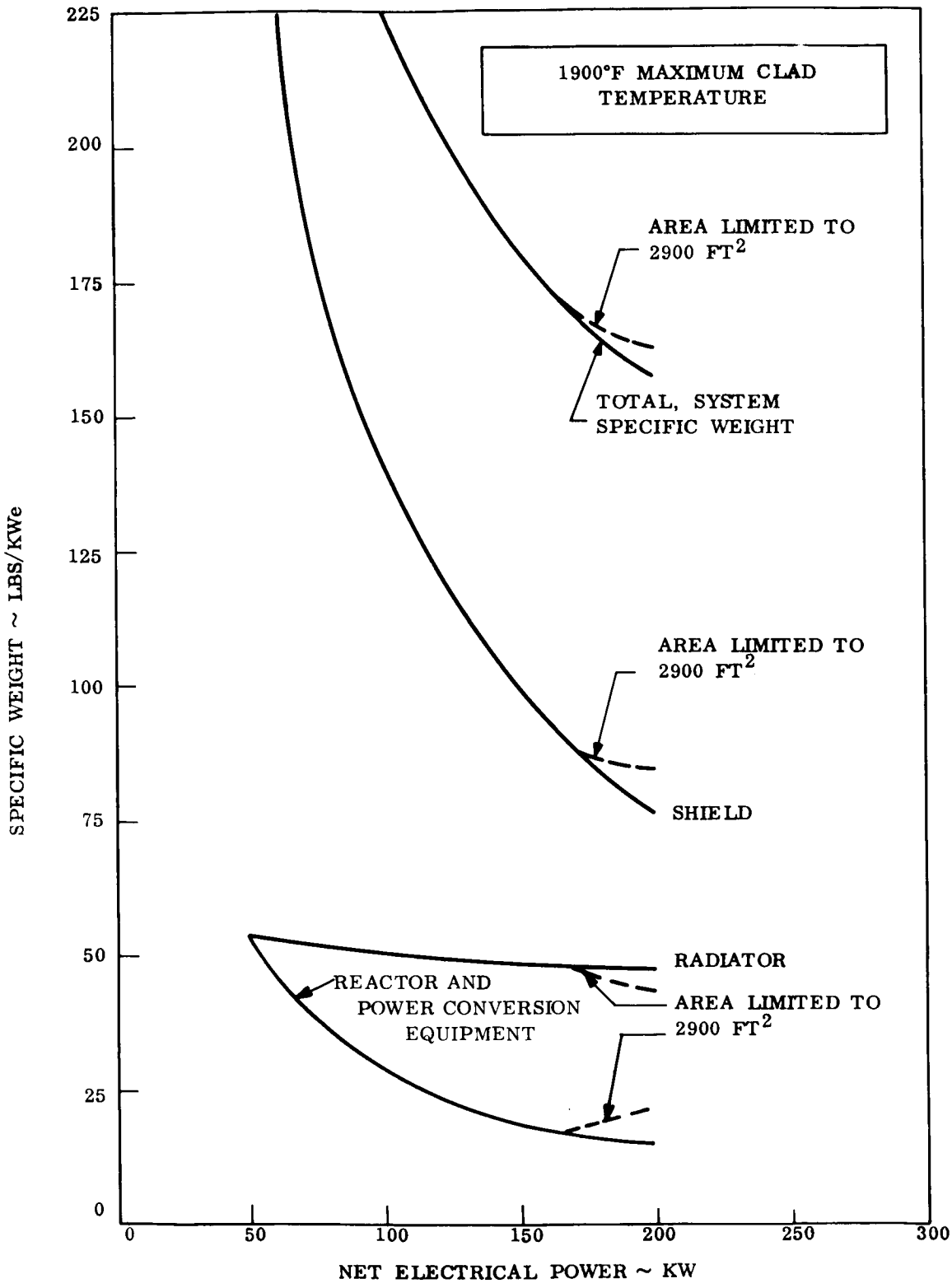

Figure 7-3. Single Use of Powerplant-Three Loop, Dual Redundancy System Shielded for Manned Applications

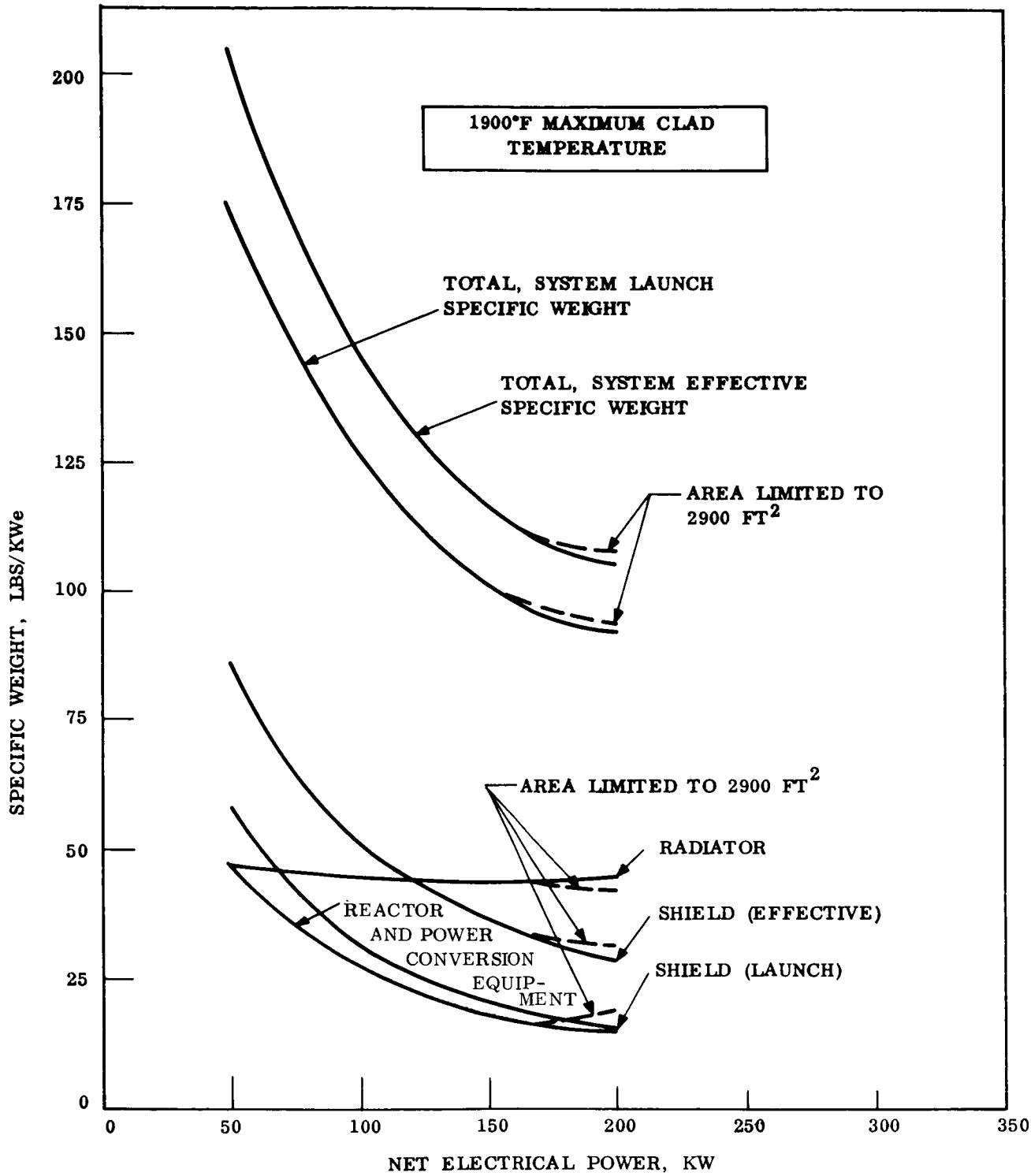

Figure 7-4. Powerplant Optimized for Five Uses - Three Loop, Dual Redundancy System Shielded for Manned Application

obtained by decreasing the pressure drop and increasing the effectiveness of the heat exchangers. Since the larger heat exchanger in the primary loop necessitates a larger radiation shield, the specific weight of the shield increases over the value obtained with an area unlimited system. It is expected that further passes with the optimization technique will net some savings in weight by trading some of the volume and pressure drop of the primary loop heat exchanger for comparable changes in recuperator, piping, and radiator heat exchanger volume. Further work is planned to include reoptimization of the system with higher fin efficiency radiators. The combination of area limited cycle optimization and area limited radiator optimization should effect some savings in system weight. Multiple use of the station mounted section of the radiation shield in this case is the total weight of the powerplant section plus 1/N of the weight of the permanent section, where N is the number of powerplants used during the life of the permanent section. This approach reduces the effective weight of the shield and thereby affects the system optimization in a substantial way. Figure 7-4 shows the specific weight of the manned space station powerplants optimized for five uses of the permanent section of the radiation shield; both system launch specific weights and effective system weights are shown. Besides the major reduction in shield weight, the radiator specific weight optimizes at a level about 10 percent lower than that found in the case of a single use of the permanent portion of the shield. This is a manifestation of the specific weight reduction of each variable weight component as the total system specific weight is reduced. Area limited systems are shown having the same trends as was found in the previous case. In both cases, the data shown was based on a maximum fuel element cladding temperature of 1900°F. For the multiple use of the permanent shield at 150 KWe the temperature difference between the turbine inlet and the maximum cladding temperature amounts to 118°F. For the single use system the difference is 157°F.

Variations in system specific weight with power level and maximum cladding temperature are shown in Figures 7-5 and 7-6. Both the one and five uses of the permanent section of the shield are shown. Lines of constant area for 2200 square feet and 2900 square feet are illustrated crossing the curves of constant maximum cladding temperature. These area lines correspond to the two Saturn SIVB stage envelopes considered. Area limited

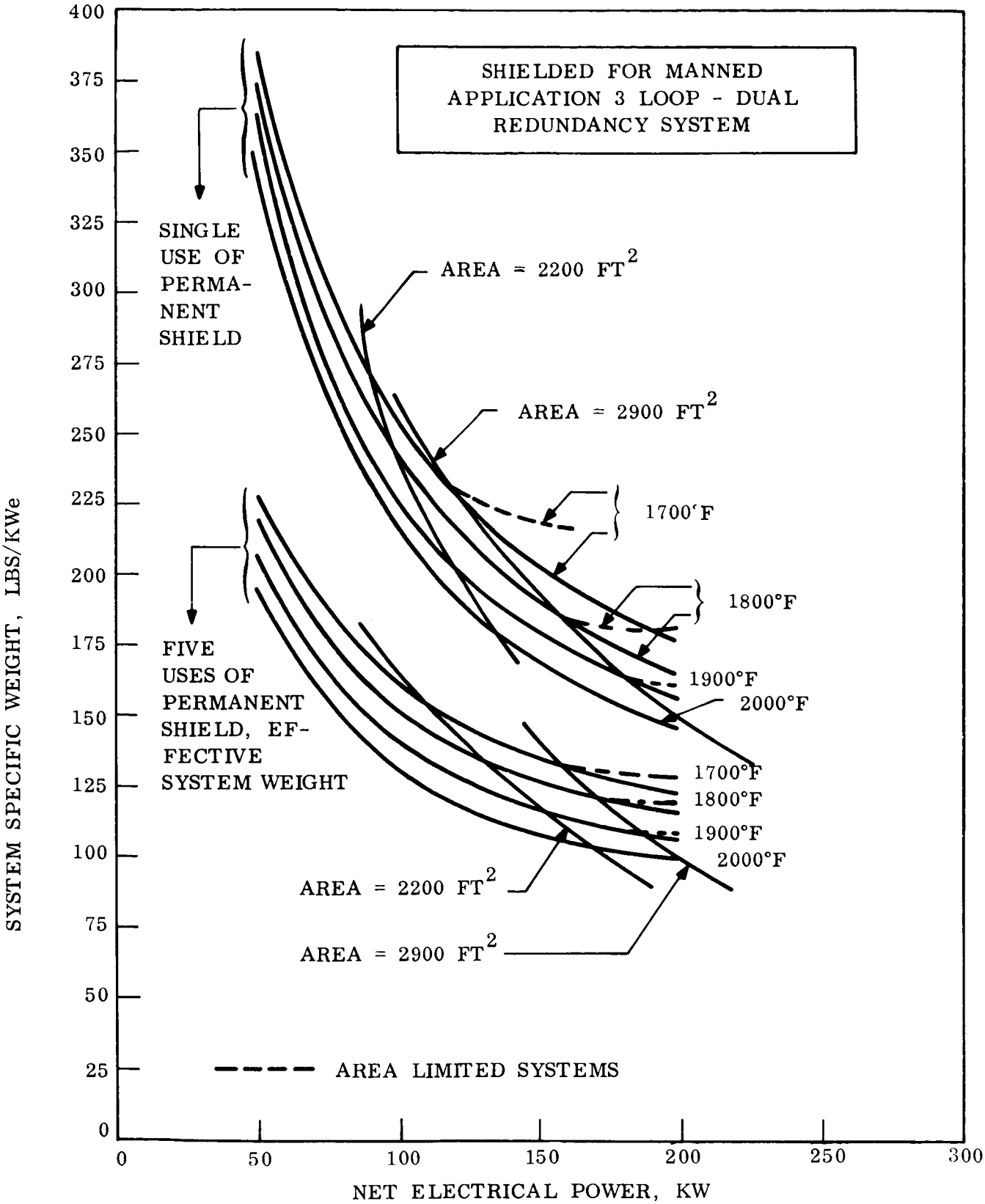

Figure 7-5. System Specific Weight as a Function of Power Level for Various Maximum Clad Temperatures

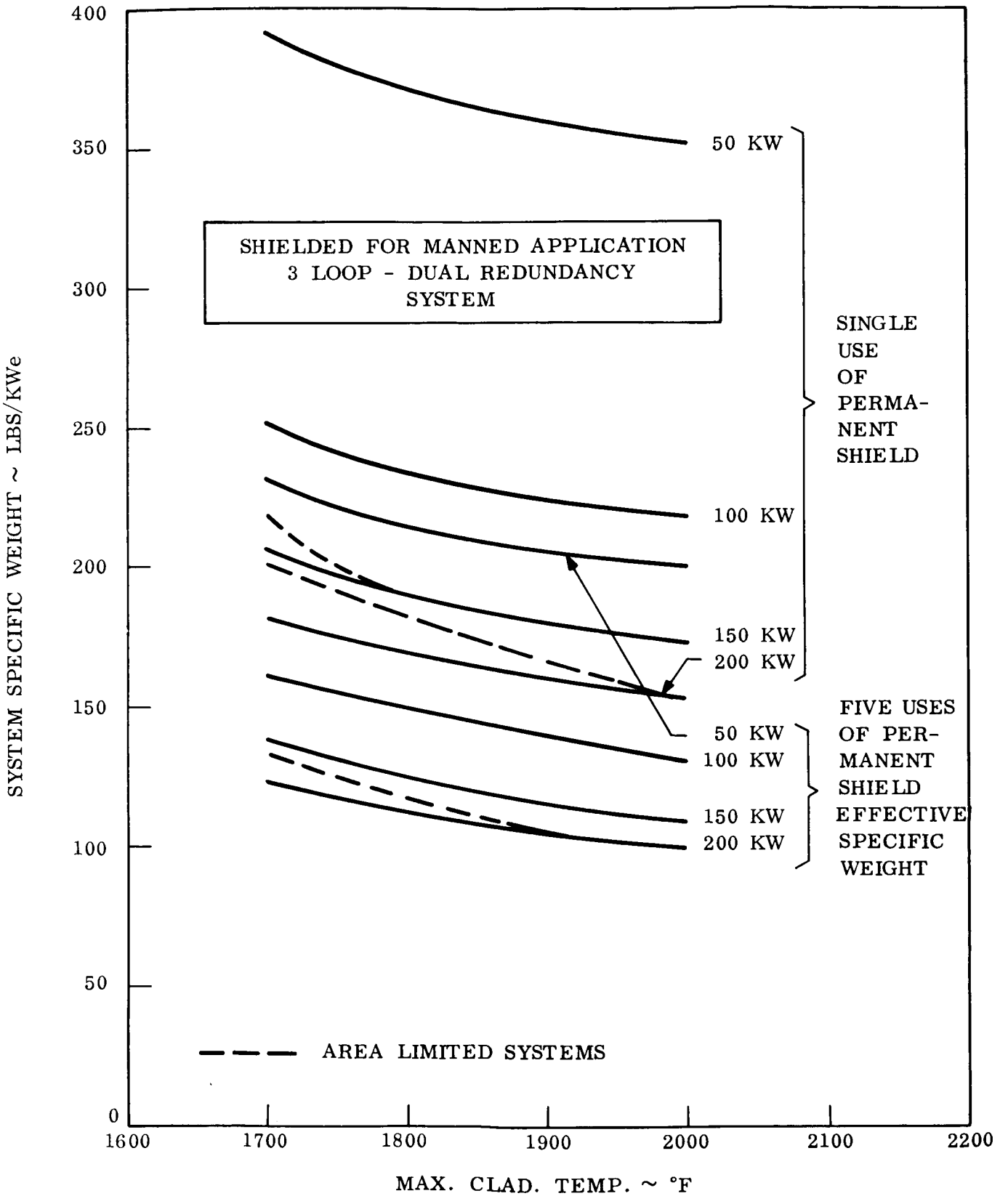

Figure 7-6. System Specific Weight as a Function of Maximum Clad Temperature for Various Power Levels

systems are shown for powerplants whose unlimited area radiators extend beyond 2900 square feet. The effect of maximum cladding temperature is seen to be reasonably constant, amounting to an average increase of about 10 lbs/KWe for each 100°F decrease in temperature. Radiator areas of optimized powerplants for both shield amortization examples are shown in Figures 7-7 and 7-8. It is seen that increased use of the station shield (which results in lower system specific weight) also causes the system to optimize with smaller radiators. Only unlimited area systems are shown. Additionally, the radiator area is found to increase almost linearly with power at all cladding temperatures; however, the optimum radiator area is not proportional to power level. The area per net kilowatt decreases with increasing power showing the increasing significance of the radiator as the power level increases. The change in system effective specific weight as the number of uses of the station shield increases is shown in Figure 7-9. Beyond five uses a further saving of only 2-1/2 lbs/KWe per additional use is realized. Infinite use of the station (permanent) section of the shield results in a minimum weight of 115 lbs/KWe. This compares to a value of 140 lbs/KWe at five uses. In both cases the numbers are based on a 100 KWe power system size.

The efficiency of the optimized cycles is shown in Figure 7-10. Efficiency increases with increasing power because the additional shielding required at the high power levels is added at the periphery of the shield. As the use of the permanent section of the shield increases, the effective shield and system weight decrease and the radiator becomes proportionally more important. As the significance of the radiator increases, so does the incentive to decrease its specific area.

At higher power levels more weight can be invested in the recuperator and radiator heat exchanger. The heat exchanger scaling laws show that the wetted surface required for a given effectiveness and pressure drop is proportional to the ratio of mass flow rate to pressure. Since the pressure level in the power conversion loop is proportional to the system power level, the performance of the heat exchangers is proportional only to their weight. Thus, when heavier heat exchangers can be used at the larger power levels lower fractional pressure drops and higher cycle efficiencies can be obtained. The weight of the

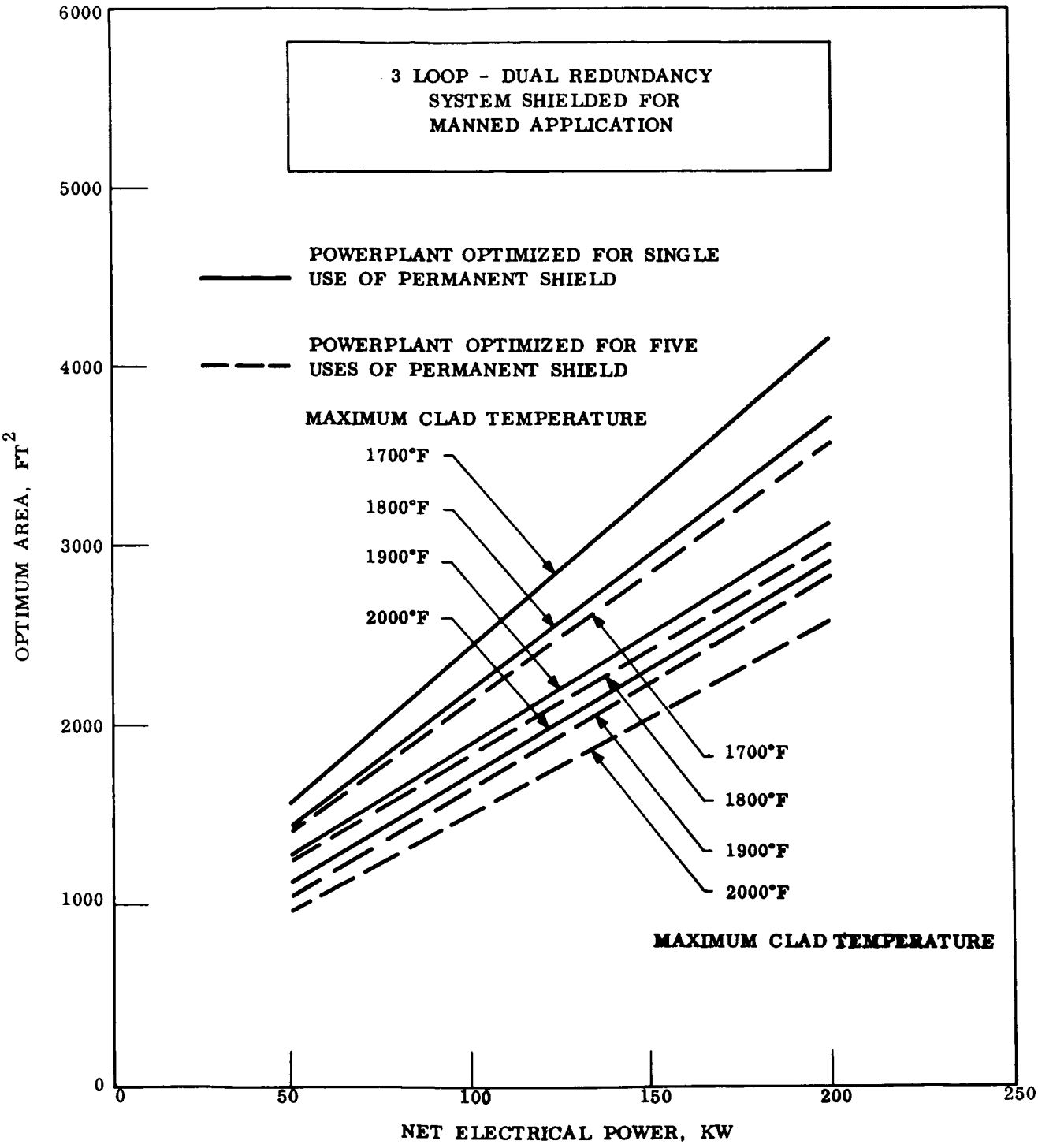

Figure 7-7. Optimum Radiator Area as a Function of Power Level for Various Maximum Clad Temperatures

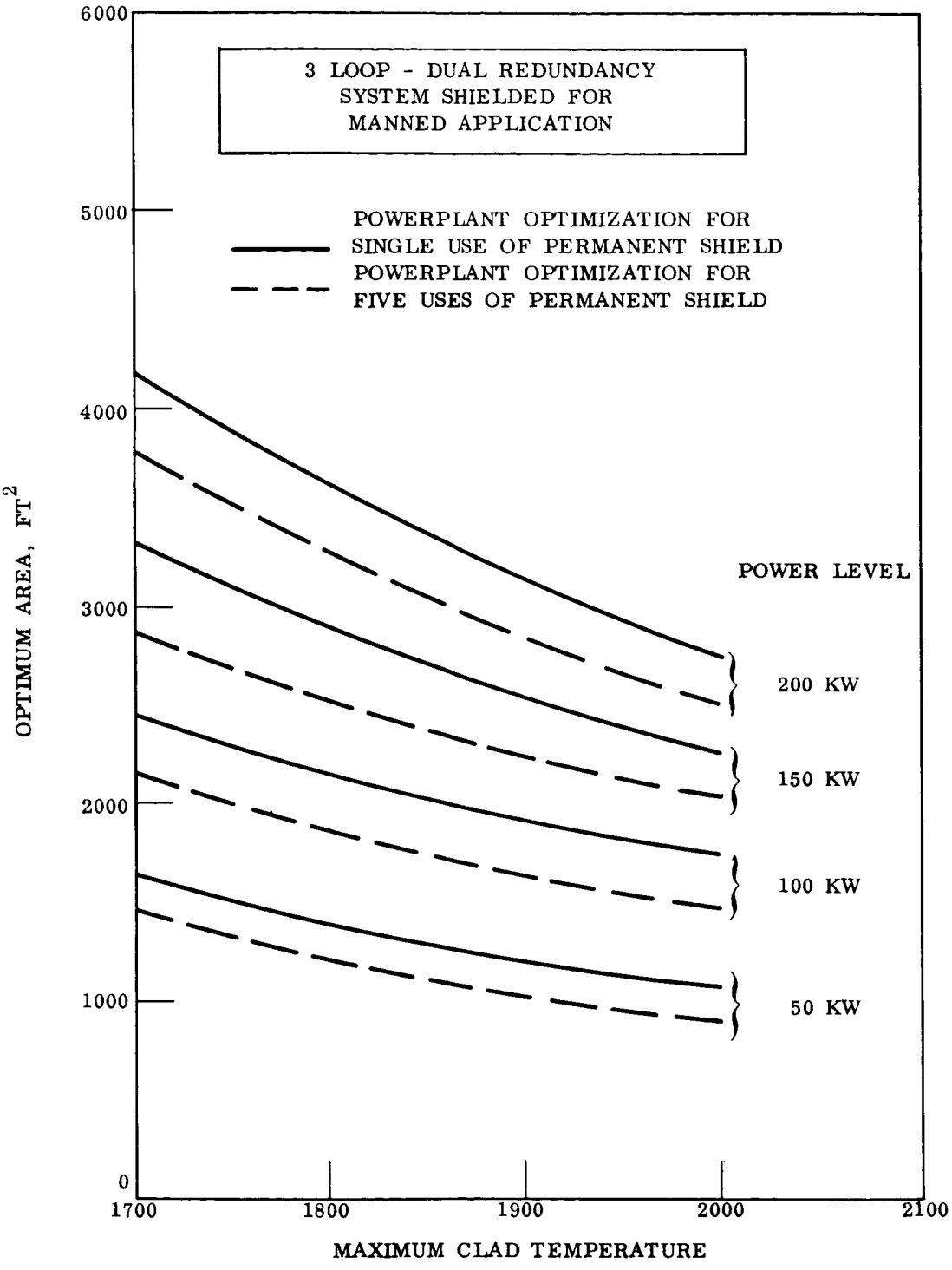

Figure 7-8. Optimum Radiator Area as a Function of Maximum Clad Temperature for Various Power Levels

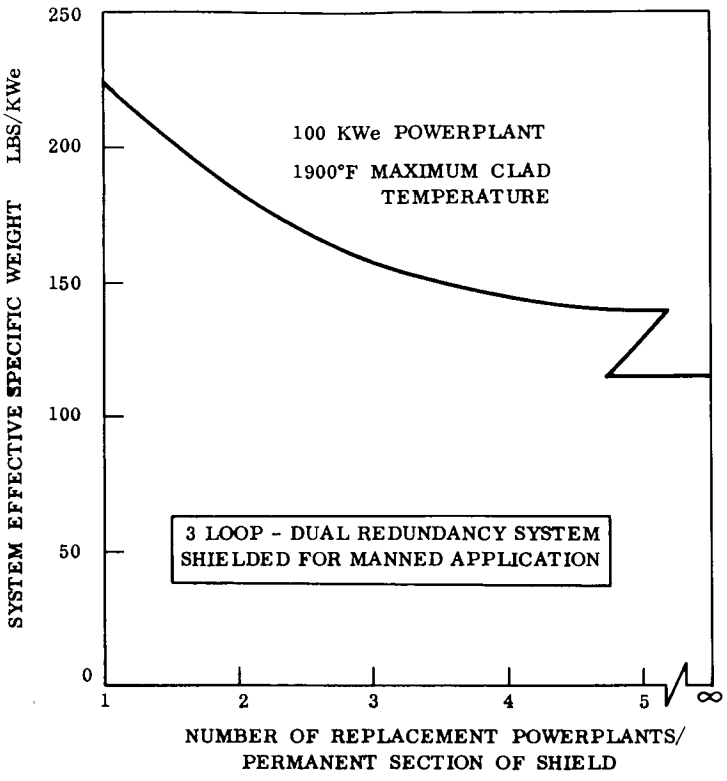

Figure 7-9. System Effective Specific Weight as a Function of the Number of Replacement Powerplants per Use of the Permanent Section of the Shield

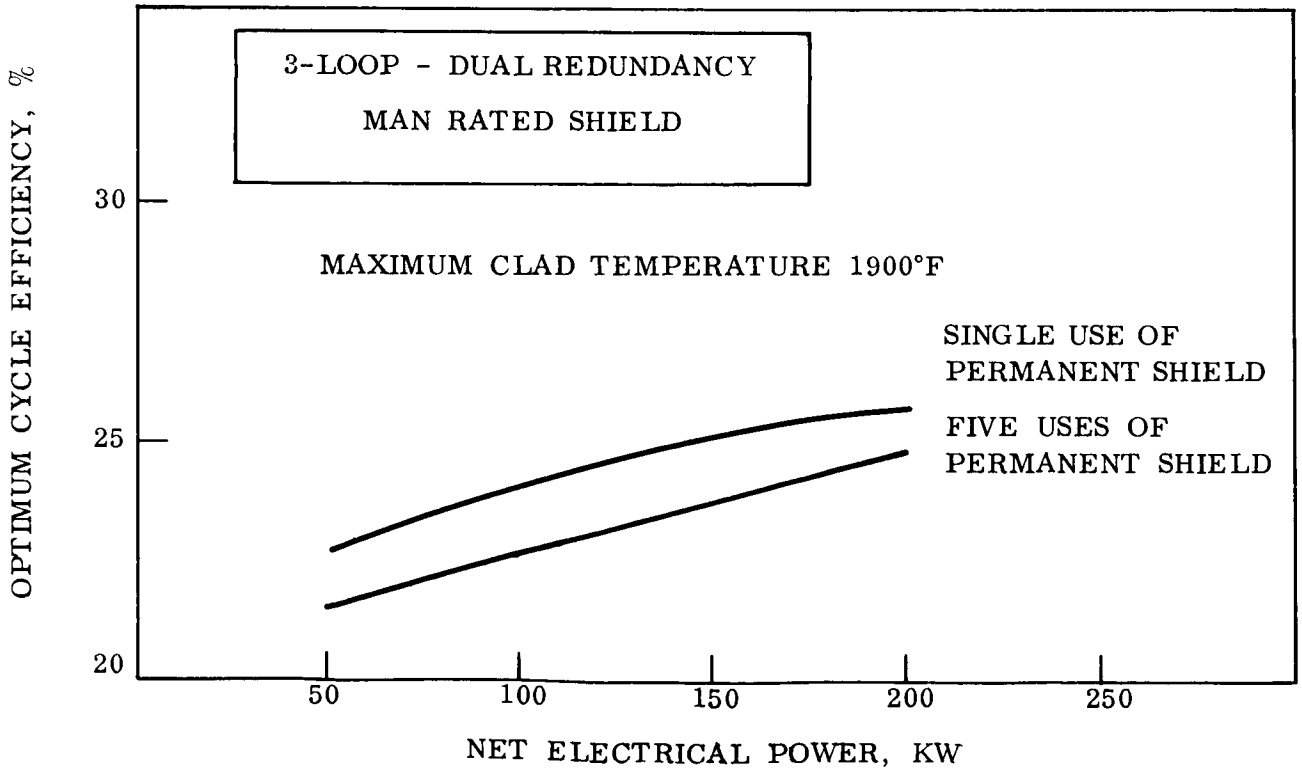

Figure 7-10. Optimum Cycle Efficiency as a Function of System Power Level

heat transfer equipment increases less rapidly than the power level, hence, specific weight decreases with increasing power. This explains the resultant lower system fractional pressure loss and higher cycle efficiencies found in the larger systems. Figure 7-11 shows the total fractional pressure loss and the fractional pressure loss in the primary loop heat exchanger as a function of power level. The volume of each of the two primary loop heat exchangers is shown in Figure 7-12. The larger power levels can afford the slightly heavier shields resulting from the increases in heat exchanger volume. Similarly, the lighter weight systems associated with multiple use of the station shield can afford to reinvest some of the direct shield weight savings back into the shield, through increased heat exchanger volume, in order to achieve a higher cycle efficiency and lower radiator area. Power level also influences the relative sensitivities of shield weight to reactor thermal power and heat exchanger volume.

7.3.2 POWERPLANTS FOR UNMANNED APPLICATIONS

The powerplant optimization program was used to obtain the specific weights, and specifications of optimized powerplants for power ratings between 50 KWe and 200 KWe, and

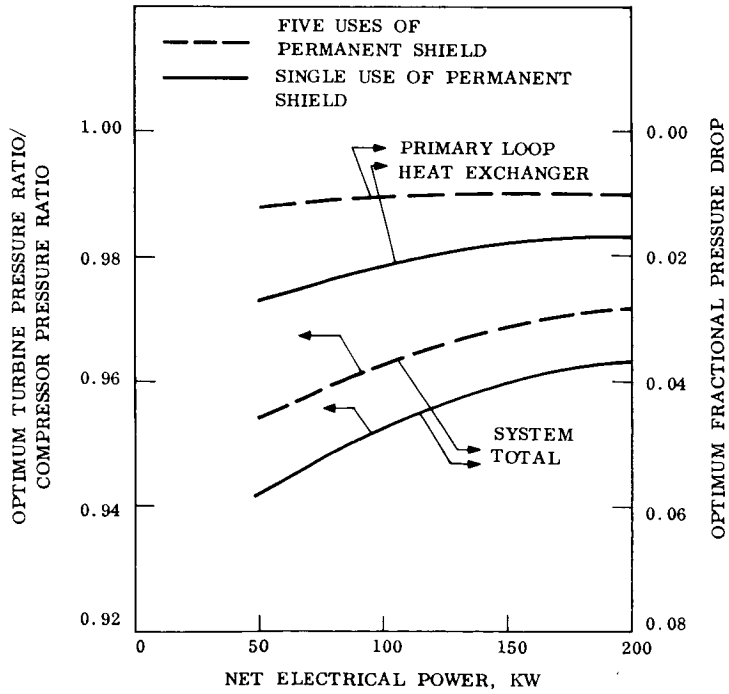

Figure 7-11. Optimum Ratio of Compressor Pressure Ratio to Turbine Pressure Ratio and Fractional Pressure Loss as a Function of System Power Level

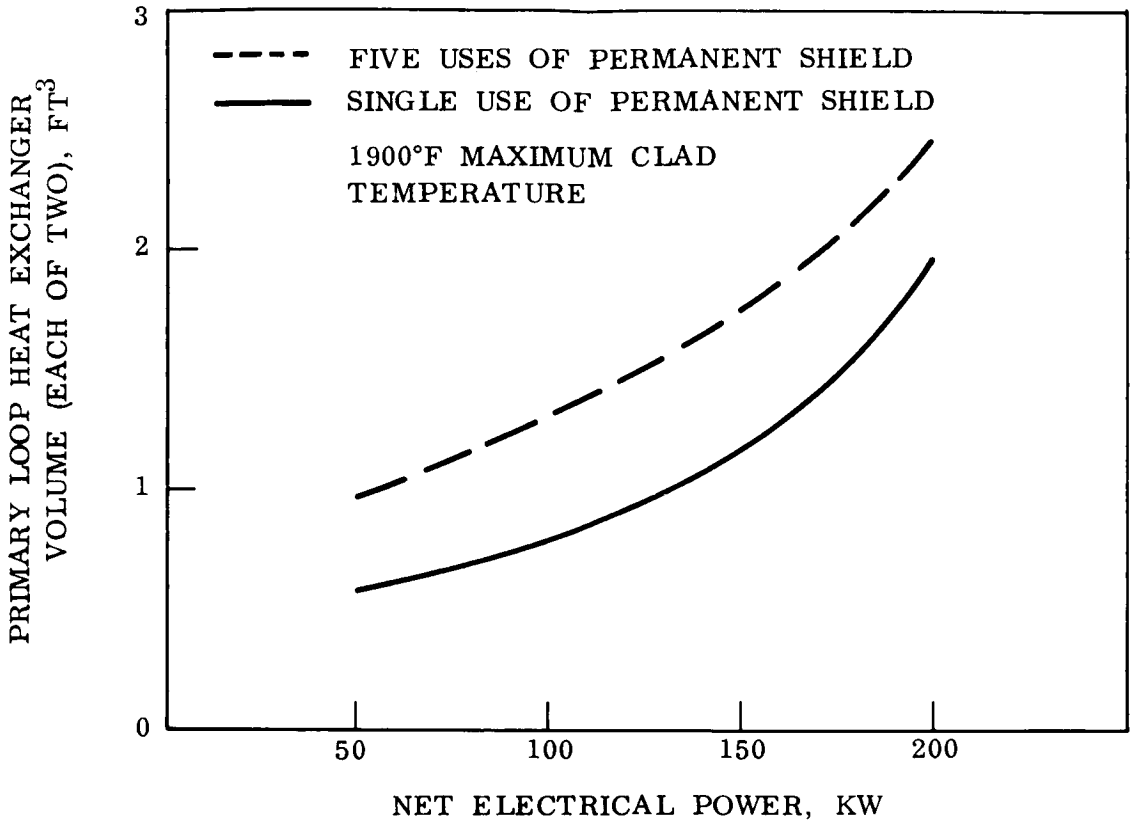

Figure 7-12. Primary Heat Exchanger Volume as a Function of System Power Level

turbine inlet temperatures between 1300° and 2200°F. All three gas-cooled reactor models were used in order to obtain a continuous picture of system performance over the range of temperatures under study. Systems investigated for use with unmanned spacecraft were a one-loop, all gas powerplant, a two-loop system having a liquid-metal filled radiator, and a three-loop system with liquid-metal radiator and reactor.

7.3.2.1 Single Loop System

A breakdown of the specific weight among the various components is shown in Figures 7-13 and 7-14. Figure 7-13 shows the component specific weights for 200 KWe powerplants as a function of turbine inlet temperature. It is seen that reactor and shield weights remain essentially constant resulting in a hyperbolic form of their specific weight curves seen in the subsequent figures . The higher efficiencies attained at higher temperatures result in lower reactor power requirements and therefore lower shield

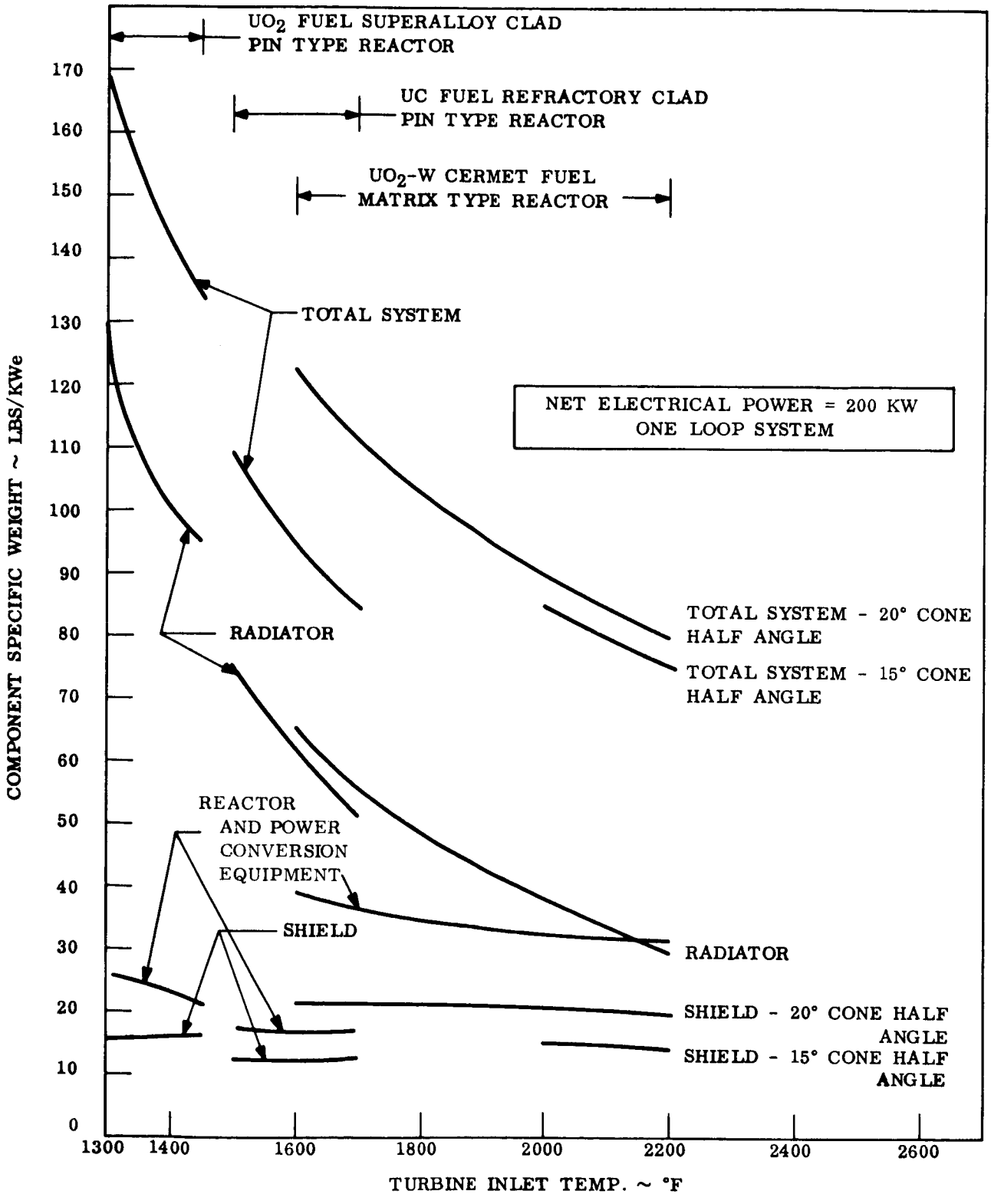

Figure 7-13. Component and System Specific Weight as a Function of Turbine Inlet Temperature, Unmanned Application

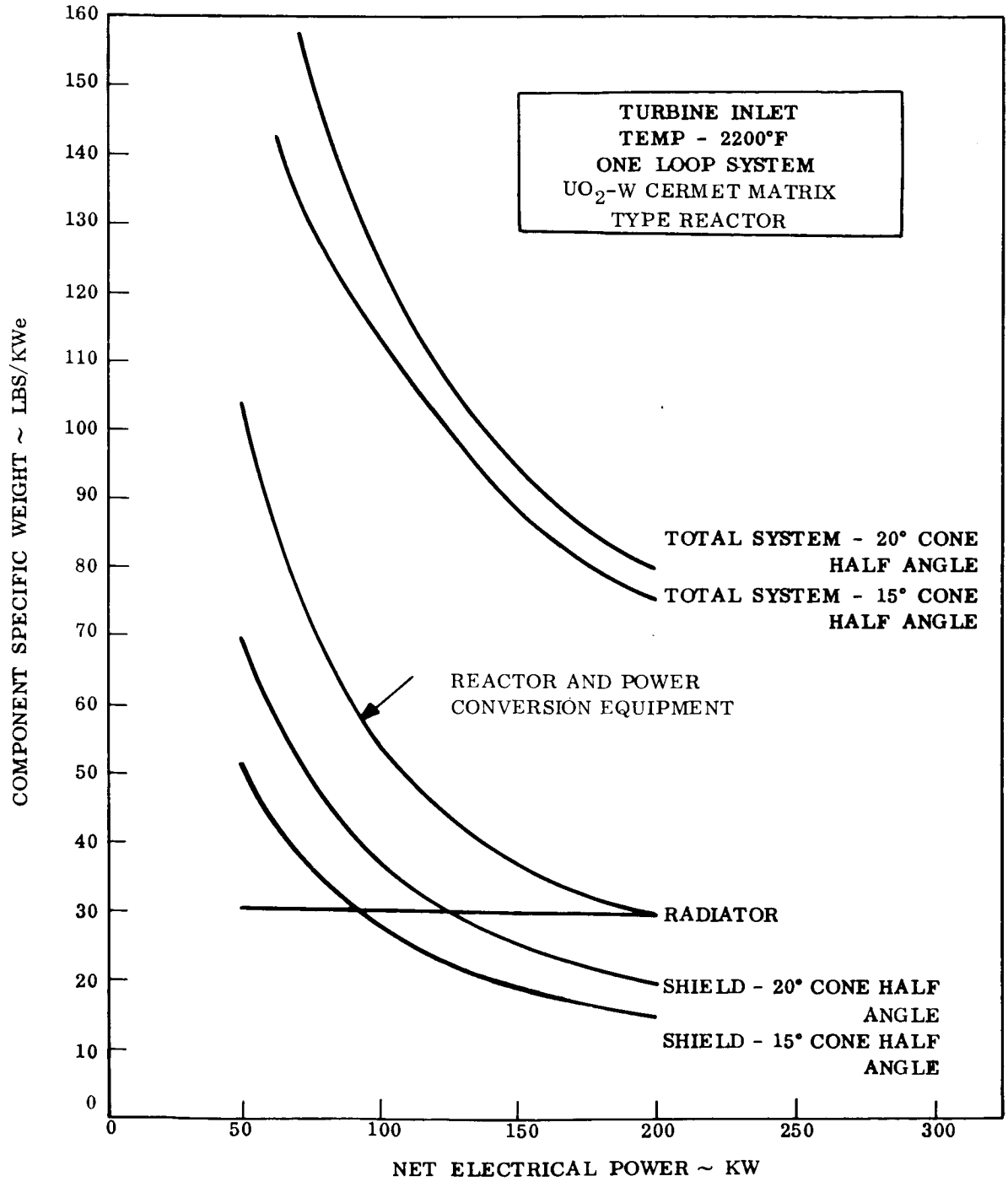

Figure 7-14. Component and System Specific Weight as a Function of System Power Level, Unmanned Application (Sheet 1 of 4)

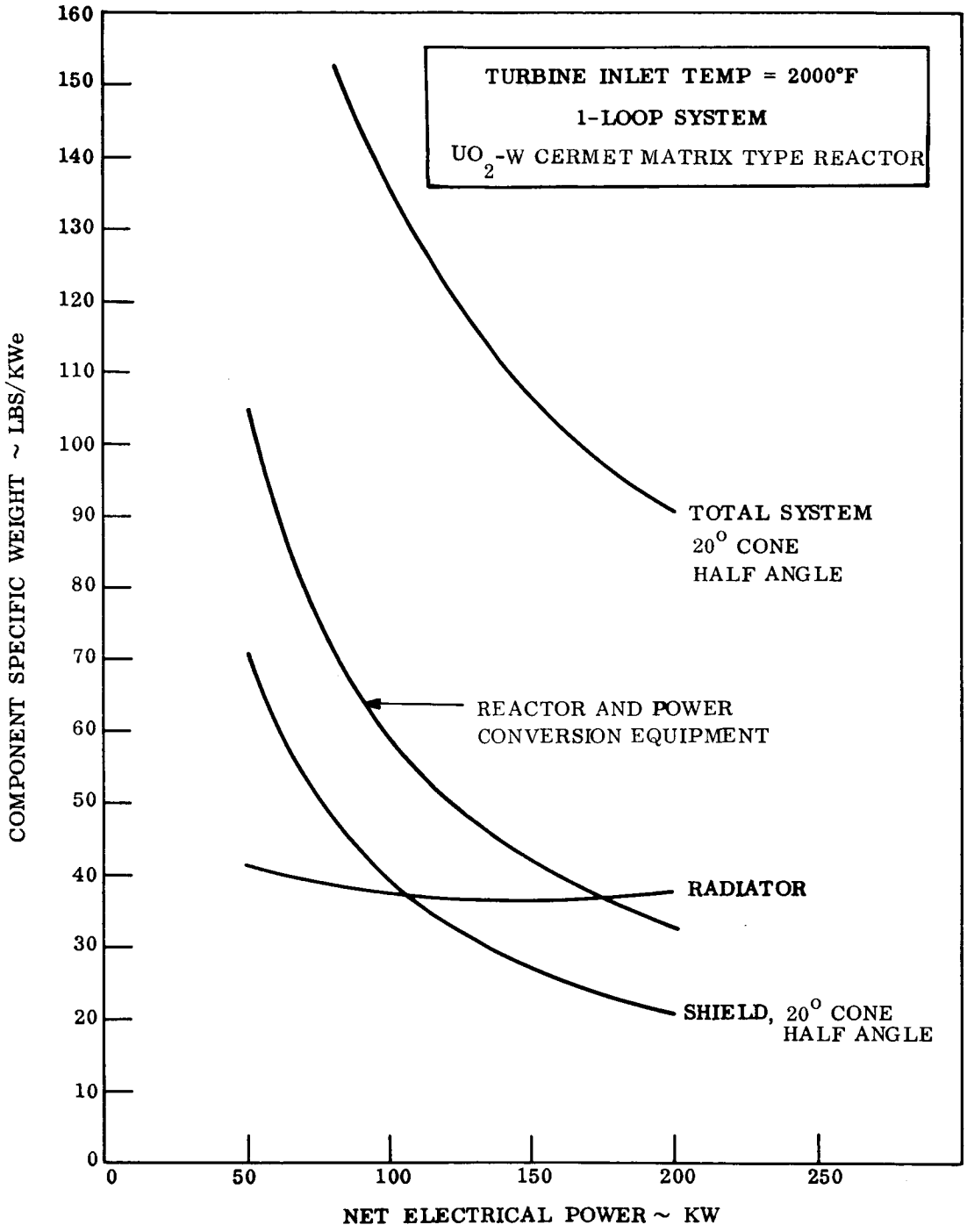

Figure 7-14. Component and System Specific Weight as a Function of System Power Level, Unmanned Application (Sheet 2 of 4)

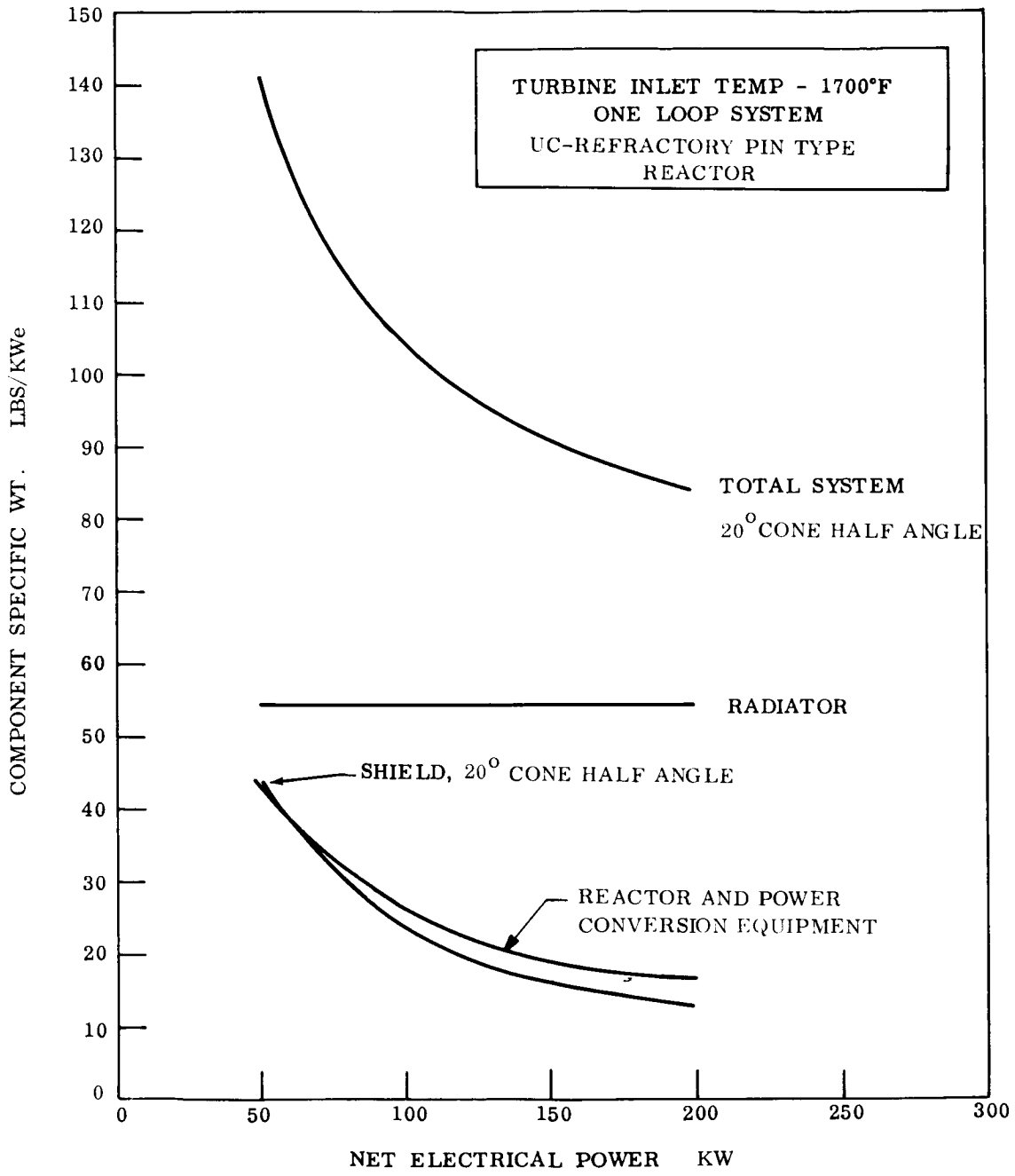

Figure 7-14. Component and System Specific Weight as a Function of System Power Level, Unmanned Application (Sheet 3 of 4)

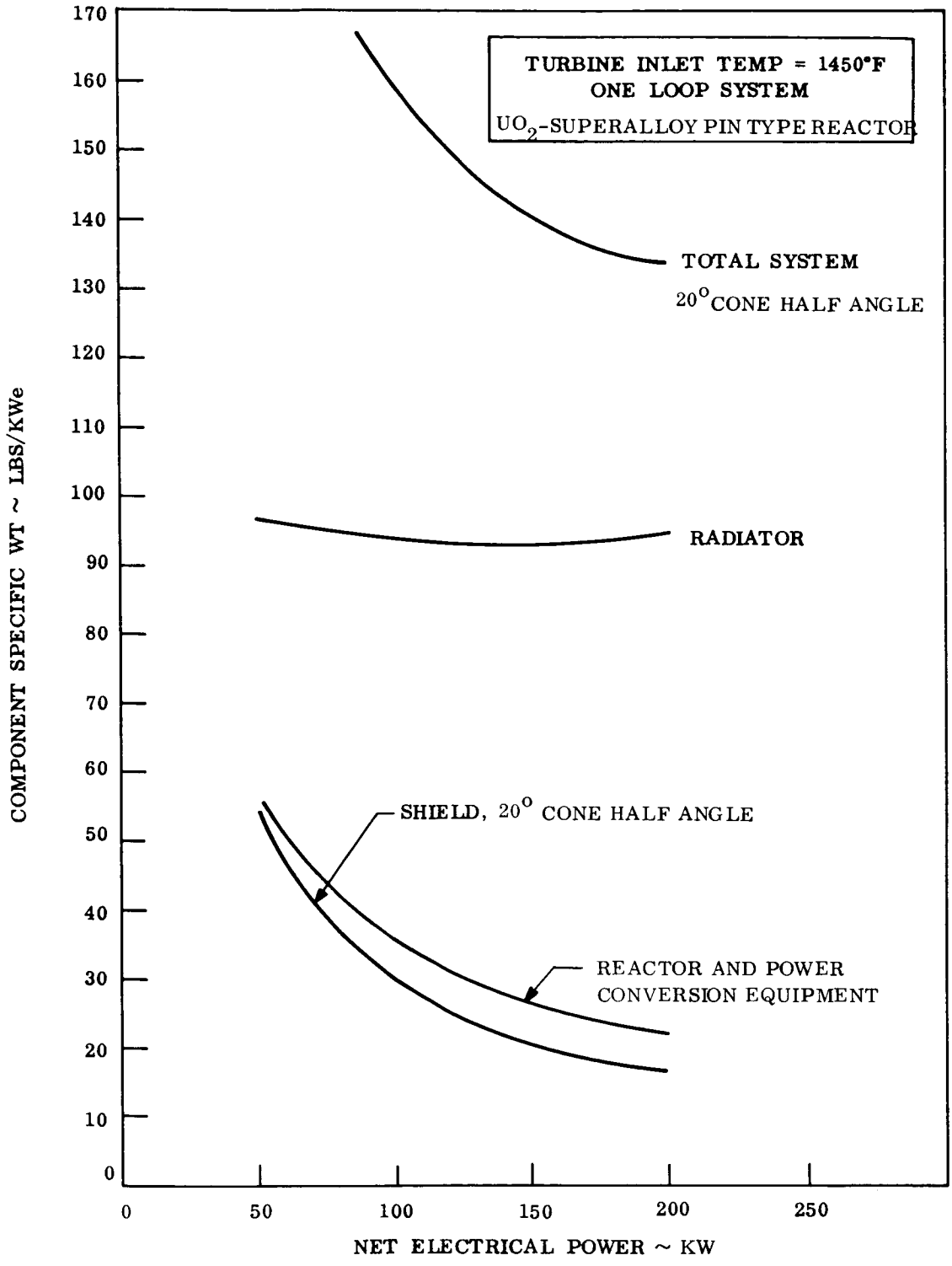

Figure 7-14. Component and System Specific Weight as a Function of System Power Level, Unmanned Application (Sheet 4 of 4)

weights. At the low turbine inlet temperatures the system specific weight is large enough to demand an increase in the piping diameter and recuperator size in an effort to raise the cycle efficiency, and thereby lower the heat rejection requirement. The radiator weight increases rapidly with decreasing cycle temperature reflecting the increased area requirement.

Results are shown for systems using all three gas-cooled reactors studied. The discontinuities in the slope reflect the different conditions at which the systems optimized, as well as the sizeable differences in reactor and shield weight. Total system and shield specific weights are shown for scatter shield cone half angles of 15 degrees at the higher turbine inlet temperatures. This angle corresponds to an all conical radiator and is consistent with the available area on the escape configuration of the SATURN V payload envelope.

A breakdown of component system weights for one-loop powerplants operating at a turbine inlet temperature of 2200°F is shown in Figure 7-14 (sheet 1). Scatter shielding is based on 15-degree and 20-degree shadow cone half angles for the all conical and cone-cylinder radiator configurations respectively. The marked flattening of the curves for radiator, piping, turbo-machinery, and recuperator specific weight occurs because these components account for a decreasing fraction of the system weight at the higher power levels. The tradeoff between cycle efficiency, shield weight, radiator, and gas ducting weight favor slight increases in radiator or piping weight in order to save on shield weight. A similar graph for systems with a turbine inlet temperature of 2000°F is shown in Figure 7-14 (sheet 2). These results were obtained with a model of the reactor having the same maximum cladding temperature as was used with a 2200°F turbine inlet temperature; however, the gas outlet temperature was reduced to 2000°F with a proportionate reduction in the gas inlet temperature. In all cases wherein the performance of specific reactor systems is compared at different temperature levels, the maximum clad temperature was held constant unless otherwise noted. In all of these cases a savings in reactor diameter, or fractional pressure drop results from the increase in the difference between the maximum clad temperature and the gas outlet temperature. However, the savings are insufficient to compensate

for the increasing radiator area requirement accompanying the decrease in turbine inlet temperature. The radiator specific weight curve shown in Figure 7-14 (sheet 2) shows the same type of bow as was found in Figure 7-3. Again, the increasing area, and the ability to accommodate a relatively heavier radiator at the high specific weights found at low power levels is evidenced. This was not found in the higher temperature case because of the basic difference in radiator area required.

The lower temperature reactor systems are shown in Figures 7-14 (sheet 3) and 7-14 (sheet 4). Radiator specific weights are seen to be appropriately greater, and because the associated pin-type reactors can be made smaller than the cermet-matrix type, the reactor and shield weights are correspondingly lower.

The efficiencies of the optimized cycles are presented in Figure 7-15. Efficiency is seen to increase with both temperature and power, as was shown in Figure 7-10 for the manned systems. The increase in temperature results in an increase in the volume flow through

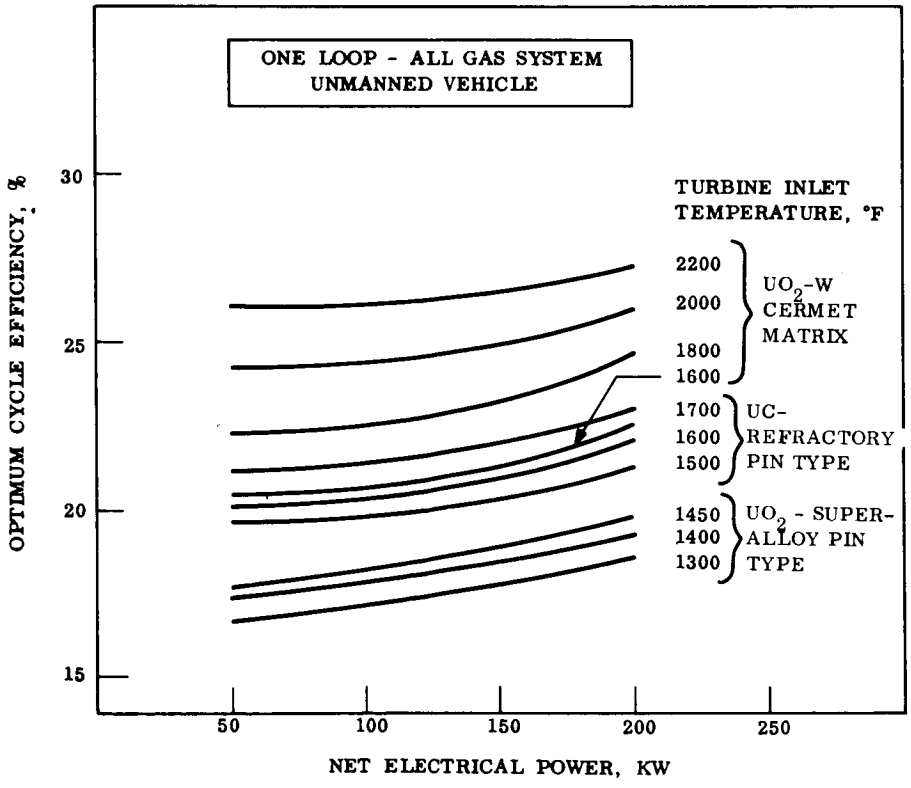

Figure 7-15. Cycle Efficiency as a Function of System Power Level

the turbine and an increase in power; this advantage is in turn distributed throughout the various components of the system. The cycle operating temperatures are shown in Figure 7-16. Discontinuities in the optimum temperatures result from shifts in the specifications for the optimum components due to the discontinuous changes in reactor and shield weight.

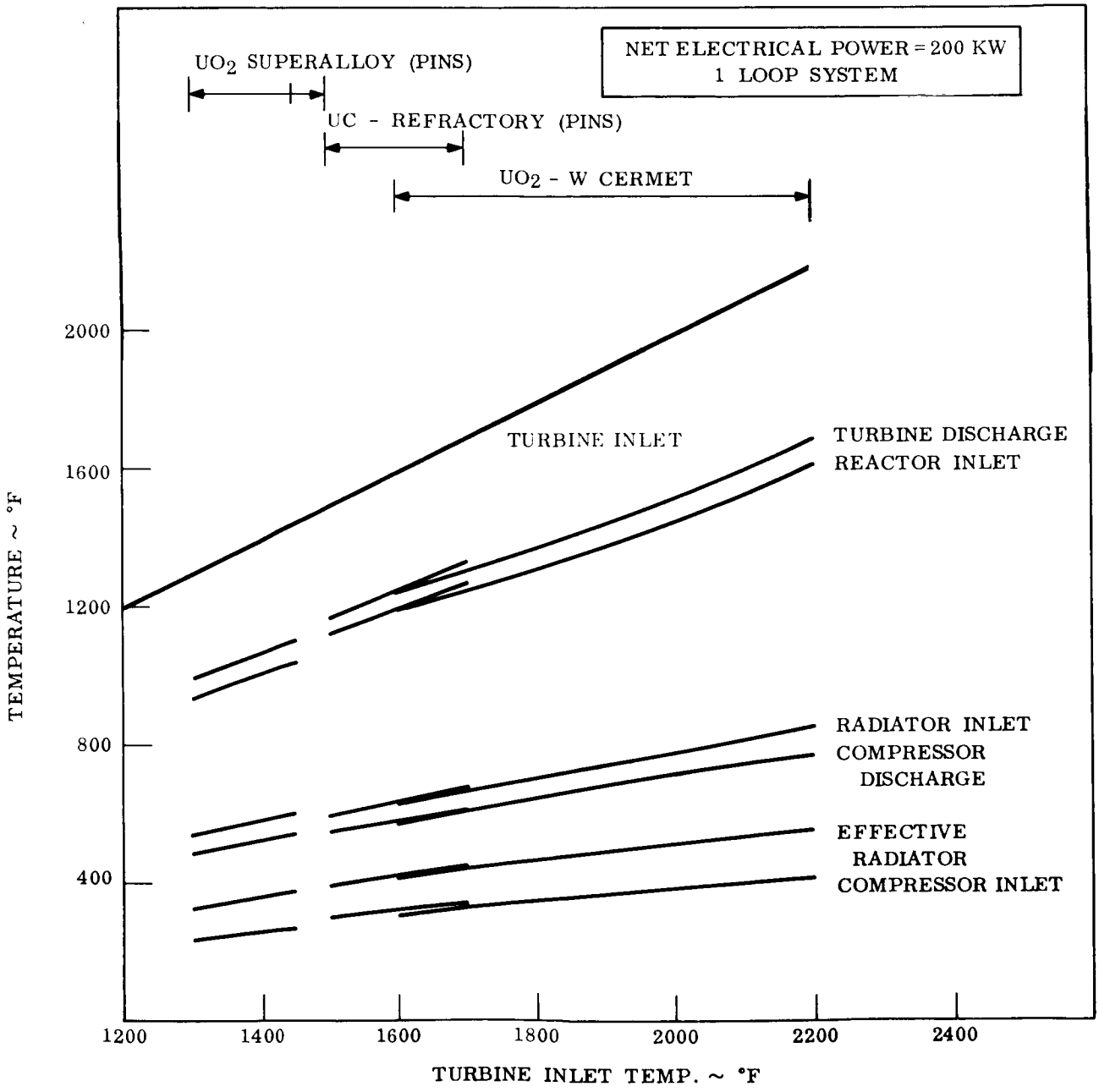

Figure 7-16. Cycle Temperatures as a Function of Turbine Inlet Temperature, Unmanned Application

The optimum fractional pressure loss and ratio of turbine pressure ratio to compressor pressure ratio is shown in Figure 7-17 for a turbine inlet temperature of 2200°F. At higher power levels more weight can be used in the heat transfer equipment and smaller fractional pressure drops result. The values of the fractional pressure loss and ratio of pressure ratios is shown in Figure 7-18 as a function of turbine inlet temperature for 200 KW systems. At low turbine inlet temperatures the cycle is very sensitive to pressure loss, and therefore seeks to minimize it. Component weights, however, increase very rapidly at lower fractional pressure drops.

The optimum compressor pressure ratio is shown in Figure 7-19 for systems with a turbine inlet temperature of 2200°F. At the higher power levels the fractional pressure loss is less and an advantage exists for going to lower pressure ratios and greater recuperation. A decrease in fractional pressure loss is similar in effect to an increase in turbo-machinery efficiency. It is well known that the optimum (maximum efficiency) pressure ratio of recuperative stationary powerplants decreases with increasing component efficiency. This

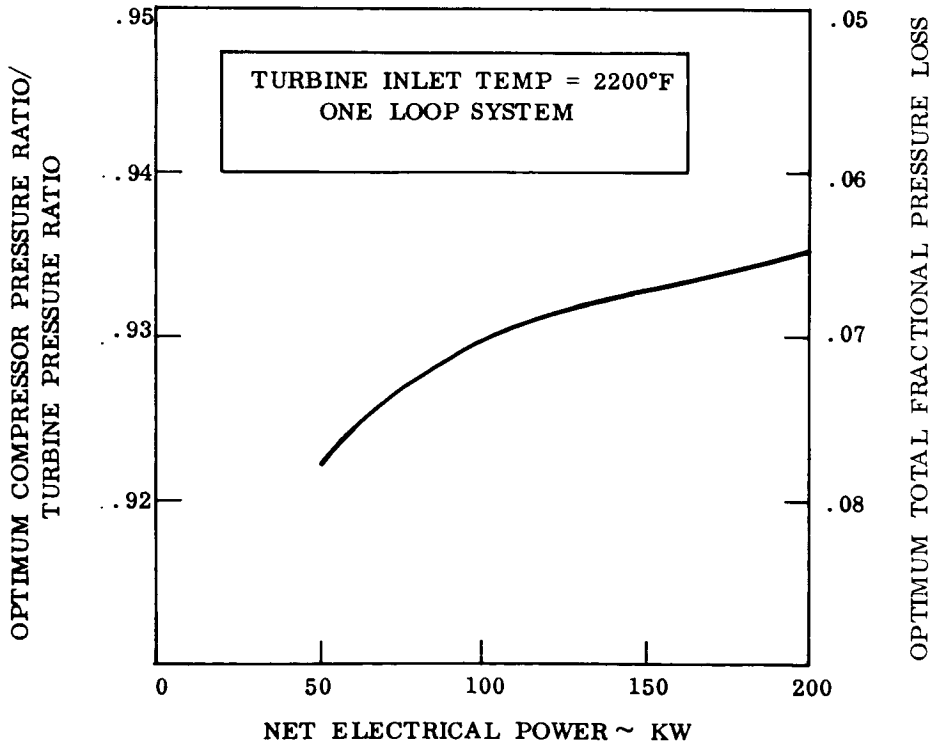

Figure 7-17. Optimum Ratio of Compressor Pressure Ratio to Turbine Pressure Ratio and Fractional Pressure Loss as a Function of System Power Level, Unmanned Application

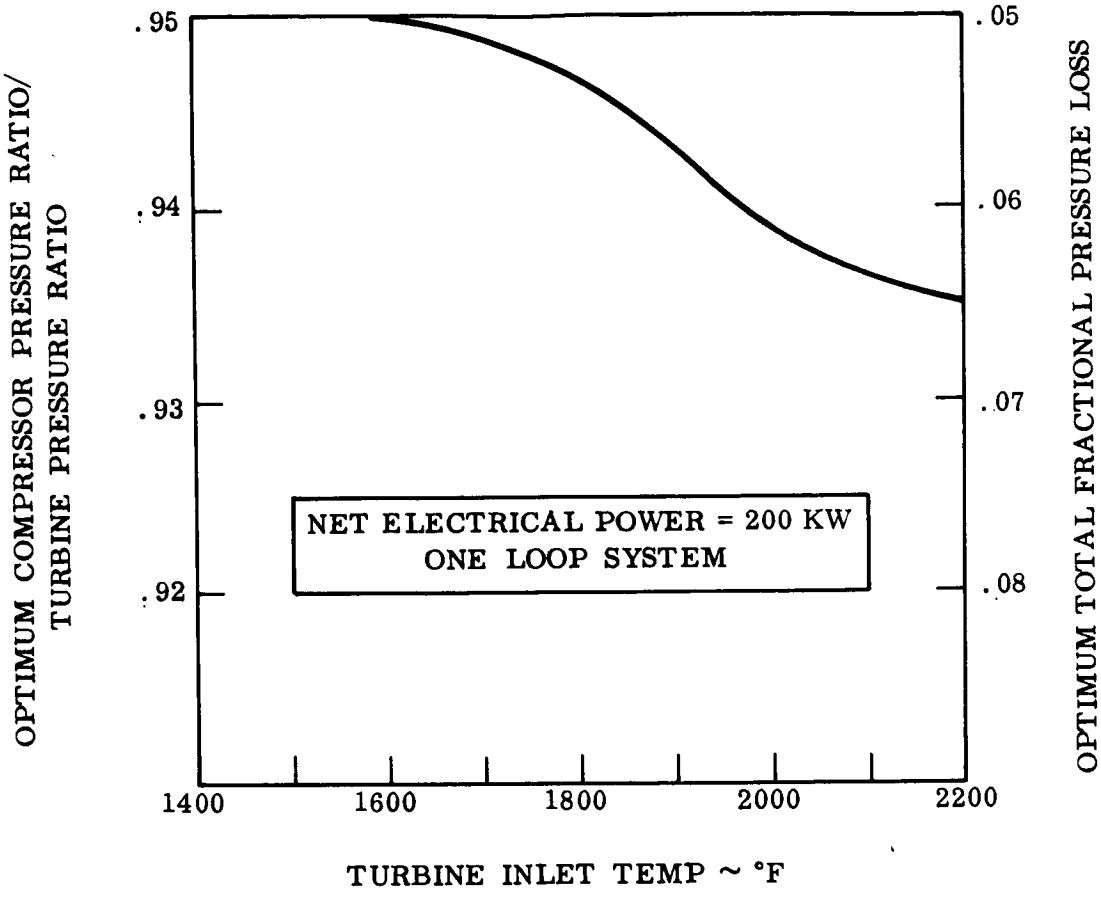

Figure 7-18. Optimum Ratio of Compressor Pressure Ratio to Turbine Pressure Ratio and Fractional Pressure Loss as a Function of Turbine Inlet Temperature

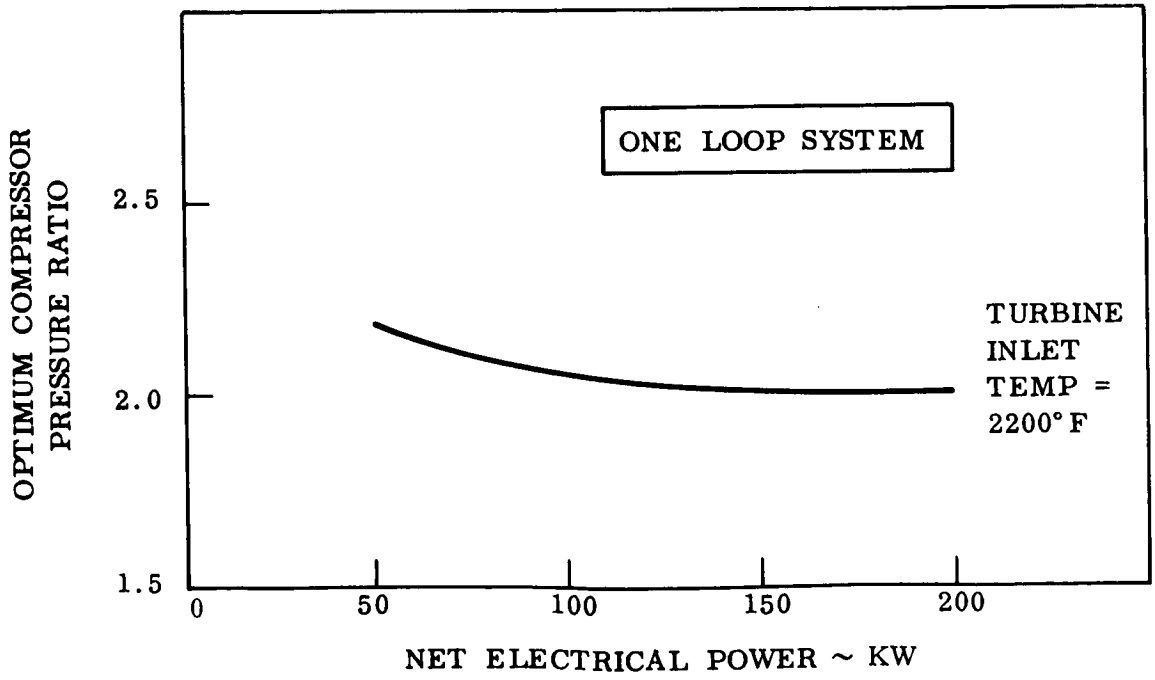

Figure 7-19. Optimum Compressor Pressure Ratio as a Function of System Power Level

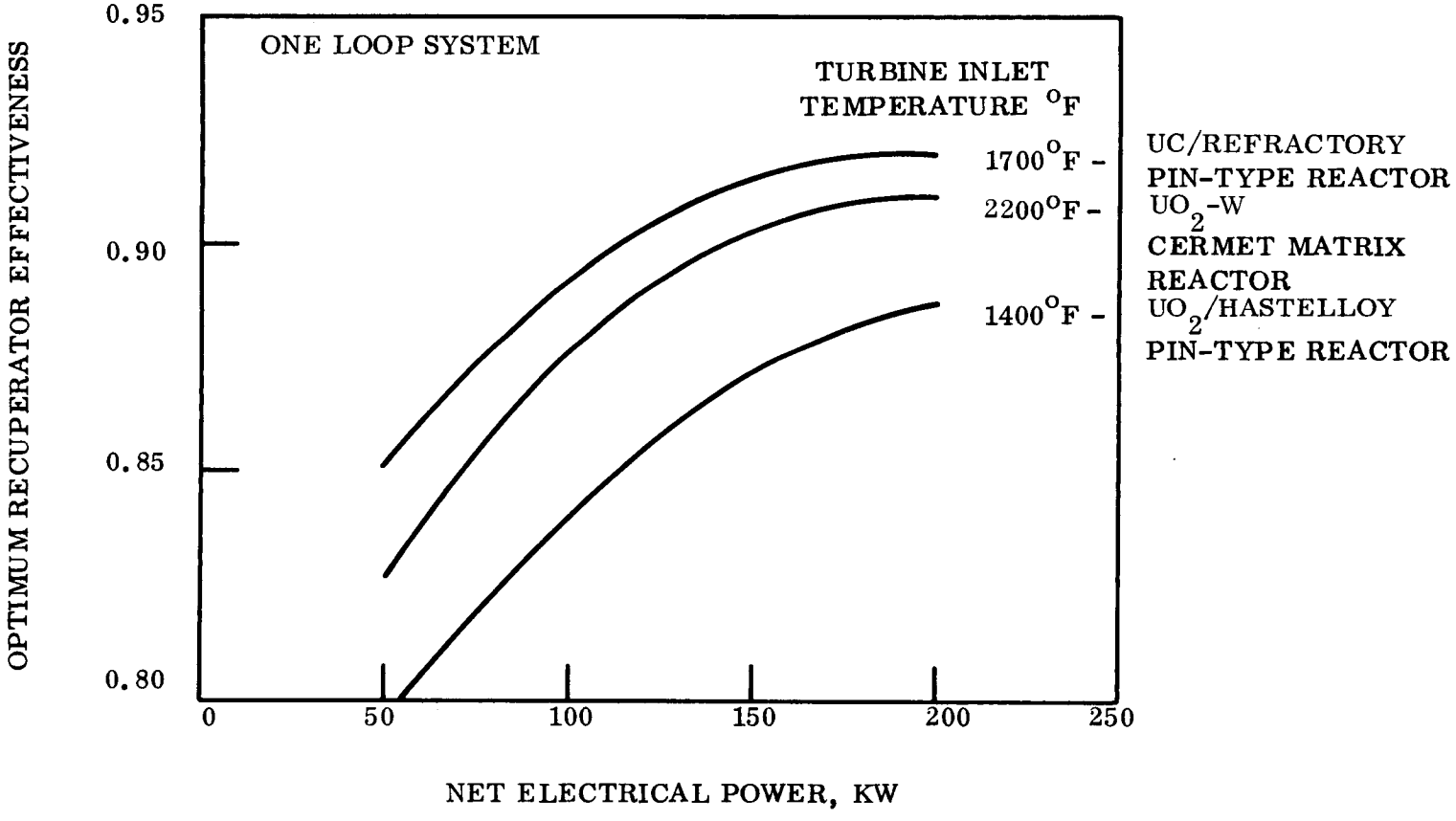

Figure 7-20. Optimum Recuperator Effectiveness for One-Loop System.

is similar to the increase in optimum pressure ratio for non-recuperative stationary powerplants and gas turbine engines resulting from increased component efficiency.

Figure 7-20 shows the optimum recuperator effectiveness for one loop systems. It is seen that the recuperator effectiveness increases with power level. This is because the power-pressure proportionality assumption would result in a constant weight recuperator if the effectiveness were held constant, and the increasing effectiveness results in an increase in recuperator weight. It is noted that the specific weight of the recuperator decreases slightly with increasing system power level. An interesting result of the computer optimization is the diameter of the piping in the optimum system (see Figure 7-21). Piping weight is traded off against the effects of the piping pressure drop as is described in Section 5 of this report. At low power levels, where heavy components can be used to advantage to offset the large specific weight of the reactor and shield, larger pipe diameters are optimum. At the larger power sizes the optimum pipe diameter stabilizes at about five inches. This results in a constant specific weight of the piping, since the wall thickness is proportional to the gas pressure level, and therefore system power. The reactor feed

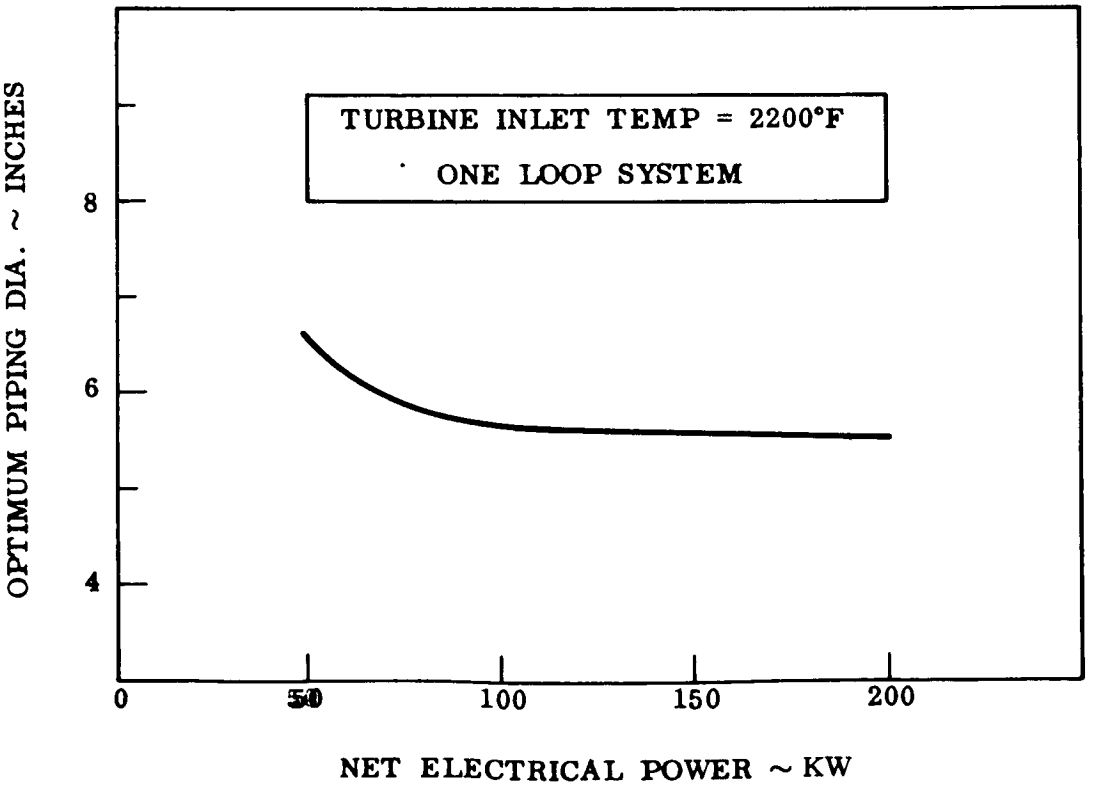

Figure 7-21. Optimum Reactor Feed Line Diameter as a Function of System Power Level

and return lines were sized for equal Mach number. Because of the high temperatures, and the low molecular weight of neon (20.18) the speed of sound in the reactor feed and return line is large. Thus, higher velocities than would normally be considered occur at conventional values of Mach number.

7.3.2.2 Two-Loop Systems

Two-loop Brayton cycle powerplants, in which gas-cooled reactors are used in conjunction with liquid metal-filled radiators, were examined for the unmanned mission. By employing a gas-to-NaK heat exchanger between the recuperator and radiator, the heat rejection system can benefit from the thermal, hydraulic and structural advantages afforded by the use of a liquid-metal heat transfer fluid. Among the major advantages of the liquid-filled radiator (relative to the gas radiator) are the lower percentage pressure drop in the loop and the associated weight savings due to the use of smaller diameter headers, tubes, and feed/return lines. Another important benefit obtained in liquid-metal radiators is the avoidance of the large film temperature drop in the radiator tubes which, in the case of gas radiators, impairs the efficiency of heat rejection by lowering the mean radiating temperature. This poor heat rejection ability of the gas radiator is a consequence of the large variation in the fluid-to-wall temperature drop from the hot end to the cold end of the radiator. Since the gas thermal conductivity varies as $T^{0.7}$, while the radiation heat flux varies at T^4, the film temperature drop in the gas will be about four times greater at the hot end than at the cold end. When a liquid metal is used as a radiator fluid, however, the high thermal conductivity of the fluid and small tube diameters result in very small film temperature drops. Thus, the improved heat rejection capability of the liquid-metal radiator loop and its lower pressure drop yielded a net reduction in system weight (in spite of the addition of a heat exchanger and pump) as well as a smaller radiator area requirement than the comparable gas radiator system.

The performance of the two-loop systems over the turbine inlet temperature range of 1450°-2200°F and over the electrical power range of 50-200 KW is shown in Figures 7-22 and 7-23. Figure 7-22, illustrating the variation in component specific weights with turbine inlet temperature, is similar to the corresponding set of curves for the one-loop systems

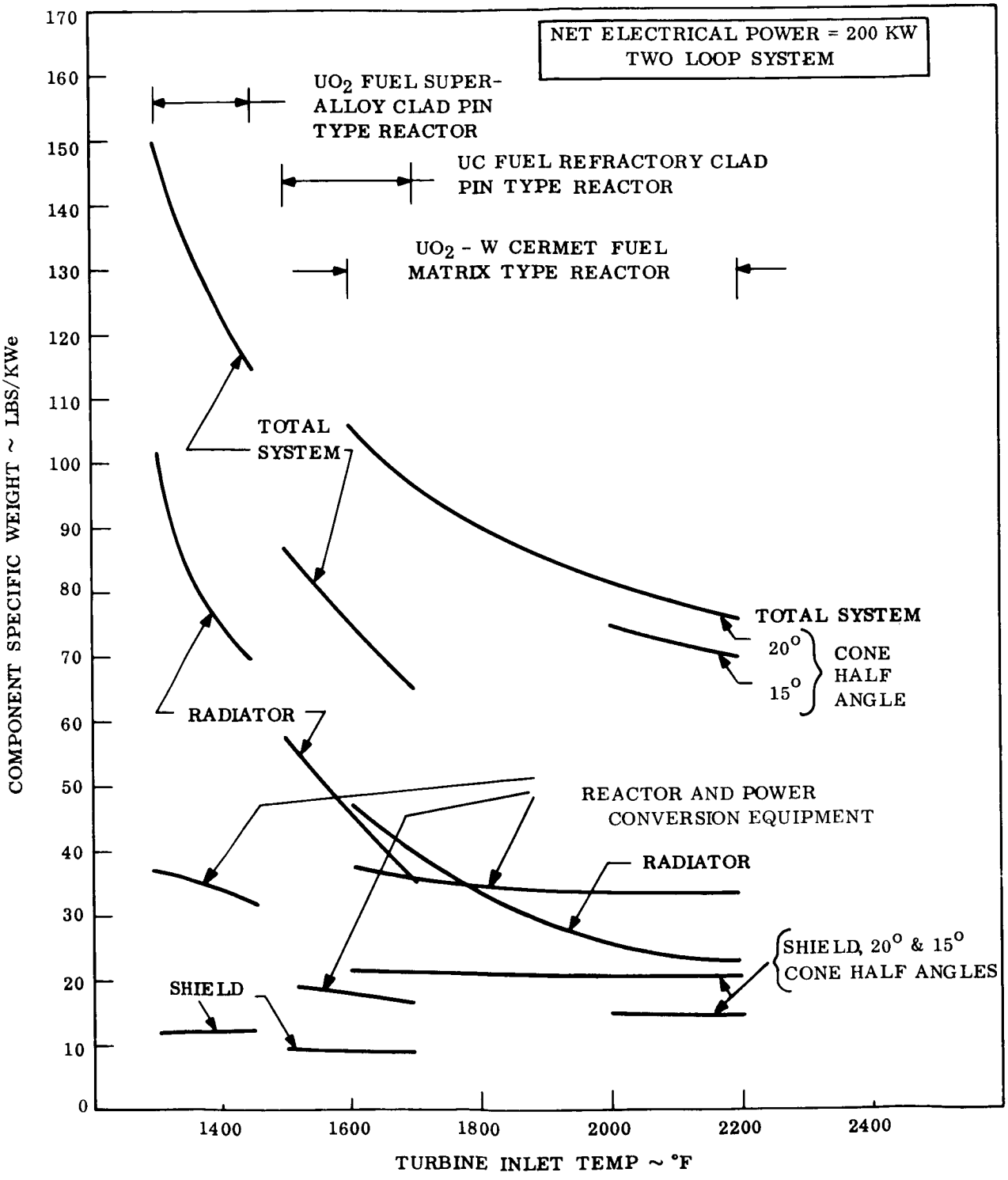

Figure 7-22. Component and System Specific Weight as a Function of Turbine Inlet Temperatures.

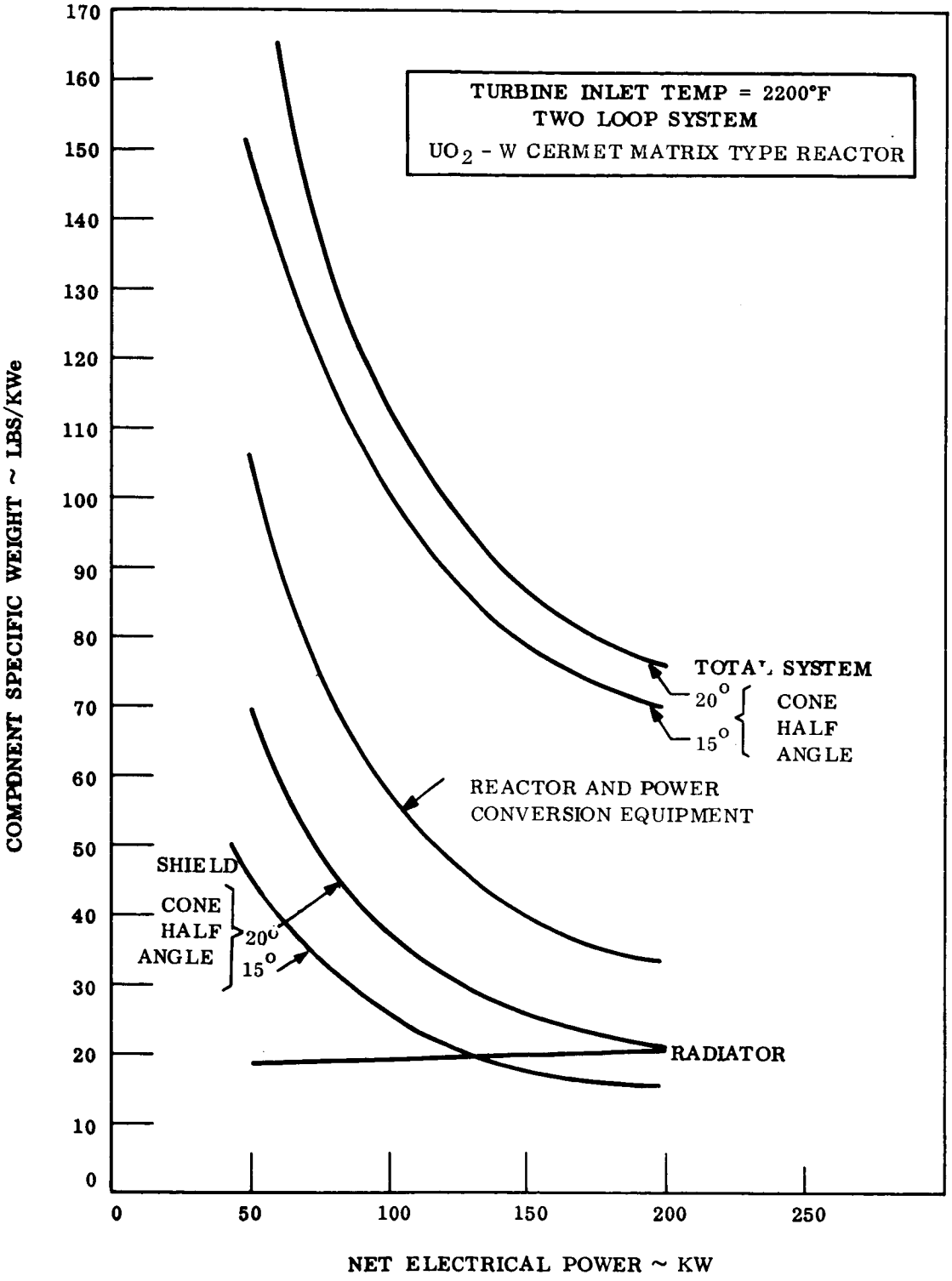

Figure 7-23. Component and System Specific Weight as a Function of System Power Level (sheet 1 of 3)

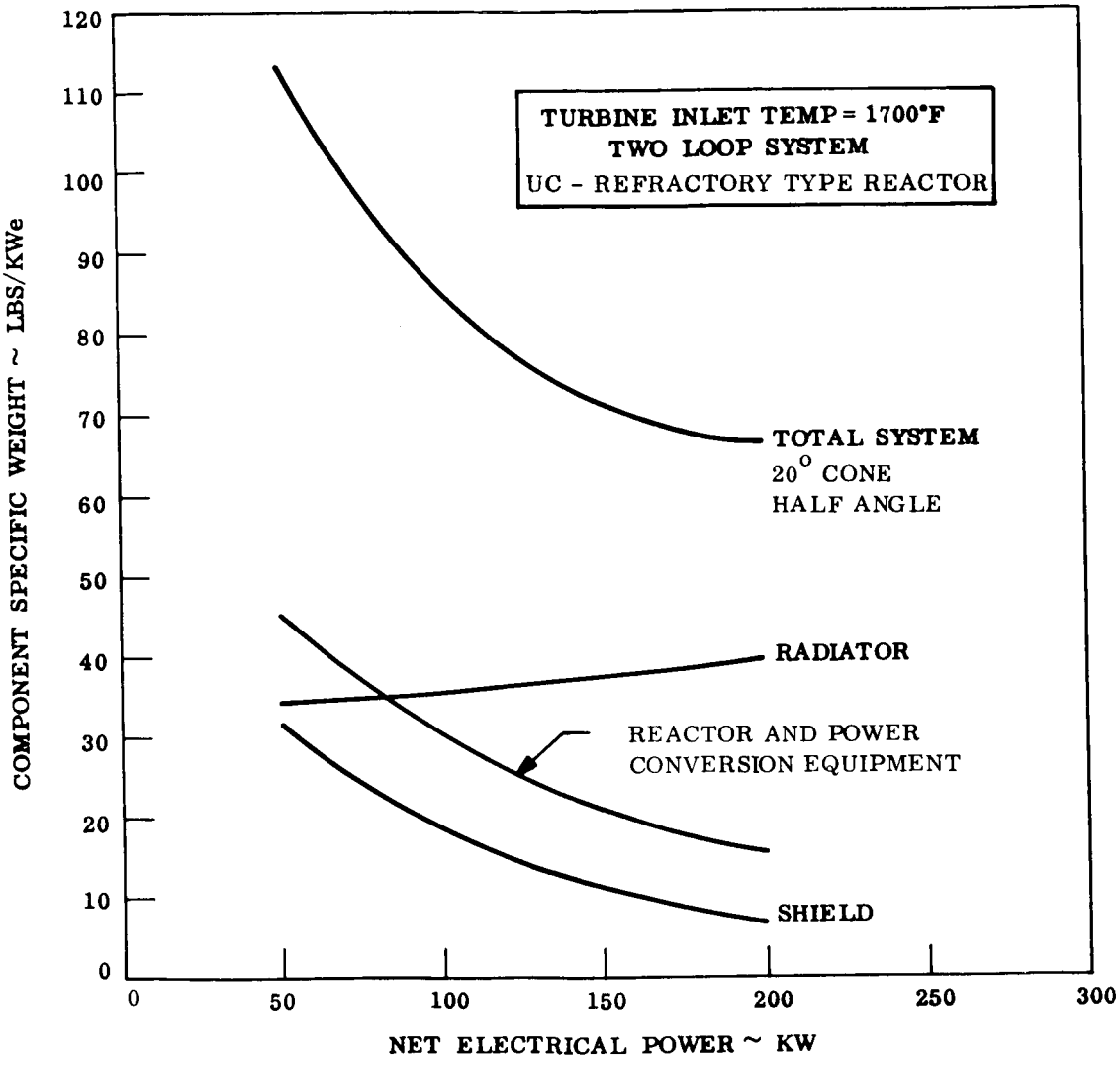

Figure 7-23. Component and System Specific Weight as a Function of System Power Level (sheet 2 of 3)

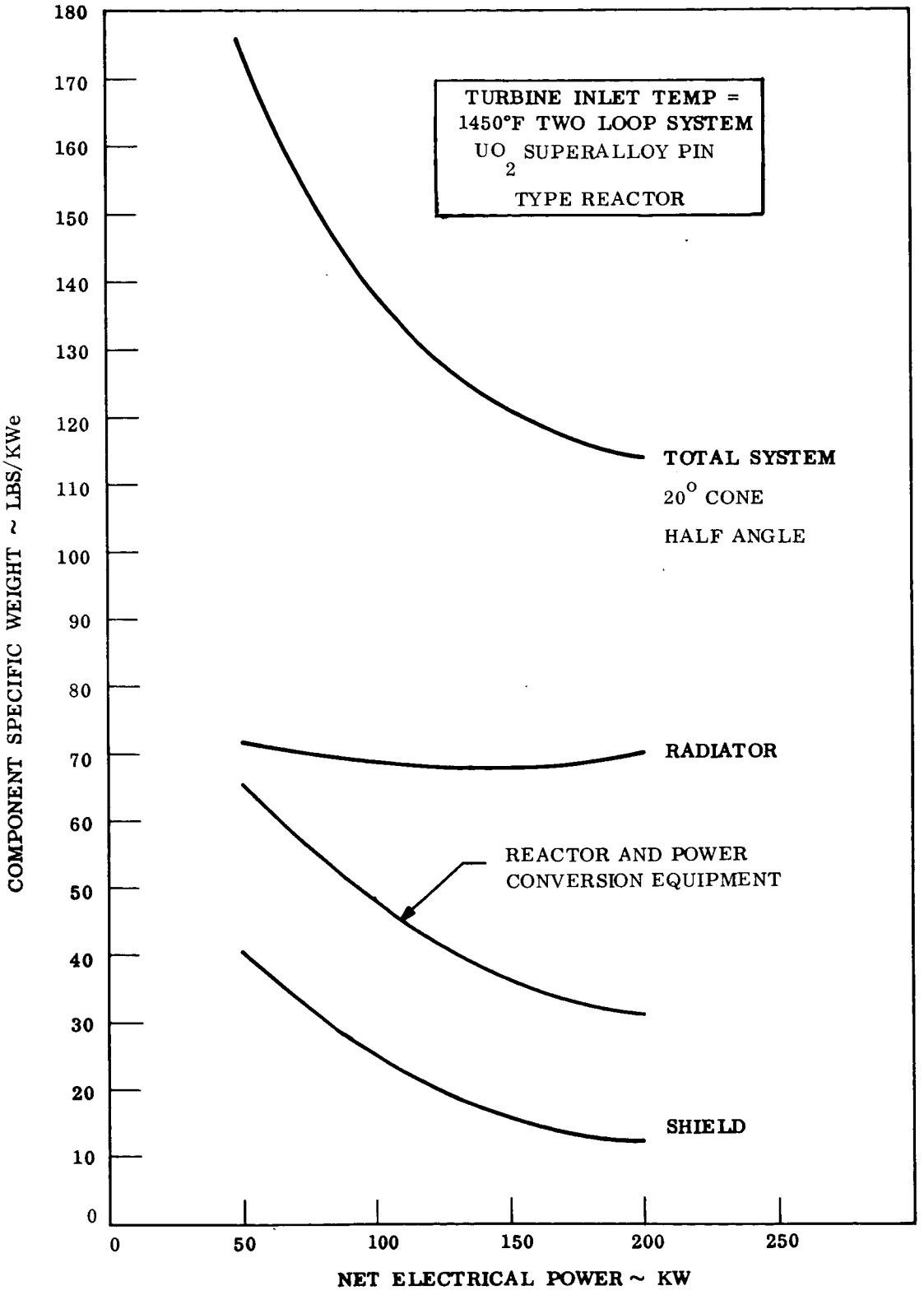

Figure 7-23. Component and System Specific Weight as a Function of System Power Level (sheet 3 of 3)

(Figure 7-12) except for the lower two-loop system radiator weights. Proportionately greater radiator weight savings are realized at the lower turbine inlet temperatures. It can also be seen, by comparing Figure 7-23 (sheets 1 through 3) with those for the one-loop systems shown in Figures 7-14 (sheets 1, 3, and 4) that the two-loop powerplants enjoy an increasing advantage in system specific weight as the power level is lowered. However, the percentage improvement in two-loop system specific weight to one-loop system specific weight varies from 0.80 to 0.95, depending on turbine inlet temperature, for the range of power levels studies.

The optimum recuperator effectiveness for two-loop systems is shown in Figure 7-24. The increase in optimum effectiveness with recuperator size represents a trend toward constant specific weight, as opposed to constant component weight, for the same reasons as those given for one-loop systems. The power-pressure proportionality results in increases in effectiveness and decreases in fractional pressure drop with increases in power level since the weight of the recuperator can increase while still holding constant (actually a slightly decreasing) recuperator specific weight. Figure 7-25 shows the recuperator fractional pressure drop (each side). This figure suffices to summarize the results of the 1-, 2-, and 3-loop systems. The spread in optimum pressure drop between the various systems is less than the scatter due to the use of finite steps in the optimization procedure. The optimum recuperator effectiveness for 1-, 2-, and 3-loop systems overlaps, however a light trend separating the systems can be seen. Figure 7-26 shows the optimum recuperator fractional pressure drop (each side) for 200 KWe systems. One-, two-, and three-loop systems can be adequately summarized by this figure. The effectiveness of the radiator heat exchanger for two-loop systems is summarized in Figures 7-27 and 7-28. It is seen that the trend toward higher effectiveness at large power levels, seen in the recuperator performance, continues. The consequences of power-pressure proportionality are again believed to be the cause of this trend. The slight decrease in optimum radiator heat exchanger effectiveness accompanying the increase in turbine inlet temperature is a consequence of the lighter overall systems at the higher temperatures, and the greater premium to be placed on weight in relation to performance. This trend is also seen in Figure 7-29 which shows that a greater pressure drop can be accommodated in the heat rejection loop at higher turbine inlet temperatures. At higher temperatures the system

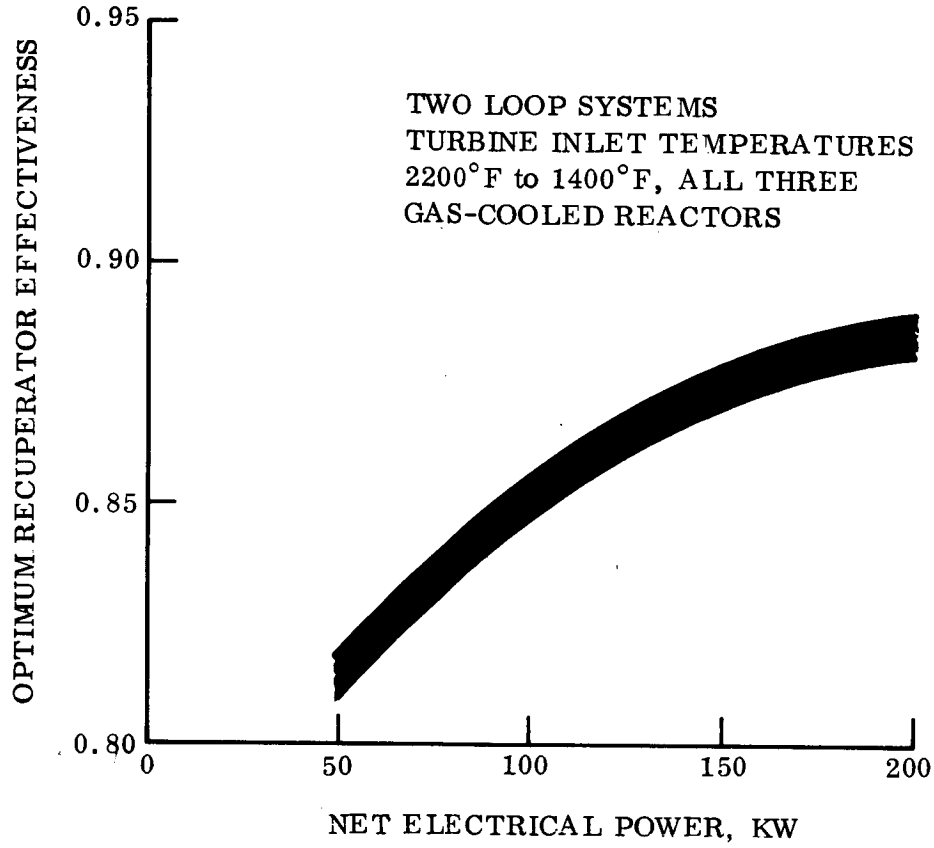

Figure 7-24. Optimum Recuperator Effectiveness

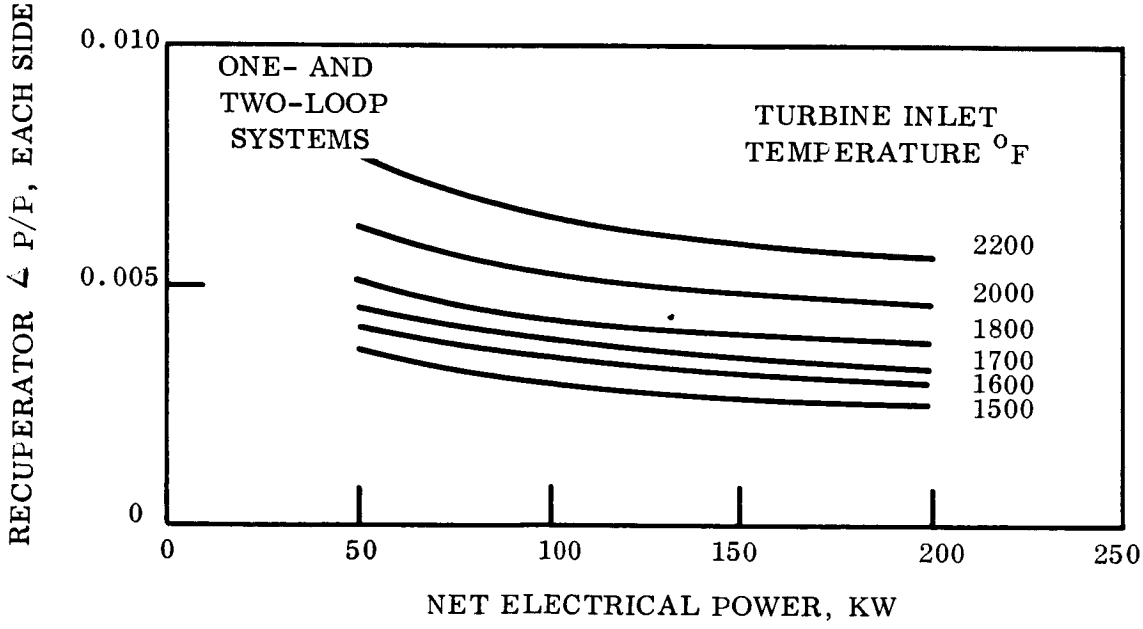

Figure 7-25. Recuperator Fractional Pressure Drop

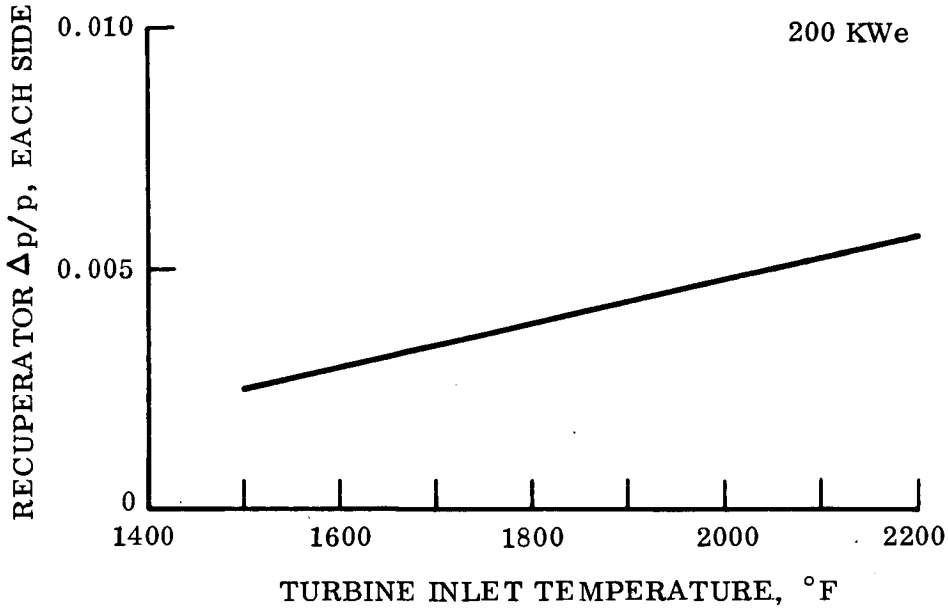

Figure 7-26. Optimum Recuperator Fractional Pressure Drop for 200 KWe Systems

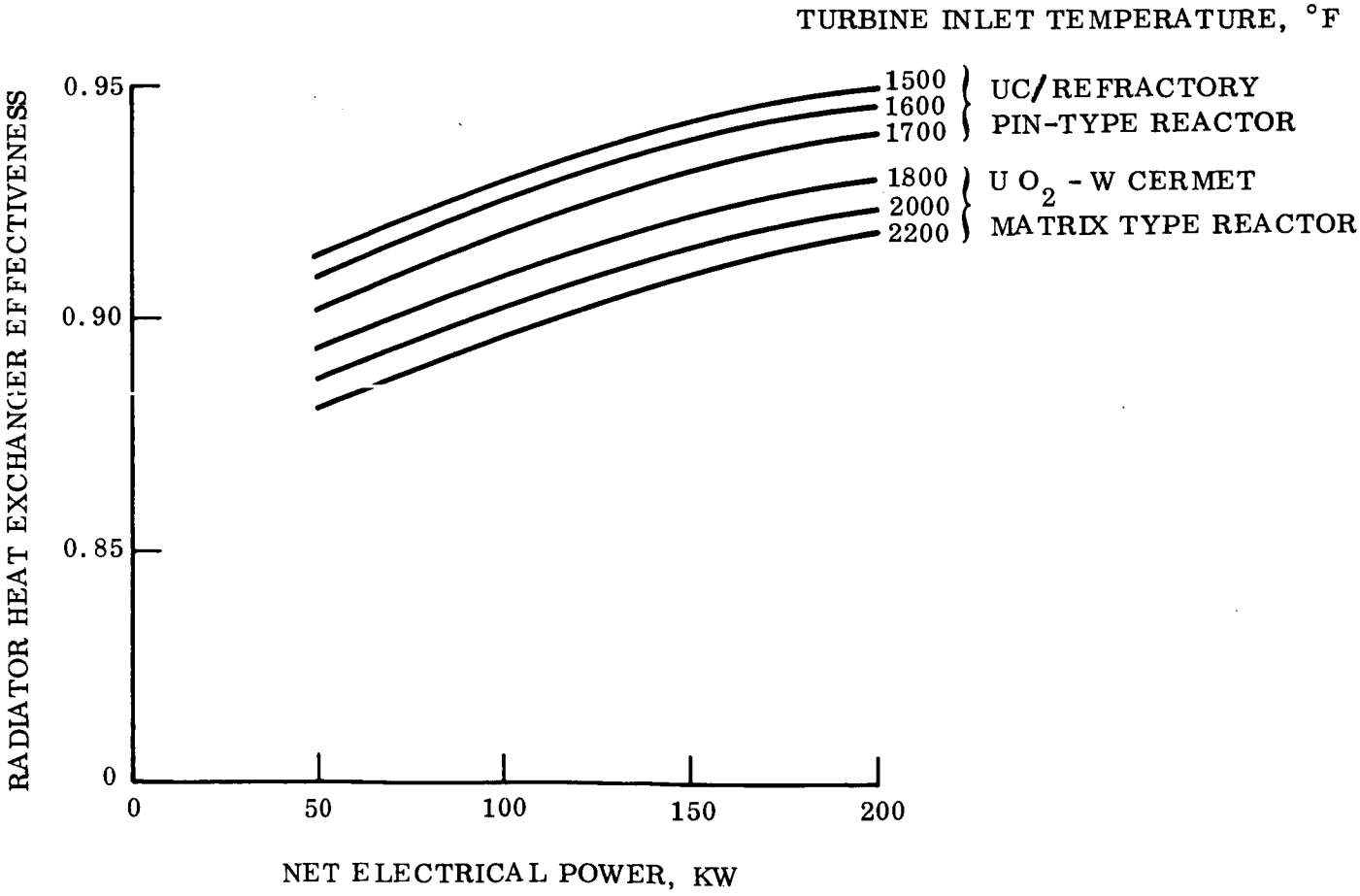

Figure 7-27. Radiator Heat Exchanger Effectiveness-Two-Loop System

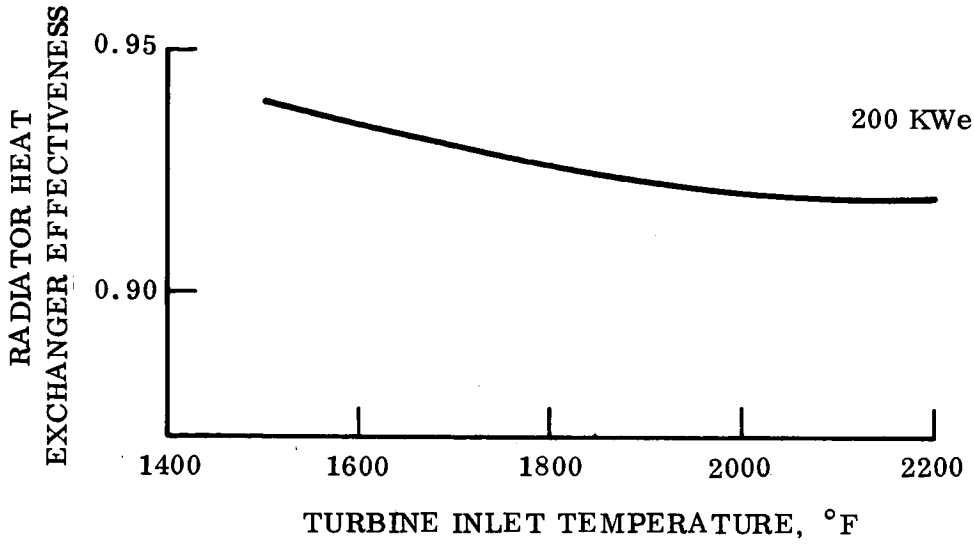

Figure 7-28. Radiator Heat Exchanger Effectiveness - 200 KWe System

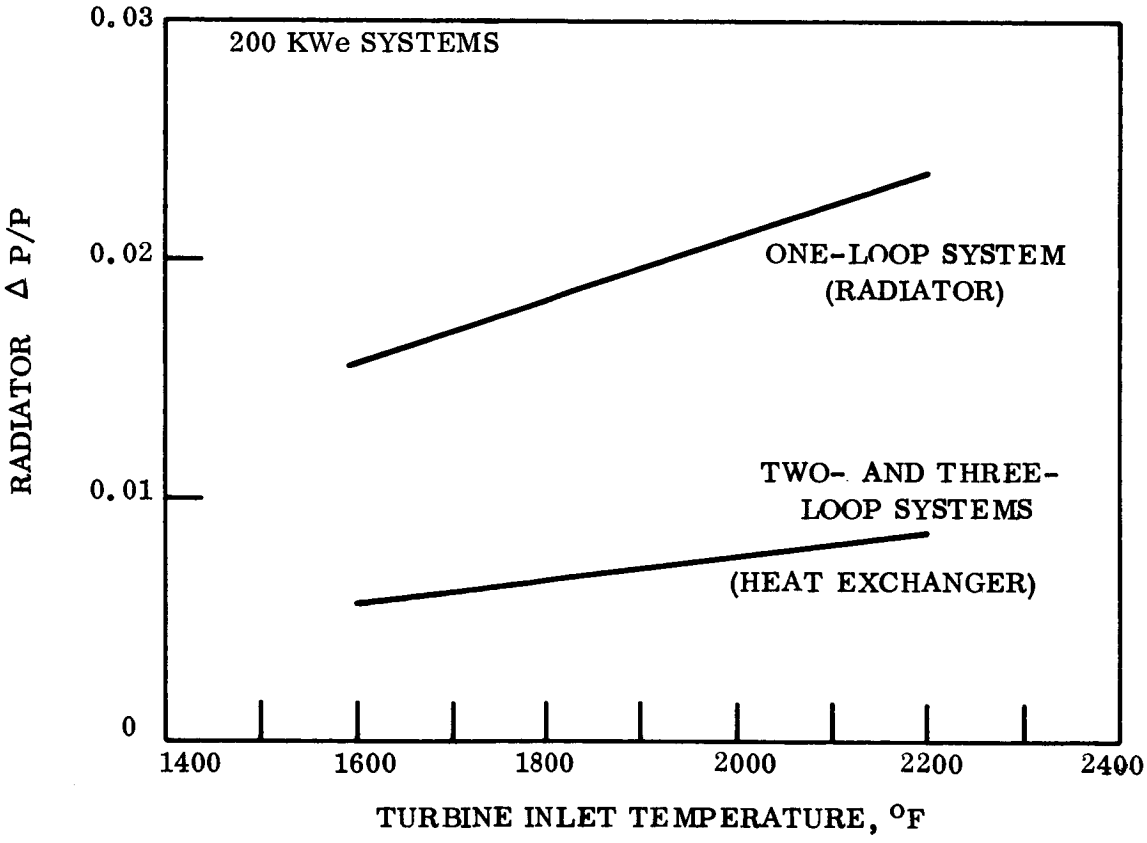

Figure 7-29. Comparison of One-Loop and Two- and Three-Loop Systems

has a small enough radiator requirement so that it pays to decrease the performance of the components, thereby making them comparatively lighter, and to slightly increase the radiator weight over what it would be for a system using the higher performance (lower system temperature) components. As the temperature increases the specific weight of the radiator decreases rapidly enough so that the weight of the other components must be somewhat reduced to keep the same weight-performance trade-off ratio for all components. Figure 7-29 also shows the savings in pressure drop possible with a separate radiator heat exchanger. The additional weight required to achieve the lower percent pressure drop in the radiator heat exchanger, is small because the increase in volume of the heat exchanger imposes no penalty due to increased meteoroid armor requirements. A decrease in the pressure drop in a direct radiator would necessitate a large increase in armor requirement.

The unmanned vehicle reference design powerplant was selected to be an all-gas system in spite of the 5 to 20 percent weight advantage of the two-loop system. The selection of a gas radiator for the reference design was based on the practical factors associated with thermal control of the NaK system (freezing difficulties) during non-operating periods.

7.3.2.3 Three-Loop System

The use of a liquid metal cooled reactor as a heat source for a Brayton cycle powerplant was evaluated using a three-loop system. The liquid-metal filled radiator was selected since comparisons of one-loop and two-loop systems using gas-cooled reactors indicated that a slight weight advantage exists for using an additional loop. The possible advantages of the liquid-metal reactor heat source for a Brayton cycle lie with the ability to separate the heat-transfer and pressure drop aspects of the heat source from the requirements for a nuclear radiation shield between the reactor and payload. Thus the primary heat exchanger can be located in a region where there is no penalty associated with its volume. The primary heat exchanger in a three-loop system can be sized for a high effectiveness and a small pressure drop, even though its weight and volume might be large. The temperature drop between the maximum cladding temperature in the reactor and that of the coolant at the exit is small compared to the film drop in a gas-cooled reactor passage.

The temperature drop from the reactor cladding to the heat-exchanger exit can be made smaller than the difference between the maximum cladding and exit gas temperature in the case of a gas-cooled reactor. Similarly the pressure drop can be reduced by using a large heat exchanger (12 cubic feet and 400 pounds in the case of a 200-KWe system). It is to be noted that about 250 pounds (net) of piping are saved with the three-loop system. Figure 7-30 shows the specific weight of the components and of the entire system of three-loop Brayton cycle powerplants where the reactor cladding temperature is limited to 1900°F. The optimum turbine inlet temperature varies from 1824°F, for the 200-KW system to 1770°F, for the 50-KW system. This variation in optimum turbine inlet temperature is attributed to the larger primary heat-exchanger weight which can be used in larger power systems. Since the mass flow rate of the gas in the power conversion loop is proportional to the pressure level, fixed effectiveness and fractional pressure drop implies constant heat exchanger weight, rather than constant specific weight. The additional turbine inlet temperature possible with the indirect cycle, as well as the opportunity to reduce the reactor and shield size (by using a uniformly enriched core) and heat source pressure drop, result in an almost flat trade-off with heat exchanger weight and the cost of reactor loop pump power. The net change in the system specific weight is an increase of less than one lb/KW when a liquid-metal cooled, rather than a gas-cooled, reactor is used. This change is less than the possible savings in system weight achievable by reducing the shield half-angle, possibly since the three-loop system, due to its higher turbine inlet temperature, required about 8 percent less radiator area. More accurate information regarding the performance of smaller items, such as the reactor loop pump would have to be obtained if any comparative judgements were to be made regarding liquid-metal and gas-cooled reactors.

7.3.3 COMPARISON SYSTEMS USING NEON AND ARGON AS THE WORKING FLUIDS

Comparisons were made of one-loop, 200 KWe, powerplants, with shadow shielding, using neon and argon as the working fluids. Reactor and radiator designs were generated for identical inlet and exit temperatures pressures and thermal power, and these comparisons were used to scale the correlations developed for neon. Changes in Mach and Reynolds numbers on the pressure drop and heat transfer rate were considered. When the designs

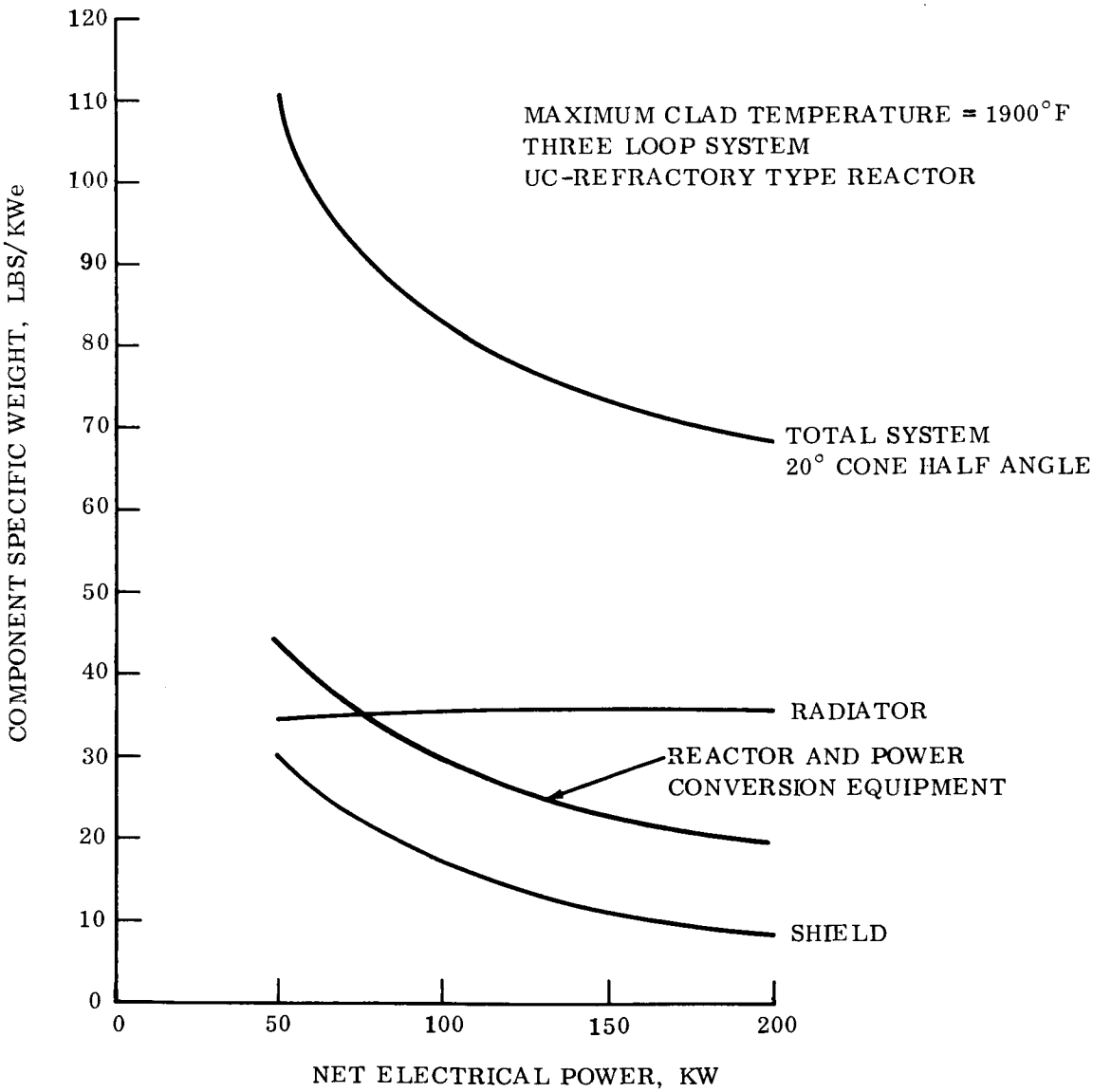

Figure 7-30. Component and System Specific Weight as a Function of Power Level, Liquid-Metal Cooled Reactor, Unmanned Application

for identical thermal and hydraulic conditions were compared it was found that an increase in weight of the component designed for neon by a factor of 1.69, for the recuperator radiator and reactor, adequately represented the argon designs.

The comparison of cycles with neon and argon working fluids is shown in Figure 7-31. The turbomachinery performance of the solar Brayton cycle machinery was used in both cases. It is seen that use of argon results in a weight penalty of about 4 lbs/KWe over the power range of 50 to 200 KWe.

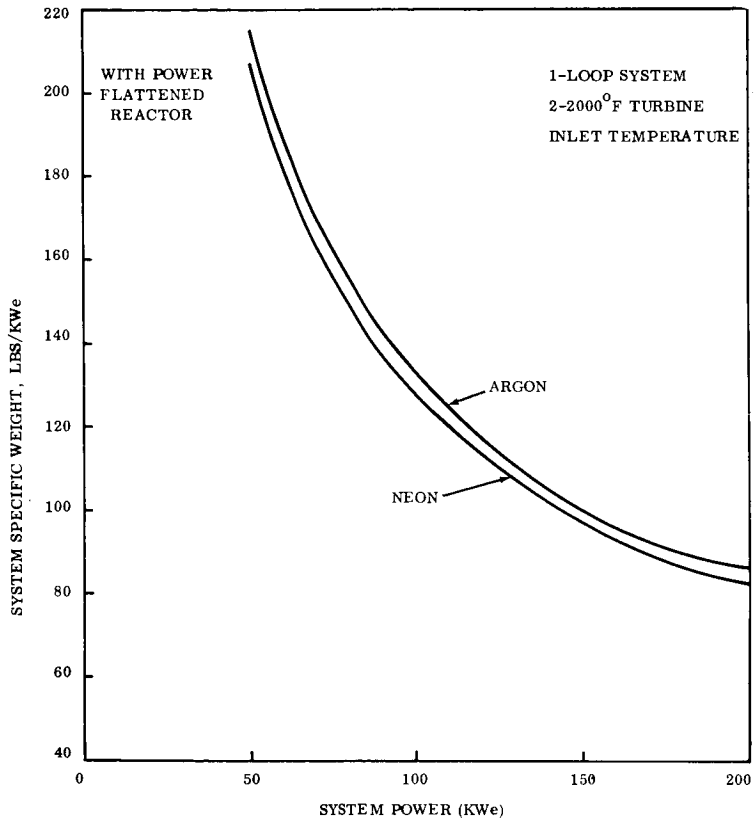

Figure 7-31. System Power vs Specific Weight

7.3.4 RADIATOR-STRUCTURE CONTRIBUTION TO SYSTEM OPTIMIZATION

One loop, unmanned vehicle powerplants were analyzed with and without the additional radiator weight necessary for structural integrity and multi-bay fabrication. Besides altering the radiator weight, the inclusion of this thermodynamically unaccountable item affects the cycle optimization. Systems with greater radiator weight per unit of area will optimize at smaller radiator areas. The reduction in area is accomplished by enlarging the

heat transfer limited equipment. The resultant pressure drop decrease improves the powerplant efficiency and thereby reduces the heat rejection load on the radiator. There is also a corresponding upward adjustment of the radiator inlet temperature.

Figures 7-32 and 7-33 when respectively compared to Figures 7-34 and 7-35 show the reduction in radiator area for optimized systems resulting from consideration of the structural requirement. The reduction encountered is typically about 20 percent. Accounting for this effect in the system optimization results in the ability to package 20 percent more power within a given booster payload envelope limitation. It also presents a more realistic assessment of the capabilities of a launchable system.

7.3.5 INFLUENCE OF VARIATIONS IN COMPONENT PERFORMANCE

Various possibilities exist for improving the powerplant performance. These include the use of higher efficiency turbo-machinery, higher maximum cladding temperatures, and non-power-flattened reactor cores. The effects of these improvements on over-all system performance was evaluated in order to determine which, if any, of these techniques would result in a significant enough savings in weight to warrant further investigation.

A model of a higher efficiency power conversion system was used, based on expected performance gains in small power level (below 200 KW) turbo-machinery supplied by NASA/ Lewis. This equipment operates at about one-third of the pressure level of the higher pressure level, lower efficiency reference turbo-machinery, and therefore has a higher volume flow rate. Table 7-1 shows a comparison of this equipment with the basic system used in the optimization analysis.

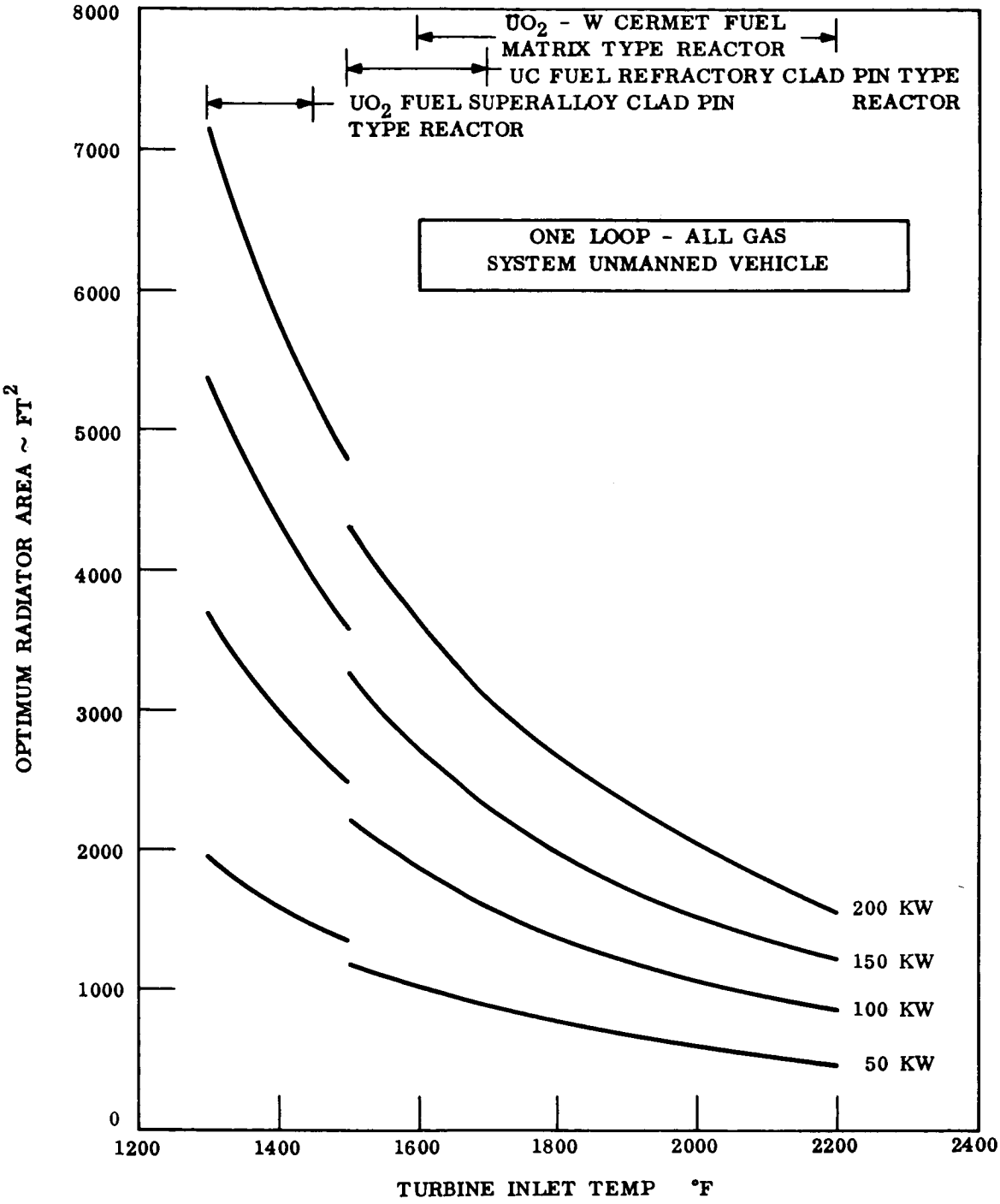

Figure 7-32. Optimum Area of Radiator of Powerplants for Unmanned Space Vehicles as a Function of Turbine Inlet Temperature for Various Power Levels, Structural Weight Included in Radiator Model

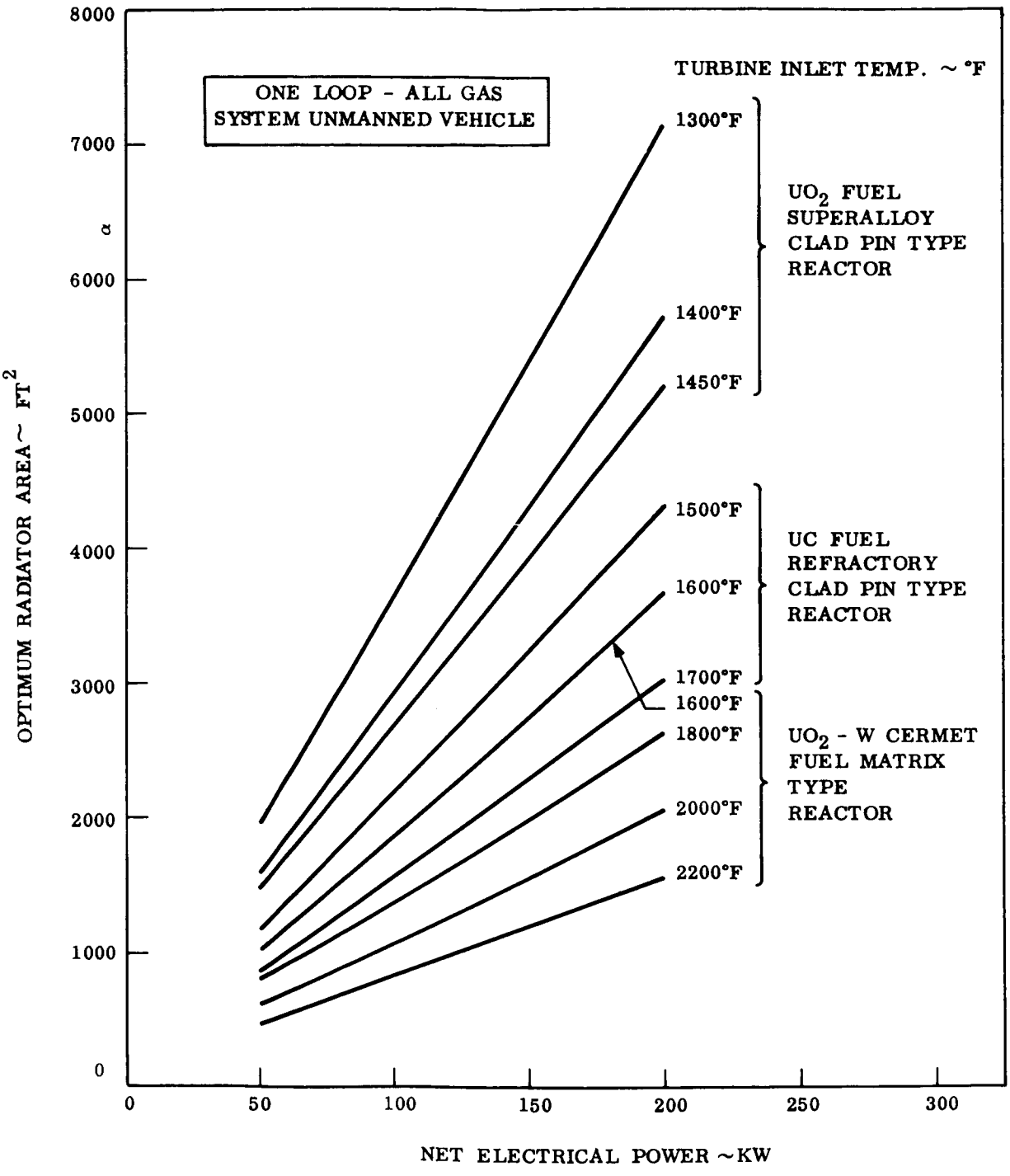

Figure 7-33. Optimum Area of Radiator of Powerplants for Unmanned Space Vehicles as a Function of System Power Level for Various Turbine Inlet Temperatures, Structural Weight Included in Radiator Model

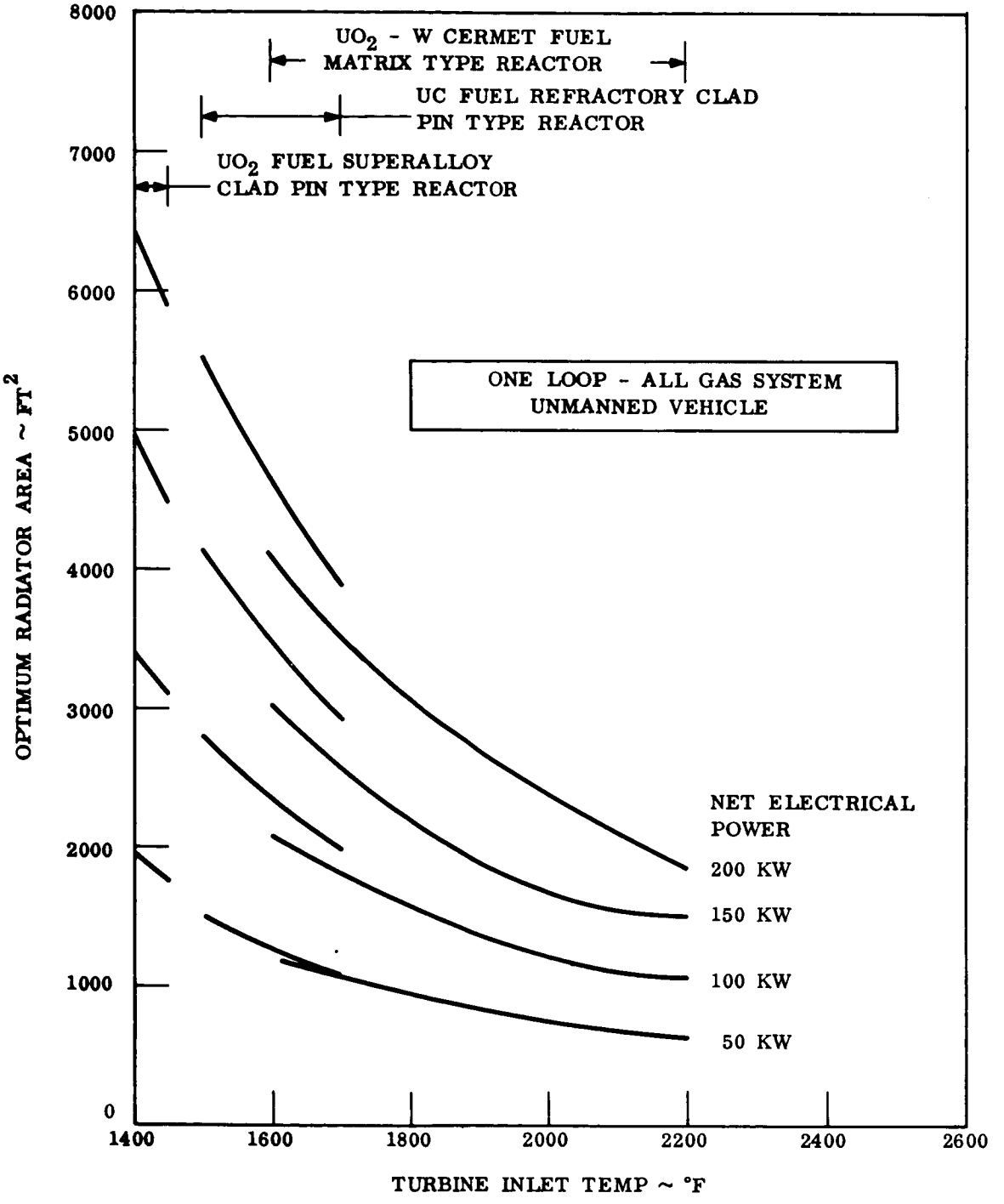

Figure 7-34. Optimum Area of Radiator of Powerplants for Unmanned Space Vehicles as a Function of Turbine Inlet Temperature for Various Power Levels, Structural Weight not Included in Radiator Model

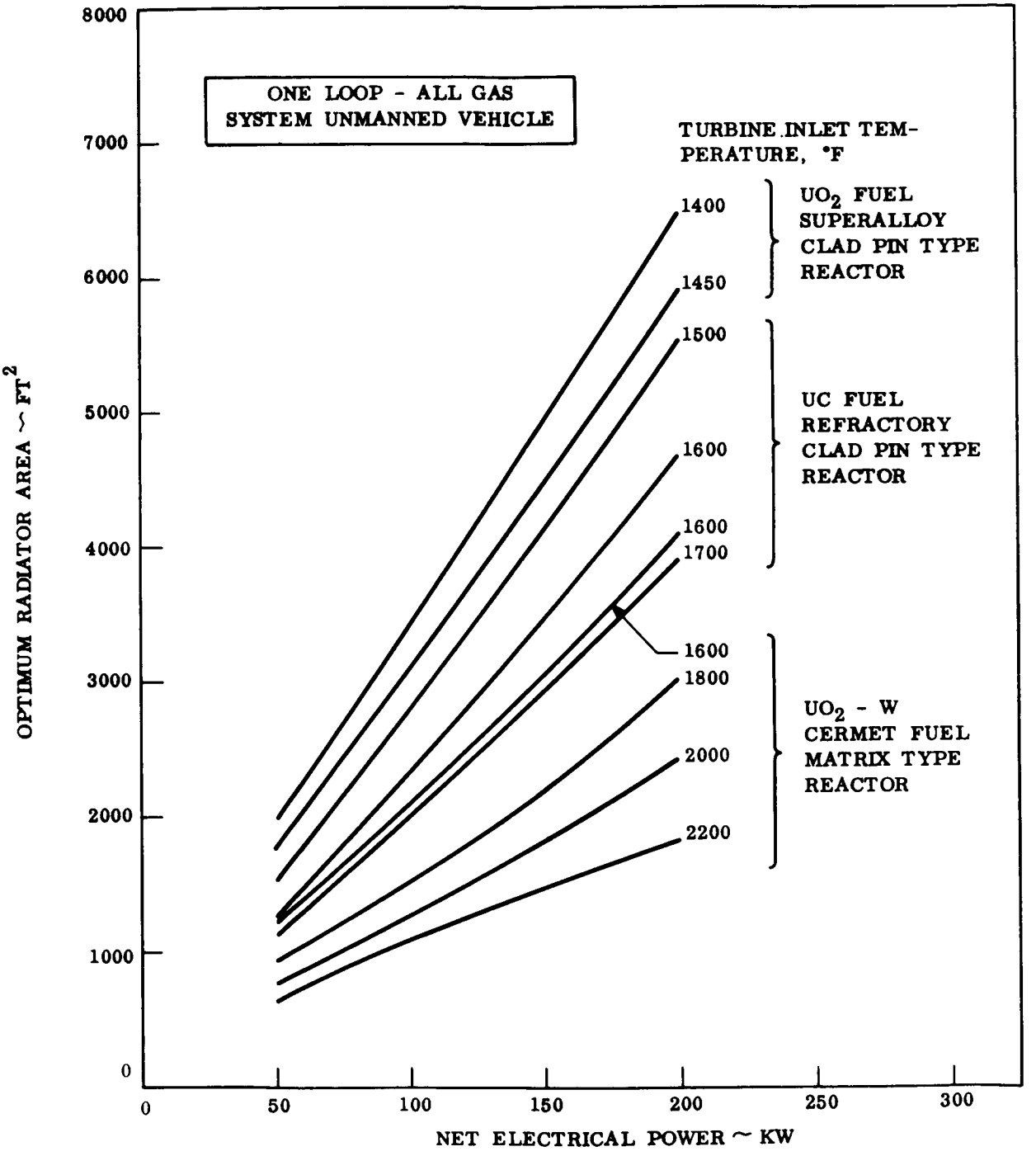

Figure 7-35. Optimum Area of Radiator of Powerplants for Unmanned Space Vehicles as a Function of System Power Level for Various Turbine Inlet Temperatures, Structural Weight not Included in Radiator Model

Table 7-1. Turbomachinery Specifications

COMPONENT	Pressure Ratio		Total-to-Total Efficiency	
	BASIC MACHINE	HIGHER PERF. MACHINE	BASIC MACHINE	HIGHER PERF. MACHINE
Compressor	2.30	2.60	0.80	0.82
Turbine (Compressor Drive)	1.56	1.60	0.88	0.90
Turbine (Alternator Drive)	1.26	1.39	0.83	0.85

The efficiency of the gas expansion through the combined turbines was computed for their design pressure ratios and this value held constant throughout the study. It is expressed by,

$$\eta_{\substack{\text{compound} \\ \text{turbine}}} = \frac{1 - \left\{1 - \eta_1 \left[1 - \left(\frac{1}{PR_1}\right)^{\frac{(\gamma-1)}{\gamma}}\right]\right\}\left\{1 - \eta_2 \left[1 - \left(\frac{1}{PR_2}\right)^{\frac{(\gamma-1)}{\gamma}}\right]\right\}}{1 - \left(\frac{1}{PR_1} \cdot \frac{1}{PR_2}\right)^{\frac{(\gamma-1)}{\gamma}}}$$

Where

PR = Pressure Ratio

PR_1; PR_2 = Turbine over-all pressure ratio

The reference turbo-machinery was scaled on the basis of a turbine inlet pressure of 13.20 psia at 9.54 KW and scaling for the higher performance turbo-machinery was based on 200 KW being developed at a turbine inlet pressure of 94.5 psia.

The purpose of evaluating the system performance was to determine whether the change made due to the introduction of the higher efficiency resulted in a decrease in system specific weight for each of the reactors considered. Table 7-2 summarizes these results.

The optimum reactor for the high efficiency turbo-machinery system using a 2200°F turbine inlet temperature was a minimum diameter core, as was found for the lower efficiency, higher pressure level system. In this case, the fractional pressure drop in the reactor was considerably greater than that obtained with the high pressure level

equipment. Similar results were obtained for the three-loop system with a man-rated shield, where the decrease in pressure level results in a proportionate increase in primary heat exchanger volume, and hence a considerable penalty in shield weight. In this case, the system optimization transfers much of the penalty associated with the increase in heat transfer equipment volume from the reactor heat exchanger to the recuperator and radiator heat exchanger where there is no weight penalty for a volume increase.

Table 7-2. Effect of Higher Efficiency - Lower Pressure Turbomachinery on System Specific Weight

Reactor/Turbine Inlet Temperature	Net Change in System Specific Weight
UO_2 - W Cermet Matrix/ 2200°F	+4 lbs/KW (1 loop)*
UC - Refractory Clad Pin Type/ 1600°F	+10 lbs/KW (1 loop)*
UC - Refractory Clad Pin Type/ 1500°F	+20 lbs/KW (2 loop)
Liquid Metal Cooled Reactor (150 KW)	+10 lbs/KW (3 loop man rated shield)
UC - Refractory Clad Pin Type/ 1800°F	-8.4 lbs/KW (3 loop unmanned shielding)

*The one loop systems were run with the radiator correlation developed for the high pressure level-power level proportionality. In reality these radiators would require larger tubes and greater diameter feeds, returns, and headers, and a corresponding weight increase.

Another reactor design constraint which influences the powerplant specific weight is the maximum allowable cladding temperature. Sample cases have shown that increases in the maximum clad temperature of the lower temperature reactors result in a direct improvement in system specific weight. This increase in performance is primarily due to the allowable increase in turbine inlet temperature. The powerplants employing high temperature reactors also behave this way if the turbine inlet temperature is allowed to go beyond the specified 2200°F maximum. However, when the maximum allowable turbine inlet temperature is fixed at 2200°F, no significant improvement in system specific weight is obtained. This is because the reactor is already at the minimum allowable size (for reactivity considerations) and the only way in which the higher allowable maximum

cladding temperature can be used is to decrease the reactor pressure drop (by increasing the coolant passage hydraulic diameter). The reactor pressure drop decreases by about 10 percent of its value per 100°F rise in maximum cladding temperature. This savings of less than one percent in fraction of pressure loss does result in some savings in radiator area. This savings is of the order of a few percent of the radiator area. Consequently the system specific weight is reduced by only one pound per kilowatt (approximately). Since this improvement is of the same order of magnitude as the cumulative inaccuracies in the analytical models, further study of higher allowable reactor cladding temperatures (without allowing a corresponding increase in turbine inlet temperature) is not warranted for the high temperature cermet-matrix reactors.

7.3.6 COMPARISON OF RESULTS

A comparison of 1-, 2-, and 3-loop Brayton cycle powerplants is shown in Figure 7-36. Each line represents the highest turbine inlet temperature considered for each of the reactor concepts. It is seen that the introduction of a liquid-metal radiator in place of the neon radiator always results in a weight savings. Operational features, such as the possibility of freezing, or of cold trapping, may make it preferable to use an all-gas system. The advantage of a three-loop system seen in this figure is primarily due to the higher turbine inlet temperature achievable with the indirect heating loop. An advantage of partially power flattening the core of the gas cooled cermet reactor is also shown. A much smaller savings in system weight would be expected with the UO_2/ super-alloy and UC/ refractory reactors,since these gas-cooled cores are already near their minimum size.

A summary of 200-KW powerplants for unmanned, and 150 KW powerplants for manned applications is given in Table 7-3. The breakdown of the pressure loss among the various components is given, as well as a summary of the performance of the various heat exchangers.

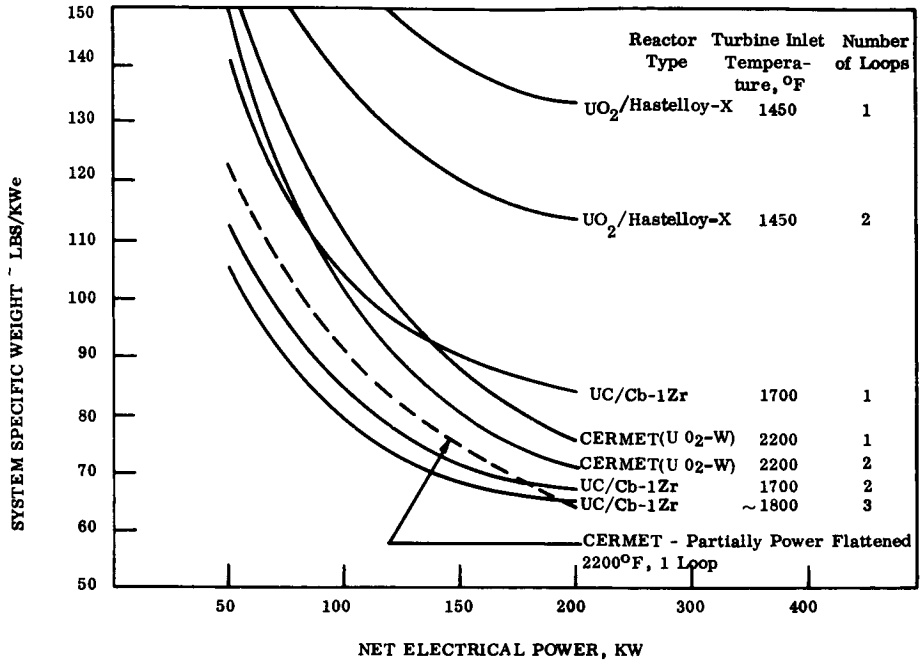

Figure 7-36. Specific Weight of Optimized Powerplants

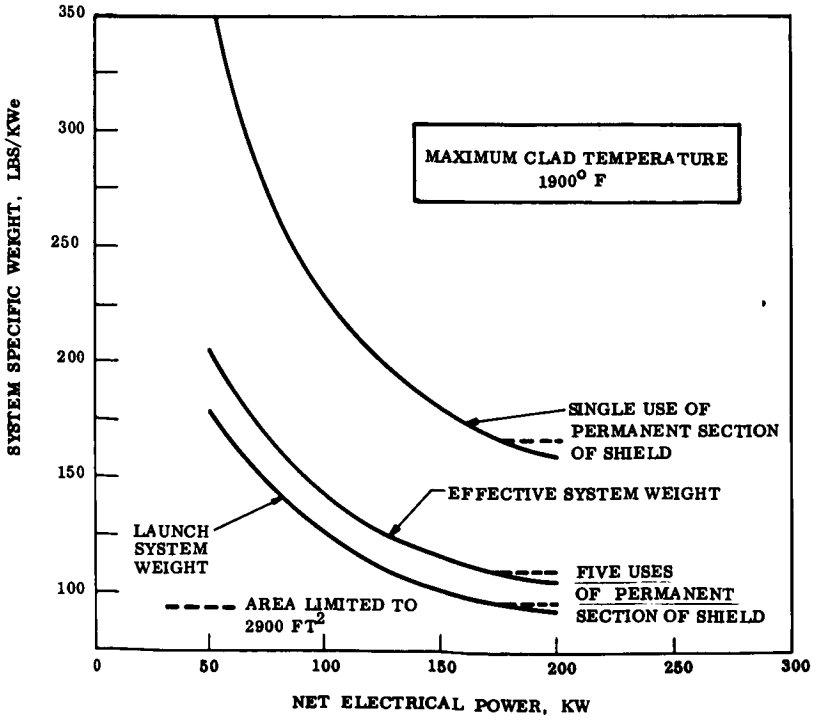

Figure 7-37. Summary of Performance of Brayton Cycle Powerplants for Use with Manned Space Station — Three Loop Systems, Dual Redundancy

A comparison of the weights of powerplants for use on manned space stations is shown in Figure 7-37. The upper line shows the total weight of a system optimized for a single use of the entire shield. The middle curve shows the effective weight of a powerplant optimized for the case when five powerplants (an original plus four replacements) are used with a single permanent section of the shield. The lower curve represents the launch weight of each of these replacement powerplants.

Table 7-3. Performance Summary

	Unmanned Scientific Probe Powerplants			Powerplants for Manned Space Station	
	1-Loop	2-Loop	3-Loop	Single Use of Shield Hub	Multiple Use of Shield Hub
Turbine Inlet Temperature, °F	2200	2200	1824*	1744*	1778*
Δ P/ P Recuperator (each side)	0.0055	0.0056	0.0034	0.0049	0.0046
Δ P/ P Radiator/Radiator Heat Exchanger	0.0215	0.0092	0.0057	0.0067	0.0062
Δ P/ P Piping	0.0066	0.0062	0.0060	0.0090	0.0066
Recuperator Effectiveness	0.92	0.89	0.92	0.91	0.90
Primary Heat Exchanger Effectiveness	-	-	0.94	0.81	0.86
Radiator Heat Exchanger Effectiveness	-	0.92	0.93	0.91	0.90

*Based on a 1900°F maximum cladding temperature (liquid metal cooled reactor)

**Five uses.

SECTION 8
SPACECRAFT POWERPLANT DESIGNS

Conceptual designs of Brayton cycle powerplants for two space applications are being examined in this study. They are:

a. A 150-KWe powerplant for application to a manned space station.
b. A 200-KWe powerplant for an unmanned planetary probe mission.

In both cases the designs are based on the use of fixed radiators. For the manned application, where shielding weight is a major design influence, selection of the compact liquid metal reactor heat source is indicated. Optimization studies also endorse a liquid metal heat rejection loop for this powerplant. By taking this approach, the savings achieved in cycle pressure loss and boundary layer temperature drop in the radiator tubes result in a five to ten percent reduction in area when compared to a corresponding gas radiator. This permits an increased system power rating to be packaged within the payload envelope of a given booster. Thus, the manned powerplant concept is a three loop, liquid-gas-liquid system. On the other hand, the unmanned system does not have the same sensitivity of shield weight to reactor volume; therefore, maximizing the turbine inlet temperature by using a gas cooled reactor is the indicated route to a minimum specific weight system. Although preliminary results show the liquid radiator to result in lighter system specific weights for this application also, it was decided to make the conceptual design a single-loop, all-gas system in order to embrace the design problems associated with a gas radiator. It was further recognized that the 10,000 hour prestart-up waiting period requirement for the unmanned system favors the gas radiator by eliminating the possibility of working fluid freeze-up.

8.1 SPACE STATION 150-KWe POWERPLANT

Integration of the nuclear Brayton cycle powerplant with a manned system is based on use of the three spoke space station illustrated by Figure 8-1. Since the station life is expected to be in the order of five years (probably much longer), and powerplant life is 10,000 hours,

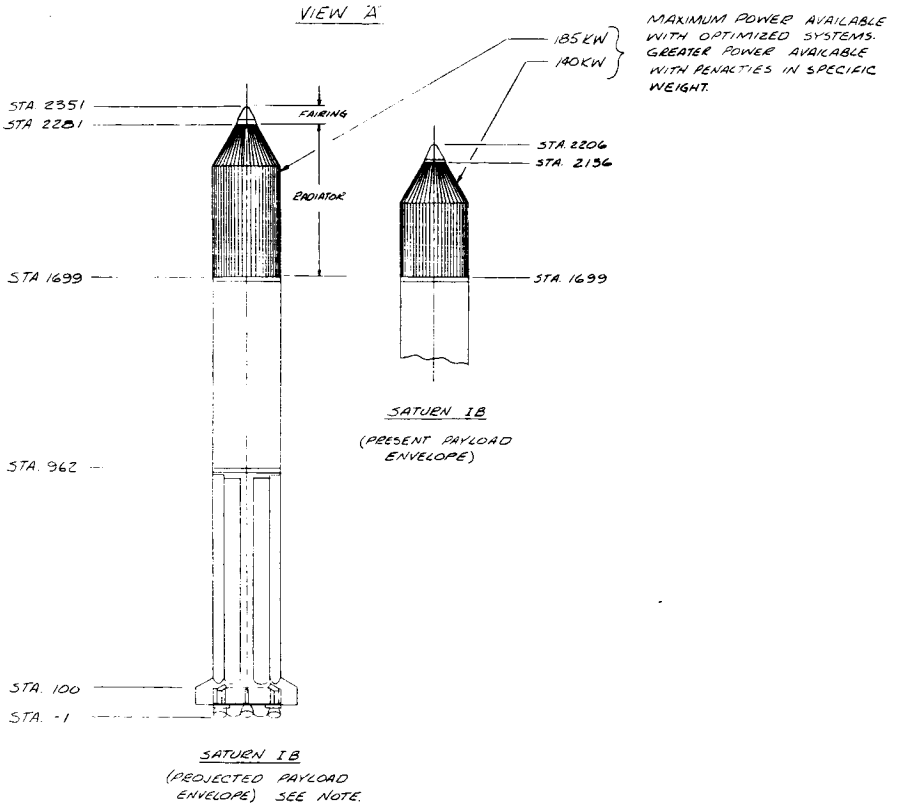

REFERENCE LAUNCH CONFIGURATION AND ASSEMBLY SEQUENCE FOR SPACE STATION NUCLEAR BRAYTON CYCLE POWERPLANT APPLICATION

Figure 8-1. Reference Launch Configuration and Assembly Sequence for Space Station Nuclear Brayton Cycle Powerplant

JETTISON FAIRING

?PLANT

WITH
ANENT
LD

VIEW "C"

EPLOY SPOKES

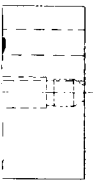

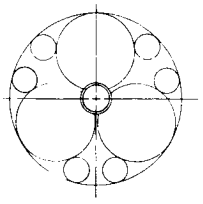

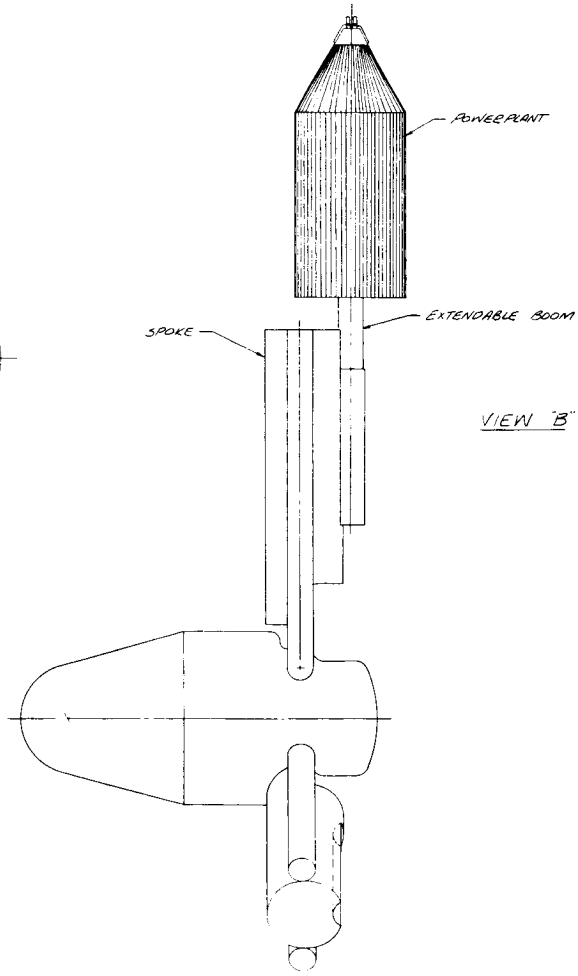

VIEW "B"

VIEW "D"

- EXTENDABLE BOOM

MANENT SECTION OF SHIELD

ATION SPOKE

ONS

FINAL ORBIT CONFIGURATION

(SPACE STATION WITH POWERPLANT)

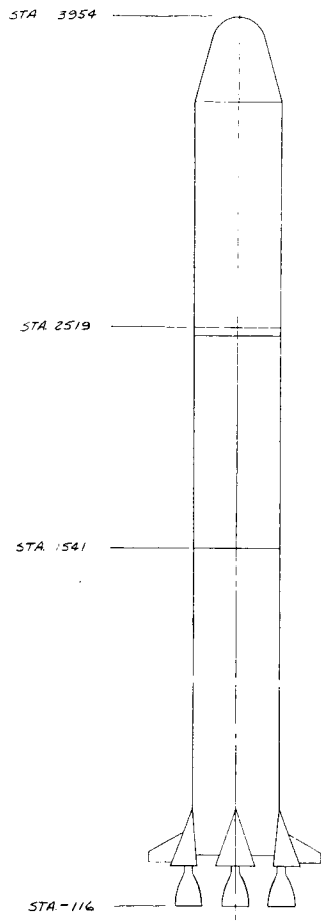

SATURN V

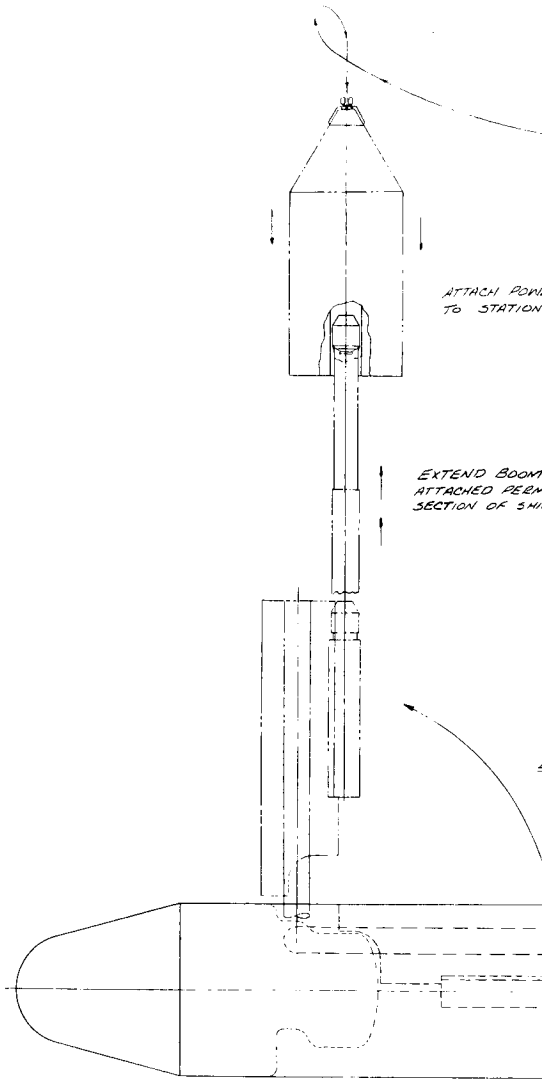

INITIAL ORBIT CONFIGURATIO
(SPACE STATION)

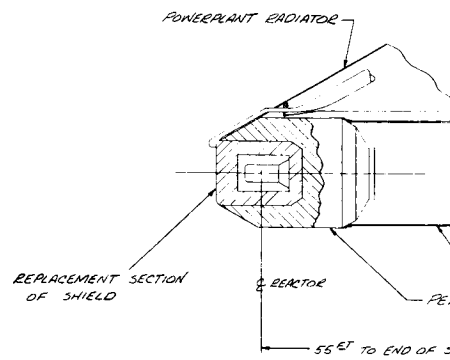

VIEW SHOWING SHIELD SEC
JOINED

rendezvous of replacement powerplants is a station requirement. In order to integrate the first powerplant in the initial launch, the radiator configuration for 150-KWe powerplant would have to be completely different from that of the replacement powerplants. This implies a large amount of duplication in the system development programs and also involves a degree of modification to the space station design. For these reasons, it was assumed that the more reasonable approach is to develop one powerplant for launch on the SATURN 1B booster and to rendezvous the first unit in the same manner as the replacement units. Beyond this, the more salient station requirements affecting the powerplant design are:

a. Maintenance logistics economics dictate that the bulk of the radiation shield be a permanent installation on the station and not replaced at the time of powerplant replacement.

b. Since primary loop components are an unacceptable high source of nuclear radiation, they must be separated and shielded from the remainder of the power conversion system, i.e., the reactor coolant must remain within the shield.

c. For increased reliability access to the power conversion system from the space station is required to permit maintenance. More specifically, the power conversion system is to be located in a sealed compartment which affords a "shirt-sleeve" environment.

d. To provide access to the power conversion equipment without passing around the reactor the powerplant should be located inboard of the reactor.

e. Except for the reactor and primary loop, reliability considerations dictate the use of two completely redundant power conversion systems.

The objective powerplant power rating is 150-KWe. Recognizing the squeeze resulting from area limitations with a fixed radiator design, two SATURN 1B alternatives were recognized. Maximum usable area of the SATURN 1B as presently defined is approximately 2200 square

feet. For the use with the SATURN V launch vehicle the SIVB stage can accommodate 2900 square feet of area. Applied to the SATURN 1B booster, use of this larger version of the SIVB stage requires structural modifications to the launch vehicle first stage. Since this is a reasonable possibility it was considered in the conceptual design study.

8.1.1 INTEGRATION WITH THE STATION

Figure 8-2 illustrates the radiation shield configuration and identifies the two separate portions and their mating interface. Composition of the shield is typically lithium hydride for neutron absorption with tungsten gamma shielding disposed in layers to absorb both primary and secondary gamma photons. The smaller portion of the shield completely encloses the reactor and incorporates a NaK-to-gas heat exchanger around itsexterior surface. All connective piping to the power conversion system is extracted through the forward end of the shield; in this way nothing crosses the interface between the shield sections. View D in Figure 8-1 shows the manner in which the shield is integrated into both the powerplant and the space station. View C shows the shield located at the terminal end of the powerplant mounting boom. As shown, the permanent part of the shield and the boom are integrated and launched with the space station.

View A shows the two powerplant sizes installed as payloads on the SATURN 1B booster. The larger one has a power level capability of 185-KWe and the smaller one has a capability of 140-KWe. In both cases the radiator is used as the aerodynamic fairing as well as the spacecraft structure. Protection of the nuclear reactor and shield during launch is achieved with a small expendable nose cap shroud. Following a separate launch, rendezvous of the powerplant with the station is achieved as illustrated in View C. A tubular structure within the radiator accommodates the extended powerplant mounting boom and the powerplant is slipped over it as illustrated.

8.1.2 POWERPLANT CONFIGURATION

The conceptual arrangement of the powerplant is shown in some detail in Figure 8-3. Since this work was conducted concurrently with the parametric study the size reflects an earlier

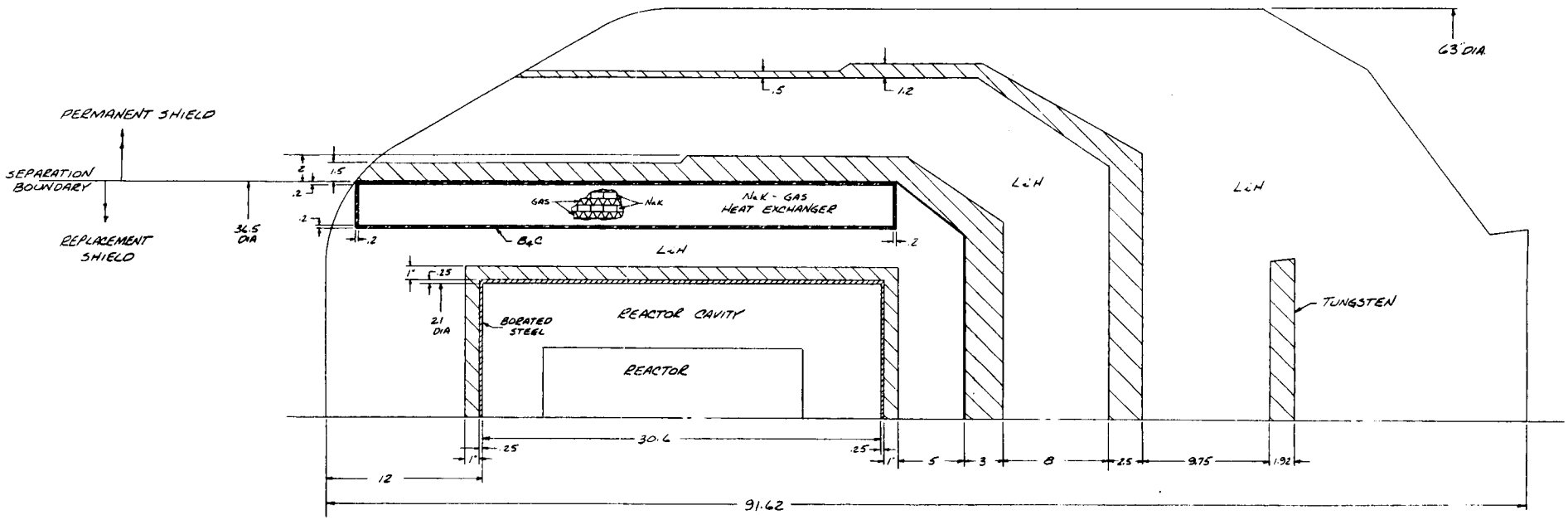

SHIELD CONFIGURATION FOR SPACE STATION NUCLEAR BRAYTON CYCLE POWERPLANT APPLICATION

Figure 8-2. Shield Configuration for Space Station Nuclear Brayton Cycle Powerplant Operation

estimate of the requirement to meet the 150-KWe power level objective. Later iterations show that this size will deliver 185-KWe without applying area-limited optimization to the radiator design. At this point in time it appears likely that the 150-KWe rating could reasonably be achieved with the standard SATURN 1B payload envelope and an area-limited optimum radiator. The effect of this change would be to shorten the cylindrical part of the radiator shown by about nine feet; this amounts to eliminating the lower bay.

Only one liquid metal reactor choice was furnished in the contract work statement and this was the one used for the space station powerplant application. The core employs uranium carbide, refractory metal clad, pin-type fuel elements with a maximum clad temperature of 1900^{o}F. The compact size of this reactor effects substantial savings in the weight of the nuclear radiation shield. As shown in Figure 8-3 the reactor shield assembly is mounted at the extreme end of the conical portion of the radiator. This is the optimum location from a shielding economy viewpoint. Section A-A shows the details of the piping arrangement concept in the vicinity of the reactor. To eliminate radiation streaming the large size gas lines to the "in-shield" primary loop heat exchanger are flattened in cross-section as they pass around the station shield support cone. All of the primary loop pumps are mounted at the extreme top end of the shield to prevent their radiating to the space station.

A tubular column connects to the station shield support cone and runs along the axis of the powerplant. This column terminates flush with the radiator base plane which is used as the secondary radiating surface providing heat rejection for the power conversion equipment. Structural support for the tube at the large diameter end of the radiator is provided by a conical shell as shown in Figure 8-3.

The conical portion of the radiator and the first cylindrical bay form the outer wall of the power conversion equipment packaging compartment. A domed pressure bulkhead mounted radially between the radiator and the central column forms its base and the inner wall is formed by the column itself. This compartment can be pressurized permitting space station personnel to service the equipment. It is visualized that the space between the radiator tubular column and the station boom could accommodate a number of pressurizable seals of

the "O" ring type mounted above and below a pair of sealed doors in the walls of the concentric cylinders. Prior to pressurizing the equipment compartment, the seals would be inflated permitting the doors to be opened without loss of pressure either from the boom or the compartment.

General arrangement of the two power conversion units and their associated piping is illustrated in Figure 8-3. Section B-B shows the mounting locations on either side of the access column. The units are identical and consist of a radial flow turbo-compressor on one shaft followed in line by an axial flow turbo-alternator. The exhaust gas stream makes a right angle bend to leave the second turbine. In this way, the alternator is sealed into the gas environment but occupies a dead-end corner. This turbo-machinery is based on solar Brayton cycle equipment under development for NASA-Lewis.

TABLE 8-1. WEIGHT SUMMARY OF A 150-KWe BRAYTON CYCLE POWERPLANT FOR USE WITH A MANNED SPACE STATION

Item	Number of Powerplants/Shield Hub Use	
	1	5
Reactor, Shield, and Power Conversion Loop Equipment**	16,365	7,995*
Radiator Heat Exchanger**	845	745
Piping**	740	870
Primary Radiator***	7,355	6,535
Secondary Radiator	450	450
	25,755 lbs.	16,595 lbs.
Specific Weight	171.7 lbs/KWe	110.6 lbs/KWe

*Effective shield weight included
Total shield weight 14,705 lbs.
Replacement shield weight 2,205 lbs.
**Total for 2 sets
***Single set of fins, double set of tubes, headers, and feeds

Redundancy in the primary radiator is provided for a minor weight penalty by using a two-loop common fin design. Since each power conversion system is capable of meeting the full load requirements, only one system need operate at any given time. By designing one radiator to satisfy this condition the redundant radiator can be obtained by adding an additional set of tubes along the fin mid-span locations and providing the appropriate additional header and feed circuit. Typical header arrangements are denoted in Views C and D. View E shows the conceptual arrangement of the booster interface joint at the base of the radiator. Included are the primary headers, the secondary headers, the support cone, and a V-band clamp. Structural requirements have not yet been fully evaluated; however, it is apparent that the secondary radiator will require some arrangement of radial and circumferential beams to resist the inertial loads occurring during launch. Table 8-1 gives a preliminary weight breakdown for 150 KWe Brayton Cycle powerplant for use with a Manned Space Station.

8.2 UNMANNED 200-KWe POWERPLANT

To represent the unmanned nuclear Brayton cycle application, the Saturn Orbiter I mission described in GE Document No. 64SD505 (Mission Analysis Topical Report) was selected. In this case the power developed is used for electric propulsion. The nuclear-electric spacecraft is a payload for the three stage SATURN V launch vehicle. As with the manned application, the conceptual design as shown in Figure 8-4 has the maximum allowable radiator area of 2900 square feet. Optimization of the cycle parameters show that this area will accommodate approximately 350-KWe. However, a rating of 200-KWe was selected for the reference design since this more closely matches the optimum size at the specific weights achieved in the Brayton cycle powerplants (approximately 70 lbs/KWe). The actual radiator area required is only 1600 square feet; hence, the reference system would be approximately 19 feet shorter than the illustration. This amounts to removal of the bottom two radiator bays. A significant additional weight saving can be achieved by changing to an all conical radiator configuration. This almost eliminates the scatter shield and results in a savings of over 1000 pounds.

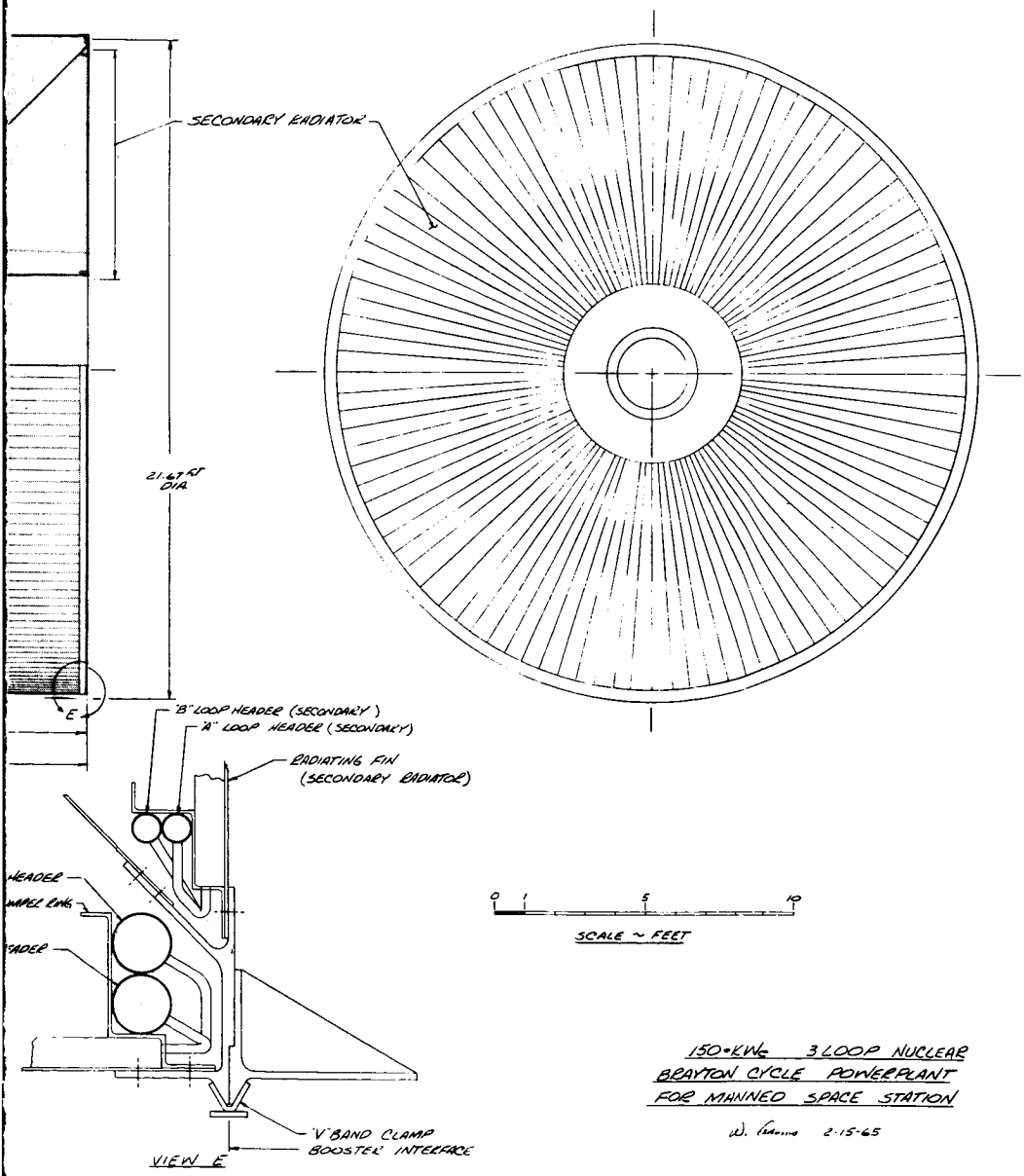

Figure 8-3. 150 KWe, Three Loop, Nuclear Brayton Cycle Powerplant for Manned Space Station

— REACTOR LOOP NaK PUMPS (4)

— REFLECTOR CONTROL MOTORS (8)

— HEAT EXCHANGER REACTOR LOOP

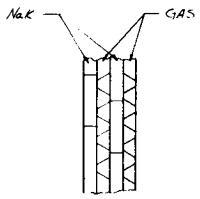

SECTION G-G
(SHOWING ALTERNATING LAYERS OF HEAT EXCHANGER)

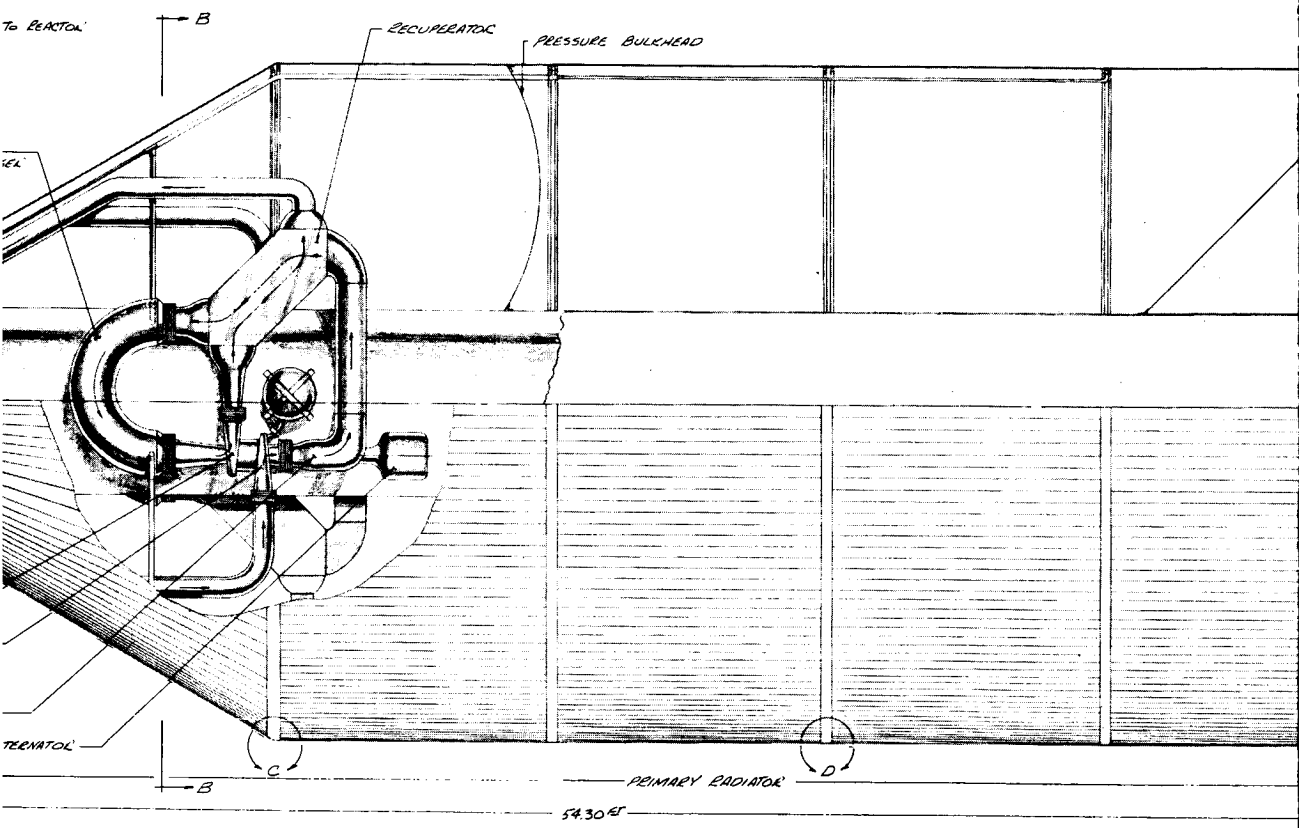

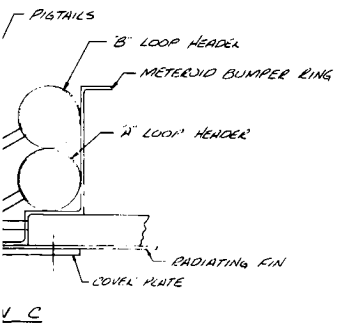

V C

INSULATION BLANKET COVERING INSIDE SURFACE OF PRIMARY & SECONDARY RADIATORS AND POWER CONVERSION SYSTEM COMPONENTS.

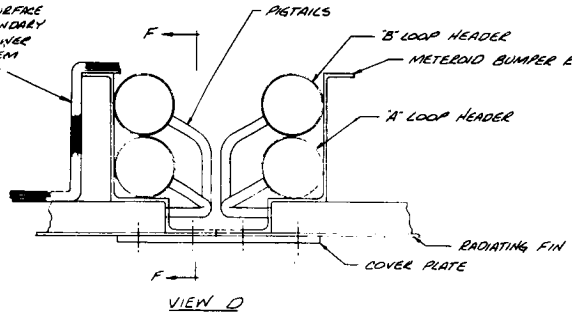

VIEW D

"B" LOOP
METEROID BU
"A" LOOP HE

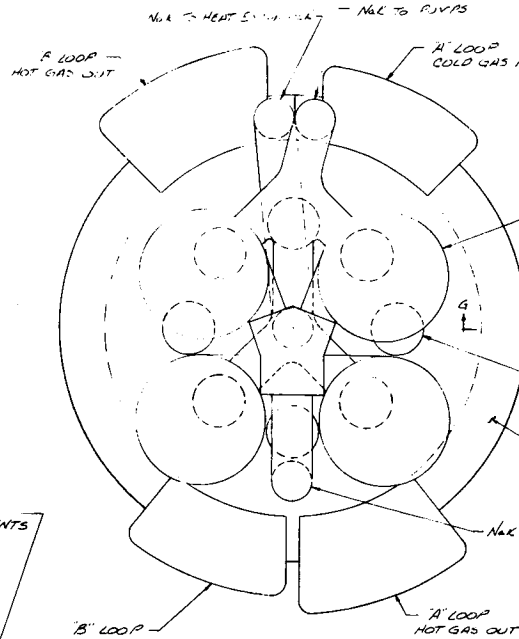

SECTION A-A

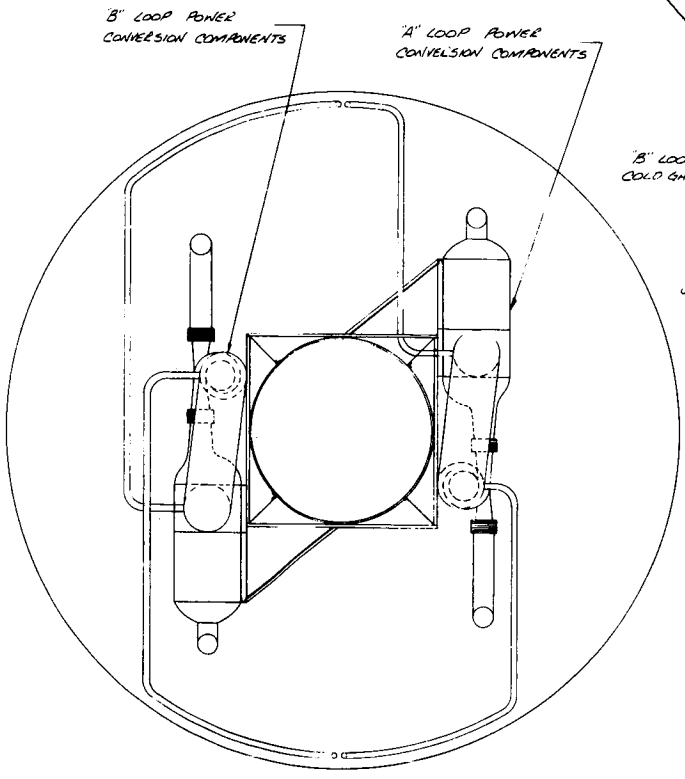

SECTION B-B

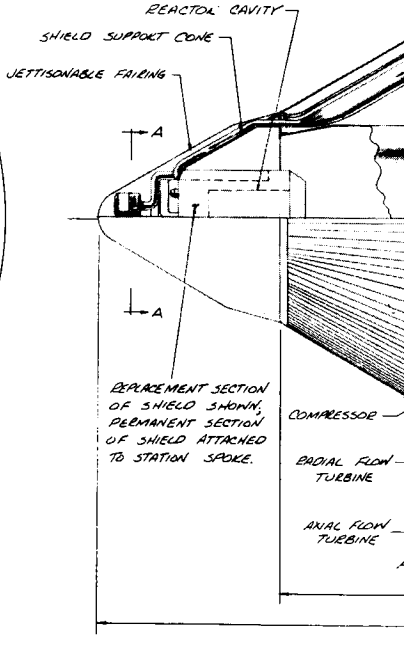

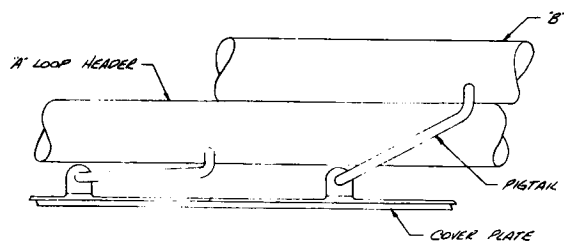

SECTION F-F

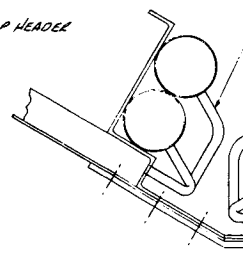

VIE

General arrangement of the vehicle consists of a 21.4-foot cylindrical section capped by a 20-degree cone with a combined over-all length of 54.3 feet. The gas-cooled reactor and shield assembly is mounted to the conical radiator shell. Reactor control drum actuator rods pass through the shield to the drive motors mounted on a support structure aft of the shield as illustrated in Sections B-B and C-C of Figure 8-4. The working fluid is transported to and from the reactor by means of rectangular ducts which pass around the shield and enter the vehicle through the secondary radiator. During launch the reactor is covered by a split fairing which is contoured to enclose these gas lines.

A single power conversion unit is mounted on an open framework supported by struts terminating at a radiator header support ring. Cooling for the alternator and reactor controls is provided by a 140-square foot radiator which occupies the uppermost bay of the conical section and rejects 28 KW. The remaining surface area on the conical portion of the vehicle and the entire cylindrical surface area are used for rejection of waste heat from the power conversion cycle. To simplify the feed-line network and thereby reduce the associated weight and pumping losses, headers spanning one-half the vehicle circumference are used. Feed-lines run parallel to the longitudinal axis of the vehicle along the inner radiator surface and are supported at each header ring. Differential thermal expansion along the axis of the feed lines is accommodated by a bellows section at each header intersection. To minimize pressure losses and maintain alignment, the joints include an internal sleeve. Meteoroid protection for feed lines and headers is provided by means of thin walled bumpers. To control the interchange of thermal energy, radiation shielding and/or a low emissivity coating are used on the inner surfaces of the radiators and the power conversion system components.

Payload systems, attitude control, and power conditioning equipment are packaged in the conical section of the deployable payload module. Landing capsules with umbilical connections for internal cooling and electrical power are mounted in a central tube. This tube is insulated and in critical areas it is jacketed by an active cooling loop to maintain the temperatures required for the payload equipment. Low temperature radiators for payload cooling are located on the flat portions of the deployable module.

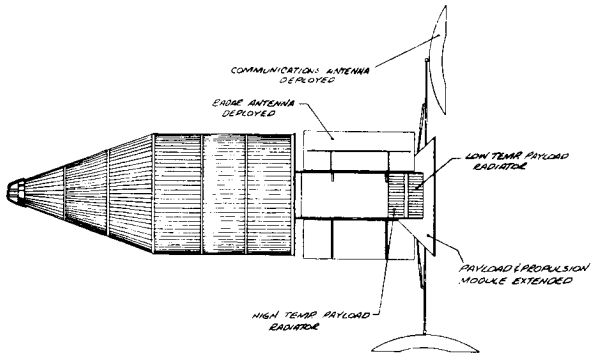

DEPLOYED CONFIGURATION

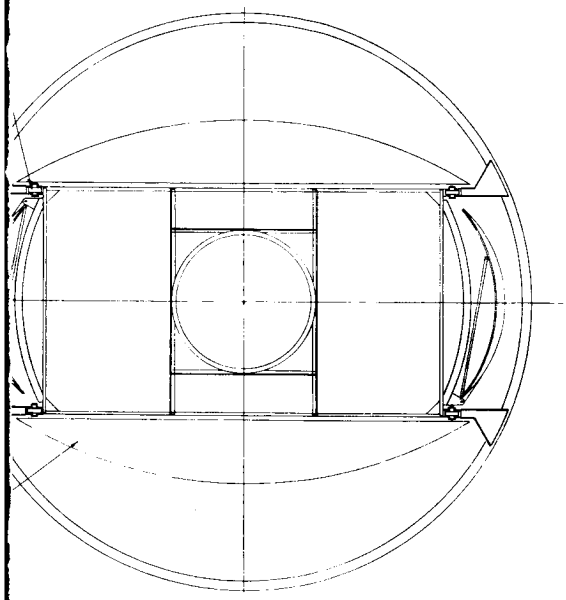

SECTION E-E

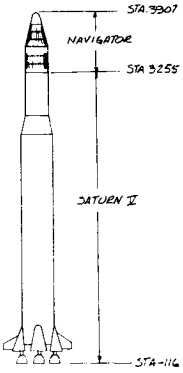

LAUNCH CONFIGURATION

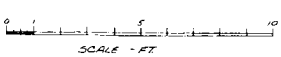

Figure 8-4. 200 KWe, Single Loop, Nuclear Brayton Cycle Powered Navigator Spacecraft

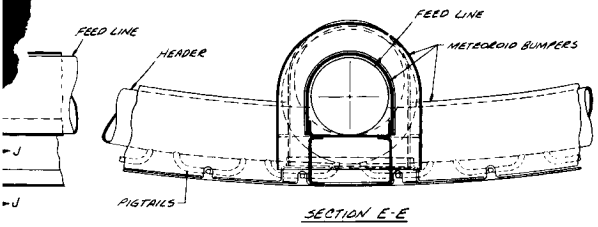

SECTION E-E

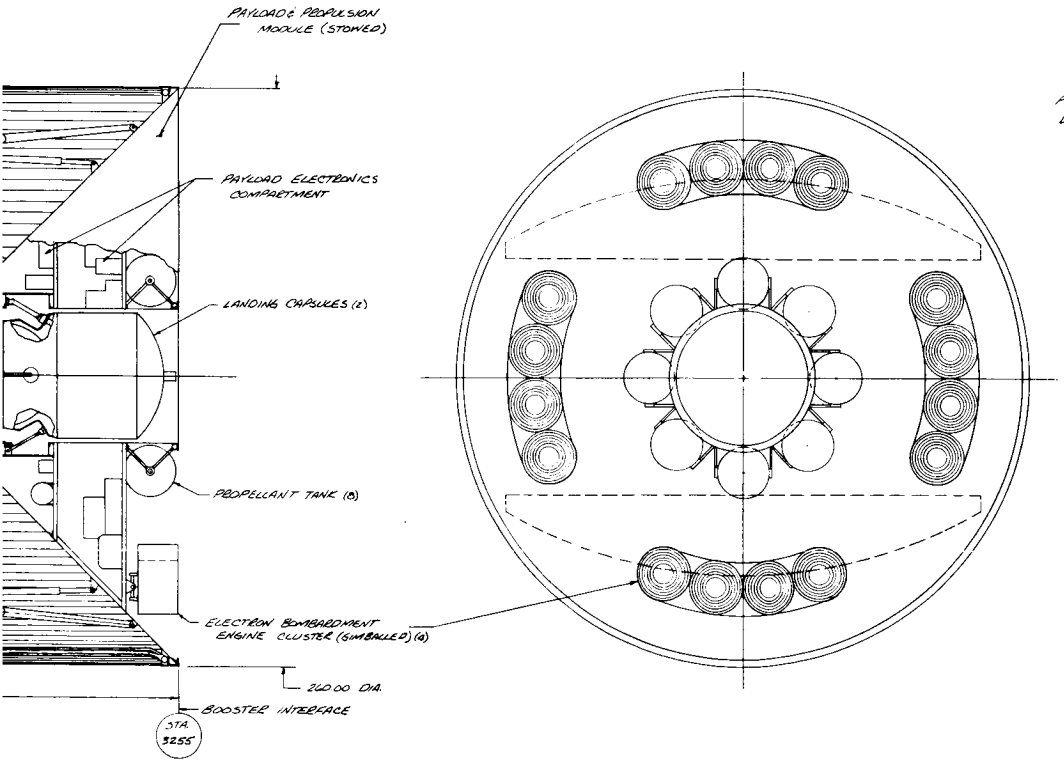

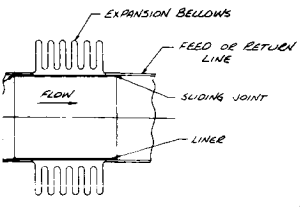

SECTION H-H

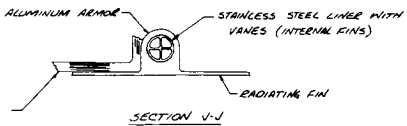

SECTION J-J

INSULATION BLANKET COVERING INSIDE SURFACE OF PRIMARY & SECONDARY RADIATORS AND POWER CONVERSION SYSTEM COMPONENTS

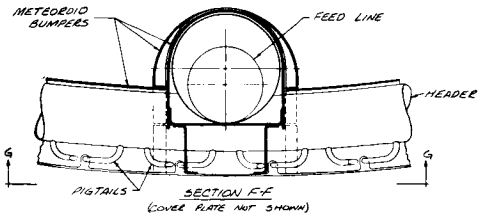

SECTION F-F
(COVER PLATE NOT SHOWN)

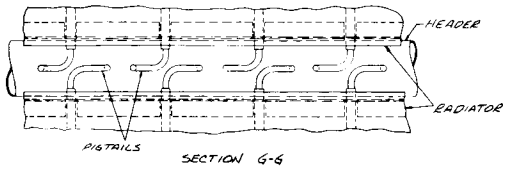

SECTION G-G

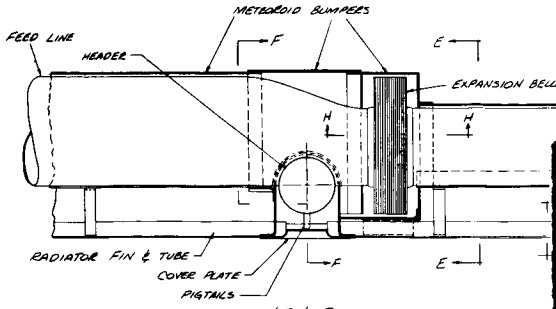

VIEW D

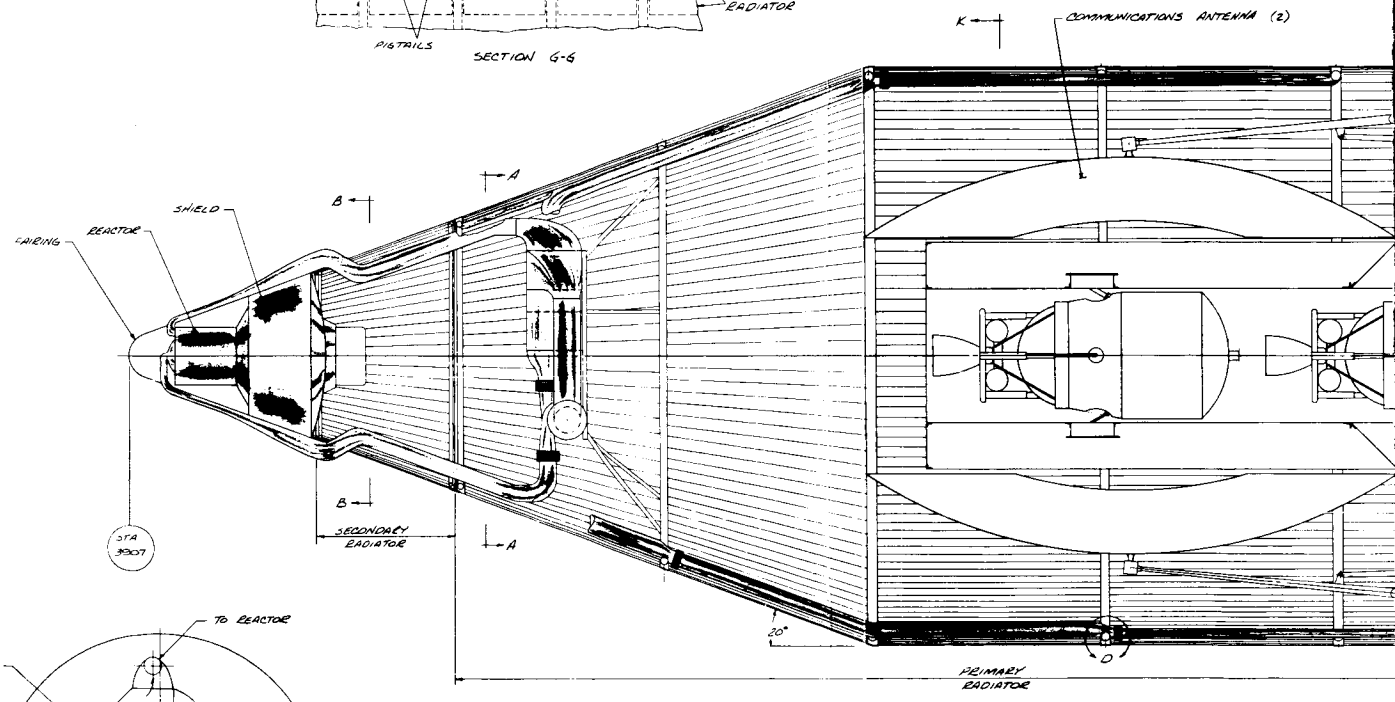

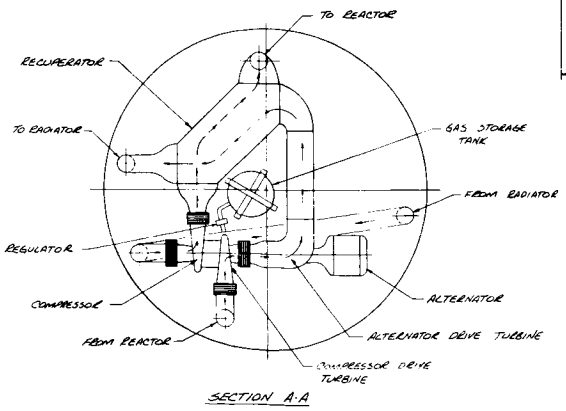

SECTION A-A
(POWER CONVERSION SYSTEM)

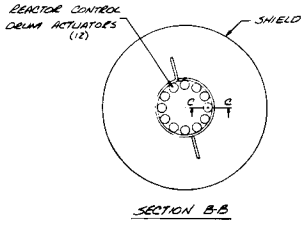

SECTION B-B

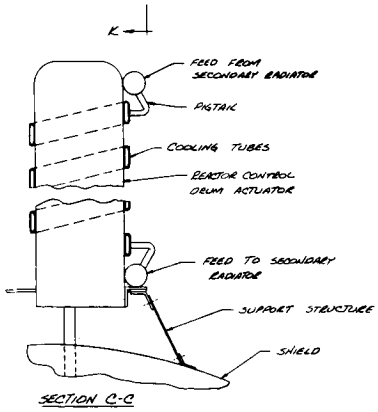

SECTION C-C
(SHOWING COOLING TUBES)

Two modified 20-foot diameter rigid dish parabolic antennas are included for long range communications. The antennas are secured to the payload module during launch and extended to operating position by telescoping arms after deployment of the module. Two rectangular radar mapping antennas have also been incorporated in this design.

Electric engines are arranged in four clusters of four engines each and cluster gimballing is provided to allow thrust vectoring. Propellant storage tanks are located around the central tube adjacent to the electric engines. The small inset in the upper right hand corner of the Figure 8-4 illustrates the deployed configuration of this spacecraft design concept. View D and Sections E-E, F-F, and G-G illustrate the conceptual details of the header and feed-line connections and bumper protection arrangements.

Table 8-2 gives a preliminary weight breakdown for this vehicle concept. As noted in the tabulation, the radiator weights reflect the actual sizes required to deliver the 200-KWe rated power.

TABLE 8-2. 200-KWe TURBOELECTRIC VEHICLE WEIGHT SUMMARY*

Powerplant	
Reactor, Shield, and Power Conversion Equipment	9978
Primary Radiator (1630 Ft^2)	5322
Secondary Radiator (140 Ft^2)***	300
	15,600 Lbs.
Propulsion System	
Power Conditioning and Bus Bars	300
Thrustors	400
Propellant and Tankage	15,785
	16,485
Payload Systems**	
Landing Capsule	2670
Mapping Radar	2000
Sensors, TV, and Radar Altimeter	430
Communications Transmitter	3000
Antennas	700
Computers, Recorders, and Receivers	125
Payload Cooling System	910
	9835 Lbs.
Spacecraft	
Navigation, Guidance, and Attitude Control	1350
Payload Support Structure	980
Tank Support Structure	750
	3080 Lbs.
Spacecraft Initial Flight Weight	45,000 Lbs.

*Net electrical power to the electric thrustor power rectifier and space vehicle load is 200 KWe, yielding a shielded powerplant specific weight of 78.0 lbs/KWe

**Payload weights are based on Saturn Orbiter I mission described in GE Document No. 64SD505 (Mission Analysis Topical Report).

***Based on an 88% efficient alternator and cooling requirements for pump-motors. Maximum temperature of coolant loop fluid, 400°F.

APPENDIX A. MINIMUM RADIATOR AREA REQUIREMENTS

The minimum radiator area requirements for Brayton cycle powerplants are shown in Figures A-2 through A-5. Figure A-1 shows the temperature-entropy diagram for the cycle. Process 1-2 is compression of the cool gas, 2-3 is heat addition in the recuperator, 3-4 heat addition in the reactor, 4-5 is expansion in the turbine, 5-6 is heat rejection in the recuperator, and 6-1 is the heat rejection in the radiator. Process 6'-1' is the heat rejection from the radiator surface including film drops. The graphs shown were drawn for systems with a recuperator effectiveness of 0.90. The minimum areas are different for systems with different effectivenesses; however, in the range of effectivenesses between 0.70 and 0.95, these variations are not large. The derivatives of the slopes of Figures A-2 through A-5 are shown in Figures A-6 through A-13 and represent influence coefficients which can be used to evaluate effects of changes of system specifications on minimum area requirements. Each point of minimum area represents an optimization with respect to both pressure ratio and radiator discharge temperature.

Results are shown for no temperature drop between the gas and the radiating surface and a case with a somewhat generous temperature drop. The ratio of temperature drops at radiator inlet and exit were selected to be in general agreement with the ratio of heat fluxes for typical cases. The results are plotted as functions of both turbine inlet temperature and the ratio of turbine to compressor pressure ratios. The curves do not contain the point at 1400 ^{o}F and 14% pressure loss since such a cycle would not operate at positive efficiencies at reasonable radiator discharge temperatures.

The influence of both turbine inlet temperature and pressure loss are large; and become more important at low turbine inlet temperatures and high pressure losses, where the cycle net power is a small fraction of the shaft power transmitted from the turbine to the compressor. At turbine inlet temperatures above 1700 ^{o}F and pressure losses below 10% the minimum radiator area requirements become less sensitive to cycle conditions.

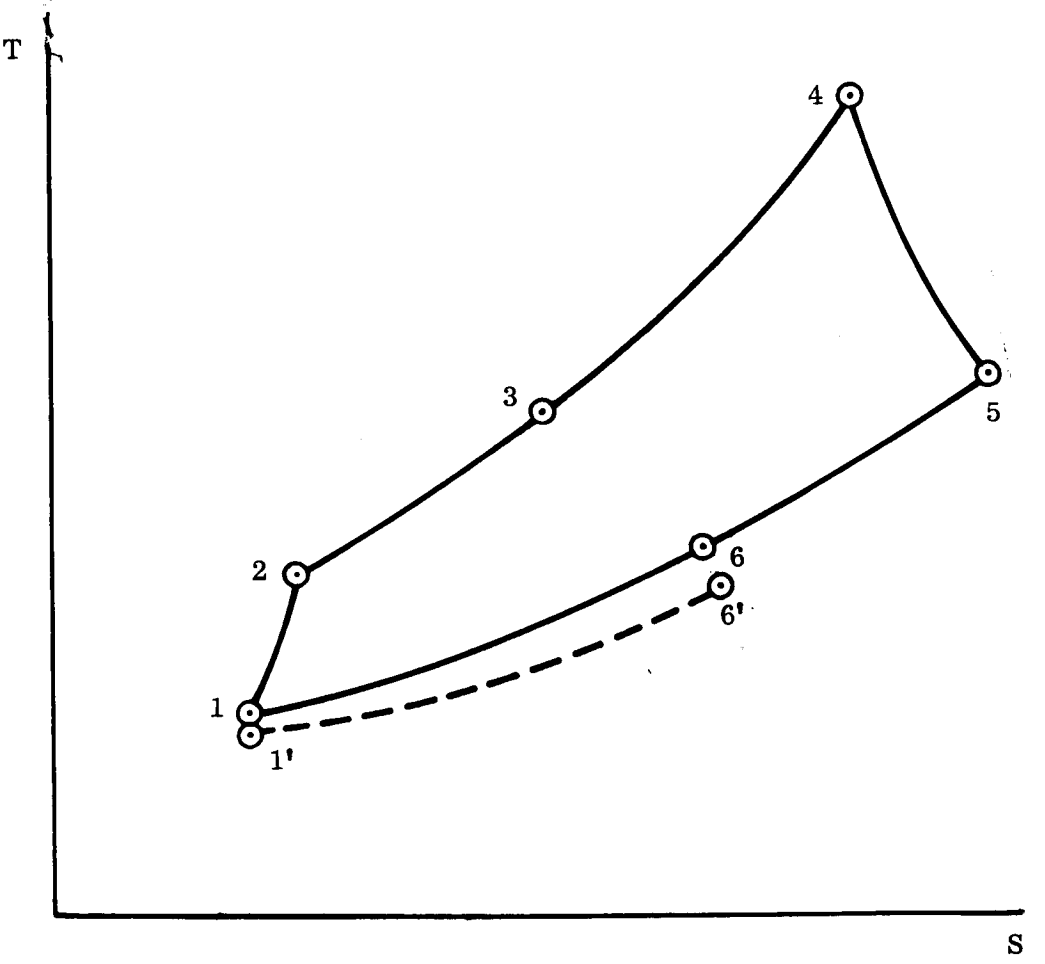

Figure A-1. Brayton Cycle Temperature - Entropy Diagram

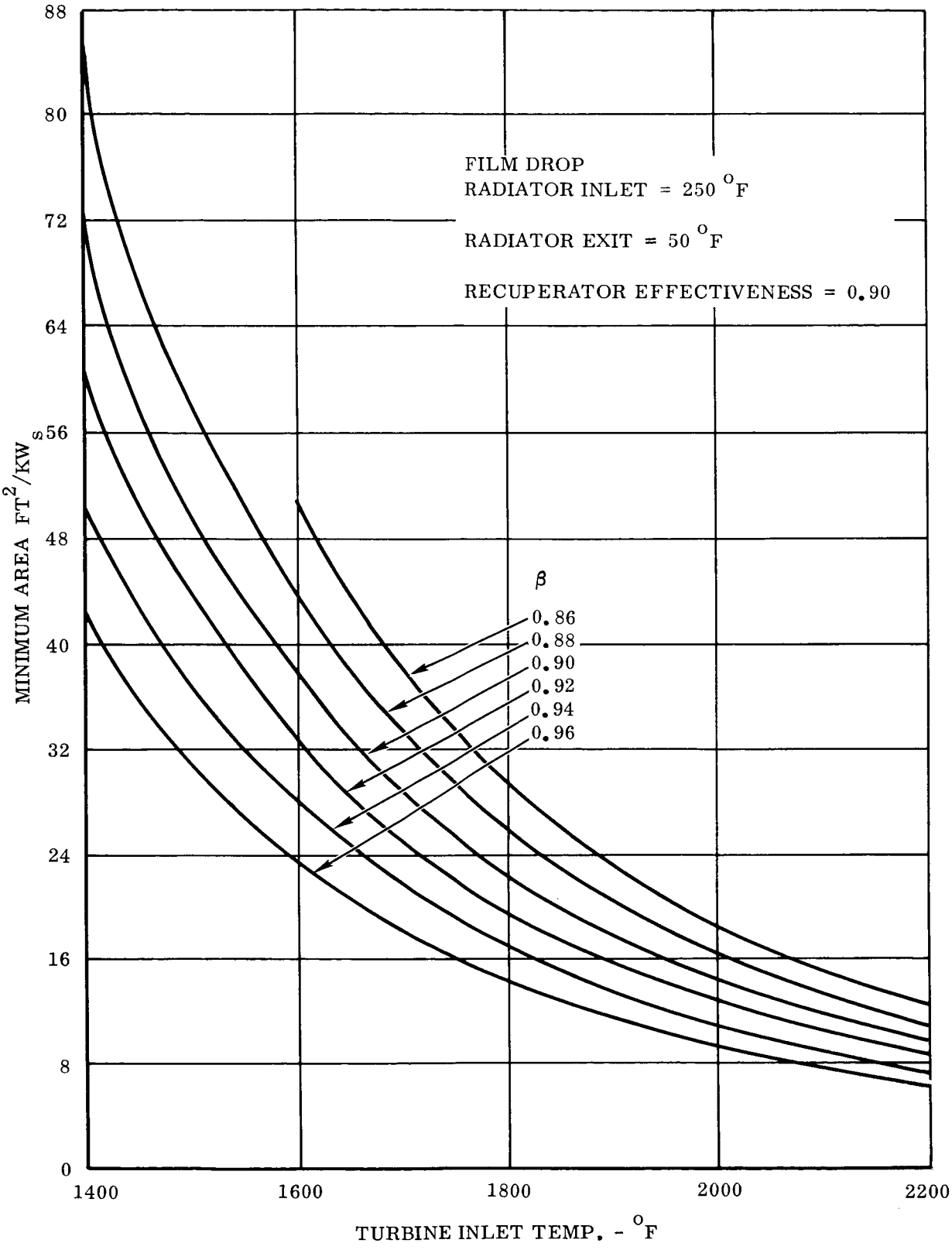

Figure A-2. Minimum Radiator Area Versus Turbine Inlet Temperature

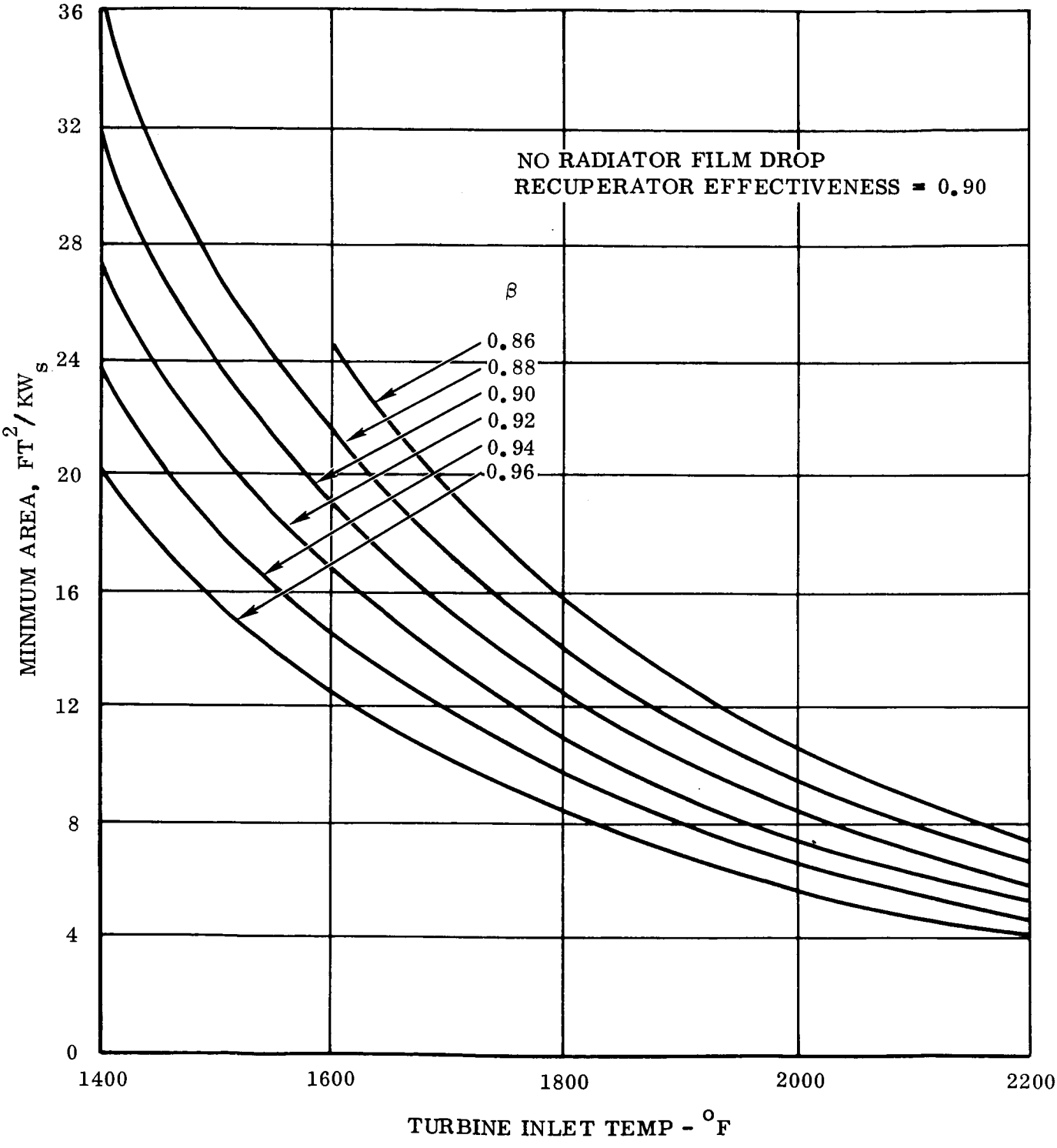

Figure A-3. Minimum Radiator Area Versus Turbine Inlet Temperature

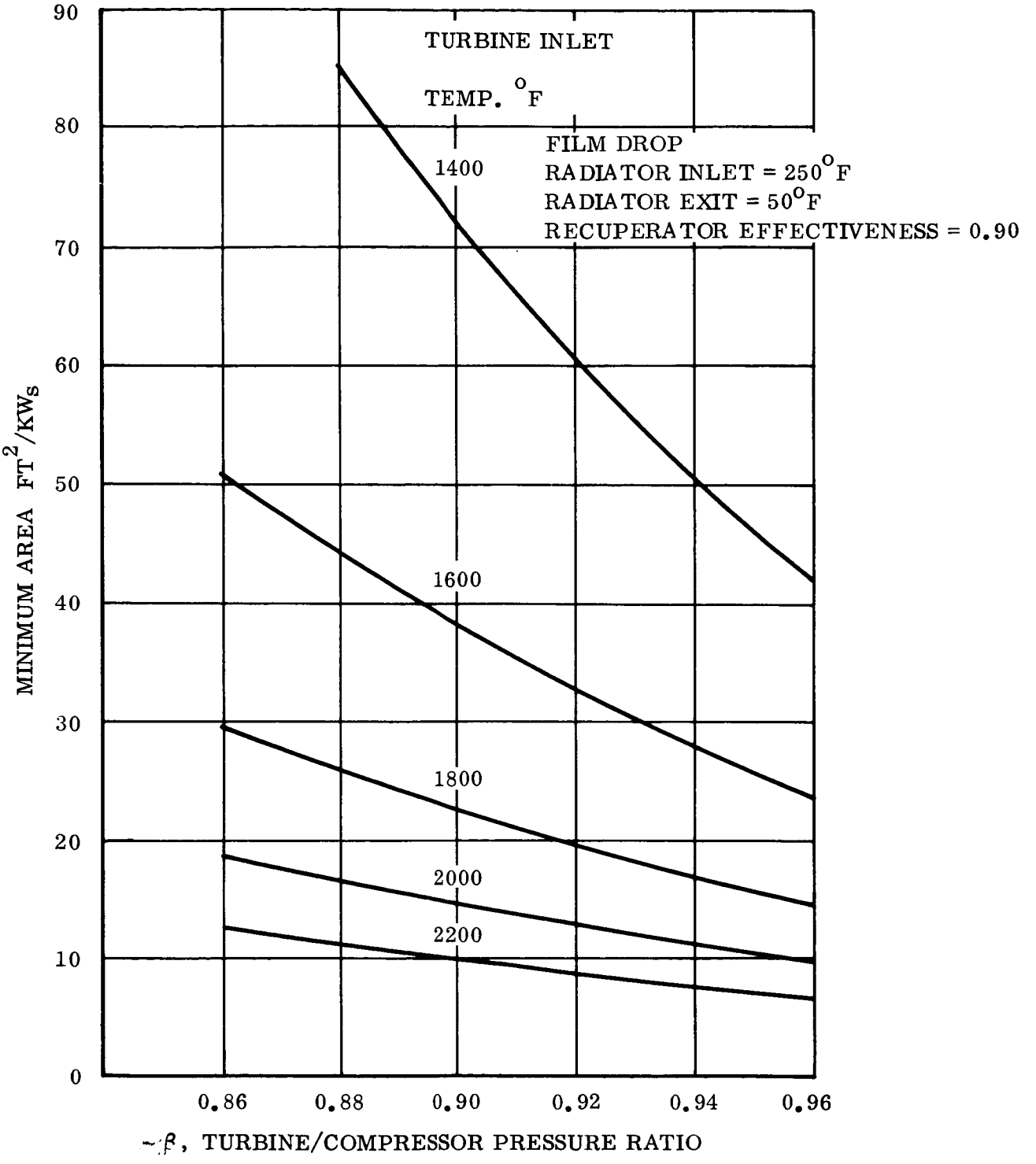

Figure A-4. Minimum Radiator Area Versus Turbine/Compressor Pressure Ratio

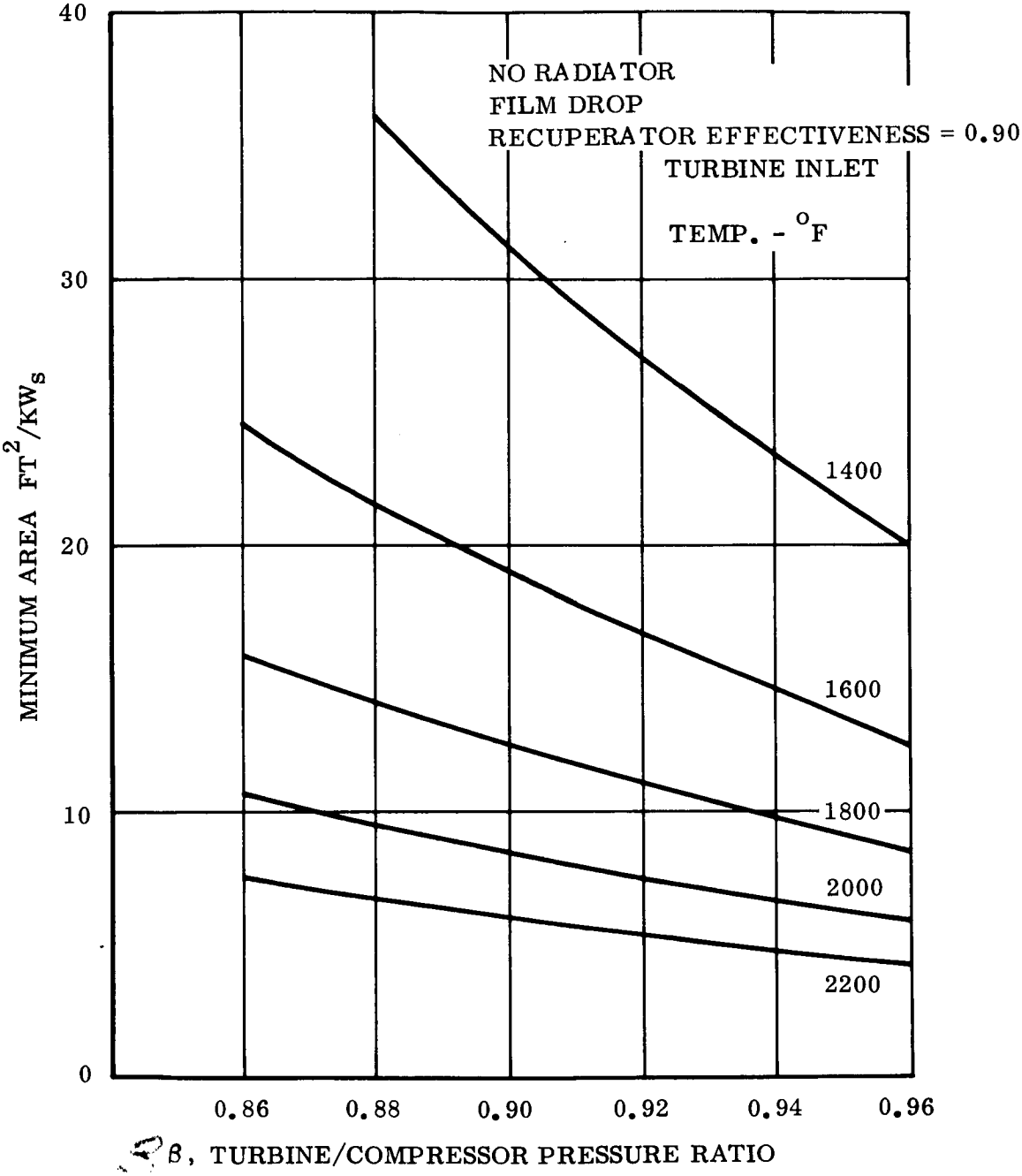

Figure A-5. Minimum Radiator Area Versus Turbine/Compressor Pressure Ratio

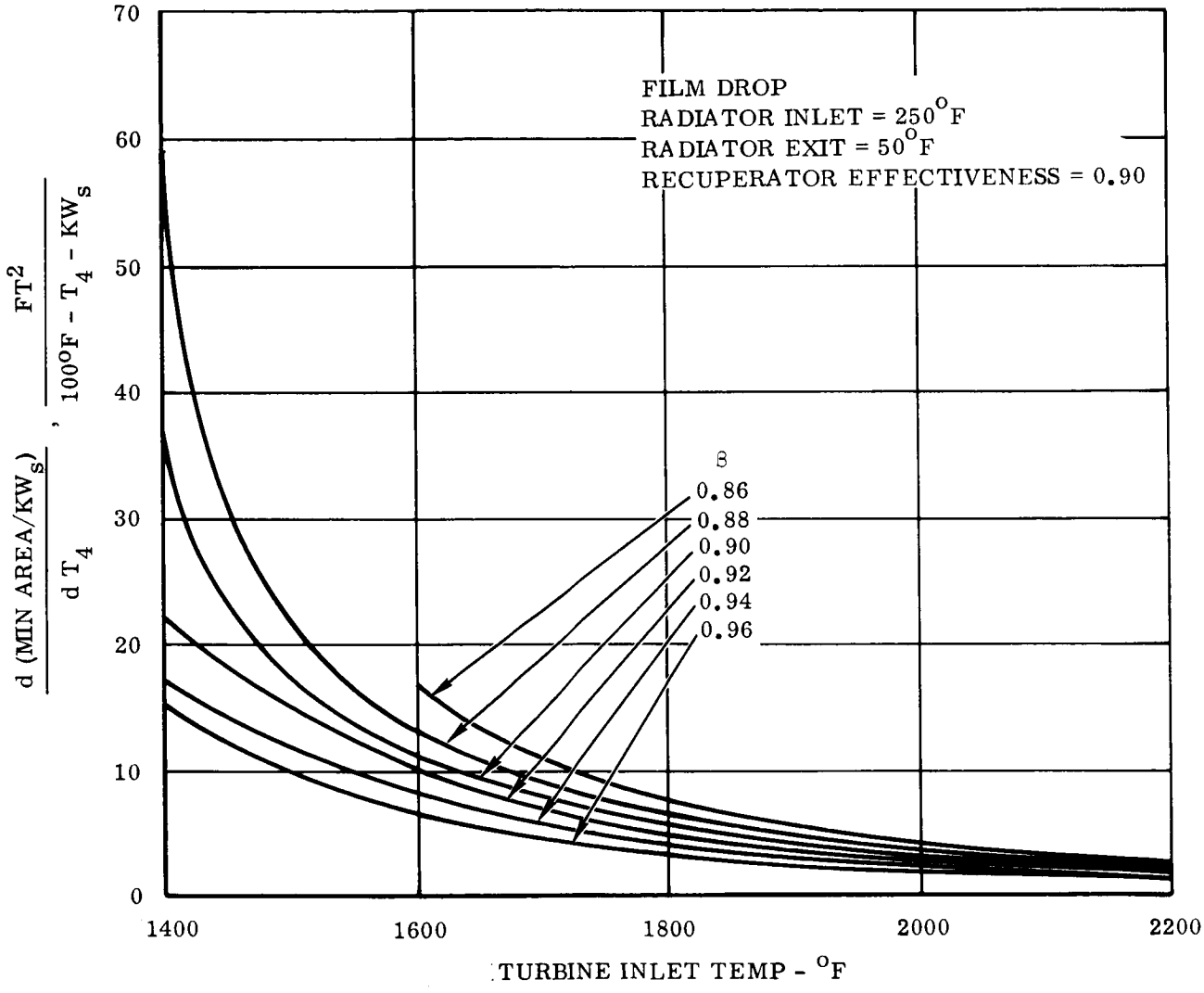

Figure A-6. $\frac{d\,(\text{Min. AREA}/KW_s)}{d\,T_4}$ Versus Turbine Inlet Temperature

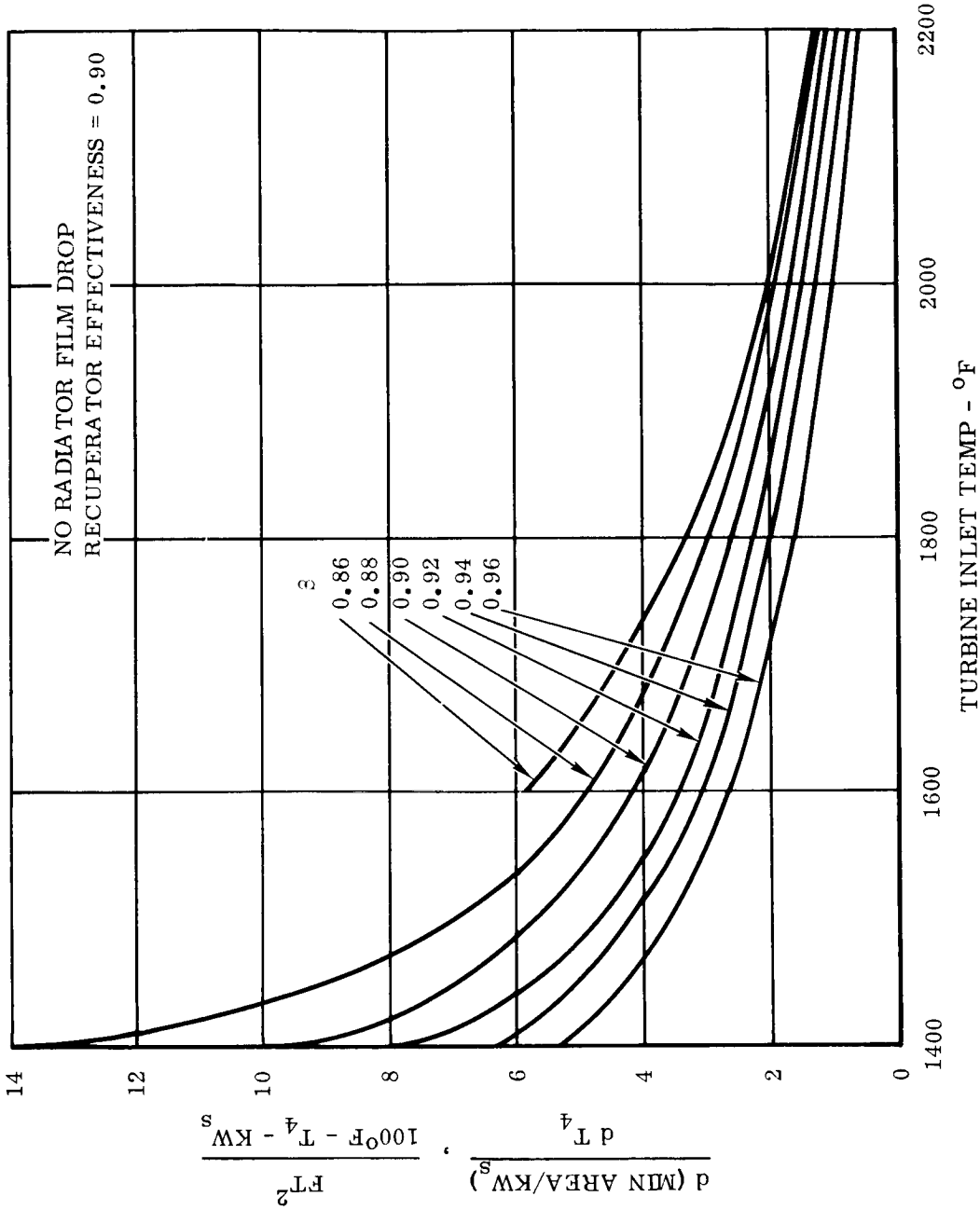

Figure A-7. $\frac{d\ (\text{Min. AREA/KW}_s)}{d\ T_4}$ Versus Turbine Inlet Temperature

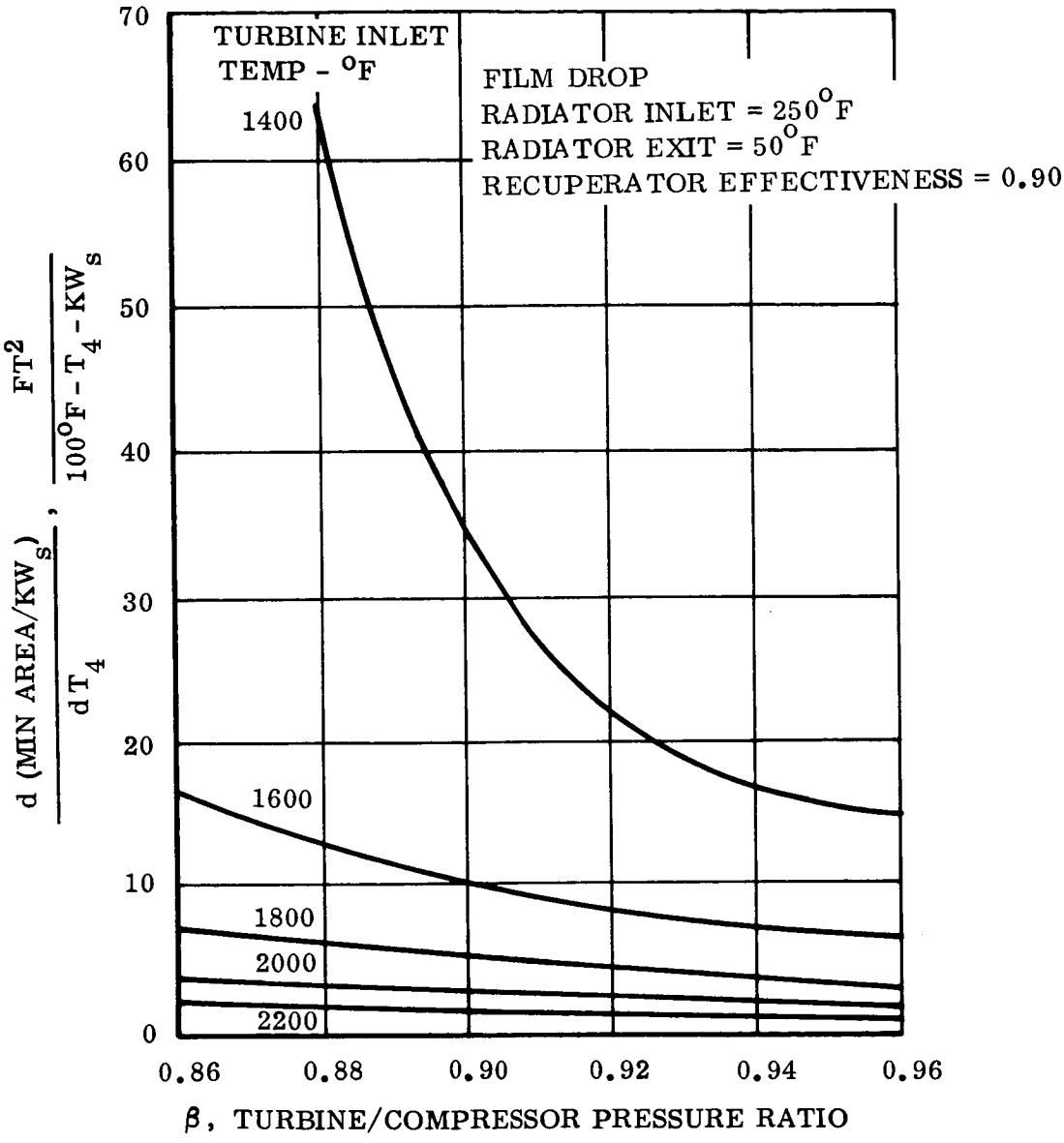

Figure A-8. $\frac{d(\text{Min. AREA/KW}_s)}{d\,T_4}$ Versus Turbine/Compressor Pressure Ratio

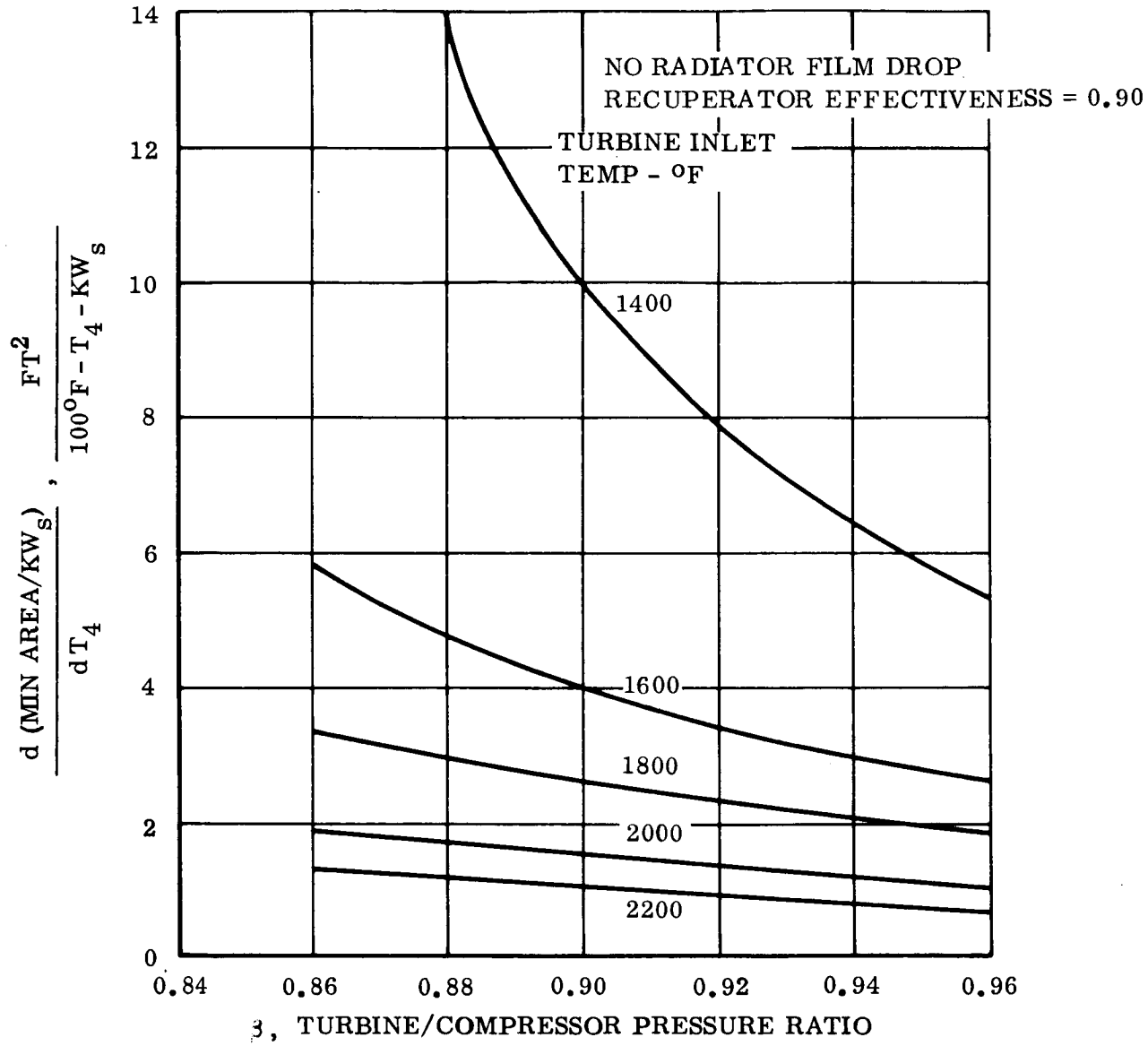

Figure A-9. $\frac{d\,(\text{Min. AREA/KW}_s)}{d\,T_4}$ Versus Turbine/Compressor Pressure Ratio

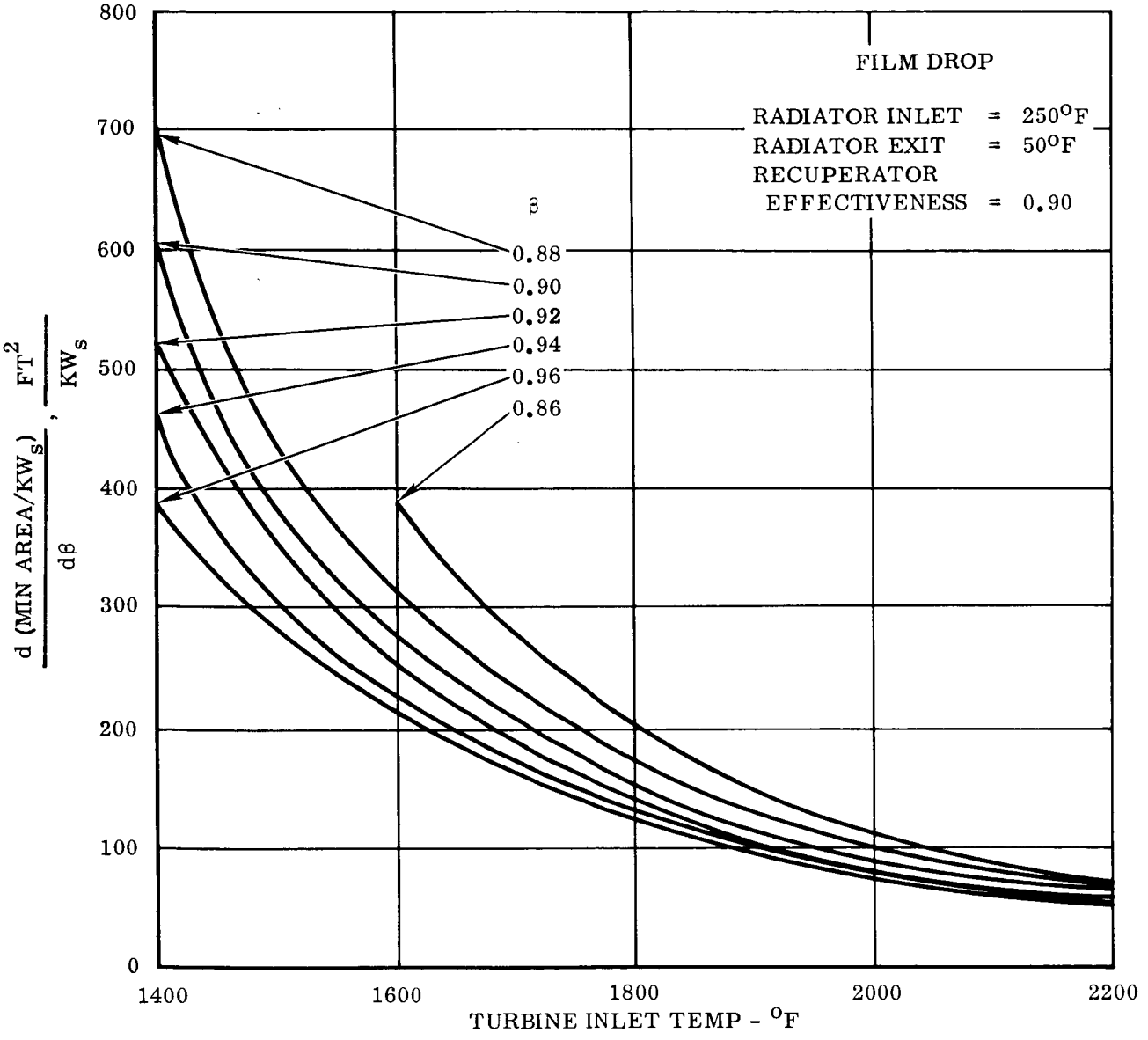

Figure A-10. $\frac{d\ (\text{Min. AREA/KW}_s)}{d\ \beta}$ Versus Turbine Inlet Temperature

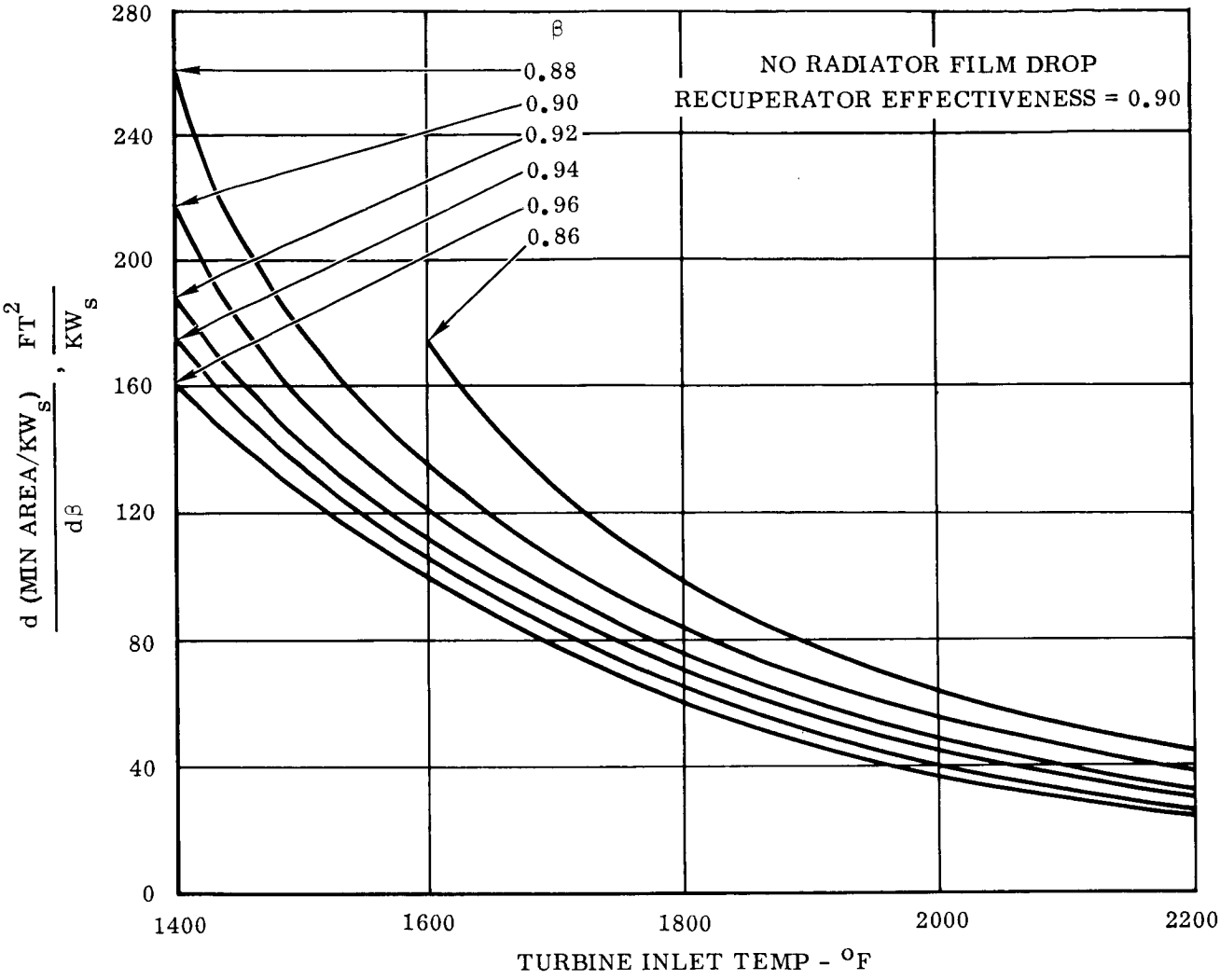

Figure A-11. $\frac{d\ (\text{Min. AREA/KW}_s)}{d\ \beta}$ Versus Turbine Inlet Temperature

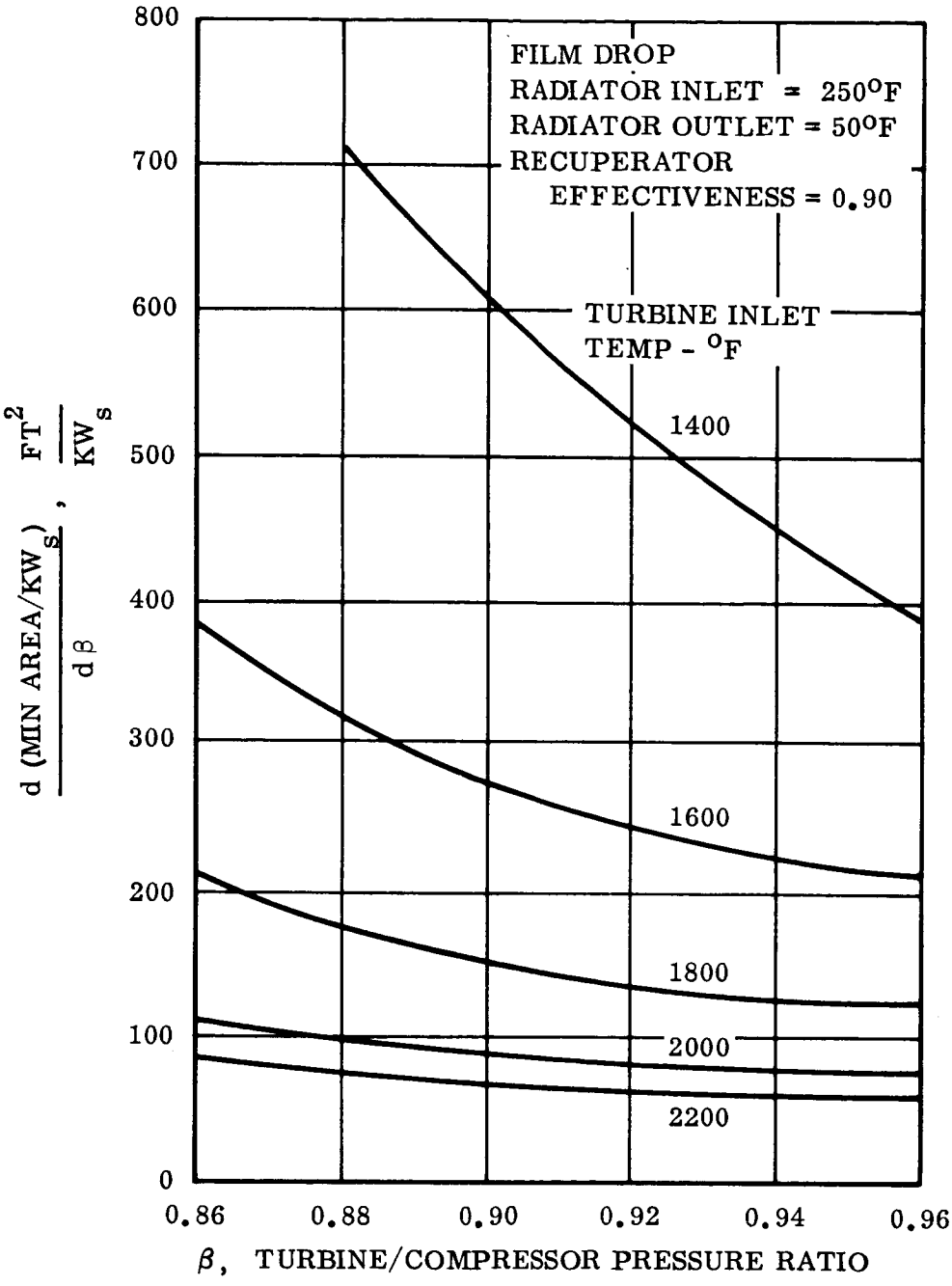

Figure A-12. $\frac{d\,(\text{Min. AREA/KW}_s)}{d\beta}$ Versus Turbine/Compressor Pressure Ratio

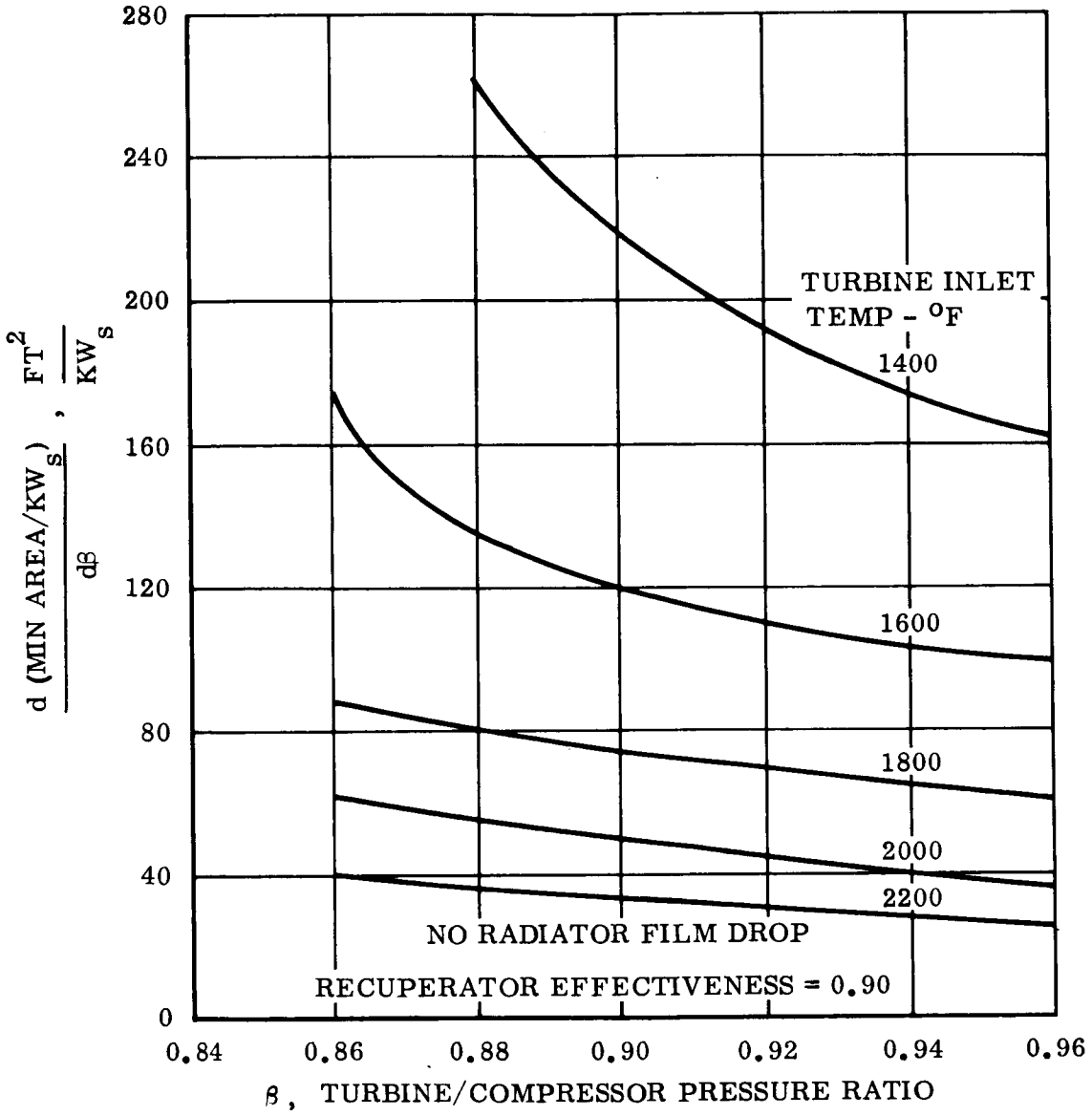

Figure A-13. $\frac{d\ (Min.\ AREA/KW_s)}{d\beta}$ Versus Turbine/Compressor Pressure Ratio

The cycle pressure ratio resulting in a minimum area radiators is shown in Figure A-14 as a function of the ratio of turbine to compressor pressure ratios. No noticeable dependence on turbine inlet temperature was found. The curves are essentially straight lines with a slope of 7.15 (change in optimum pressure ratio of 0.9715 per %). The efficiencies of minimum area cycles is shown in Figure A-15. The minimum are cycles with no film drop have an efficiency about 2% greater than those with the typical film drop shown. The influence of fractional pressure loss on cycle efficiency is not very great. Efficiency of minimum area systems are shown in Figures A-15 and A-16 as a function of the ratio of turbine to compressor pressure ratios. The sensitivity of efficiency to fractional pressure loss is less for the cycle with no radiator film drop and higher turbine inlet temperatures.

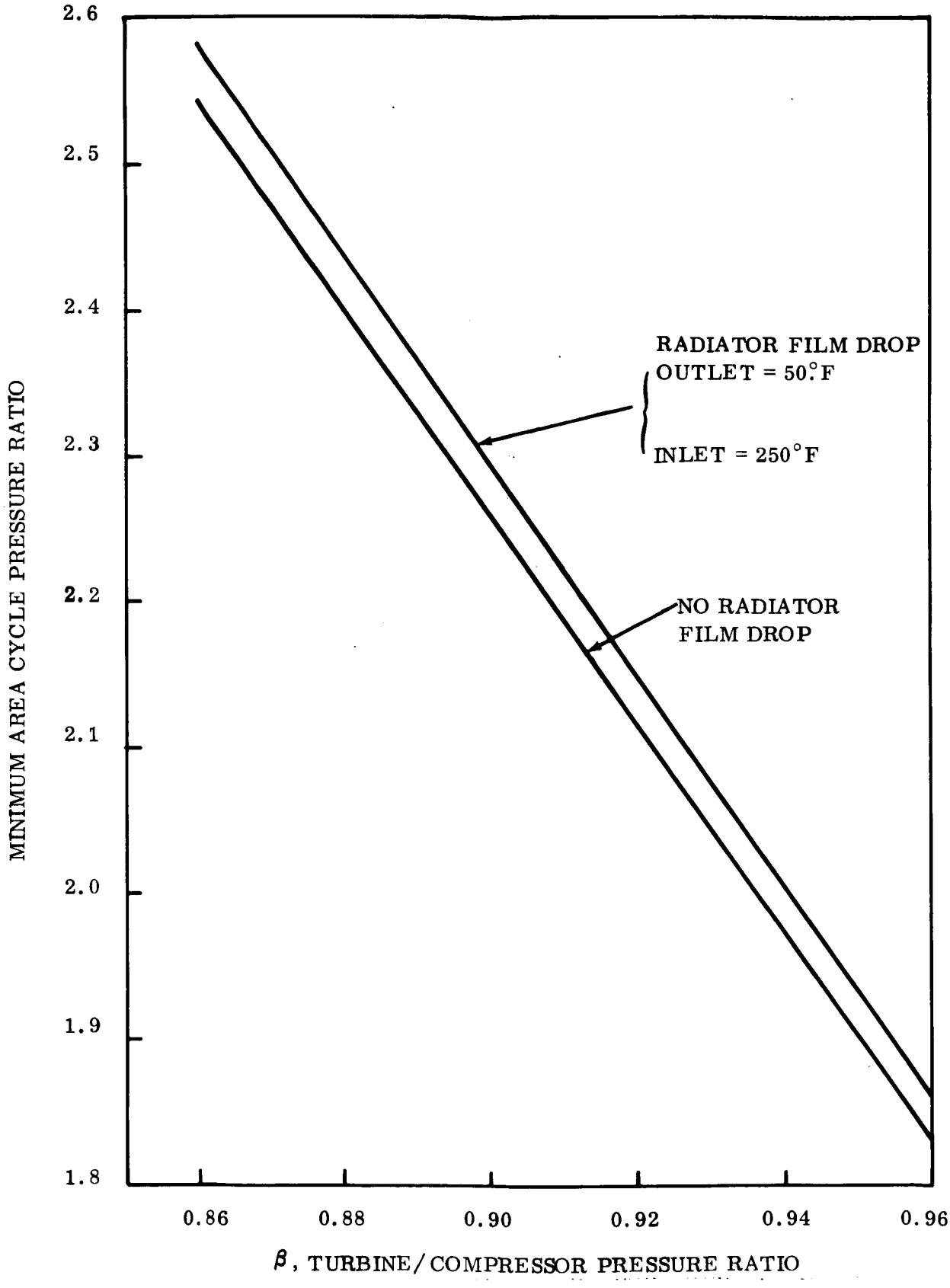

Figure A-14. Minimum Area Cycle Pressure Ratio vs. Turbine/Compressor Pressure Ratio

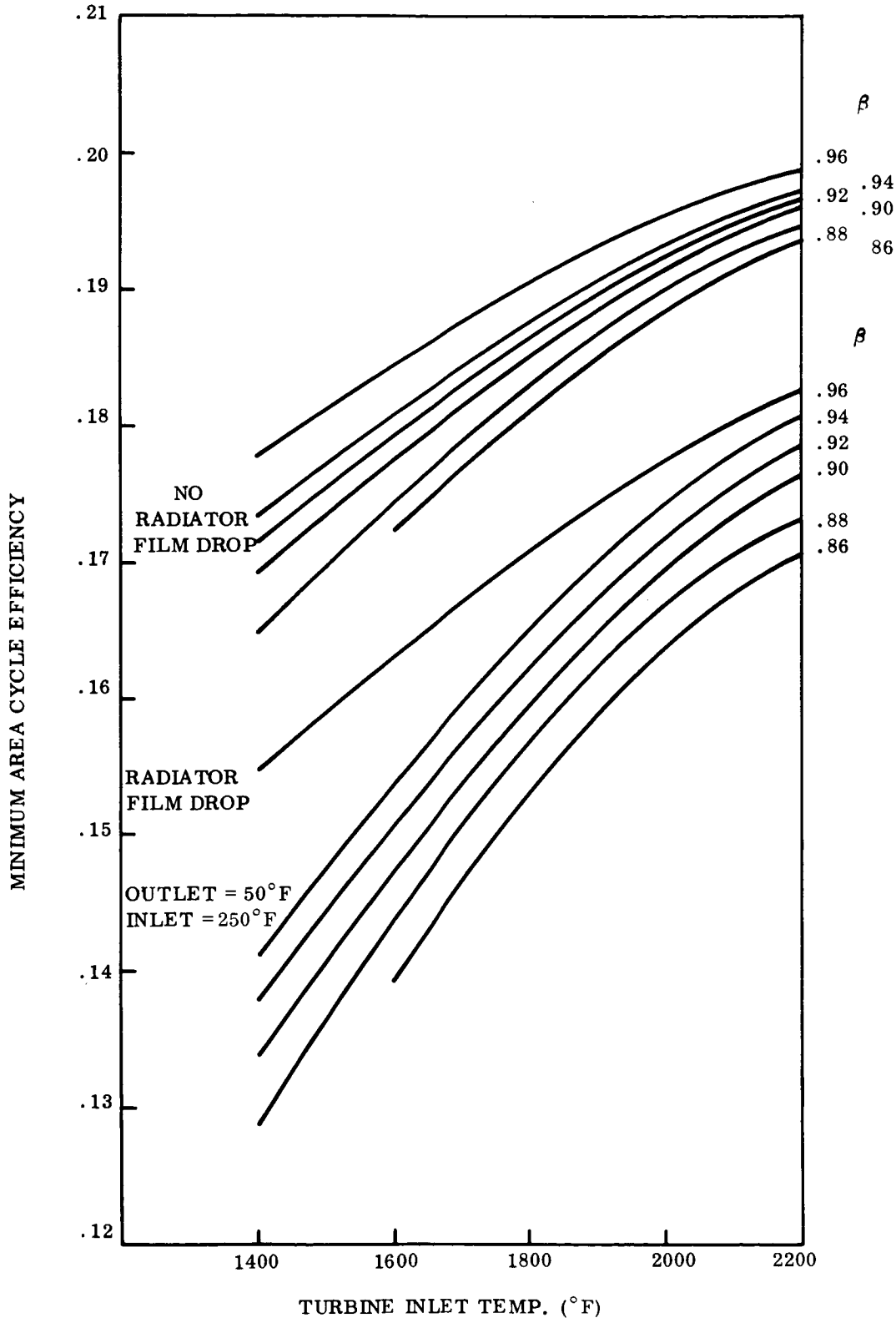

Figure A-15. Minimum Area Cycle Efficiency vs. Turbine Inlet Temperature

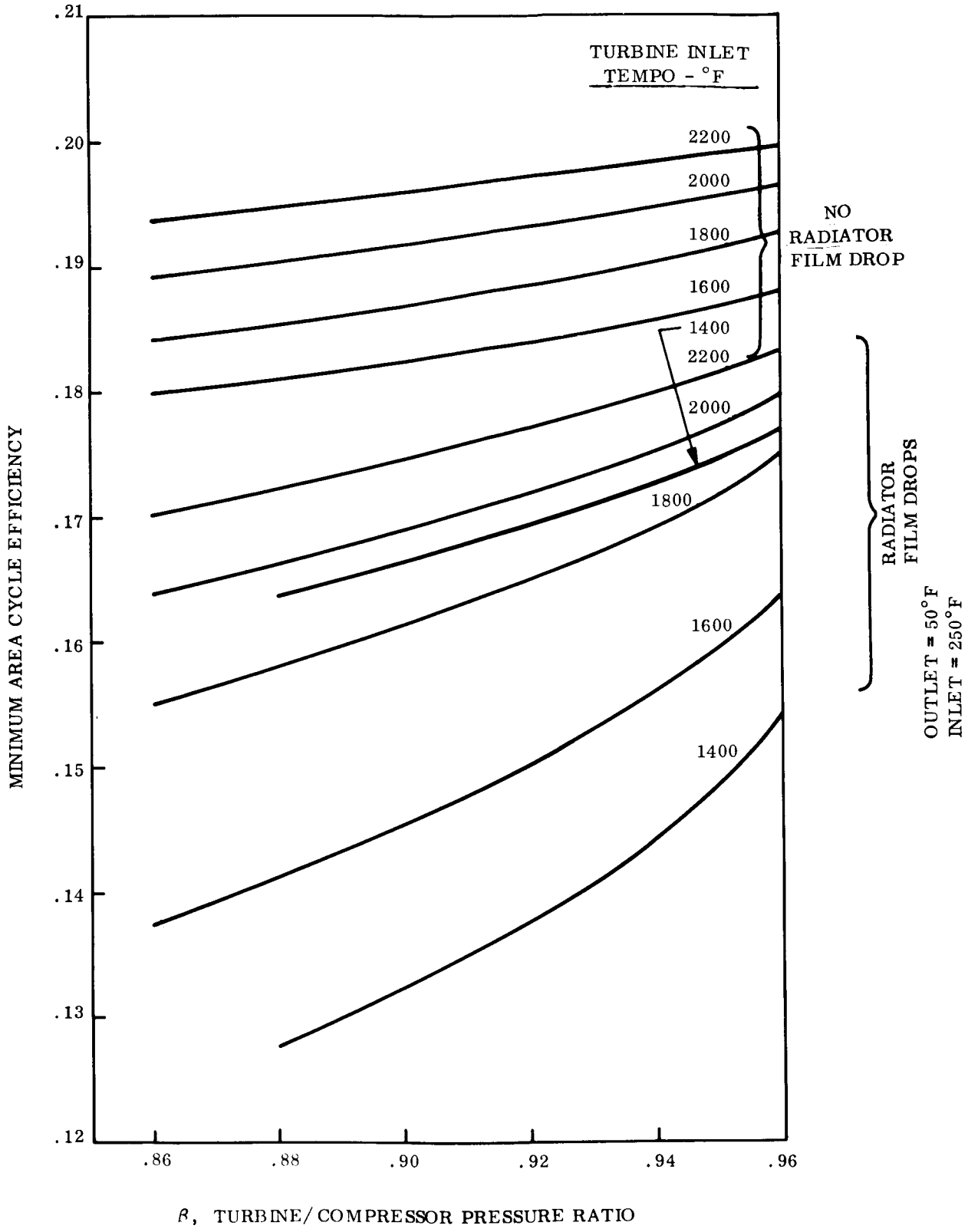

Figure A-16. Minimum Area Cycle Efficiency vs. Turbine/ Compressor Pressure Ratio

DISTRIBUTION LIST

Advanced Research Projects Agency
The Pentagon
Washington 25, DC (1)

Aerojet General Nucleonics
San Ramon, California
Attn: K. Johnson (1)

Flight Vehicle Power Branch
Air Force Aero Propulsion Lab.
Wright-Patterson AFB, Ohio 45433
Attn: APIP-I George Thompson (1)

Aeronutronics, Div of Philco Corporation
Ford Road
Newport Beach, California
Attn: Library (1)

AiResearch Manufacturing Company
PO Box 1927
Phoenix, Arizona
Attn: Lyle Six (1)

AiResearch Manufacturing Company
9851 Sepulveda Boulevard
Los Angeles, California
Attn: R. Trusala (1)

Argonne National Laboratory
9700 South Cass Avenue
Argonne, Illinois 60440
Attn: C. F. Chwierut,
Library Services Dept. (1)

Atomics International
PO Box 309
Canoga Park, California
Attn: Library (1)

AVCO Rand Corporation
201 Lowell Street
Wilmington, Massachusetts
Attn: Dr. J. G. Lundholm (1)

Battelle Memorial Institute
Columbus Laboratories
505 King Avenue
Columbus, Ohio 43201
Attn: D. Dingee (1)

Battelle-Northwest
PO Box 999
Richland, Washington 99352
Attn: H. Hardy (1)

Boeing Company
PO Box 3707
Seattle, Washington 98124
Attn: S. Silverman (1)

Chrysler Corporation
Space Division
Technical Information Center
Service Engineering Branch
PO Box 26018
New Orleans, Louisiana 70126 (1)

Douglas Aircraft Company, Inc.
3000 Ocean Park Boulevard
Santa Monica, California
Attn: Library (1)
G. McKahn (1)

Electro Optical Systems, Inc.
300 North Halstead Avenue
Pasadena, California
Attn: R. S. Toms (1)

Electronic Research Center
North Eastern Office
Cambridge, Massachusetts
Attn: Library

General Atomic
PO Box 608
San Diego 12, California
Attn: R. W. Pidd (1)

General Electric Company
Nuclear Materials & Propulsion Operation
Cincinnati, Ohio 45215
Attn: Jack Simpson (1)

Jet Propulsion Laboratory
California Institute of Technology
4800 Oak Grove Drive
Pasadena, California
Attn: R. Beale (1)
Jack Stearns (1)
John W. Goldsmith (1)
Library (1)

Lockheed Missiles and Space Division
Lockheed Aircraft Corporation
PO Box 504
Sunnyvale, California
Attn: Librarian (1)

S. V. Manson & Company, Inc.
2420 Wilson Boulevard
Arlington, Virginia 22201
Attn: S. V. Manson (1)

Martin-Nuclear
Division of Martin-Marietta Corp.
PO Box 5042
Middle River 3, Maryland
Attn: J. Levedahl

Massachusetts Institute of Technology
Cambridge 39, Massachusetts
Attn: Myron A. Hoffman (1)

National Aeronautics & Space Adm.
Manned Spacecraft Center
Houston, Texas 77001
Attn: G. Hagey (1)
Library (1)

National Aeronautics & Space Adm.
1512 H Street, NW
Washington, DC 20546
Attn: B. Resnick RNW (2)
James J. Lynch RNP (1)
T. Albert (1)
F. Schulman (1)
H. Rochen 20R3 (1) RN

National Aeronautics & Space Adm.
Lewis Research Center
21000 Brookpark Road
Cleveland, Ohio 44135
Attn: R. Mather, MS 500-309 (1)
B. Lubarsky, MS 500-201 (1)
W. Moeckle, MS 301-1 (1)
R. Denington, MS 500-309 (2)
R. Cummings, MS 500-201 (1)
J. Heller, MS 500-201 (1)
John E. Dilley, MS 500-309 (1)
D. Bernatowicz, MS 500-201 (1)
Library, MS 3-7 (1)
L. Shure, MS 500-309 (2)
W. Stewart, MS 5-9 (1)
D. Bogart, MS 49-2 (1)
R. English, MS 500-201 (1)
J. J. Weber, MS 3-16 (1)
Report Control Office, MS 5-5 (1)

National Aeronautics & Space Adm.
Ames Research Center
Moffett Field, California 94035
Attn: Library (1)

National Aeronautics & Space Adm.
Goddard Space Flight Center
Greenbelt, Maryland 20771
Attn: Library (1)
R. C. Wells (1)

National Aeronautics & Space Adm.
Langley Research Center
Langley Field, Virginia 23365
Attn: Library (1)

National Aeronautics & Space Adm.
Marshall Space Flight Center
Huntsville, Alabama 35812
Attn: Library (1)
Jerry Smith (1)
Heinz Koelle (1)
MRP-S (1)

National Aeronautics & Space Adm.
Office of Manned Space Flight
Washington, DC 20546
Attn: Warren Gillespie (1)
Fred Kassel (1)

National Aeronautics & Space Adm.
Scientific and Technical Information Facility
Box 5700
Bethesda, Maryland 20014
Attn: NASA Representative (1)

North American Aviation, Inc.
Space and Information Systems Div.
Downey, California
Attn: Library (1)

Oak Ridge National Laboratory
Oak Ridge, Tennessee
Attn: Art Fraas (1)

Pratt & Whitney Aircraft Division
Connecticut Operations CANEL
PO Box 611
Middletown, Connecticut
Attn: R. Meyers (2)

Pratt & Whitney Aircraft Corporation
East Hartford 8, Connecticut
Attn: William Lueckel (1)

The Rand Corporation
1700 Main Street
Santa Monica, California
Attn: Ben Pinkel (1)

Republic Aviation Corporation
Farmingdale, Long Island, New York
Attn: Library

Space General Corporation
9200 E. Flair Drive
El Monte, California
Attn: O. W. Welles (1)

Space Technology Laboratory
One Space Park
Redondo Beach, California
Attn: Librarian (1)

TRW Equipment Laboratories
7209 Blatt Avenue
Cleveland, Ohio 44104
Attn: D. Southam (1)

United Aircraft Research Lab.
East Hartford, Connecticut
Attn: H. O. Rix,
Chief, Library (1)

US Naval Research Lab.
Washington, DC 20390
Attn: Librarian

National Bureau of Standards
Washington 25, DC
Attn: Librarian

US Atomic Energy Commission
Division of Reactor Development
Washington 25, DC
Attn: Auxiliary Power Branch (1)
SNAP Reactors Branch/R. Oehl (1)
H. Rochen (1)
Col. Douthet (1)
T. W. McIntosh (1)
Army Reactors Branch (1)

US Atomic Energy Commission
Technical Reports Library
Washington 25, DC
Attn: J. M. O'Leary (1)

US Atomic Energy Commission
Dept. of Technical Information Ext.
PO Box 62
Oak Ridge, Tennessee (1)

US Atomic Energy Commission
CANEL Project Office
PO Box 1102
Middletown, Connecticut
Attn: H. Pennington (2)

Westinghouse Electric Corporation
Astronuclear Laboratory
PO Box 10864
Pittsburgh, Pennsylvania
Attn: Mr. Sinclair (1)

US Army Engineer R&D Labs
Gas Turbine Test Facility
Fort Belvoir, Virginia

Office of Naval Research
Department of the Navy
Washington 25, DC
Attn: Dr. Ralph Roberts

Bureau of Naval Weapons
Department of the Navy
Washington, DC
Attn: Code RAPP

Bureau of Ships
Department of the Navy
Washington 25, DC
Attn: G. L. Graves

Sunstrand Denver
2480 West 70 Avenue
Denver 21, Colorado
Attn: Librarian

Aerojet General Corporation
Azusa, California
Attn: Librarian

Union Carbide Corporation
Linde Division
61 East Park Drive
Tonawanda, New York
Attn: Librarian

Institute for Defense Analyses
400 Army Navy Drive
Arlington, Virginia 22202
Attn: Librarian

Solar
2200 Pacific Highway
San Diego 12, California
Attn: Librarian

Lockheed Missiles & Space Company
PO Box 504
Sunnyvale, California
Attn: Librarian

Bendix Research Laboratories Div.
Southfield (Detroit), Michigan
Attn: Librarian

Mechanical Technology, Inc.
968 Albany-Shaker Road
Latham, N. Y.
Attn: Librarian